

RESEARCH & REVIEWS IN SCIENCE AND MATHEMATICS - I

DECEMBER, 2021

EDITORS

PROF. DR. HASAN AKGÜL
PROF. DR. ALPASLAN DAYANGAÇ

İmtiyaz Sahibi / Publisher • Yaşar Hız

Genel Yayın Yönetmeni / Editor in Chief • Eda Altunel

Editörler/ Editors • Prof. Dr. Hasan AKGÜL

Prof. Dr. Alpaslan DAYANGAÇ

Kapak & İç Tasarım / Cover & Interior Design • Gece Kitaplığı

Birinci Basım / First Edition • © Aralık 2021

ISBN • 978-625-8075-30-4

© copyright

Bu kitabın yayın hakkı Gece Kitaplığı'na aittir.

Kaynak gösterilmeden alıntı yapılamaz, izin
almadan hiçbir yolla çoğaltılamaz.

The right to publish this book belongs to Gece Kitaplığı.

Citation can not be shown without the source, reproduced in any way
without permission.

Gece Kitaplığı / Gece Publishing

Türkiye Adres / Turkey Address: Kızılay Mah. Fevzi Çakmak 1.

Sokak Ümit Apt. No: 22/A Çankaya / Ankara / TR

Telefon / Phone: +90 312 384 80 40

web: www.gecekitapligi.com

e-mail: gecekitapligi@gmail.com

Baskı & Cilt / Printing & Volume

Sertifika / Certificate No: 47083

Research & Reviews in Science and Mathematics - I

December, 2021

Editors

Prof. Dr. Hasan AKGÜL
Prof. Dr. Alpaslan DAYANGAÇ

CONTENTS

Chapter 1

RECENT WORKS ON THE ASYMMETRIC REDUCTION OF KETONES BY ORGANOBORON CATALYSTS

Tülay YILDIZ 1

Chapter 2

MOLECULAR DOCKING TOOLS AND THEIR BASIC USAGE IN DRUG DESIGN AND DISCOVERY

Can YILMAZ..... 17

Waleed MOHAMMED KHORSHEED..... 17

Chapter 3

EVENT DENSITY VISUALIZATION WITH PYTHON FOLIUM LIBRARY FOR PUBLIC COMPLAINT MANAGEMENT: AN APPLICATION WITH 311 CALLS

Emre OZMEN..... 41

Chapter 4

THE INFLUENCE OF PH VALUES ON THE OPTOELECTRONIC, ELLIPSOMETRIC, AND SURFACE PROPERTIES IN THE PRODUCTION OF COBALT-DOPED ZNO FILMS

Olcaý Gençýılmaz..... 51

Chapter 5

DRUGS USED IN THE TREATMENT OF VIRAL INFECTIONS AND INNOVATIONS IN ANTIVIRAL THERAPY

Fatma ÇETİNKAYA 71

Hülya ÇELİK 71

Chapter 6

SYNTHESIS OF BORON NITRIDE BY SOLID STATE REACTIONS: DESIGNATION OF BARIUM SALTS EFFECT

Muhammed OZ 105

Asaf Tolga ULGEN 105

Chapter 7

DYNAMICS OF CHIRONOMIDAE (DIPTERA) LARVAL IN OĞULPAŞA STREAM (EDİRNE/TURKEY)

Nurcan ÖZKAN..... 121

Chapter 8

INFLUENCE OF CADMIUM ADDITION ON ELECTRICAL
AND SUPERCONDUCTING FEATURES OF BULK
Bi₂Sr₂O₂Ca_{1-x}Cu₂O_y SUPERCONDUCTING MATERIALS

Asaf Tolga ULGEN	139
Mustafa Burak TURKOZ	139
Muhammed OZ	139

Chapter 9

ENERGY LOSS AND CSDA RANGE CALCULATIONS OF A-150
TISSUE EQUIVALENT PLASTIC AND MYLAR FOR ALPHA
PARTICLE AND PROTONS

Metin USTA.....	153
-----------------	-----

Chapter 10

ON THE ZAGREB AND RANDIC INDICES OF A GRAPH

Gül Özkan Kızılırmak.....	169
Emre SEVGI	169

Chapter 11

VERTICES OF SUBORBITAL GRAPH $F_{u,N}$ AND SEQUENCE
 d_n DEFINED IN HECKE GROUP

İbrahim GÖKCAN.....	187
Ali Hikmet DEĞER.....	187

Chapter 12

ON THE CHARACTERIZATION OF DUAL LINES IN D^3

Muhsin Incesu.....	205
--------------------	-----

Chapter 1

RECENT WORKS ON THE ASYMMETRIC REDUCTION OF KETONES BY ORGANOBORON CATALYSTS

Tülay YILDIZ¹

¹ Istanbul University-Cerrahpaşa, Engineering Faculty, Chemistry Department. Organic Chemistry Division, 34320 Avcılar-İstanbul/TURKEY. ORCID ID: <https://orcid.org/0000-0001-5857-2480>.

Chiral alcohols and their derivatives obtained by enantioselective hydrogenation of prochiral ketones are very important starting or intermediates for the synthesis of biologically active or natural compounds. For this purpose, chiral alcohols are worth materials for drug, food, agriculture, and cosmetic industries owing to their biological activity based on their optical purity. Therefore, chemists, have broadly explored various synthetic methods to synthesize enantiomerically pure chiral alcohols (Wallbaum & Martens, 1992; Singh, 1992; Deloux & Srebnik, 1993; Seyden-Penn, 1995).

The compounds having carbonyl groups are amongst the most effective starting materials to synthesize enantiomerically enriched alcohols for synthetic organic chemists. A principal way to synthesize chiral alcohols is the asymmetric reduction of corresponding prochiral ketones. This kind of reduction method can be grouped into two classes, chemically and biochemically. Chemical methods contain the use of chiral ligands, reagents, or complexes are frequently utilized. In recent years, many important synthetic operation methods have been found to synthesize chiral valuable alcohols from corresponding ketones. The most famous among them are chiral catalysts based on some chemical or biochemical methods. Chemical methods involve generally chiral complexes of boron, ruthenium, or phosphoric acid with some chiral ligands. In biochemical methods, it is used enzymes or enzymes sources such as yeast, bacteria, plant, or fungi.

One of the most important methods was developed by Noyori and his friends. Noyori developed bifunctional Ru(II) - diphosphine/diamine catalyst system in 1995 (Noyori & Hashiguchi, 1997). This method and its chiral ligands over recent years have been used and ensured a wide range of diphosphines appropriate to obtain Ru(II) based catalyst in the asymmetric reduction of unactivated ketones.

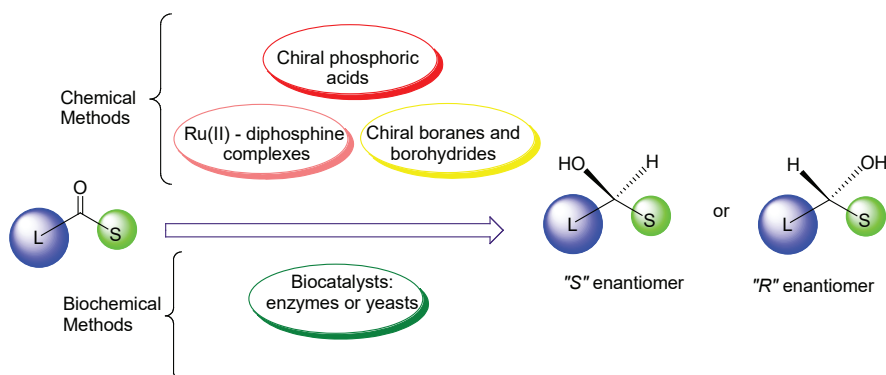


Figure 1. Most favored asymmetric reduction methods

On the other hand, chiral borohydrides and boranes are important reagents using asymmetric reductions as well. Brown made the greatest contribution to the development of this method (Brown & Krishnamurthy, 1979; Brown & Ramachandran, 1996). Even though sodium borohydride is a very general reducing agent, there are only a few in a number of works using NaBH_4 as a chiral reagent (Nishizawa & Noyori, 1991; Kucuk et al., 2017).

Corey and Itsuno are pioneers in the oxazaborolidine method and after their works, a number of concerned chiral catalysts have been developed for enantioselective borane reduction (Hirao, et al., 1981; Corey, et al., 1987; Wallbaum & Martens, 1992). Since the prominent Corey-Bakshi-Shibata (CBS) oxazaborolidine catalyst was discovered by Corey et al. from prolines enantiomers, most novel chiral oxazaborolidines have been synthesized and used broadly in asymmetric reductions. (Itsuno et al., 1989).

The second class of asymmetric reduction of carbonyl substrates is biocatalytic methods which are useful and suitable for green chemistry preparative methods to obtain chiral compounds. These methods offer environmentally friendly, easy bioavailability, mild and cheap reaction conditions (Csuk & Glanzer, 1991). Enzymes are interesting natural biocatalysts in stereoselective reactions (Nakamura, et al. 2003; Ni et al. 2009; Yaşa & Yusufoglu, 2018; Ludeke, et al. 2009; Kucuk & Yusufoglu, 2013).

In recent years, asymmetric reduction studies of carbonyl compounds have increasingly continued and new catalysts have been developed. Especially organoboron compounds have been playing an increasingly important role in organic synthesis and asymmetric reduction of prochiral ketones. Since the asymmetric synthesis of chiral alcohols in the presence of (S)-diphenylvalinol was reported by Itsuno et al (Itsuno, 1998; Itsuno, et al., 1983), chemists have studied extensively borane chemistry trying varied chiral amino alcohols. There have been using different types of chiral catalysts, for example, sulfoximines (Bolm & Felder, 1993), phosphoramides (Li, et al., 2003), BINOL derivatives (Lin et al., 2001), and sulfonamides (Li et al., 2008) for asymmetric borane reduction of prochiral ketones.

When we look at the prominent works of the last ten years, we see a lot of important studies. Asami et al. obtained some new chiral diamines for the catalytic enantioselective borane reduction of ketones in 2013. They succeeded in synthesizing chiral secondary alcohols with very high enantiomeric excesses (up to 98% ee) (Hosoda, et al., 2013).

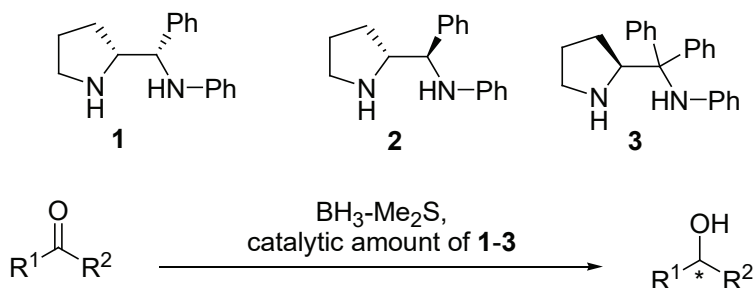


Figure 2. Asymmetric reduction of prochiral ketones in the presence of chiral diamines.

Zhang et al. synthesized new chiral polyethers derived from 1,1'-bi-2-naphthol (BINOL) as very effective catalysts for the synthesis of chiral secondary alcohols with borane. They obtained the desired products with up to 98% yields and over 99% ee values using polyethers (Zhang et al., 2015a; Zhang et al., 2015b).

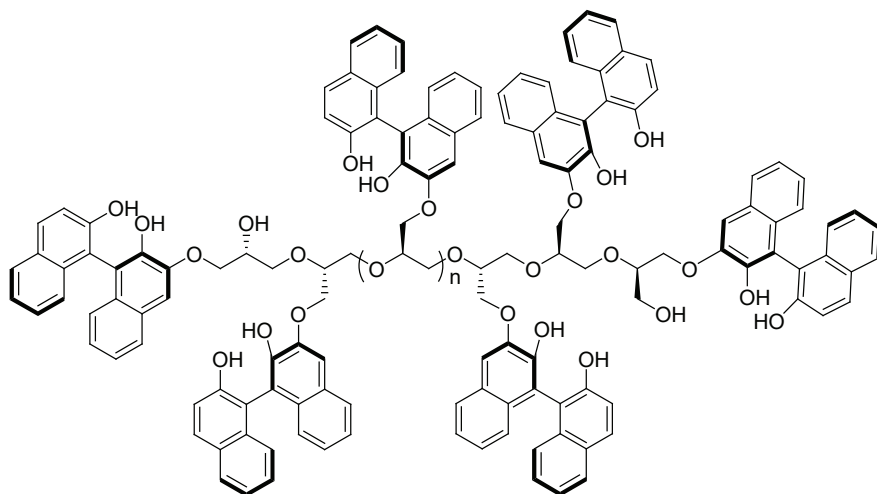


Figure 3. Chiral polyether ligand (Poly5) derived from BINOL.

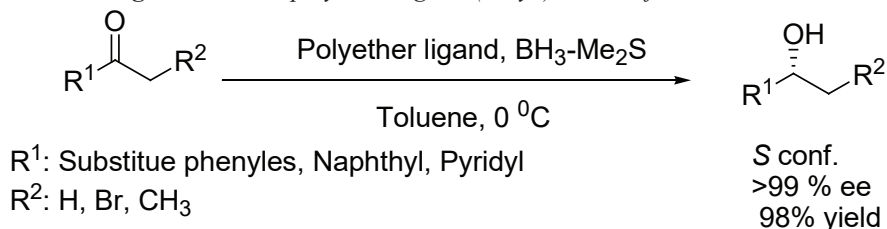


Figure 4. Asymmetric borane reduction using chiral polyether ligand.

Turgut and his friends were prepared several β -hydroxyamide-based ligands for enantioselective reductions of prochiral ketones. While new derivatives of β -hydroxyamide-based ligands were obtained from salicylic acid in their studies in 2013 (Turgut et al., 2013) (Figure 5), another type of β -hydroxyamide-based ligands were derived from 3-hydroxy-2-naphthoic acid in other studies in 2015 (Azizoglu, et al., 2016) (Figure 6).

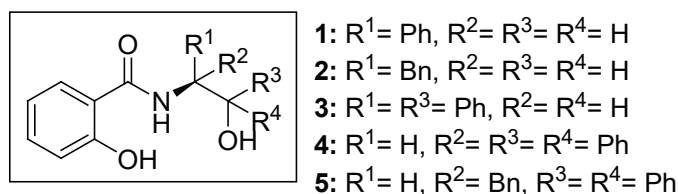


Figure 5: New β -hydroxyamide-based ligands were obtained from salicylic acid.

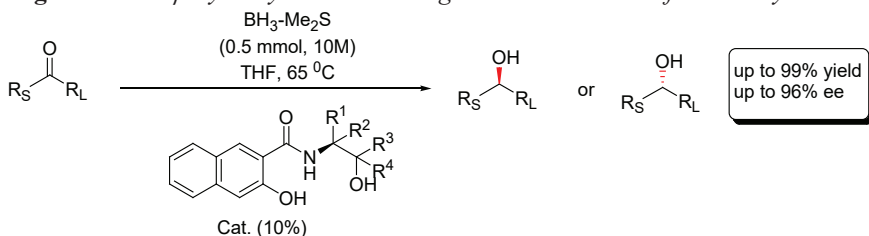


Figure 6: Asymmetric borane reduction using β -hydroxyamide-based ligands obtained from 3-hydroxy-2-naphthoic acid.

Cifunte and Tonn synthesized 2-methoxy-dioxaborolane from 2 α ,3 α -dihydroxycativic acid as a new chiral borane catalyst for asymmetric reduction of prochiral ketones. They obtained very good chemical yields with 85-97% and high enantioselectivities 62-96% ee (Cifunte & Tonn, 2012).

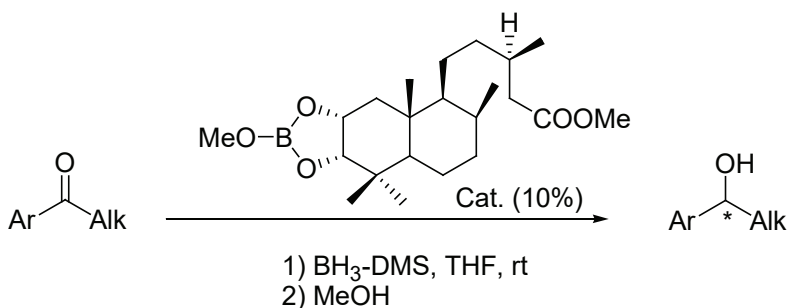


Figure 7: Asymmetric borane reduction using 1,3,2-dioxaborolane derived from a natural diterpene.

In another work, new chiral oxazaborolidine complexes were prepared for asymmetric reduction of prochiral ketones. For this purpose,

the chiral oxazaborolidine complex was immobilized by two-dimensional silica SBA-15 using 3-aminopropyltriethoxysilane as a reactive surface modifier (Balakrishnan et al., 2010). Along with this work, the effect of the immobilized chiral oxazaborolidine ligands was explored by a new synthetic approach for the asymmetric reduction of aromatic prochiral ketones.

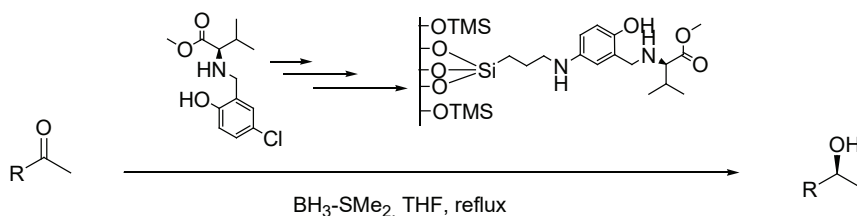


Figure 8: *Asymmetric borane reduction using chiral oxazaborolidine complex immobilized SBA-15.*

As an alternative catalyst, spiroborate esters are used in enantioselective carbonyl reduction. Especially their chiral amino acids or 1,2-amino alcohols derivatives show excellent catalytic activity in the enantiomeric inductions of prochiral ketones. In a recent study, a new synthesis of spiroborate esters, derived from terpene amino alcohols was achieved as catalysts in the borane-based reduction of prochiral ketones. In this work, chiral secondary alcohols were obtained with very good yields and with high ee values up to 98% ee (Cwiklinska et al., 2015).

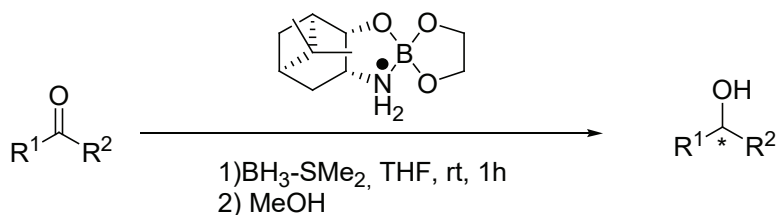


Figure 9: *Asymmetric borane reduction using spiroborate esters.*

Another study of spiroborate ester catalysts has been reported by Chopade et al. in 2021. In this study, a chiral spiroborate ester was used successfully as a catalyst in the enantioselective reduction of some benzyl-derived ketones. A new borane reduction method has been successfully used to obtain a chiral benzofuran compound via enantioselective reduction of a benzyl-derived ketone using a chiral spiroborate catalyst (Patil et al., 2021).

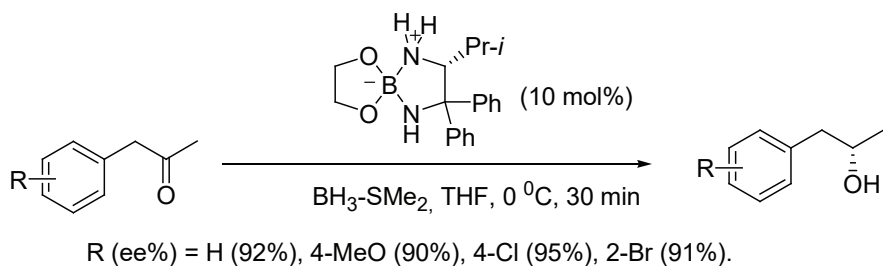


Figure 10: Asymmetric benzyl keton reduction by chiral spiroborate catalyst.

Singh and his friends developed a new ligand for asymmetric borane reduction in 2015. They synthesized α,α -diphenyl-(L)-prolinol modified with imidazolium ionic liquids (ILs) with tetrafluoroborate and hexafluorophosphate anions (Chauhan et al., 2015).

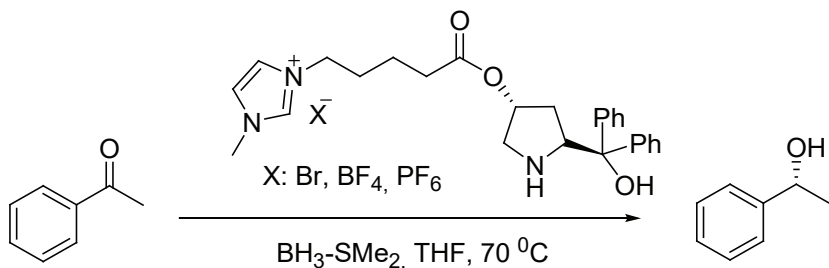


Figure 11: Asymmetric reduction of acetophenone via α,α -diphenyl-(L)-prolinol modified with imidazolium ionic liquids (ILs).

Cimarelli et al. reported in 2010 novel tridentate 1-(aminoalkyl) naphthols, and γ -amino alcohols as chiral ligand. The ligands were properly applied as catalytic sources in the borane-mediated enantioselective reduction of acetophenone with borane dimethylsulfide with very good yields (Cimarelli et al., 2010).

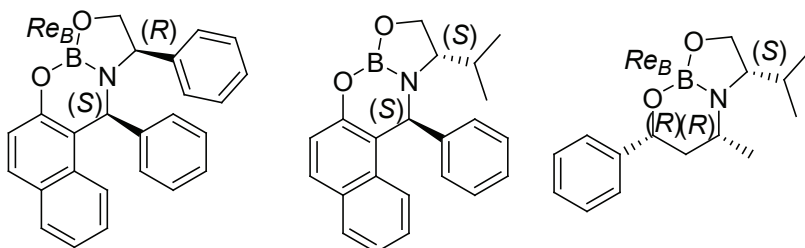


Figure 12: Structures of oxazaborolidines formed by tridentate 1-(aminoalkyl) naphthols, and γ -amino alcohols.

Lindsay and his friend developed new chiral N-heterocyclic carbene (NHC)–borane and diorganoborane complexes for asymmetric reduction of prochiral ketones in 2010. They obtained desired chiral secondary alcohols with enantioselectivities up to 75% and 85% ee, respectively (Lindsay & McArthur, 2010).

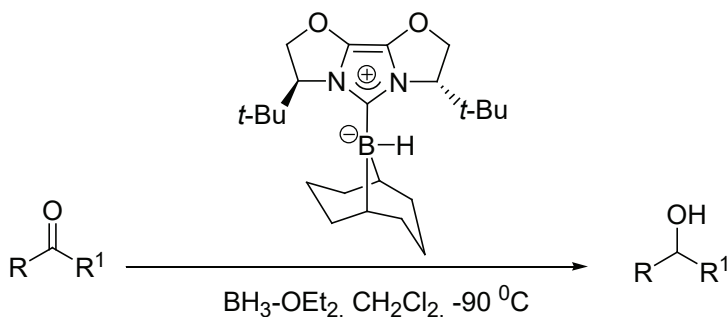


Figure 13: Asymmetric ketone reduction by NHC–borane complex.

Besides the classical oxazaborolidines, two novel tricyclic 1,3,2-oxazaborolidines were synthesized in seven steps by Breuning et al. in 2016. This new type of tricyclic oxazaborolidine derivative ensures perfect enantioselectivities of up to 98% ee for the asymmetric borane reduction of ketones and its activity is comparable to that of the standard CBS catalyst (Kaldun et al., 2016).

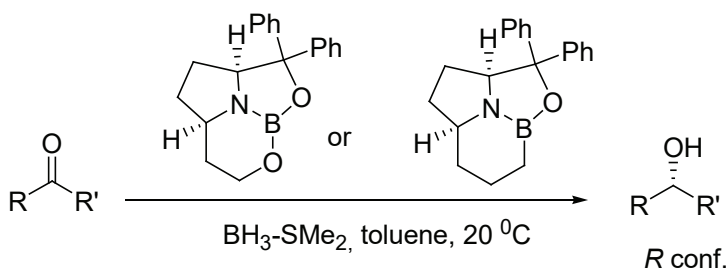


Figure 14: Reduction of prochiral ketones in the presence of tricyclic 1,3,2-oxazaborolidines.

In another important study, cyclic trimeric borazine derivatives were synthesized from chiral β -amino alcohol-derived *N*-borane catalysts and their catalytic activities in the asymmetric reduction of prochiral ketones were investigated. The study showed that both the noncyclic and cyclic catalysts successfully catalyzed this reaction, giving the desired secondary alcohols in up to 82% isolated yield and with up to 80% enantioselectivity (Pinaka et al., 2013).

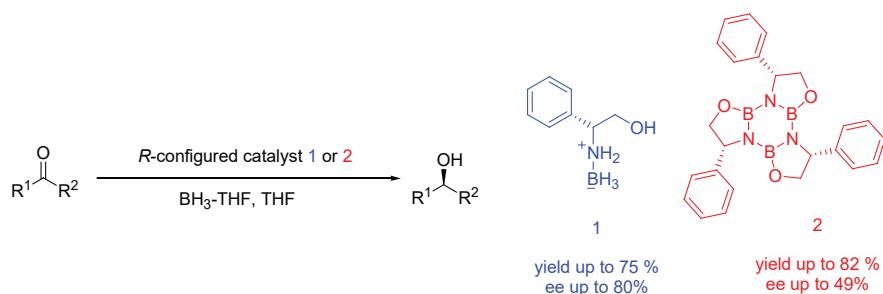


Figure 15: Reduction of prochiral ketones in the presence of cyclic trimeric borazines.

Ortiz-Marciales et al. reported an example of asymmetric reduction of α -halo ketones using aminoborate complexes (Huang et al., 2011). In this study, spiroaminoborate ester derived from diphenylprolinol was used to synthesize chiral α -halo secondary alcohols very effectively.

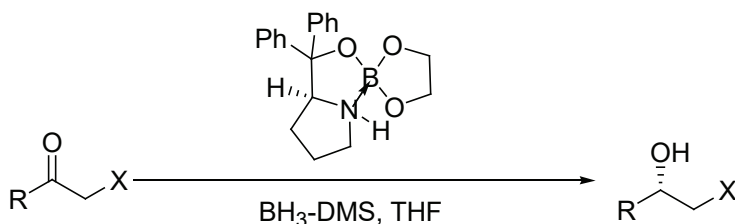


Figure 16: Asymmetric reduction of α -halo ketones via spiroaminoborate ester complex.

In 2010, Yıldız and Yusufoglu synthesized some long-chain secondary alcohols as enantioselective in the presence of chiral oxazaborolidine catalysts. Therefore new chiral alcohols configured *S* with alkyl (C_{11} – C_{19}) and aryl, substituted aryl, heteroaryl, and biaryl groups were obtained by asymmetric borane reduction with very good yields and enantioselectivities (Yıldız & Yusufoglu, 2010).

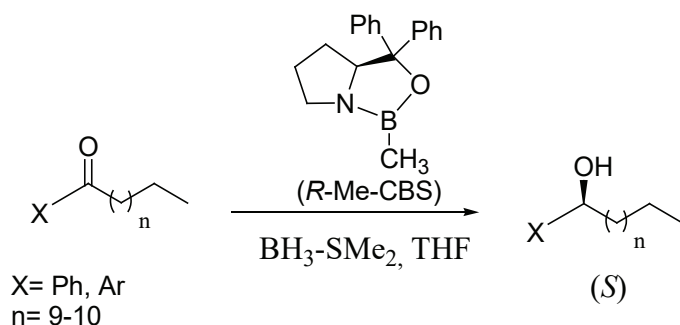


Figure 17: Asymmetric reduction of long-chain prochiral ketones by *R*-Me-CBS.

In another study, Yıldız achieved synthesizing of chiral allylic alcohols using chiral oxazaborolidine catalysts. She reported the first enantioselective reduction of tetralone, indanone, and n-alkane with a longer chain length of the derivatives of α,β -unsaturated ketones (chalcones) in the presence of chiral oxazaborolidine catalyst obtained from various chiral amino alcohols and boron reagents (Yıldız, 2015).

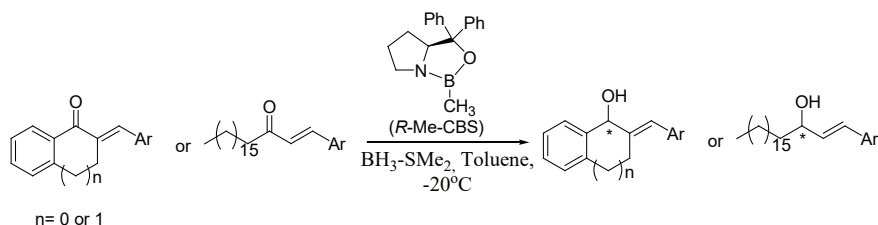


Figure 18: Asymmetric synthesis of chiral allylic alcohols in the presence of chiral oxazaborolidine catalyst.

Mahale et al. reported an example of asymmetric reduction of ketones using in situ prepared N, N-diethylaniline borane (DEANB), and oxazaborolidine catalyst from sodium borohydride, N, N-diethylaniline hydrochloride and (S)- α,α -diphenylprolinol. This study shows that a new method for asymmetric reduction of prochiral ketones yielding chiral alcohol intermediates useful for the synthesis of some selective serotonin reuptake inhibitors (SSRIs) and selective norepinephrine reuptake Inhibitors (SNRIs) (Mahale et al., 2012).

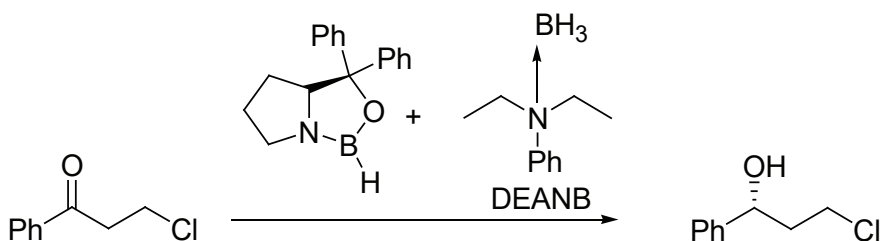


Figure 19: Asymmetric reduction of ketones in the presence of N, N-diethylaniline borane (DEANB), and oxazaborolidine catalyst.

Sakai and his friends presented in 2010 that trifluoroacetophenone could be reduced to chiral alcohol up to 90% ee by using an electronically tuned-CBS catalyst with BH_3 . They claim that such electronic control of CBS catalysis should be efficient for other highly reactive substrates if the relationship between catalyst and substrate is well designed (Sakai et al., 2010).

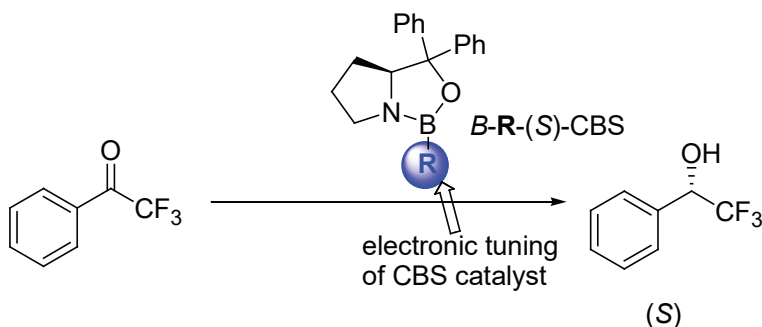


Figure 20: Rational electronic tuning of CBS catalyst for highly enantioselective borane reduction of trifluoroacetophenone.

In 2011, Kawanami et al. developed a kind of oxazaborolidine catalyst composed in situ from chiral lactam alcohol. They achieved the enantioselective reduction of α,β -enones in toluene at $-40\text{ }^\circ\text{C}$ with high enantioselectivity in the presence of chiral lactam alcohol and 4-I-PhOBH₂ (Kawanami et al. 2011).

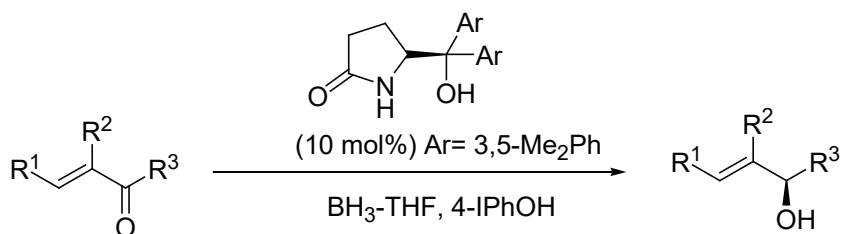


Figure 21: Enantioselective reduction of α,β -enones using oxazaborolidine catalyst derived from chiral lactam alcohol.

The same group demonstrated that the reaction of BF₃-THF to an oxazaborolidine catalyst obtained from chiral lactam alcohol and borane enhanced the enantioselectivities (up to 90% ee) and yield (up to 91%) during the reduction of some aryl trifluoromethyl ketones at room temperature (Harauchi Et Al., 2015).

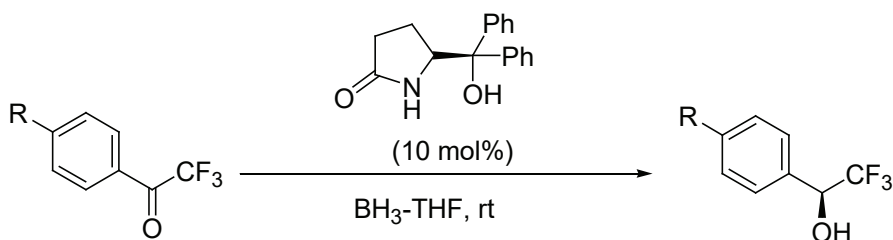


Figure 22: Enantioselective reduction of trifluoromethyl ketones in the presence of chiral lactam alcohol.

Dong et al. reported in 2011 the use of the prolinol-squaramide catalyst obtained from squaric acid and proline for asymmetric reduction of prochiral ketones. They achieved high yields and excellent enantioselectivities (up to 95% yield, 93% ee) using only 5 mol % novel C3-symmetric prolinol-squaramide catalyst prepared in two steps from commercially available squaric acid and proline with excellent yields.

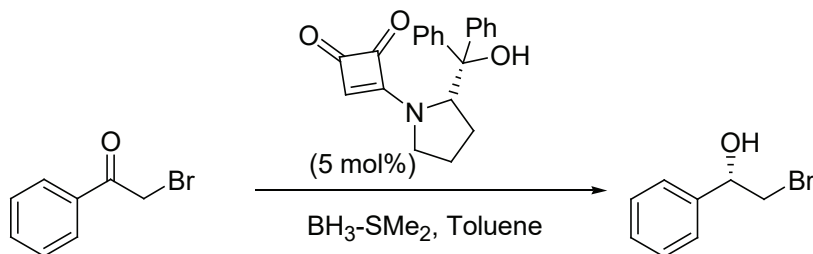


Figure 23: Asymmetric reduction of prochiral ketones using C3-symmetric prolinol-squaramide catalyst.

REFERENCES

- Azizoglu, M., Erdogan, A., Arslan, N., Turgut, Y., Hosgoren, H., & Pirinccioglu, N., (2016). A series of novel β -hydroxyamide based catalysts for borane-mediated enantioselective reductions of prochiral ketones. *Tetrahedron: Asymmetry*, 27, 614–622.
- Balakrishnan, U., Ananthi, N., Selvan, S. T., Pal, R., Ariga, K., Velmathi, S., & Vinu, A., (2010). Preparation and Characterization of Chiral Oxazaborolidine Complex Immobilized SBA-15 and Its Application in the Asymmetric Reduction of Prochiral Ketones. *Chem. Asian J.*, 5, 897–903.
- Bolm, C., & Felder, M. (1993). β -Hydroxysulfoximines in the catalyzed enantioselective reduction of ketones with borane. *Tetrahedron Lett.* 34, 6041–6044.
- Brown, H.C., & Krishnamurthy, S. (1979). Forty years of hydride reductions. *Tetrahedron*, 35, 567–607.
- Brown, H.C., & Ramachandran, P.V. (1996). Sixty years of Hydride Reduction, in *Reductions in Organic Synthesis*. (ed. A.F. Abdel - Magid), American Chemical Society, Washington, DC
- Chauhan, M.M.S., & Singh, S. (2015). Asymmetric reduction of ketones catalyzed by α,α -diphenyl-(L)-prolinol modified with imidazolium ionic liquid and $\text{BH}_3 \cdot \text{SMe}_2$ as a recoverable catalyst. *Journal of Molecular Catalysis A: Chemical*, 398, 184–189.
- Cifuentes, D. A. & Tonn, C.E., (2012), A chiral 1,3,2-dioxaborolane derived from a natural diterpene for asymmetric reduction of prochiral ketones. *Org. Commun.* 5(2), 77-82.
- Cimarelli, C., Fratoni, D., & Palmieri, G. (2010). Borane-mediated asymmetric reduction of acetophenone by enantiopure aminonaphthols and aminoalcohols as catalytic source. *Chirality*, 22, 655–661.
- Corey, E.J., Bakshi, R.K., & Shibata, S. (1987). Highly enantioselective borane reduction of ketones catalyzed by chiral oxazaborolidines. Mechanism and synthetic implications. *Journal of the American Chemical Society*, 109, 5551–5553.
- Csuk, R., & Glanzer, B. I. (1991). Baker's Yeast Mediated Transformations in Organic Chemistry. *Chem. Rev.* 91 (1) 49–97.
- Cwiklinska, M., Krzeminski, M. P., & Tafelska-Kaczmarek, A., (2015). Chiral terpene auxiliaries III: spiroborate esters from (1*R*,2*S*,3*R*,5*R*)-3-amino-apopinane-2-ol as highly effective catalysts for asymmetric reduction of ketones with borane. *Tetrahedron: Asymmetry*, 26, 1453–1458.
- Deloux, L., & Srebnik, M. (1993). Asymmetric boron-catalyzed reactions. *Chem. Rev.* 93, 763-784.
- Harauchi, Y., Takakura, C., Furumoto, T., Yanagita, R. C., & Kawanami, Y. (2015). Effect of BF_3 on the enantioselective reduction of trifluoromethyl ketones using a chiral lactam alcohol with borane. *Tetrahedron: Asymmetry*, 26, 333–337.

- Hirao, A., Itsuno, S., Nakahama, S., & Yamazaki, N. (1981). Asymmetric Reduction of Aromatic Ketones with Chiral Alkoxy-amineborane Complexes. *Journal of the Chemical Society, Chemical Communications*, 315–317.
- Hosoda, N., Kamito, H., Takano, M., Takebe, Y., Yamaguchi, Y., & Asami, M. (2013). Synthesis of chiral 2-(anilinophenylmethyl)pyrrolidines and 2-(anilindiphenylmethyl)pyrrolidine and their application to enantioselective borane reduction of prochiral ketones as chiral catalysts. *Tetrahedron*, 69, 1739–1746.
- Huang, K., Wang, H., Stepanenko, V., Jesus, M.D., Torruellas, C., Correa, W., & Ortiz-Marciales, M., (2011). Chiral Epoxides via Borane Reduction of 2-Haloketones Catalyzed by Spiroborate Ester: Application to the Synthesis of Optically Pure 1,2-Hydroxy Ethers and 1,2-Azido Alcohols. *J. Org. Chem.*, 76, 1883–1886.
- Itsuno, S., (1998). Enantioselective Reduction of Ketones. *Org. React.* 52, 395–576.
- Itsuno, S., Ito, K., Hirao, A., & Nakahama, S. (1983). Asymmetric reduction of aromatic ketones with the reagent prepared from (S)-(-)-2-amino-3-methyl-1,1-diphenylbutan-1-ol and borane. *J. Chem. Soc., Chem. Commun.* 469–470.
- Itsuno, S., Sakurai, Y., Shimizu, K., & Ito, K. (1989). Asymmetric reduction of ketoxime O-alkyl ethers with sodium borohydride–Lewis acid. *J Chem Soc Perkin Trans 1*, 1548–1549.
- Kaldun, J., Krimalowski, A., & Breuning, M. (2016). Enantioselective borane reduction of ketones catalyzed by tricyclic 1,3,2-oxazaborolidines. *Tetrahedron Letters*, 57, 2492–2495.
- Kawanami, Y., Mikami, Y., Kiguchi, K., Harauchi Y., & Yanagita, R. C. (2011). Enantioselective reduction of α,β -enones using an oxazaborolidine catalyst generated in situ from a chiral lactam alcohol. *Tetrahedron: Asymmetry*, 22, 1891–1894.
- Korenaga, T., Nomura, K., Onoue, K., & Sakai, T., (2010). Rational electronic tuning of CBS catalyst for highly enantioselective borane reduction of trifluoroacetophenone *Chem. Commun.*, 2010, 46, 8624–8626.
- Kucuk, H., & Yusufoglu, A. (2013). Enantioselective synthesis of 3-hydroxytetradecanoic acid and its methyl ester enantiomers as new antioxidants and enzyme inhibitors. *Monatshefte Fur Chemie*, 144(7), 1087–1091.
- Kucuk, H., Yasa, H., Yildiz, T. & Yusufoglu, A. (2017). Detailed studies on the reduction of aliphatic 3-, 4-, 6-, and 13-oximino esters: Synthesis of novel isomeric amino esters, oximino alcohols, and amino alcohols. *Synthetic Communications*, 47(22), 2070–2077.
- Li, K., Zhou, Z., Wang, L., Chen, Q., Zhao, G., Zhou, Q., & Tang, C. (2003). Asymmetric carbonyl reduction with borane catalyzed by chiral phosphinamides derived from l-amino acid. *Tetrahedron: Asymmetry*, 14, 95–100.

- Li, K., Zhou, Z., Wang, L., Chen, Q., Zhao, G., Zhou, Q., & Tang, C. (2003). Asymmetric carbonyl reduction with borane catalyzed by chiral phosphinamides derived from l-amino acid. *Tetrahedron: Asymmetry*, 14, 95–100.
- Lindsay, D.M., & McArthur, D. (2010). Enantioselective borane reduction of ketones catalyzed by tricyclic 1,3,2-oxazaborolidines. *Chem. Commun.*, 46, 2474–2476.
- Ludeke, S., Richter, M., & Muller, M. (2009). Stereoselective Synthesis of Three Isomers of tert-Butyl 5-Hydroxy-4-methyl-3-oxohexanoate through Alcohol Dehydrogenase-Catalyzed Dynamic Kinetic Resolution. *Adv. Synth. Catal.*, 351, 253–259.
- Mahale, R.D., Chaskar, S.P., Patil, K.E., Maikap, G.C., & Gurjar, M., K. (2012). Corey–Itsuno Reduction of Ketones: A Development of Safe and Inexpensive Process for Synthesis of Some API Intermediates. *Org. Process Res. Dev.* 16, 710–713.
- Nakamura, K., Yamanaka, R., Matsuda, T., & Harada, T. (2003). Recent developments in asymmetric reduction of ketones with biocatalysts. *Tetrahedron: Asymmetry*, 14, 2659–2681.
- Ni, H. L., Guan, Y. X., & Yao, S. J. (2009). A combined process of biocatalysis and cell activity regeneration for the asymmetric reduction of 3-oxo ester with immobilized baker's yeast. *J. Chem. Technol. Biotechnol.*, 84, 186–191.
- Nishizawa, M., & Noyori, R. (1991). Comprehensive Organic Synthesis : Selectivity, strategy and efficiency in modern organic chemistry. Ed. B. M. Trost and I. Fleming, *Pergamon Press, Oxford*, 8, p 159.
- Noyori, R., & Hashiguchi, S. (1997). Asymmetric Transfer Hydrogenation Catalyzed by Chiral Ruthenium Complexes. *Accounts of Chemical Research*, 30, 97–102.
- Patil, H. S., Nikalje, M. D., Chopade, A. U., & Chopade, M. U. (2021). Enantioselective Reduction of Ketones and Synthesis of 2-Methyl-2,3-dihydro-1-benzofuran Catalyzed by Chiral Spiroborate Ester. *Russian Journal of Organic Chemistry*, 57(4), 611–618.
- Pinaka, A., Dimotikali, D., Chankvetadze, B., Papadopoulos, K., & Vougioukalakis, G.C. (2013). Catalytic Asymmetric Reduction of Prochiral Ketones with Chiral β -Amino Alcohol N-Boranes and the Corresponding Tris(oxazaborolidine)borazines. *Synlett*, 24(18), 2401–2406.
- Seyden-Penn, J. (1995). Chiral auxiliaries and ligands in asymmetric synthesis. *John Wiley&Sons.Inc.*; New York.
- Singh, V. K. (1993). Practical and Useful Methods for the Enantioselective Reduction of Unsymmetrical Ketones. *Synthesis*, 605–617.
- Turgut, Y., Azizoglu, M., Erdogan, M., Arslan, N., & Hosgoren, H. (2013). β -Hydroxyamide derivatives of salicylic acid as organocatalysts for enantioselective reductions of prochiral ketones. *Tetrahedron: Asymmetry*, 24, 853–859.
- Wallbaum, S. & Martens, J. (1992). Asymmetric syntheses with chiral oxazaborolidines. *Tetrahedron: Asymmetry*, 3, 1475–1504.

Wu, X.-F., Min, C., Nyamzundui, E., Zhou H.-B., & Dong, C. (2011). A novel C₃-symmetric prolinol-squaramide catalyst for the asymmetric reduction of ketones by borane. *Tetrahedron: Asymmetry*, 22, 1640–1643.

Yasa, H., & Yusufoglu, A. (2018). Synthesis of New Medium- and Large- Sized Racemic and

Chiral Lactones. *Journal of Turkish Chemical Society, Section A: Turkish Journal of Chemistry*, 5(5), 539–550.

Yıldız T., & Yusufoglu, A. (2010). Asymmetric synthesis of new chiral long chain alcohols. *Tetrahedron: Asymmetry*, 21, 2981–2987.

Yıldız, T. (2015). An oxazaborolidine-based catalytic method for the asymmetric synthesis of chiral allylic alcohols. *Tetrahedron: Asymmetry*, 26, 497–504.

Zhang, A.L., Yu, Z.d., Yang, L.W., & Yang, N.F. (2015a). Synthesis of several polyethers derived from BINOL and their application in the asymmetric borane reduction of prochiral ketones. *Tetrahedron: Asymmetry*, 26, 173–179.

Zhang, A.L., Yu, Z.d., Yang, L.W., Yang, N.F., & Peng, D. (2015b). Chiral polyethers derived from BINOL and ECH as highly enantioselective and efficient catalysts for the borane reduction of prochiral ketones. *Journal of Molecular Catalysis A: Chemical*, 398, 407–412.

Chapter 2

MOLECULAR DOCKING TOOLS AND THEIR BASIC USAGE IN DRUG DESIGN AND DISCOVERY

Can YILMAZ¹

Waleed MOHAMMED KHORSHEED

¹ Asst. Prof. Dr. Can YILMAZ^{1*}, BSc. Waleed MOHAMMED KHORSHEED¹

(¹) Van Yuzuncu Yil University, Inst. of Applied Sciences, Dpt. of Molecular Biology and Genetics

C.Y. ORCID: 0000-0002-0028-6614

W.M.K ORCID: 0000-0003-1063-4165

(*): corresponding author, cyilmaz@yyu.edu.tr

In molecular docking, two or more substances interact to form a stable adduct as part of bioinformatics modelling (Dar & Mir, 2017). With the assistance of computer graphics, molecules can be manually docked or automatically by computer algorithms (Schleinkofer, Wang, & Wade, 2006).

Manually docking is accomplished via molecular visualization tools, occasionally in combination via stereo viewing hardware, and commonly via haptic devices that provide force input to the user's hand. There are various docking methods available. The molecular flexibility treatment and binding conformational changes associated with rigid-body and flexible docking techniques distinguish them. Docking procedures are chosen and established based on the types and quantities of molecules that will be docked. If two macromolecules must be docked, they are typically docked using separate algorithms instead of one algorithm for each. More computationally demanding and accurate procedures are required when docking a single ligand to just a receptor, rather than searching a vast chemical library for compounds that bind the macromolecular target. Structure-based drug design uses docking, a well-proven technique that will become increasingly important as structural genomics and proteomics project findings are put to good use (Schleinkofer et al., 2006).

1. Molecular Docking for the discovery of drugs: inhibition mechanism by *in silico* tools

This method is frequently utilized in drug discovery to anticipate ligands orientation by using electrostatic interactions and form-function relationships when bound to proteins such as receptors or enzymes. Van der Waals interactions are as crucial as Coulombic interactions and hydrogen bond formation. A docking score is used to get a rough estimate of the total of these interactions. This value indicates the molecule's binding potential. This ligand is examined in a six-dimensional rotational or translational region as just a lead molecule for drug discovery in the most straightforward rigid-body systems (Pagadala, Syed, & Tuszynski, 2017).

New therapeutic targets for drug development have emerged since the human genome project was completed. Research on protein structure and protein-ligand complexes has been aided by the simultaneous development of high-throughput crystallography, nuclear magnetic resonance spectroscopy mechanisms and purifications; As a result of these developments, computational strategies are now used in virtually every aspect of drug discovery, from hit detection to lead optimization. Traditional testing high bandwidth screening (HTS) is less direct and rational than virtual screening (VS), which also has the advantage of being less expensive and more effective. Ligand-based and structure-based VS

are the two main types of VS. While a collection of active ligand molecules is identified, structural analysis on targets is sparse or nonexistent, ligand-based techniques like pharmacophore modelling and quantitative structure-activity relationship (QSAR) methodologies could be utilized. Since the early 1980s, molecular docking has been the most popular method for designing drugs with a structure-based approach. In pharmaceutical research, molecular docking is becoming an increasingly essential tool thanks to developing programs based on various algorithms. In the past, there have been several excellent docking reviews and comparison studies that evaluated the programs' overall performance (Meng, Zhang, Mezei, & Cui, 2011).

2. Tools for molecular Docking of protein-ligand interactions and valuable utilities

2.1. Softwares

2.1.1. AutoDock Vina

AutoDock Vina was the bioinformatics tool for performing in-silico docking of proteins with ligands. It offers a variety of options based on the user's requirements. Following the success of previous AutoDock versions, Trott and Olson at the Scripps Research Institute in La Jolla, California, developed the recent version (Vieira & Sousa, 2019). This tool also allows blind docking and binding in a specific pocket, which can be more difficult when the binding location is already known.

For Docking with AutoDock Vina, one needs the following files:

1. Pdbqt files for the protein and ligand
2. Configuration document
3. Grid document

AutoDock 4 training set testing shows that AutoDock Vina is two many orders of magnitude quicker than the molecular docking software previously developed at a Scripps Research Institute's Molecular Graphics Lab (AutoDock 4) in addition to enhancing the binding mode predictions' accuracy significantly. Furthermore, multithreading on multicore machines, which achieves parallelism via multithreading, allows for even greater speed. Using grid maps and transparent clustering, AutoDock Vina generates grid maps and clusters them for the user (Trott & Olson, 2010).

A large number of people can use AutoDock Vina because It is freely available. Even though AutoDock Vina borrows from AutoDock 4, it is conceptually distinct. It can range from one to two orders of magnitude more accurately than AutoDock 4 at predicting binding mode than the previous version. New search and scoring functions combine empirical

and knowledge-based scoring in this version as well. As evidenced by the high number of citations to the original paper because of its multicore capabilities, fast performance, and improved precision and its simplicity of use contributed to its rapid spread throughout the docking community. This program is also a viable virtual screening alternative because of its high computational efficiency and ability to utilize multiple CPUs or CPU cores (Vieira & Sousa, 2019).

2.1.2. AutoDock

Docking software AutoDock is the first of its kind to take conformational flexibility into account. The package is made up of two programs, AutoGrid and AutoDock. Before using AutoGrid, the noncovalent energy of a receptor-probe-atom interaction is calculated using the rigid part's grid points on the lattice. AutoGrid can also generate the electrostatic potential grids mapping and a desolvation map. AutoDock guides the docking process of the chosen ligands using the entire collection of grid maps as well as the receptor's movable part (Gromiha, 2010).

Blind Docking, updated grid maps on binding sites, and a free-energy scoring method based on linear regression analysis are some of the features of this receptor; the force field AMBER, as well as the vast numbers of the protein-ligand complexes via known inhibition constants, are the main advantages of AutoDock. <http://autodock.scripps.edu/> is where one can find it (Gromiha, 2010).

2.1.3. Dock

DOCK is a program that solves the problem of molecules docking to each other. The identification of a small molecule's (ligand) low-energy binding modes docking occurs within the active sites of a macromolecule (receptor) which composition is understood. A drug is a substance that strongly interacts with, or binds, a disease-related receptor and thus inhibits its function. Therefore, an accurate description of molecular energetics, and a quick method for exploring possible binding modes, were developed, are required for computationally solving the docking problem ("Overview of DOCK," n.d.).

Previously, The DOCK technique treated rigid-body docking by superimposing the ligand onto the binding pocket's negative picture and using a geometric matching approach. To increase the algorithm's capacity to discover the lowest-energy compulsory mode, essential characteristics like force-field based scoring and on-the-fly optimization were implemented. improved rigid bodies docking matching algorithm, and an algorithm for flexible ligand docking were added over time.

2.1.4. Genetic Optimization for Ligand Docking (GOLD)

According to the method (Jones, Willett, Glen, Leach, & Taylor, 1997), researchers use genetic optimization to optimize ligand docking. Using the genetic algorithm, GOLD investigates the full extent of ligand conformational flexibility in combination via the partial flexibility of the protein. Thus, it meets the fundamental requirement that the ligand displaces loosely bound water when it binds.

2.1.5. Glide

Schrödinger is the source of this information. To simulate high-throughput natural screening (HTVS), Glide calculates empirical scoring functions to determine protein-ligand binding modes. Glide docks flexibility ligands into stiff receptors structure by quickly collecting the ligand's conformational, orientational, as well as positional degrees of freedom. Glide can be run in three ways, each with its sampling function and scoring function for ligand degrees of freedom. These three techniques create a large number of conformers for a ligand as well as utilize a series of hierarchical filters to assess the degrees of freedom of the ligand swiftly. It utilizes an anchor-and-grow algorithm to fine-tune the predicted docking modes and better sample the degrees of freedom of the ligands before using XP Glide. The XP GlideScore scoring function contains unique recognition words for recognizing and rewarding structural motifs, essential for binding (Repasky, Shelley, & Friesner, 2007).

2.1.6. SCIGRESS

Fujitsu developed SCIGRESS, a computer simulation software capable of simulating the behaviour of atoms and molecules. Experiments are required during the drug design phase in the pharmaceutical industry to verify the effectiveness of a design; however, performing all the necessary experiments without computer simulation takes a long time and costs a lot of money. SCIGRESS can run virtual experiments on a computer to assist with real-world experiments, saving time and money. SCIGRESS is frequently used in universities to teach organic chemistry. When students only listen to lectures and read textbooks, they are more likely to misunderstand the resonance of aromatic compounds. SCIGRESS can visualize aromatic compounds using 3D graphics and assist people in understanding them correctly (Marchand, Nicolas, Lienard, Philippe, Siehl, Hans-Ullrich, Izato, 2014).

2.1.7. GlamDock

GlamDock is a flexible ligand docking tool. Using GlamDock is as simple as using a Monte Carlo simulation and then minimizing the error rate. The rigid body movement, as well as rotation, are described using

a mapping-based model in conjunction with internal ligand conformation coordinates and the regularly differentiable empirical potential (Tietze & Apostolakis, 2007).

2.1.8. FlexAID

FlexAID is indeed a small-molecule docking method that considers targeted side-chain flexibility and uses a soft scoring system based on surface complementarity that is not excessively reliant on particular geometric criteria. The pairwise energy parameters were calculated using Monte Carlo simulations from the massive dataset of accurate positive poses as well as negative decoys from a PDB-bind database. The widely utilized Astex dataset and a HAP2 dataset are used to test binding pose prediction, while the subset of a DUD dataset is used to evaluate virtual screening performance. The University of Sherbrooke in Canada provides precompiled Linux, macOS, and Windows versions (Gaudreault & Najmanovich, 2015).

2.1.9. GEMDOCK

When it comes to molecular docking, GEMDOCK employs the empirical scoring function as well as a Generic Evolutionary Method. It uses a combination of discrete as well as continuous world searching strategies, along with local search strategies to rate convergence, while it uses rapid recognition of potential ligands to speed up convergence. Molecular recognition can be made more accessible with GEMDOCK's molecular recognition tool, which could be utilized to test and improve the scoring function of various tests. This method emphasizes the empirical scoring function and a much more robust evolutionary process than traditional evolutionary approaches in various domains. When it comes to GEMDOCK, the various types of potential energies come together. For the steric and hydrogen bonding potential, a simple linear model was used to identify possible complexes quickly. The evolutionary approach's central idea is to create multiple cooperating operators using a family competition paradigm like a local search procedure (Yang & Chen, 2004).

2.1.10. iGEMDOCK

From the preparatory through the post-screening analyses, the structure-based VS framework iGEMDOCK is used. iGEMDOCK is a comprehensive and simple-to-use environment for post-screening studies as well as predicting pharmacological interactions based on screening substances. Non-experts who are interested in biology will appreciate the user interface. The findings show that pharmacological interactions are frequently required for active compound binding and participate in biochemical pathways. Pharmacological combinations could improve hit

rates in VS by mitigating the detrimental impacts of energy-based scoring functions (Hsu, Chen, Lin, & Yang, 2011).

2.1.11. HomDock

HomDock is a docking system that combines GMA with optimization methods. Crystal structures of a targeted protein and the structure of a template ligand in a binding site are the starting points for a HomDock application. The primary idea behind the method is to utilize GMA to arrange candidate ligands onto such a pattern, optimize their location in the protein's domain, and finally rank the ligands based on their interaction with the proteins and the similarity of a ligand (J. Marialke, S. Tietze, & Apostolaki*, 2007).

2.1.12. ICM

Internal Coordinate Mechanics (ICM) has indeed been widely confirmed in bioinformatics as well as drug development applications. ICM has been demonstrated to be capable of re-creating crucial protein-ligand interactions and finding high-affinity ligands for the most significant therapeutic targets, including enzymes, receptors, ion channels, and transport proteins, in investigations. This has been demonstrated in both prospective as well as retrospective research (Neves, Totrov, & Abagyan, 2012).

2.1.13. FlexE (Flex-Ensemble)

FlexE's docking calculations take protein structure variations into account. Docking ligands into a protein ensemble with flexibility, point mutations, or alternate models is possible with FlexE. The ensemble of superimposed protein structures was used to generate the single, unified protein description, then used in FlexE. Different regions of the protein can have discrete alternative conformations that could be combined to create a recent valid protein structure. These alternative conformations are explicitly considered. Using FlexE, one can view the ensemble's superimposed structures. FlexE is built using the so-called united protein description. Like sections of the structures are merged, whereas different parts were considered as independent alternatives. Several other structures can be combined to form recent overall structures as part of the docking system. Rotamer libraries can easily benefit from this concept. Because FlexE is a descendant of FlexX, the interaction strategy, the incremental construction method, and other essential topics are all covered. The scoring function has indeed been tailored to the ensemble method (Claußen, Buning, Rarey, & Lengauer, 2001).

2.1.14. Fleksy

Using Fleksy, it's possible to place small molecule ligands precisely on protein receptors while also accounting for changes in receptor flexibility. This approach involves docking a ligand into a structural ensemble of receptor conformations, followed by a complicated optimization step in which both the ligand and the protein can move. The approach largely depends on receptor ensembles to explain protein elasticity (Nabuurs et al., 2010). This source was developed by Radboud University Nijmegen's Centre for Molecular as well as Biomolecular Informatics. Fleksy considers protein elasticity while docking tiny molecules to a protein structure. Fleksy is broken down into two stages: During the first step, all docking-related files are collected, processed, produced, verified, and saved. For each kind of protein or protein description, a separate project directory was created. Multiple ligands can be considered per project, and additional ligands, such as newly designed ligands, can be added to the existing projects. The second stage of a workflow involves Docking, optimization, as well as scoring of the ligand (Wagener, Ve Vlieg, & Nabuurs, 2012).

2.1.15. FITTED

FITTED (Flexibility Induced Through Targeted Evolutionary Description) is the set of programs that rely on a genetic algorithm that focuses on speed (G.A.). Because it can handle both macromolecule flexibility and bridging "displaceable" water molecules, this docking software is unique. In addition to the more traditional crossover and mutation operators, resulting in a significant speed boost. These operators model learning (through various stages of energy minimization) and early individual selection based on a rough fitness estimate. To make the ligands as well as proteins, two modules (ProCESS and SMART) are required, as well as a novel potential energy expression to simulate the interactions via displaceable water molecules. This program utilizes a genetic algorithm to compensate for the elasticity of the two compounds and the position of bridging water molecules (Corbeil, Englebienne, & Moitessier, 2007).

2.1.16. FORECASTER

FORECASTER is a web-based interface which permits users to build and modify drug design processes. It was created to encourage medicinal chemists to use SBDD. Due to resource constraints, it was unable to accomplish standard drug design operations such as creating a protein structure as well as setting up a ligand using several command-line programs. As just a proof of concept, a medical chemist utilized FORECASTER to generate virtual combinatorial libraries, filter them and extract a diversified library from the NCI database. In one of sample studies

these concentrated libraries were subsequently docked to the estrogen receptor (E.R.) in retrospective experiments, data attributes known as E.R. modulators. Several of those programs have also been used in independent studies of radiolabeled kinase inhibitors (Moitessier et al., 2016).

2.1.17. VLifeDock

VLifeDock offers a variety of molecular docking methods to its users. VLife's GRIP docking, Grid-based Docking & G.A. Docking, are three methods that provide the user with unique 'Accuracy - Speed' options ranging from rapid screening to exhaustive precision docking. VLifeDock had the batch docking feature that makes it simple to prioritize ligands based on their binding scores. VLifeDock is a genuinely versatile application thanks to its selection of systematic and stochastic mechanisms and the array of scoring functions. VLifeDock is compatible with both Linux and Windows systems ("Overview of DOCK," n.d.).

2.1.18. Parallel Docking Suite (ParaDockS)

ParaDockS (Parallel Docking Suite) is a tool that makes it simple to combine old and new methods to describe ligand-receptor interactions and find native poses. The framework is designed to be highly modular and is written in C++. As a result, developers will be able to concentrate solely on their areas of expertise. ParaDockS is capable of analyzing, processing, and storing a wide range of input structures. It is also a top priority to implement scoring functions. ParaDockS allows users to create and apply target-specific scoring functions and the built-in scoring functions PScore, PMF04, and Drugstore (Pippel, Scharfe, Meier, & Sippl, 2012).

2.1.19. Molegro Virtual Docker

An integrated computational environment is provided by Molegro Virtual Docker, which allows us to run docking simulations on proteins and ligand molecules. For Windows, Linux, and Mac OS X users, Molegro is pleased to announce the release of a new version of Molegro Virtual Docker. For protein-ligand docking, Molegro Virtual Docker uses cutting-edge optimization techniques and an intuitive user interface focused on efficiency and usability (Bitencourt-Ferreira & de Azevedo, 2019).

2.1.20. DAIM-SEED-FFLD

Daim can identify and compute the properties of the most promising fragments in a molecule. Daim can also compare the found fragments to already existing and fully prepared molecules, as the components docked by SEED should be minimized. Another feature is the ability to search databases for the presence of specific fragments in molecules. Finally, using the FFLD program, the molecules were recreated *in situ* from the

docked fragment. Additionally, entire databases can be analyzed to obtain information on rotatable bond counts and donors/acceptors (Kolb, 2010).

2.1.21. VinaMPI

Utilizing the large numbers of the core, VinaMPI was designed to reduce its time to complete substantial actual drug screens on powerful computing sources. There are many docking tasks that VinaMPI can handle in parallel because of the massively parallel nature of the program and the ability to use multithreading. AutodockVina, a multithreaded virtual docking program, serves as the foundation for this application. According to the task complexity, which is determined by the rotatable bonds in a chemical compound under investigation, VinaMPI distributes tasks evenly among workers. Using VinaMPI, multiple proteins can be efficiently docked at once, enabling high-throughput opposite docking and unique approaches for increasing the efficiency of a drug development pipeline (Ellingson, Smith, & Baudry, 2013).

2.1.22. FlipDock

Using Flexible LIgand–Protein Docking (FLIPDock), flexible ligand molecules can be automatically docked into the active site of the flexibility receptor molecules. FLIPDock encodes molecule conformational gaps using a newly developed data structure called the Flexibility Tree (F.T.). To selectively encode conformational subspaces of giant biologically macromolecule, the F.T. was initially intended to be a hierarchical as well as multiresolution data structure (Zhao & Sanner, 2007).

2.1.23. PharmDock

The most critical ligand-protein interactions for binding as well as biological activities would be utilized for virtual screening (VS) to discover novel actives or produce ligand alignments for future QSAR simulations. Pharmacophore models were usually classified from structural features that biologically active ligands share and were thought to be crucial for biological activities. PharmDock, a docking program based on protein pharmacophores, has been released as a PyMOL plugin (Hu & Lill, 2014).

2.1.24. POSIT

POSIT makes use of experimental structural data to extrapolate pose predictions as well as confidence evaluations. Ligand representation relies on 3D molecular shape can assist via this. The molecular shape can be defined using an inside or outside volume function based on atom-centered parts, or immediately from electron densities or numerical simulations. POSIT utilizes shape overlap and chemical similarities to extrapolate a distance from the experimental structure, resulting in more accurate

prediction confidence calculate. These confidence intervals enable more effective use of structural data by generating better critical evaluations (Kelley, Brown, Warren, & Muchmore, 2015).

2.1.25. Hammerhead

This docking approach utilizes an empirically calibrated scoring function and an autonomous method for finding as well as defining a protein's binding site. Furthermore, Hammerhead is fully automated and fast. According to Hammerhead, a screen for compounds that bind to known ligands in proteins predicts that the natural ligand will come out on top in many cases, from weak connections via little ligand elasticity to strong contacts with substantial ligand flexibility. A library of 10,000 to 100,000 small organic compounds can be screened in the few days using this algorithm, as well as it's thorough and accurate enough to predict crystallographic poses as well as binding affinities for the several of known ligand (Welch, Ruppert, & Jain, 1996).

2.1.26. idock

To create idock, researchers took the accurate scoring formula as well as an effective optimization technique from AutoDock Vina and then worked to improve the fundamental implementation and numerical model further so that it could run even faster. As a result, on average, idock delivers a speedup of 3.3 in CPU time as well as 7.5 in elapsed time (H. Li, Leung, & Wong, 2012).

2.1.27. Rosetta Ligand

New software called RosettaLigand predicts the interactions between proteins and small molecules. RosettaLigand's highest-scoring interfaces were all within 2Å of the crystal structures, according to benchmark studies. In addition, multiple ligands can be docked simultaneously, fragments of ligands can be represented for greater flexibility, the docking interface was redesigned, and the XML script-based interfaces gives the user complete control over ligand docking protocol are all included in Rosetta's latest release. With RosettaLigand, the ligand's rigid body position and orientation are sampled utilizing Monte Carlo minimization via side-chain conformations (Lemmon & Meiler, 2012).

2.1.28. Cdocker

To the CHARMM family of docking solutions, the adaptable CDOCKER method was added recently. Using this method, protein, as well as ligand configuration, can simultaneously search their conformational gap while maintaining efficiency by combining atomically exact side-chain elasticity using grid-based docking techniques. This contrasts with

existing methods that use iterative protein or ligand space sampling, like Glide or Autodock, which use induced-fit samples. Re-docking trials on the subset of a CCDC/Astex set have shown that the CHARMM docking methodology has been enhanced to include receptor flexibility and an improved sampling protocol. CDOCKER's improvements in docking accuracy are on par with or better than those of other widely used docking programs (Gagnon, Law, & Brooks, 2015).

2.1.29. LigandFit

LigandFit is a recent shape-based docking technique for proteins with active ligand docking sites. The method utilizes the cavity detection algorithm to look for protein tests that could be active site regions. To produce ligand poses that are compatible via the structure of the active site, a shape compare filter, as well as a Monte Carlo conformational search, are utilized. Candidate poses were minimized about the active site utilizing the grid-based technique for measuring protein-ligand interactions energies. The recent non-linear interpolation scheme drastically reduces grid interpolation errors (Venkatachalam, Jiang, Oldfield, & Waldman, 2003).

2.1.30. rDock

For the high-throughput virtual screening (HTVS) applications, Vernalis developed rDock, a molecular docking program. Since it is based on RiboDock, the program could dock nucleic acids as well as proteins. It is also created to be computationally efficient, with the user having the option of adding additional restrictions as well as knowledge as a bias to aid docking (Ruiz-Carmona et al., 2014).

2.1.31. Lead Finder

To simulate protein-ligand interactions, researchers use the Lead Finder program, which is a computational chemistry tool. Quantitative ligand binding and biological activity can both be assessed using Lead Finder. It shows 3 scoring functions optimized for 3D docked ligand poses, protein-ligand binding energy, and active and inactive compounds' ranking inaccurate screening tests with Lead Finder. Lead Finder was developed for computational and medicinal chemists working on drug discovery, toxicologists and pharmacologists evaluating ADME/T property models *in silico*, and biochemists and enzymologists studying enzyme specificity and rational design (Stroganov, Novikov, Stroylov, Kulkov, & Chilov, 2008).

2.1.32. YASARA Structure

A biocatalytic reaction system or an enzyme could be reviewed structurally utilizing computational methods like homology- or molecular modelling. Protein molecular modelling computer software is required

for this type of computational work. Molecular docking and molecular dynamics simulations are included in the protocols for two specific biocatalytic applications, including energy minimization. The applications were chosen to show how structural knowledge gained through homology and molecular modelling can guide biocatalytic and protein engineering research in real-world applications (Land & Humble, 2018).

2.1.33. HADDOCK (High Ambiguity Driven biomolecular DOCKing)

HADDOCK is a docking method and related software which uses chemical shift perturbation data via NMR titration studies or data from mutagenesis (high ambiguity driven docking method), for instance. As ambiguous interaction restraints (AIRs), information about the interacting residues is introduced to drive docking. Finally, the structures are ordered based on their intermolecular energy, calculated using a mix of electrostatic, van der Waals, and AIR energy factors. Notably, NMR was the first to solve symmetric dimer structures with ambiguous distance restraints. These restraints were now widely utilized in protein structure determination and NOE assignment techniques that are automated (Dominguez, Boelens, & Bonvin, 2003).

2.1.34. MS-Dock

MS-DOCK is a DOCK-based flexible rigid-body docking approach with multiple conformational rigid bodies. This technique could be utilized as the first step in a docking/scoring procedure with several stages. A multistep structure-based screening protocol can easily use MS-DOCK to create multiple conformer libraries as well as perform shape-based filtering to reduce computation times (Sauton, Lagorce, Villoutreix, & Miteva, 2008).

2.1.36. DockoMatic

To make job submission easier, DockoMatic uses a user-friendly graphical user interface (GUI) and extends the capabilities of the widely used AutoDock docking tool suite. It uses Linux as its operating system and Java and Perl as its programming languages. The LGPL license governs its use. Grid coordinate files (gpf) and experimentally determined or predicted ligand-binding domains on receptor proteins are both supported by DockoMatic. DockoMatic sets up and runs the AutoDock jobs associated with text files containing peptide ligands and receptors lists. It is designed for high-throughput screening on a computational cluster, although DockoMatic can run AutoDock jobs locally. As many as 100,000 jobs can be managed concurrently using DockoMatic on a computational cluster (Jacob, Bullock, Andersen, & McDougal, 2011).

2.2. Web services

2.2.1. SwissDock

Using SwissDock, small molecules can dock with specific proteins via a web server on a remote computer. For fixing common problems and preparing input files for the target protein and ligand, it utilizes an EADock DSS engine. A well-designed and implemented Ajax/HTML interface makes it easy for scientists to submit dockings and retrieve predicted complexes. You can download templates written in Perl, Python, and PHP from a programmatic SOAP interface for automated docking tasks. To create a database of manually curated complexes, the Ligand Protein Database is utilized. After then, the database may be viewed through the website. For community promotion, a wiki, as well as a forum, are provided for user interaction (Grosdidier, Zoete, & Michielin, 2011). It is possible to access SwissDock's website at <http://www.swissdock-ch/>

2.2.2. DockingServer

This web-based application handles the whole principle of molecular docking, including ligand, protein setup, and results representation. It does this by integrating a variety of commonly used computational chemistry programs. While DockingServer's user-friendly interface makes docking calculations and outcomes evaluation accessible to researchers across the biochemistry spectrum, advanced users have complete control over the setup parameters for ligands and proteins and docking calculations. The software can be used to dock and analyze a single ligand as well as to dock ligand libraries in high throughput to specific proteins (Eszter, Sándor, László, & Zsolt, 2009). The website for DockingServer is <http://www.dockingserver.com/web/>.

2.2.3. 1-Click Docking

Many researchers use 1-click Docking, a web server-based molecular docking tool. The AutoDock Vina docking algorithm is used in the 1-Click Docking web-based server. It includes scPDB, which allows users to choose from a database of 10,000 target structures. There is no need to download, upload, or choose a binding site. Instead, select a target and click dock with 1-ClickDocking, then browse the results. Ideal for gaining a basic understanding of ligand-target interactions and affinity (Kanerria, Parmar, & Rakholiya, 2019). The website is <http://mcule.com/apps/1-click-docking/>

2.2.4. Blaster

DOCK Blaster is a new docking tool that can be accessed anonymously for free at <http://blaster.docking.org>. DOCK Blaster can often start

from a PDB code or the target's structure and binding site specification. UCSF's Department of Pharmaceutical Chemistry's Irwin and Shoichet Laboratories manufacture DOCK Blaster (Irwin et al., 2009).

2.2.5. Docking @ UTMB

AutoDock Vina is used by Docking@UTMB to automate the docking process. The docking complex's PDB file and the binding affinity values for each of the docking sites are included in the output. The Watowich lab at the University of the Texas Medical Branch is in charge of keeping it up to date (Sarbin et al., 2013).

2.2.6. ParaDock

ParaDock is a brand-new protein-DNA docking algorithm that has been built from the ground up. ParaDock incorporates narrow DNA fragments which have been strictly docked to the protein rely on geometric complementarity to generate bent horizontal DNA molecules of any series (Banitt & Wolfson, 2011).

2.2.7. FlexPepDock

The Rosetta FlexPepDock provides an interface to the Rosetta framework's high-resolution peptide docking (refinement) protocols for modelling peptide-protein complexes. Using a protein receptors design and an estimated, perhaps incorrect modeling of the peptide within the receptor-binding region, a FlexPepDock server refines a peptide to high resolution, providing full elasticity to the peptide backbone as well as any side chains (London, Raveh, Cohen, Fathi, & Schueler-Furman, 2011). The website is <http://flexpepdock.furmanlab.cs.huji.ac.il/>

2.2.8. PLATINUM

Investigation of Protein-Ligand Attractions Using NUMerically (PLATINUM), biomolecules' hydrophobic/hydrophilic properties in 3D structures can be analyzed and visualized. Furthermore, using PLATINUM's various tools, such as docking poses, hydrophobic/hydrophilic match in biomolecular complexes can be quantified. These additional functions are in addition to the standard ones. Molecular Hydrophobicity Potential, based on empirical data, is used to calculate the results (MHP) (Pyrkov, Chugunov, Krylov, Nolde, & Efremov, 2009). A free resource for the academic user is available at <http://model.nmr.ru/platinum/>

2.2.9. PatchDock

When predicting complexes between proteins and small molecules, PatchDock is a helpful tool. Molecular docking algorithm PatchDock utilizes geometry. Its goal is to find molecular shape complementarity-friendly docking transformations. When such modifications are used,

they produce large interface areas as well as a small number of steric clashes. A comprehensive interface is established by many matching local characteristics of the attached molecules with complementary properties (Schneidman-Duhovny, Inbar, Nussinov, & Wolfson, 2005). The website for PatchDock is <https://bioinfo3d.cs.tau.ac.il/PatchDock/>.

2.2.10. MEDock

The MEDock web server incorporates an information-theory-based global search strategy that uses the Gaussian probability distribution's maximum entropy property. Due to the worldwide search strategy, MEDock's optimization algorithm performs significantly better when dealing with complex energy landscapes. In addition, MEDock also enhances the accuracy rate for all benchmark cases across the board (Chang, Oyang, & Lin, 2005). <http://medock.csie.ntu.edu.tw/> and <http://bioinfo.mc.ntu.edu.tw/medock/> are two places where you can find MEDock.

2.2.11. BSP-SLIM

Models of target proteins with unknown ligand binding sites can benefit from BSP-SLIM (Binding Site Prediction via SLIM) Docking. Template-based ligands binding sites predictions algorithms are used in conjunction via a SLIM docking approach to creating BSP-SLIM (Lee & Zhang, 2012). At <http://zhanglab.ccmh.med.umich.edu/BSP-SLIM/>, an accessible online BSP-SLIM server is available.

2.2.12. BioDrugScreen

There is a database called BioDrugScreen that ranks compounds docked against the human proteome. More than 3 million receptor-ligand complexes were found on 1589 human targets, outcomes in over 200000 TeraGrid cpu-hours and about 1600 molecules from the freely exist NCI diversity set. The targeting for BioDrugScreen was derived from the Human Tumor Protein Interaction Network, which the researchers updated and the Human Druggable Proteome, which they formed specifically for this project (L. Li et al., 2010).

2.2.13. GPCRautomodel

Using the three-dimensional structures of existing GPCRs, GPCRautomodel automates O.R. homology modelling based on odorant docking. As a result, current alignment methods frequently fail to find an accurate match for O.R.s. Fold recognition is used to get a good initial alignment (Launay et al., 2012). The website for GPCRautomodel is <http://genome.jouy.inra.fr/GPCRautomodel>

2.2.14. kinDOCK

Protein kinase ATP-binding sites can be analyzed using kinDOCK, a web server. Researchers used the docking of ligands that had crystallized with other protein kinases to arrive at this conclusion. This protein kinase-ligand complex structural library was obtained from Protein Data Bank (PDB) (Martin, Catherinot, & Labesse, 2006). The server, and its documentation, could be found at <http://abcis.cbs.cnrs.fr/kindock/>

2.2.15. iScreen

Custom *de novo* drug design is possible with iScreen's TCM docking and the small web server. An additional tool that the researchers created extracts proteins of interest from raw input files while also approximating the size of the protein's ligand-binding site was also developed by them (Tsai, Chang, & Chen, 2011). Users who aren't familiar with command-line systems appreciate iScreen's friendly graphic interface. <http://iScreen.cmu.edu.tw/> is the URL for the TCM docking and screening server.

2.2.16. idTarget

This server uses the divide-and-conquer docking method to predict potential binding targets for small chemical molecules in conjunction utilizing our newly created scoring algorithms based on robust regression analysis as well as quantum chemical charging models (Wang, Chu, Chen, & Lin, 2012). idTarget is a free web-based service that can be found at <http://idtarget.rcas.sinica.edu.tw>

2.2.17. METADOCK

Using parameterized and parallel metaheuristics, METADOCK is a new molecular docking methodology designed to take advantage of heterogeneous computers with heterogeneous architectures. By defining a configuration scheme, the application determines the optimization technique at runtime (Imbernón, Cecilia, Pérez-Sánchez, & Giménez, 2017).

2.2.18. Score

Enables one to compute various dock scores for just a ligand-receptor complex, which may be supplied as a single file via both interaction partners or even as two separate files. VEGA is in charge of the calculation phase. The University of Milano's Drug Design Laboratory provided this information (Chen, 2015).

2.2.19. Pose & Rank

Pose & Rank is a free service that scores protein-ligand complexes based on two atomic distance-dependent statistical functions: PoseScore

and RankScore. PoseScore is designed to recognize native ligand binding geometries from another pose. The RankScore algorithm was created to distinguish ligands from non-binding molecules (Fan et al., 2011).

References

- Banitt, I., & Wolfson, H. J. (2011). ParaDock: a flexible non-specific DNA—rigid protein docking algorithm. *Nucleic Acids Research*, *39*(20), e135. <https://doi.org/10.1093/NAR/GKR620>
- Bitencourt-Ferreira, G., & de Azevedo, W. F. (2019). Molegro Virtual Docker for Docking. *Methods in Molecular Biology (Clifton, N.J.)*, *2053*, 149–167. https://doi.org/10.1007/978-1-4939-9752-7_10
- Chang, D. T. H., Oyang, Y. J., & Lin, J. H. (2005). MEDock: a web server for efficient prediction of ligand binding sites based on a novel optimization algorithm. *Nucleic Acids Research*, *33*(Web Server issue). <https://doi.org/10.1093/NAR/GKI586>
- Chen, Y. C. (2015). Beware of docking! *Trends in Pharmacological Sciences*, *36*(2), 78–95. <https://doi.org/10.1016/J.TIPS.2014.12.001>
- Claußen, H., Buning, C., Rarey, M., & Lengauer, T. (2001). FlexE: efficient molecular docking considering protein structure variations. *Journal of Molecular Biology*, *308*(2), 377–395. <https://doi.org/10.1006/JMBI.2001.4551>
- Corbeil, C. R., Englebienne, P., & Moitessier, N. (2007). Docking ligands into flexible and solvated macromolecules. 1. Development and validation of FITTED 1.0. *Journal of Chemical Information and Modeling*, *47*(2), 435–449. https://doi.org/10.1021/CI6002637/SUPPL_FILE/CI6002637.PDF
- Dar, A. M., & Mir, S. (2017). Molecular Docking: Approaches, Types, Applications and Basic Challenges. *Undefined*, *08*(02). <https://doi.org/10.4172/2155-9872.1000356>
- Dominguez, C., Boelens, R., & Bonvin, A. M. J. J. (2003). HADDOCK: A protein-protein docking approach based on biochemical or biophysical information. *Journal of the American Chemical Society*, *125*(7), 1731–1737. https://doi.org/10.1021/JA026939X/SUPPL_FILE/JA026939X-SI20021128_085857.TXT
- Ellingson, S. R., Smith, J. C., & Baudry, J. (2013). VinaMPI: facilitating multiple receptor high-throughput virtual docking on high-performance computers. *Journal of Computational Chemistry*, *34*(25), 2212–2221. <https://doi.org/10.1002/JCC.23367>
- Eszter, H., Sándor, K., László, D., & Zsolt, B. (2009). [DockingServer: molecular docking calculations online]. *Acta Pharmaceutica Hungarica*, *79*(1), 17–21. Retrieved from <https://europepmc.org/article/med/19526678>
- Fan, H., Schneidman-Duhovny, D., Irwin, J. J., Dong, G., Shoichet, B. K., & Sali, A. (2011). Statistical potential for modeling and ranking of protein-ligand interactions. *Journal of Chemical Information and Modeling*, *51*(12), 3078–3092. <https://doi.org/10.1021/CI200377U>

- Gagnon, J. K., Law, S. M., & Brooks, C. L. (2015). Flexible CDOCKER: Development and application of a pseudo-explicit structure-based docking method within CHARMM. *Journal of Computational Chemistry*, 37(8), 753–762. <https://doi.org/10.1002/JCC.24259>
- Gaudreault, F., & Najmanovich, R. J. (2015). FlexAID: Revisiting Docking on Non-Native-Complex Structures. *Journal of Chemical Information and Modeling*, 55(7), 1323–1336. https://doi.org/10.1021/ACS.JCIM.5B00078/SUPPL_FILE/CI5B00078_SI_001.PDF
- Gromiha, M. M. (2010). Protein Bioinformatics. From Sequence to Function. *Protein Bioinformatics. From Sequence to Function*, 209–145.
- Grosdidier, A., Zoete, V., & Michielin, O. (2011). SwissDock, a protein-small molecule docking web service based on EADock DSS. *Nucleic Acids Research*, 39(Web Server issue). <https://doi.org/10.1093/NAR/GKR366>
- Hsu, K. C., Chen, Y. F., Lin, S. R., & Yang, J. M. (2011). Igemdock: A graphical environment of enhancing gemdock using pharmacological interactions and post-screening analysis. *BMC Bioinformatics*, 12(SUPPL. 1), 1–11. <https://doi.org/10.1186/1471-2105-12-S1-S33/FIGURES/5>
- Hu, B., & Lill, M. A. (2014). PharmDock: A pharmacophore-based docking program. *Journal of Cheminformatics*, 6(1), 1–14. <https://doi.org/10.1186/1758-2946-6-14/FIGURES/11>
- Imbernón, B., Cecilia, J. M., Pérez-Sánchez, H., & Giménez, D. (2017). META-DOCK: A parallel metaheuristic schema for virtual screening methods: <https://doi.org/10.1177/1094342017697471>, 32(6), 789–803. <https://doi.org/10.1177/1094342017697471>
- Irwin, J. J., Shoichet, B. K., Mysinger, M. M., Huang, N., Colizzi, F., Wassam, P., & Cao, Y. (2009). Automated docking screens: a feasibility study. *Journal of Medicinal Chemistry*, 52(18), 5712–5720. <https://doi.org/10.1021/JM9006966>
- J. Marialke, S. Tietze, A., & Apostolaki*, J. (2007). *Similarity Based Docking*. <https://doi.org/10.1021/CI700124R>
- Jacob, R. B., Bullock, C. W., Andersen, T., & McDougal, O. M. (2011). Docko-Matic: automated peptide analog creation for high throughput virtual screening. *Journal of Computational Chemistry*, 32(13), 2936–2941. <https://doi.org/10.1002/JCC.21864>
- Jones, G., Willett, P., Glen, R. C., Leach, A. R., & Taylor, R. (1997). Development and validation of a genetic algorithm for flexible docking. *Journal of Molecular Biology*, 267(3), 727–748. <https://doi.org/10.1006/JMBI.1996.0897>
- Kaneria, M., Parmar, J., & Rakholiya, K. (2019). Molecular docking and drug design of phytoconstituents from *Couroupita guianensis* – An in silico perspective. *Journal of Pharmacognosy and Phytochemistry*, 8(6), 53–60. Retrieved from <https://www.phytojournal.com/archives/2019.v8.i6.9990/>

molecular-docking-and-drug-design-of-phytoconstituents-from-ltemgt-couroupita-guianensis-ltemgt-ndash-an-ltemgtin-silico-ltemgtperspective

- Kelley, B. P., Brown, S. P., Warren, G. L., & Muchmore, S. W. (2015). POSIT: Flexible Shape-Guided Docking for Pose Prediction. *Journal of Chemical Information and Modeling*, 55(8), 1771–1780. https://doi.org/10.1021/ACS.JCIM.5B00142/SUPPL_FILE/CI5B00142_SI_001.PDF
- Kolb, P. (2010). *Decomposition And Identification of Molecules*.
- Land, H., & Humble, M. S. (2018). YASARA: A Tool to Obtain Structural Guidance in Biocatalytic Investigations. *Methods in Molecular Biology (Clifton, N.J.)*, 1685, 43–67. https://doi.org/10.1007/978-1-4939-7366-8_4
- Launay, G., Téletchéa, S., Wade, F., Pajot-Augy, E., Gibrat, J. F., & Sanz, G. (2012). Automatic modeling of mammalian olfactory receptors and docking of odorants. *Protein Engineering, Design and Selection*, 25(8), 377–386. <https://doi.org/10.1093/PROTEIN/GZS037>
- Lee, H. S., & Zhang, Y. (2012). BSP-SLIM: A Blind Low-Resolution Ligand-Protein Docking Approach Using Predicted Protein Structures. *Proteins*, 80(1), 93. <https://doi.org/10.1002/PROT.23165>
- Lemmon, G., & Meiler, J. (2012). Rosetta Ligand docking with flexible XML protocols. *Methods in Molecular Biology (Clifton, N.J.)*, 819, 143–155. https://doi.org/10.1007/978-1-61779-465-0_10
- Li, H., Leung, K. S., & Wong, M. H. (2012). idock: A multithreaded virtual screening tool for flexible ligand docking. *Undefined*, 77–84. <https://doi.org/10.1109/CIBCB.2012.6217214>
- Li, L., Bum-Erdene, K., Baenziger, P. H., Rosen, J. J., Hemmert, J. R., Nellis, J. A., ... Meroueh, S. O. (2010). BioDrugScreen: a computational drug design resource for ranking molecules docked to the human proteome. *Nucleic Acids Research*, 38(Database issue). <https://doi.org/10.1093/NAR/GKP852>
- London, N., Raveh, B., Cohen, E., Fathi, G., & Schueler-Furman, O. (2011). Rosetta FlexPepDock web server—high resolution modeling of peptide–protein interactions. *Nucleic Acids Research*, 39(Web Server issue), W249. <https://doi.org/10.1093/NAR/GKR431>
- Marchand, Nicolas, Lienard, Philippe, Siehl, Hans-Ullrich, Izato, H. (2014). Applications of Molecular Simulation Software SCIGRESS in Industry and University. *Fujitsu Scientific and Technical Journal*, 50(3), 46–51.
- Martin, L., Catherinot, V., & Labesse, G. (2006). kinDOCK: a tool for comparative docking of protein kinase ligands. *Nucleic Acids Research*, 34(suppl_2), W325–W329. <https://doi.org/10.1093/NAR/GKL211>
- Meng, X.-Y., Zhang, H.-X., Mezei, M., & Cui, M. (2011). Molecular docking: a powerful approach for structure-based drug discovery. *Cur-*

- rent Computer-Aided Drug Design*, 7(2), 146–157. <https://doi.org/10.2174/157340911795677602>
- Moitessier, N., Pottel, J., Therrien, E., Englebienne, P., Liu, Z., Tomberg, A., & Corbeil, C. R. (2016). Medicinal Chemistry Projects Requiring Imaginative Structure-Based Drug Design Methods. *Accounts of Chemical Research*, 49(9), 1646–1657. <https://doi.org/10.1021/ACS.ACCOUNTS.6B00185>
- Nabuurs, S. B., Wagener, M., De Vlieg J ; Claussen, H., Buning, C., Rarey, M., & Lengauer, T. (2010). Fleksy: a flexible approach to induced fit docking. *Journal of Cheminformatics* 2010 2:1, 2(1), 1–1. <https://doi.org/10.1186/1758-2946-2-S1-O24>
- Neves, M. A. C., Totrov, M., & Abagyan, R. (2012). Docking and scoring with ICM: the benchmarking results and strategies for improvement. *Journal of Computer-Aided Molecular Design*, 26(6), 675. <https://doi.org/10.1007/S10822-012-9547-0>
- Overview of DOCK. (n.d.). Retrieved November 8, 2021, from http://dock.compbio.ucsf.edu/Overview_of_DOCK/index.htm
- Pagadala, N. S., Syed, K., & Tuszynski, J. (2017). Software for molecular docking: a review. *Biophysical Reviews*, 9(2), 91–102. <https://doi.org/10.1007/S12551-016-0247-1>
- Pippel, M., Scharfe, M., Meier, R., & Sippl, W. (2012). ParaDockS – an open source framework for molecular docking. *Journal of Cheminformatics* 2012 4:1, 4(1), 1–1. <https://doi.org/10.1186/1758-2946-4-S1-F3>
- Pyrkov, T. V., Chugunov, A. O., Krylov, N. A., Nolde, D. E., & Efremov, R. G. (2009). PLATINUM: a web tool for analysis of hydrophobic/hydrophilic organization of biomolecular complexes. *Bioinformatics (Oxford, England)*, 25(9), 1201–1202. <https://doi.org/10.1093/BIOINFORMATICS/BTP111>
- Repasky, M. P., Shelley, M., & Friesner, R. A. (2007). Flexible Ligand Docking with Glide. *Current Protocols in Bioinformatics*, 18(1), 8.12.1-8.12.36. <https://doi.org/10.1002/0471250953.BI0812S18>
- Ruiz-Carmona, S., Alvarez-Garcia, D., Foloppe, N., Garmendia-Doval, A. B., Juhos, S., Schmidtke, P., ... Morley, S. D. (2014). rDock: a fast, versatile and open source program for docking ligands to proteins and nucleic acids. *PLoS Computational Biology*, 10(4). <https://doi.org/10.1371/JOURNAL.PCBI.1003571>
- Sarbini, S., Nayan, M. N., Chik, W. W. D., Radzi, M. M. N., Akbar, R., & Jusoh, S. A. (2013). Molecular docking studies of a quassinoid and P-glycoprotein. *IEEE Symposium on Computers and Informatics, ISCI 2013*, 138–142. <https://doi.org/10.1109/ISCI.2013.6612391>
- Sauton, N., Lagorce, D., Villoutreix, B. O., & Miteva, M. A. (2008). MS-DOCK: Accurate multiple conformation generator and rigid docking protocol for


- multi-step virtual ligand screening. *BMC Bioinformatics*, 9(1), 1–12. <https://doi.org/10.1186/1471-2105-9-184/FIGURES/3>
- Schleinkofer, K., Wang, T., & Wade, R. (2006). *Molecular Docking*. https://doi.org/10.1007/3-540-29623-9_3820
- Schneidman-Duhovny, D., Inbar, Y., Nussinov, R., & Wolfson, H. J. (2005). PatchDock and SymmDock: servers for rigid and symmetric docking. *Nucleic Acids Research*, 33(Web Server issue). <https://doi.org/10.1093/NAR/GKI481>
- Stroganov, O. V., Novikov, F. N., Stroylov, V. S., Kulkov, V., & Chilov, G. G. (2008). Lead finder: an approach to improve accuracy of protein-ligand docking, binding energy estimation, and virtual screening. *Journal of Chemical Information and Modeling*, 48(12), 2371–2385. <https://doi.org/10.1021/CI800166P>
- Tietze, S., & Apostolakis, J. (2007). GlamDock: development and validation of a new docking tool on several thousand protein-ligand complexes. *Journal of Chemical Information and Modeling*, 47(4), 1657–1672. <https://doi.org/10.1021/CI7001236>
- Trott, O., & Olson, A. J. (2010). AutoDock Vina: improving the speed and accuracy of docking with a new scoring function, efficient optimization and multithreading. *Journal of Computational Chemistry*, 31(2), 455. <https://doi.org/10.1002/JCC.21334>
- Tsai, T. Y., Chang, K. W., & Chen, C. Y. C. (2011). iScreen: world's first cloud-computing web server for virtual screening and de novo drug design based on TCM database@Taiwan. *Journal of Computer-Aided Molecular Design*, 25(6), 525–531. <https://doi.org/10.1007/S10822-011-9438-9>
- Venkatachalam, C. M., Jiang, X., Oldfield, T., & Waldman, M. (2003). LigandFit: a novel method for the shape-directed rapid docking of ligands to protein active sites. *Journal of Molecular Graphics & Modelling*, 21(4), 289–307. [https://doi.org/10.1016/S1093-3263\(02\)00164-X](https://doi.org/10.1016/S1093-3263(02)00164-X)
- Vieira, T. F., & Sousa, S. F. (2019). Comparing AutoDock and Vina in Ligand/Decoy Discrimination for Virtual Screening. *Applied Sciences* 2019, Vol. 9, Page 4538, 9(21), 4538. <https://doi.org/10.3390/APP9214538>
- Wagener, M., Ve Vlieg, J., & Nabuurs, S. B. (2012). Flexible protein-ligand docking using the Fleksy protocol. *Journal of Computational Chemistry*, 33(12), 1215–1217. <https://doi.org/10.1002/JCC.22948>
- Wang, J. C., Chu, P. Y., Chen, C. M., & Lin, J. H. (2012). idTarget: a web server for identifying protein targets of small chemical molecules with robust scoring functions and a divide-and-conquer docking approach. *Nucleic Acids Research*, 40(Web Server issue). <https://doi.org/10.1093/NAR/GKS496>

- Welch, W., Ruppert, J., & Jain, A. N. (1996). Hammerhead: fast, fully automated docking of flexible ligands to protein binding sites. *Chemistry & Biology*, 3(6), 449–462. [https://doi.org/10.1016/S1074-5521\(96\)90093-9](https://doi.org/10.1016/S1074-5521(96)90093-9)
- Yang, J. M., & Chen, C. C. (2004). GEMDOCK: a generic evolutionary method for molecular docking. *Proteins*, 55(2), 288–304. <https://doi.org/10.1002/PROT.20035>
- Zhao, Y., & Sanner, M. F. (2007). FLIPDock: docking flexible ligands into flexible receptors. *Proteins*, 68(3), 726–737. <https://doi.org/10.1002/PROT.21423>

Chapter 3

EVENT DENSITY VISUALIZATION WITH PYTHON FOLIUM LIBRARY FOR PUBLIC COMPLAINT MANAGEMENT: AN APPLICATION WITH 311 CALLS

Emre OZMEN¹

¹ Graduate School of Management, Nisantasi University, Istanbul, emre.ozmen@nisantasi.edu.tr,  <https://orcid.org/0000-0001-5541-1155>

INTRODUCTION

When products or services face with its audience, risk occurs. The risk is that audience either does not like it, thinks it does not meet expectations and/or falsely advertised. When the audience is getting bigger this even turns to more probable and needs more attention. They are not always right and more importantly it does not really matter. The truth is that there is likely no chances that an organization leave the situation alone. In the end, most majority of these happenings rarely has self-resolving nature. However, knowing that there is a need for answers is usually not enough to have a generic solution. Attempts to manage this with no methodology may jeopardize organization's reputation. In other words, when it comes to complaint management, ad-hoc attributes do not make a good fit. Therefore, establishing a complaint management process is vital.

Machines cannot complaint, complaints are rooted with human behavior and they usually burst emotions. A good complaint management system will not only help to manage the emotional side of the complaints, but it also helps to improve quality.

Quality may relate to products, features and services, where it also may consist of environmental aspects, safety or simply others, especially if it is public administration domain. Complaint management has its standard, ISO 10002:2018 declares definitions, duties and responsibilities. Complaints are expected to be assessed regularly and systematically. Feedbacks help to strength both loyalty and assurance of quality. Complaint management is also a part of customer relationship management (Stauss et al., 2019)

Complaint management systems can be drilled into two parts: direct complaint management processes and indirect complaint management processes. (Figure 1)



Figure 1: Principles of Complaint Management (Stauss et al, 2019)

Direct complaint management process includes four steps. It starts with stimulation and continues as acceptance, processing and reaction. Indirect complaint management process includes four steps. Indirect complaint management starts with evaluation, continues as management controlling, reporting and information using.

Direct complaints channels include phone, email and social media accounts. Stimulation favors the first handling and attempts to seek an immediate resolution. In the case it needs an escalation acceptance is to be applied, where processing works on variations about possible solutions. Reacting triggers a decision and a proper communication. It is important to not create an extra complaint, this especially true when stimulation phase occurs, since it is easy to make it conditional and ‘who is right’ extent. Most of the time, being able to listen at first point is more important the solution itself, since solution can address a wide selection of choices anyways, where we cannot say the same for someone waiting on queue for ten minutes. The latter can only help to guarantee incremental complaints and explicit posts on social media. When we say social media, it’s not necessarily social media accounts, it is more often unstructured and everywhere and this time it falls into the second group’s area, which is hypothetically tied with ‘hard to catch and difficult to resolve’ coupling.

Indirect complaints channels include social media, not only organization accounts, but everywhere with hashtags. It more likely becomes viral, requires more extensive technologies and expertise. Unstructured data technically refers to anything which is not structured. Structured data is known as tabular form and historically easier to analyze. Regression and classification techniques are old as data understanding itself, easy to interpret per tables and query nature. However, when it comes to free form text, speeches, audio, video and image processing everything turns to a different level. There are three reasons for that. First, the size of unstructured data is enormous, 10 times more than structured data on earth, which is also known as its volume dimension (Cibaroglu et al., 2019). Second, the data is not batch, it has streaming nature, thanks to petabit per second network speeds, then it requires real-time attention, which is also known as its velocity dimension. Third, the data formats vary from txt, png to avro, mpeg, where variety makes it only more challenging. Regardless this tripartite view, event density brings natural hurdles that makes complaint management even more difficult, since it requires more resources and minute you are late more chances to observe exponentialities (Alemi et al., 2012; Lin et al., 2020).

Complaint management in public and 311 services

Complaint management is historically tied with for-profit organizations, in other words companies. The reason is that the complainant is accepted as client, who paid money for something, a product or service. Knowing that the possibility of having complaints only increases with larger groups, public institutions should have been more interactions with complaints domain and maybe even had earlier attempts to make complaint management more institutionalized. It is relatively late that the power of voters was recognized, where vote has analogy with money that the audience spent, therefore expects services, maybe not the product. Knowing that they have an ultimate luxury to vote for alibi next time and they do, in other words the world not is not as 1970s anymore, municipalities decided to replicate corporations in local level, with similar practices (Stewart, 2014).

311 services were reserved for non-emergency calls by Federal Government on 1996 and first piloted in Baltimore, MD. On its first year it yields a 25% of 911 (emergency) calls (Dursun et al., 2020). As of today, more than 100 major cities in the US utilizes and per its first decade it reached out to over 8 Millions, where now welcomes more than 10 Millions of calls with 60% service requests, where New York City (NYC) is not only one the largest not in regards to the US, but also worldwide including Finland, Germany, Turkey (Mavi/Beyaz Masa), Sweden and the UK.

Methodology and Folium discussions

Both private and public compliant management systems deal with millions of people and uses same dynamics, have same concerns and technical bottlenecks, where number is event density. There are three basic questions that normal (batch) complaint management wonders to predict the density and manage resources accordingly:

- What is the problem?
- Where does it occur?
- When does it happen?

Traditionally, event density is considered as life distribution function (F) and yields to a survival function (S) in respect to probability distribution and probability density functions (Kerigan, 2015; Ajao, 2019).

$$s(t) = S'(t) = \frac{d}{dt} S(t) = \frac{d}{dt} \int_t^{\infty} f(u) du = \frac{d}{dt} [1 - F(t)] = -f(t)$$

However, when it comes to manage complaint of millions, there are only two basic questions that real-time (streaming) complaint management

wonders to know (no need to predict, no formulas) the density and manage resources accordingly:

- What is the problem?
- Where does it occur?

In the simplest way, based on this exploration, there can exist four facts on compatibility management for over-million audiences:

- Not knowing event density diminishes resource allocation efforts
- Batch predictions on resource allocations deteriorate complaint management efforts, especially in the sake of first response (stimulating) and responding (reaction) phase
 - If this happens, it only helps to observe more complaints with more exponentialities thru Avalanche Effect, therefore data needs to be processed real-time
 - It is only possible when event density is being marked real-time, not batch

This study favors real-time data but demonstration perspective it utilizes batch data. Visualizations have instant demonstrations and streaming data will make them change in seconds. Folium is one the alternatives with Plotly, developed by MIT laboratories, utilized for geolocation and GIS data visualization for scientific and engineering purposes. It is a part of Python ecosystem that you can manipulate and works with Leaflet.js libraires that you can visualize.

Folium enables both the binding of data to a map for choropleth visualizations as well as Vincent/Vega visualizations as markers on the map (Figure 2). Its library has a number of built-in sets from OpenStreetMap, MapQuest Open, MapQuest Open Aerial, Mapbox to Stamen, and supports custom sets with Mapbox or Cloudmade API keys. Folium supports both GeoJSON and TopoJSON overlays, as well as the binding of data to those overlays to create choropleth maps with color-brewer color schemes (Folium, 2015).

NYC Complaints Analysis - Mapping with Folium

Cleaning and Map visualization with Folium and GeoJson

- 311 complaints in NYC
- 100K rows within the year 2019, 40+ attributes/columns
- Cleaning function for zip codes
- Few queries for specifics

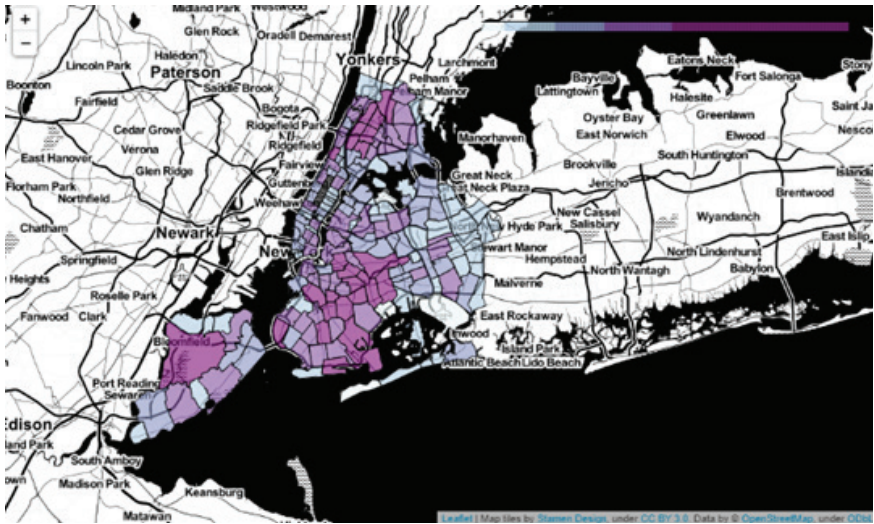


Figure 3: New York City Complaints Event Density

Connection point from Kings/Brooklyn County to Staten Island has 5 times differences amongst two neighbor Brooklyn zip codes, 11209 vs 11228, has around 50K population, but day-and-night polarization in complaints density. (Figure 4)



Figure 4: Event density anomaly: Similar populations – Polarized complaint size

CONCLUSION

Complaint management is a discipline that deals with millions of groups as an audience and not knowing the event’s density deteriorates resource allocation efforts, where batch predictions on resource allocations

diminish complaint management efforts, especially in the sake of first response (stimulating) and responding (reaction) phase (Senoglu et al., 2016). After all, when it happens, it only helps to observe more complaints with more exponentialities thru Avalanche Effect, therefore streaming data processing an ultimate need. Although this study favors real-time data, demonstration perspective it utilizes batch data. Visualizations have instant demonstrations and streaming data will make them change in seconds.

Per New York City (NYC) data analysis, leading complaints were listed as city noise, traffic, heat/water systems and illegal parking and final figure shows that that similarity in populations does not necessarily produces the same amount of complaints, aka events density connection point from Kings/Brooklyn County to Staten Island has 5 times differences amongst two neighbor zip codes.

This information is crucially meaningful for proper resource allocation in complaint management and it is only possible when it is real-time. This is one of those moments that rule based predictions would not help. To ground the study with a larger base, further applications with other major world cities stated earlier is suggested.

Future directions - Istanbul

Istanbul, based on United Nations' Department of Economic and Social Affairs Population Dynamics report per World Urbanization Prospects 2018 studies, is in the Top 12 cities in world, amongst over 10,000 cities per population (United Nations, 2019). Per PPP adjusted GDP, it is in top 25 with more than \$347B and has s dominating actor with over \$3B annual municipality budget (OECD, 2012). 153 calls are being managed by Beyaz Masa and yearly calls are around 15M, almost half the of NYC's (the oldest practitioner) annual numbers, which is highly significant. Being native Istanbul citizen, I am biased to replicate this Istanbul. However, unlike NYC open source data sharing platform and although there are many others with IBB (Istanbul Municipality, Istanbul Buyuksehir Belediyesi) Open Data Portal, there is no available data for 153 services, yet or it is not explicitly (either only the last month or locked to pivot, no raw data) shared, which is noted as further discussions.

REFERENCES

- Stauss B., Seidel W. (2019). Principles of Complaint Management. In: Effective Complaint Management. Management for Professionals. Springer, Cham. https://doi.org/10.1007/978-3-319-98705-7_4
- Cıbaroğlu, M. O., & Yalcinkaya, B. (2019). Belge ve Arşiv Yönetimi Süreçlerinde Büyük Veri Analitiği ve Yapay Zeka Uygulamaları. *Bilgi Yönetimi*, 2(1), 44-58.
- Liu, B. S. C., Sudharshan, D., & Hamer, L. O. (2000). After-service response in service quality assessment: a real-time updating model approach. *Journal of Services Marketing*.
- Alemi, F., Torii, M., Clementz, L., & Aron, D. C. (2012). Feasibility of real-time satisfaction surveys through automated analysis of patients' unstructured comments and sentiments. *Quality Management in Healthcare*, 21(1), 9-19.
- Stewart, R. G. (2004). Public sector reform knowledge production: validation and evidence as 'agreement'. *Australian journal of public administration*, 63(1), 58-65.
- Dursun, E , Varbak Nese, S , Kılıc, B . (2020). Green building certification of urban public railway transport systems for sustainable cities . *Balkan Journal of Electrical and Computer Engineering* , 8 (1) , 7-15 . DOI: 10.17694/bajece.649183
- Kerrigan, H. (2015). Learning from the best city 311 systems. Retrieved from <https://www.govloop.com/community/blog/learning-best-city-311-systems/#:~:text=Baltimore%20was%20the%20first%20in,generating%205.5%20million%20service%20requests>
- Ajao, L . (2019). A Secure Tracking Automobile System for Oil and Gas Distribution using Telematics and Blockchain Techniques . *Balkan Journal of Electrical and Computer Engineering* , 7 (3) , 257-268 . DOI: 10.17694/bajece.520979
- Folium. (2015). Project description. Retrieved from <https://pypi.org/project/folium/0.1.5/>. Folium 0.1.5.
- Şenoğlu, A., Yavanoğlu, U., & Özdemir, S. (2016). A New Supervised Epidemic Model for Intelligent Viral Content Classification. *International Journal of Intelligent Systems and Applications in Engineering*, 216-221.
- United Nations, Department of Economic and Social Affairs, Population Division (2019). *World Urbanization Prospects: The 2018 Revision (ST/ESA/SER.A/420)*. New York: United Nations.

OECD (2012). Redefining "Urban": A New Way to Measure Metropolitan Areas,
OECD Publishing, Paris, <https://doi.org/10.1787/9789264174108-en>

Chapter 4

THE INFLUENCE OF PH VALUES ON THE OPTOELECTRONIC, ELLIPSOMETRIC, AND SURFACE PROPERTIES IN THE PRODUCTION OF COBALT-DOPED ZNO FILMS

Olcay GENÇYILMAZ¹

¹ Doç. Dr. Olcay Gençyılmaz, ogencyilmaz@karatekin.edu.tr, Orcid ID: 0000-0002-7410-2937

1. Introduction

Recently, studies on binary and ternary compounds transparent conductive oxide (TCOs) films have been increasing and TCOs have been the focus of studies in both the technological and scientific fields due to their expandability and wide usability. TCOs have a wide range of applications such as optoelectronics devices, solar cells, flat panels, diodes, lasers [1, 2]. The most important characteristics of TCOs are that they can be transparent and conductive at the same time. This provides a great advantage over only materials that are transparent or conductive. TCOs can also be doped to improve these properties. There are many Al, Mg, In, Ga, Au, Ni, Co, Cu, Fe and Mn elements used in the contribution of TCOs. The basis of the doping process is to further develop the films without disturbing the general properties of the TCOs. Therefore, the doping ratio and the compatibility of the doping element in the structure need to be well defined.

Easy accessibility and economical production methods are an important factor in the choosing of TCO materials. The films such as ZnO, In_2O_3 , SnO_2 and ITO are the most studied TCOs [3]. Among these films, ZnO is an alternative material for tin oxide (SnO) which is rarely found in nature and it is the most studied and developed film in recent years [4, 5]. ZnO films generally have the following characteristics: High transparency and conductivity, wide band range (3.2-3.7 eV), large exciton bonding energy (60 meV), high carrier density and high electron mobility, reflect near infrared and n- type conductivity [6- 8]. Especially, these films are attractive on semiconductors applications such as solar cells, gas sensors, photodetector, UV light emission diodes, photocatalysts [9-15]. In recent years, additions have been made with transition metal oxides such as Mn, Co, Fe, Cu and Ni to improve the usage potential of ZnO films. With the doping process, the magnetic ions replace in the ZnO matrix without disturbing the structure and new features can be added to ZnO films. The radius of the Co atom is smaller than the radius of the Zn atom. This is an advantage in terms of lattice mismatch. Thus, the conductivity, band structure, magnetic and surface properties can be changed without disturbing the structure of the films.

Cobalt doped ZnO (ZnO:Co) films can be produced by various techniques such as sol-gel, spray, magnetron sputtering, hydrothermal method, pulsed laser deposition, electrochemical method [16-27]. Among these techniques, chemical methods are more preferred because they are economical and practical. For this reason, we used the spray technique that allows changing experimental parameters and deposition on large surfaces in our study.

A part of the works carried out in literature related to ZnO:Co in recent years is given in Table 1. These studies show that the structural, optical, magnetic, surface and electrical properties of ZnO:Co films are generally examined. Also, the techniques used in film production are both physical and physical techniques. Notable here are no studies on the pH effect, which is one of the production parameters of ZnO films. From the studies we have done about ZnO films before, we have determined that the pH effect affects the film quality very much [28]. In addition, another absence in the literature is that there is not enough information about the ellipsometric studies of ZnO and ZnO:Co films. In order to overcome these shortcomings and contribute to the literature, we produced cobalt doped ZnO (ZnO:Co) films at different pH values and examined the ellipsometric, optical, surface and electrical properties of the films in detail.

Table 1. Literature studies about ZnO:Co

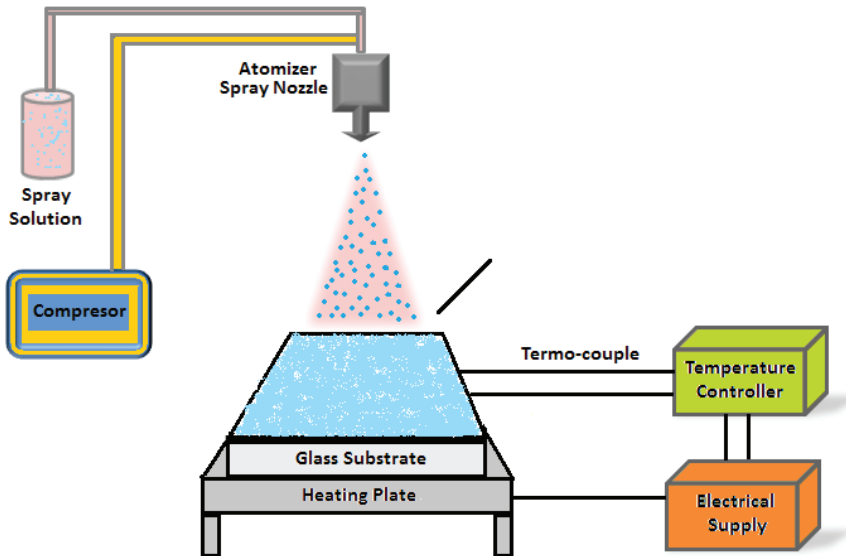
Method	Characterization	References
Sol-gel	X-ray diffraction (XRD), UV-visible (UV-vis) Current-voltage (I-V) Capacitance-voltage (C-V) Deep-level transient spectroscopy (DLTS) Laplace-transform deep-level transient spectroscopy (L-DLTS)	[16]
Sol-gel	XRD, FTIR, SEM	[17]
Hydrothermal	XRD, XRF, TEM, UV-vis and magnetic	[18]
DC magnetron sputtering	XRD and UV-vis	[19]
Electrochemical	XRD, UV-vis, SEM, EDX, TEM, XPS	[20]
Chemical method	XRD and UV-vis, Q-DLTS parameters	[21]
Solution method	XRD, UV-vis, FESEM, Vibrating sample magnetometer (SQUID-VSM)	[22]
Solvothermal	XRD, TEM and HR-SEM	[23]
Sol-gel	XRD, SEM	[24]
Sol-gel	XRD, SEM, PL and Raman	[25]
Spray	XRD, FESEM, EDX, UV-vis	[26]
Spray	XRD, FTIR-ATR, SEM	[27]

In this study, ZnO:Co films were produced using ultrasonic spray pyrolysis method. The films were sprayed on glass substrates and two different pH values were used in the production process. The effect of both Co doping and solution pH change on ellipsometric, optic, surface and electrical properties of ZnO films were investigated in detail. The change of optical properties of films such as transmittance, absorption and reflection were determined. Optical measurements indicated the presence

of characteristic peaks of the Co^{2+} ions in the ZnO host matrix. In addition, optical constants of thickness, refractive index and extinction coefficient values which were closely affected by the optical properties of the films were calculated by spectroscopic ellipsometry technique. The alterations were examined in the band structure and band gap of the films using optical method. Surface morphology and roughness values, other factors affecting the ellipsometric, optical and electrical properties of the ZnO films, were also investigated using atomic force microscopy. Also, the electrical resistivity of films was investigated by four-point probe method and figure of merit values were calculated. As a result, this study showed that ZnO:Co films produced at low pH value will have higher usage potential in optoelectronic devices.

2. Experimental

ZnO and ZnO:Co films of two different pH values of precursor were produced on glass substrates (Objektträger $1 \times 1 \text{ cm}^2$) by spray pyrolysis. The substrates were washed with deionized water and then dried. According to our optimization studies we have done before [28], we have determined pH values of precursor as 6.9 and 3.5. Both solutions were prepared as 100 ml and the doping rate was set to 3 %. The substrates were heated up to $300 \text{ }^\circ\text{C}$ and spraying was carried out. After spraying was finished, the films were left to cool in the same environment. After the films reached room temperature, they were removed and cleaned with ethanol and characterized. Detailed experimental parameters and photographs of films are given in Table 2 and Fig. 1.



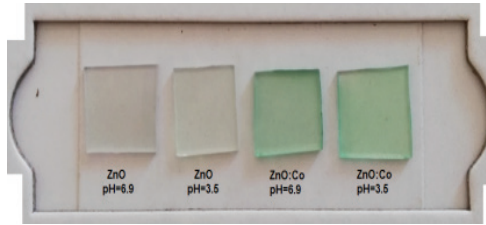


Figure 1. Spray pyrolysis set-up and photographs of ZnO:Co films

Table 1. Experimental details

Films	ZnO and ZnO:Co
Chemical Salts (SigmaAldrich)	Zinc acetate dihydrate [$\text{Zn}(\text{CH}_3\text{COO})_2 \cdot 2\text{H}_2\text{O}$] Cobalt (II) chloride hexahydrate ($\text{CoCl}_2 \cdot 6\text{H}_2\text{O}$)
Molarity - pH	0.05 M- 6.9 and 3.5
Doping rate	0 % and 3 %
Substrate Temperature	300 ± 5 C
Solution Amount	100 cc
Spraying Rate/Time	5 cc/dk-20 min

Optical, ellipsometric, surface and electrical properties of the produced films were examined. All analyzes were done at room temperature. The optical properties of films were examined a double beam Shimadzu-SolidSpec-3700 UV-VIS-NIR spectrophotometer and wavelength range set to 300-800 nm. The optical transmittance, reflectance and absorbance spectra were obtained from this analysis. Park System XE-70 AFM was used to take surface images and surface roughness values of films. AFM measurements were taken in non-contact mode and 0.6 Hz scan rate. AFM images of all films were scanned in an area of $5 \times 5 \mu\text{m}^2$ and the R_q (rms/root-mean-square), R_a (average) and R_{pv} (peak to valley) roughness values of the film in this area were determined. Also, the ellipsometric analysis of films was performed using PHE-102 spectroscopic ellipsometry. As a result of this analysis, the optical parameters such as $\psi - \Delta$, thickness (d), refractive index (n) and extinction coefficient (k) values of ZnO and ZnO:Co films by Cauchy-Urbach dispersion model. The resistivity and Haacke's factor values of films were examined by four-point probe technique.

3.Result and discussion

3.1. Ellipsometric Analysis

The spectroscopic ellipsometry (SE) is a technique used frequently in determining the thickness and optical parameters of semiconductor films in recent years. It is an optical technique which has important advantages such as sensitive, contactless and non-destructive. We used this technique for determination of the optical parameters including the thickness

refractive index (n), and extinction coefficient (k) of films. The basis of the SE technique is based on measuring the change in polarization as a result of the reflection of the light coming on the material surface. By making use of this change, it analyzes how the material surface gives light to the light. This polarization change can be expressed as:

$$tg \psi e^{(i\Delta)} = \frac{R_p^{polarize}}{R_s^{polarize}} = \frac{E_p^{out}/E_p^{in}}{E_s^{out}/E_s^{in}} \quad (1)$$

where R_p and R_s are ratios of the reflected wave amplitude to the incident wave amplitude for the p and s orientations, respectively [30, 31]. Delta (Δ) and psi (ψ) express the change between p-polarized component δ_1 and the s-polarized component δ_2 in polarization of incident and reflected light. Also, $tg(\psi)$ is defined as the absolute value of R_p/R_s . Δ and ψ parameters are examined at each wavelength and SE spectra are obtained. In our study, SE measurements of the films were taken in the range of 300-900 nm and Δ and ψ spectra were obtained. Fig. 2 shows Δ and ψ fit to the experimental data of films for different pH values. According to Fig. 2, model and experimental data were obtained by a computer-based modeling [32, 33]. It shows the spectral variation of experimental and model data. This spectral change shows that the thickness and optical parameters of the material change.

We used the Cauchy-Urbach model as it is more suitable for semiconductor films than other models in determining optical parameters. Also, this model is only appropriate over a region of the spectrum where there is normal dispersion. The Cauchy equation as follows:

$$n(\lambda) = A_n + \frac{B_n}{\lambda^2} + \frac{C_n}{\lambda^4} \quad (2)$$

$$k(\lambda) = A_k e^{B_k(E-E_b)} \quad (3)$$

where A_n , B_n , C_n , A_k , and B_k are model parameters [34]. The incident angle is a very important parameter in SE analysis. So, we take measurements at 70° incident angles in terms of the previous studies due to polarization effect. Thus, the fitting of model and experimental data was obtained by minimizing the mean square error (MSE) which is a Levenberg–Marquardt algorithm by a computer-based modeling [35]. As a result of this fitting, film thickness, model parameters, refractive index and extinction coefficient was determined. These model parameters and fitting graphics are exhibited in Table 2 and Fig. 2, respectively.

Fig. 3 and 4 shows the refractive index (n) and extinction coefficient (k) obtained from the fitted parameters for ZnO and ZnO:Co which

is produced different pH values. It is clear that pH values of precursor have an important effect on refractive index and extinction coefficient for these films. pH=6.9 have lower refractive index values for ZnO films. But ZnO:Co films have lower refractive index values for pH=3.5. So, ZnO:Co films, which are produced at pH=3.5, are more suitable for the alternative applications and the TCO materials. Therefore, the extinction coefficient values of films have shown a similar behavior for both pH values in Fig. 4 and these values nearly have remained stable when $\lambda > 300$ nm.

Table 2. Film thickness and ellipsometric model parameters

Films		d (nm)	A_n	$B_n \times 10^{-2}$ (nm) ²	$C_n \times 10^3$ (nm) ⁴	A_k	B_k (eV) ¹	MSE
pH=6.9	ZnO	94	1.95	0.05	0.001	0.23	0.05	0.52
	ZnO:Co	199	1.01	0.01	0.012	0.15	0.02	0.84
pH=3.5	ZnO	143	1.18	0.05	0.013	0.11	0.34	0.28
	ZnO:Co	137	1.92	0.04	0.003	0.19	0.27	0.97

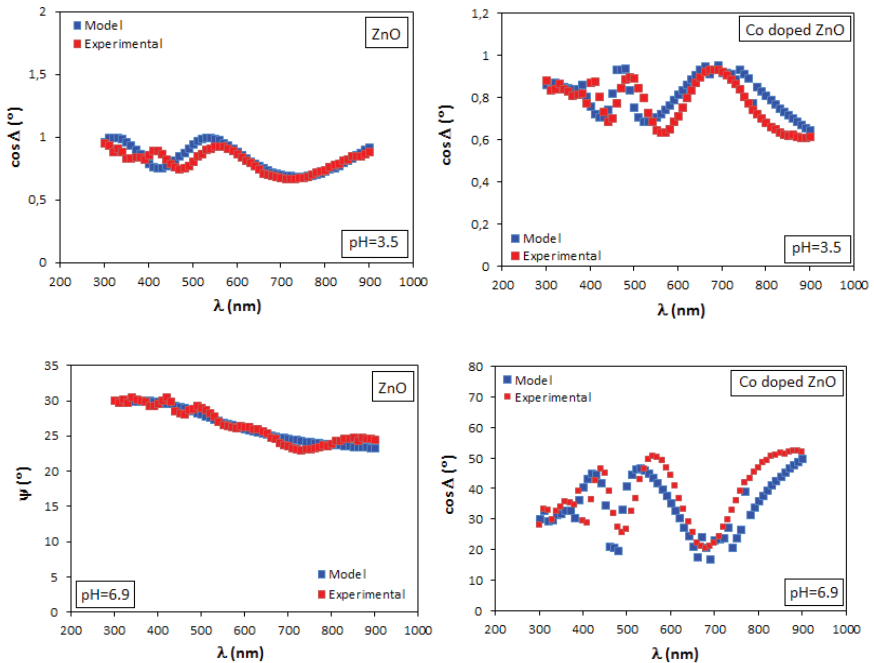


Figure 2. Measured and model fit ψ and $\cos\Delta$ ellipsometric parameters

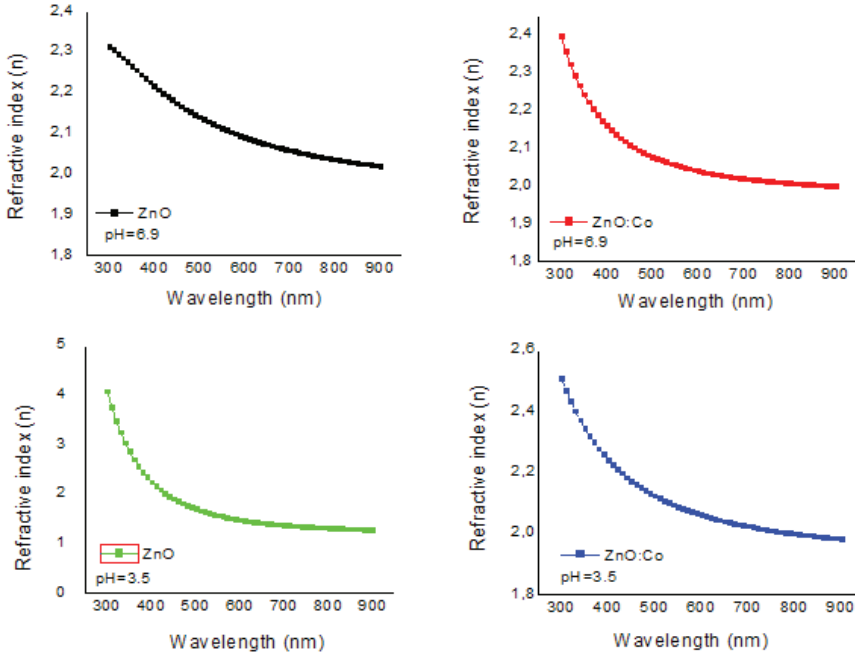


Figure 3. Refractive index (n) spectra

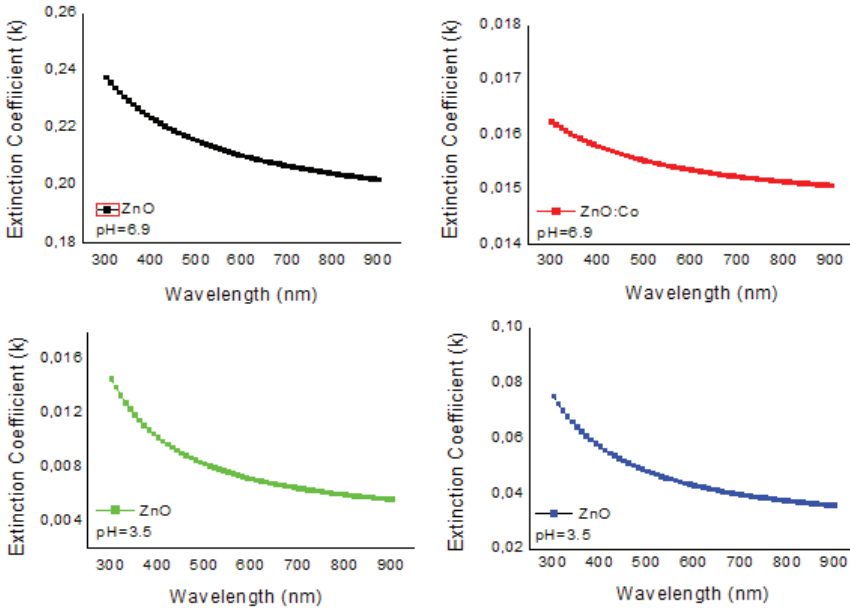


Figure 4. Extinction coefficient (k) spectra

3.2. Optical analysis

Fig. 5 shows the reflectance and transmittance spectra in the wavelength range 300–800 nm at room temperature. As is seen from Fig. 5, the transmission is low at short wavelength while the long wavelength is higher. So, the films exhibit transparent properties in long wavelength. The average transmittance values are almost the same for both films in the range of 400–700 nm. The absorption edge shifts toward longer wavelength and shaper with decreasing pH values of precursor. We can say that the sharper absorption edge can be clearly observed for pH=3.5 as shown in the inset of Figure 3. We think that our undoped and Co doped film has deformation and defects near band edges for high pH values.

Therefore, the characterization absorption peaks ((a)-(b)-(c)) belongs to ZnO:Co films were achieved for pH=3.5. These peaks were not seen in the same films for pH=6.9. These characteristic absorption peaks, which are pointed out the d–d electron transitions of high spin Co^{+2} ions in a tetrahedral crystal lattice: $4A_2(4F) \rightarrow 2E(2G)$ (2.23 eV), $4A_2(4F) \rightarrow 2T_1(2P)$ (2.06 eV) and $4A_2(4F) \rightarrow 2A_1(4G)$ (1.89 eV), are at 556 (a), 600 (b) and 655 (c) nm [36, 37]. As seen in Fig. 1, the change of the typical d-d transitions on the colors of the films is evident in the film photos. The changing of the green color of the films is allocated the typical d–d transitions. Similar color changes have been seen in the literature [38]. Also, we investigated reflectance spectra of ZnO and ZnO:Co films. The reflectance values are low for both pH values of precursor in the range of 400–700 nm because films have smooth surfaces, more tightly bounded particles and low surface scattering as shown in AFM micrographs (Fig. 8). The band gap values of the films were calculated using the Tauch equation [39]. This equation;

$$(\alpha h\nu)^{1/p} = A(h\nu - E_g) \quad (4)$$

where A is a constant, E_g is the band gap, α is the absorption coefficient corresponding to a particular transition occurring in the film, ν is the transition frequency and p can take the values 1/2, 3/2, 2 or 3, when the transitions are direct allowed, direct forbidden, indirect allowed and indirect forbidden respectively. The ZnO and ZnO:Co is considered as a material with direct band gap energy and hence $p=1/2$ is expected for direct allowed transition. The band gap were determined by extrapolating the linear region of the plots $(\alpha h\nu)^2$ versus $h\nu$ on the energy axis (Fig. 6). It is noted that the band of 3.22 eV and 3.24 eV obtained for undoped ZnO and then decreases with Co doping for both pH values. As seen in Fig. 7, the absorption coefficient dependence on photon energy in the spectral range of the near-band-edge empirically follows the exponential law (Urbach tail), which can be expressed as [40]:

$$\alpha(h\nu) = \alpha_0 e^{(h\nu/E_u)} \tag{5}$$

where α_0 is a constant, E_u is Urbach energy which corresponds to the width of the band tail and could be determined as the width of the localized states. Urbach energy gives information about the localization conditions and changes in the band structure of the films. In addition, the change of Urbach energy depends on factors such as temperature and structural defects. [41]

Fig. 7 shows the variation of $\ln\alpha$ vs. photon energy for the films.

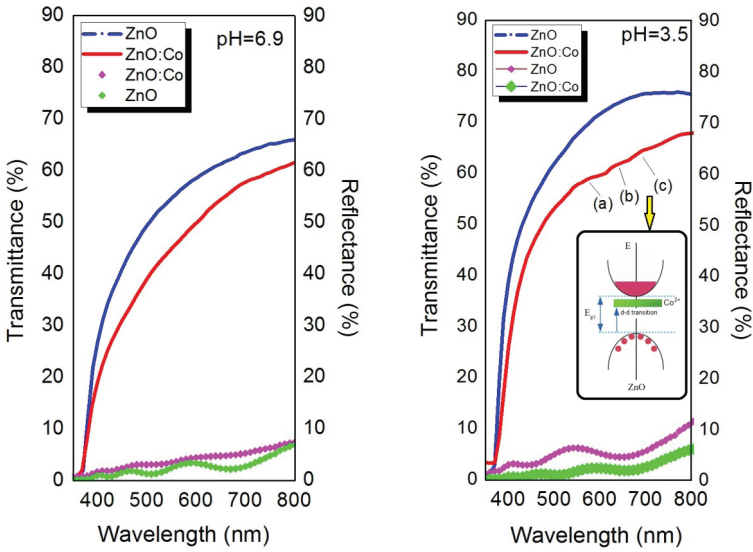


Figure 5. Transmittance and reflectance spectra of ZnO:Co films

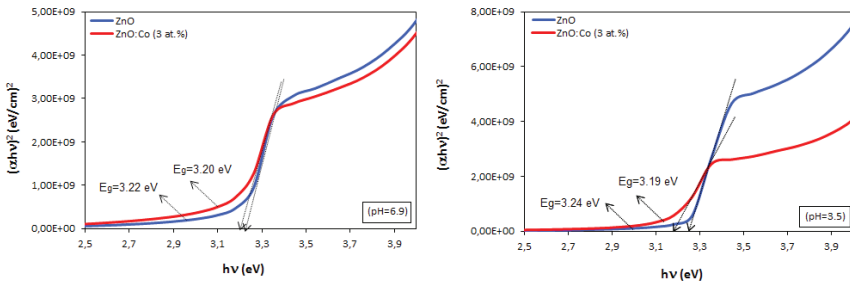


Figure 6. The plots $(\alpha h\nu)^2$ versus $h\nu$ of films

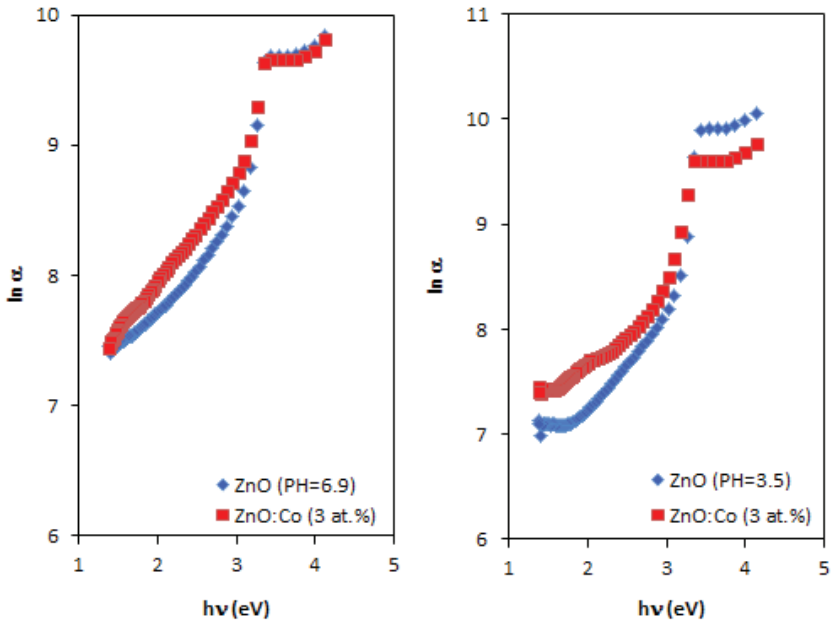


Figure 7. The Urbach plots of films

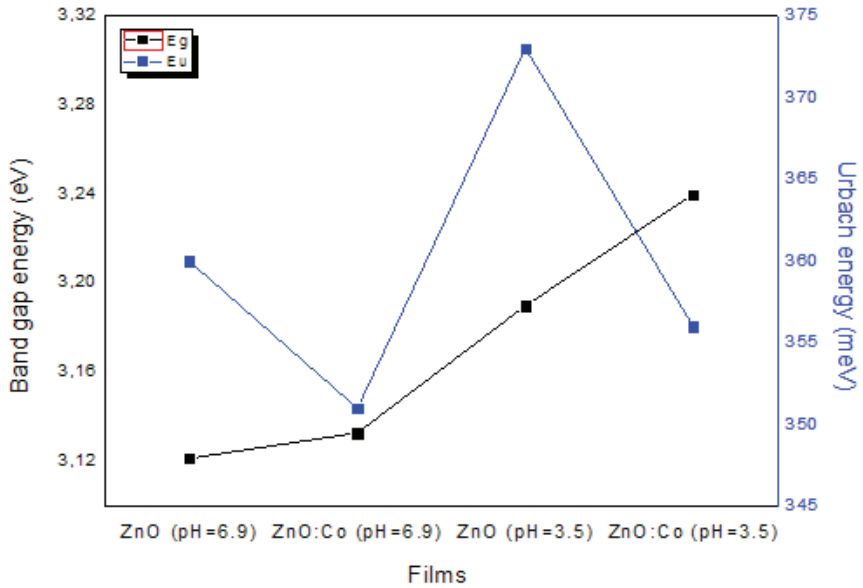


Figure 8. The change of the band gap and Urbach energy

3.3. Surface and electrical analysis

The morphology of the films was examined by atomic force microscopy. Fig. 9 shows AFM images of films with different pH values. We can clearly see the surface differences between ZnO and ZnO:Co films. ZnO:Co films have pointed structure while ZnO films have more granular structure. Fig. 9 indicated that, there are different regions on the film surface as deposited ZnO film with various heights. But, with decreasing pH values, the surface morphology of films starts to change. When the pH decreases in both films, it is seen that the granular and pointed structure starts to deteriorate. The AFM images of both ZnO and ZnO:Co films with pH 6.9 are nearly same, which have higher particle than the others (see Fig. 9). When the pH value is 3.5, we can see that the surface morphology of the films is more uniform, granular, and homogeneous. Especially, the produced films have a more uniform surface with distinguishable particles and these films have more acicular structure according to other films with both Co doping and changing of pH values. It was understood that this change on the surface had an effect on the changes we determined on the optical properties of the films. Besides, the roughness measurement results for $5 \times 5 \mu\text{m}^2$ areas are given in Table 3.

Table 3. The roughness and resistivity of films

Films	pH=6.9		pH=3.5	
	ZnO	ZnO:Co	ZnO	ZnO:Co
R_q (average roughness)	52	48	39	50
R_a (rms/root-mean square)	41	36	31	36
R_{pv} (peak-valley)	384	510	264	485
Resistivity ($\Omega\cdot\text{cm}$)	2.17×10^{-1}	4.14×10^{-2}	1.04×10^{-1}	2.21×10^{-3}

The electrical resistivity of the films was measured by four-point probe methods and these values are given in Table 4. Especially in the Co doped films, the change of pH value caused significant changes in resistivity values. The lowest resistivity value was determined in ZnO:Co films produced at pH = 3.5 (Table 3). In addition, Haacke's figure of merit (FOM), which is generally used to determine the potential of TCOs in solar cell applications, was used to investigate the electrical performance of the films.

FOM is a correlation associated with the average optical transmittance and sheet resistance of the films. This relation;

$$\text{FOM}(\phi) = \frac{T_{\text{average}}^{10}}{R_{\text{sheet}}} \quad (6)$$

where T is average optical transmittance and R_{sheet} is the sheet resistance. While determining the sheet resistance of the films, the resistivity and thickness values that were determined previously were used. Fig. 10 shows FOM and the sheet resistance graphics. It was determined that ZnO and ZnO:Co films produced with pH = 3.5 have high permeability (in the range of 400-700 nm) and low layer resistance. It is determined that ZnO and ZnO:Co films produced with pH=3.5 have high transmittance (in the range of 400-700 nm) and low layer resistance compared to other films. The highest FOM value was determined in ZnO: Co films produced at pH = 3.5, so it is highly usable for optoelectronic applications among the produced films. Similar results were found in the literature [42].

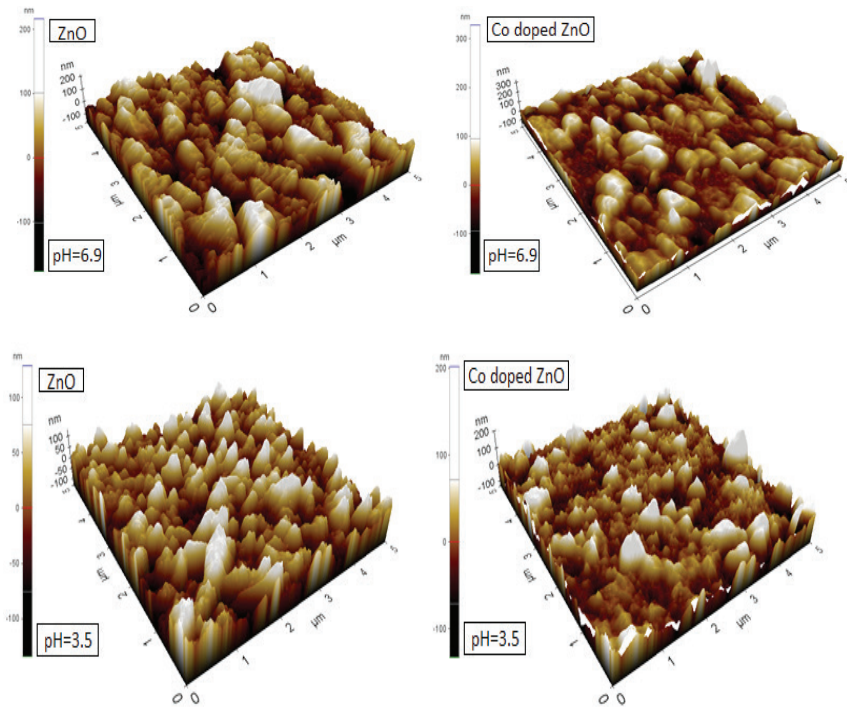


Figure 9. AFM images of films

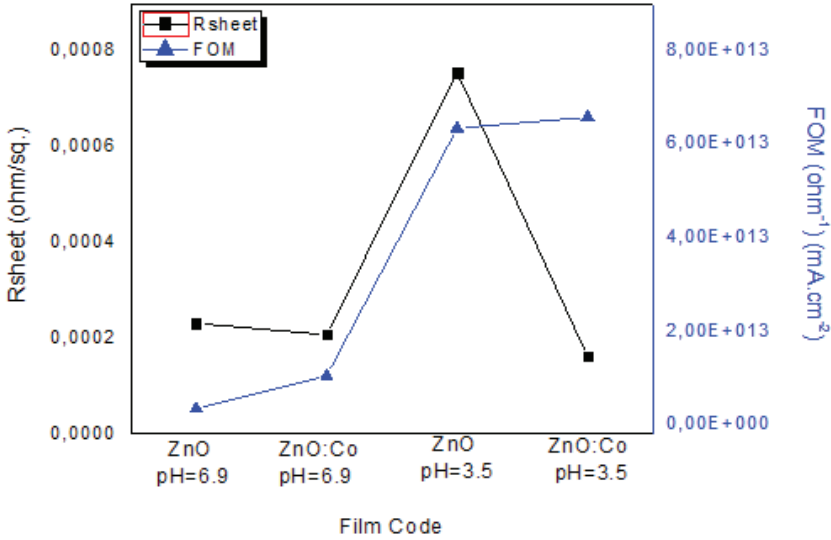


Figure 10. Figure of merit and sheet resistance of films

4. Conclusions

In summary, ZnO and ZnO:Co films were produced with various pH values by simple and low cost spray pyrolysis. The effect of pH values of precursor on the optical, ellipsometric and surface properties of ZnO and ZnO:Co films were broadly examined. We determined that pH values of precursor have distinctly effect on the some physical properties of these films. The optical parameters such as refractive index, extinction coefficient, and thickness, values were acquired by Cauchy–Urbach dispersion model using spectroscopic ellipsometry. The thicknesses of films increased with decreasing pH values of precursor. The refractive index and band gap values of ZnO:Co films have significantly decreased when pH value decreased. The variations in optical absorption edges of films were also investigated. We obtained shaper absorption edge and Co characterization peaks at three different wavelengths with decreasing pH values of precursor. AFM analysis revealed that roughness values of films have not alteration but surface morphology have smoother images and settlement with decreasing pH values. In addition to, ZnO: Co films have the lowest resistivity at pH = 3.5 and have the highest FOM value compared to other films.

According to these analysis results, the optical, ellipsometric parameters, surface and electrical properties of ZnO and ZnO:Co films were controlled by changing the pH values of precursor for various applications. As a result of this study, ZnO:Co showed that the physical properties of the films have changed positively not only in Co doping but also in the pH

of the solution. Also, these results can offer different perspectives in other researchers which focus on the different optoelectronic areas of ZnO:Co films.

Acknowledgements

Author is thankful to Prof. Dr. Ferhunde ATAY and Prof. Dr. İdris AKYÜZ, Eskişehir Osmangazi University, Eskişehir, Turkey, for providing processing and the analysis opportunities. A part of this study was presented orally at International Mardin Artuklu Multidisciplinary Studies Congress in 2019.

REFERENCES

- [1] Technical Paper, Transparent Conductive Oxide Thin Films, <https://materion.com/media/files/advancedmaterials%20group/me/technicalpapers/transparentconductiveoxidethinfilms.pdf>
- [2] Stadler, A. (2012). Transparent Conducting Oxides An Up-To-Date Overview. *Materials*, 5, 661-683.
- [3] Coutts, T. J., Perkins, J. D., Ginley, D. S., Mason, T. O. (1999). Transparent Conducting Oxides: Status and Opportunities in Basic Research. National Renewable Energy Laboratory, Presented at the 195th Meeting of the Electrochemical Society Seattle, Washington.
- [4] Lee, J. H., Park, B. O. (2003). Transparent conducting ZnO:Al and Sn thin films deposited by sol-gel method. *Thin Solid Films*, 426, 94-99.
- [5] Kumar, V., Singh, R. G., Singh, F., Purohit, L. P. (2012). Highly transparent and conducting boron doped zinc oxide films for window of Dye Sensitized Solar Cell applications. *Journal of Alloys of Compounds*, 544, 120-124.
- [6] Hong, R., Qi H., Hunag, J., He H., Fan, Z., Shao, J. (2002). Influence of oxygen partial pressure on the structure and photoluminescence of direct current reactive magnetron sputtering ZnO thin films. *Thin Solid Films*, 473 (1), 58-62,.
- [7] Kuo, S.Y., Chen, W. C., Cheng, C. P. (2006). Investigation of annealing-treatment on the optical and electrical properties of sol-gel derived zinc oxide thin films, *Superlattice Microstructures*, 39, 162-170.
- [8] Yan, Z., Song, Z. T., Liu, W. L., Wan, Q., Zhang, F. M., Feng, S. L. (2005). Optical and electrical properties of p-type zinc oxide thin films. *Thin Solid Films*, 492, 203-206.
- [9] Goktas, A., Aslan, F., Tumbul, A., Gunduz, S. H. (2016). Tuning of structural, optical and dielectric constants by various transition metal doping in ZnO:TM (TM=Mn, Co, Fe) nanostructured thin films: A comparative study. *Ceramic International*, 43, 704-713.
- [10] Wang, M., Liang, W., Yang, Y., Yang, J., Cheng, X., Hahn, S. H., Kim, E. J. (2012). Sol-gel derived transparent conducting ZnO:Al thin films: Effect of crystallite orientation on conductivity and self-assembled network texture. *Journal of Mater Chemical Physics*, 134, 845-850.
- [11] Muchuweni, E., Sathiaraj, T. S., Nyakoty, H. (2016). Effect of gallium doping on the structural, optical and electrical properties of zinc oxide thin films prepared by spray pyrolysis. *Ceramic International*, 42, 10066-10070.

- [12] Galstyan, V., Comini, E., Baratto, C., Faglia, G., Sberveglieri, G. (2015). Nanostructured ZnO chemical gas sensors. *Ceramic International*, 41, 14239-14244.
- [13] Herero, J., Gutierrez, M. T., Guillen, C., Dona, J. M., Martinez M. A., Chapparro A. M. and Bayon R. (2000). Photovoltaic windows by chemical bath deposition. *Thin Solid Films*, 28, 361–362.
- [14] Muchuweni, E., Sathiaraj, T. S., Nyakoty, H. (2016). Low temperature synthesis of radio frequency magnetron sputtered gallium and aluminium co-doped zinc oxide thin films for transparent electrode fabrication. *Applied Surface Science*, 390, 570-577.
- [15] Prepelita, P., Medianu, R., Sbarcea, B., Garoi, F., Filipescu, M. (2010). The influence of using different substrates on the structural and optical characteristics of ZnO thin films *Applied Surface Science*, 256, 1807-1811.
- [16] Ahmeda, M. E. I., Taghizadeh, F., Auret, F. D., Meyer, W. E., Nel, J. M. (2019). The effect of alpha particle irradiation on electrical properties and defects of ZnO thin films prepared by sol-gel spin coating. *Materials Science in Semiconductor Processing*, 101, 82-86.
- [17] Valeikiene, L., Paitian, R., Grigoraviciute-Puroniene, I., Ishikawa, K., Kareiva, A. (2019). Transition metal substitution effects in sol-gel derived Mg_xM_x/Al_1 (M = Mn, Co, Ni, Cu, Zn) layered double hydroxides. *Materials Chemistry and Physics*, 237, 121863.
- [18] Barbosaa, C. C. S., Peixotoa, E. B., Jesusa, A. C. B., Jesusa, J. R., Fabianb F. A., Costac, I. M., Almeida, J. M. A., Duquea, J. G. S., Meneses, C. T. (2019). Effect of doping in $Ce_{1-x}TM_xO_2$ (TM = Mn, Cr, Co and Fe) nanoparticles obtained by hydrothermal method. *Materials Chemistry and Physics*, 225, 187-191.
- [19] Panyajirawuta, P., Pratumswana, N., Meesombada, K., Thanawattana, K., Chingsungnoen, A., Boonyopakorn, N., Aiempakit, M., Pecharapa, W. (2017). Preparing transparent cobalt-doped ZnO thin films by DC magnetron sputtering. *Materials Today: Proceedings*, 4, 6311–6316.
- [20] Miao, Y., Wang, X., Wang, W., Zhou, C., Feng, G., Cai, J., Zhang, R. (2017). Synthesis of cobalt-doped ZnO/rGO nanoparticles with visible-light photocatalytic activity through a cobalt-induced electrochemical method. *Journal of Energy Chemistry*, 26, 547-555.
- [21] Zia, A., Ahme, S., Ali, M. (2019). Defects anomaly in cobalt-doped ZnO nanostructures using optical and charge transient analysis. *Chinese Journal of Physics*, 58, 159-165.
- [22] Thanh Hoai Ta, Q., Namgung, Noh, J. S., (2018). Morphological evolution of solution-grown cobalt-doped ZnO nanostructures and their properties. *Chemical Physics Letters*, 700, 1-6.
- [23] Vahtrus, M., Šutka, A., Polyakov, B., Oras, S., Antsov, M., Doebelin, N., Löhmus, R., Nömmiste E. and Vlassov S. (2016). Effect of cobalt doping

- on the mechanical properties of ZnO nanowires. *Materials Characterization*, 121, 40-47.
- [24] Stoica, A. O., Andronescu, E., Ghitulica C. D., Voicu, G., Grumezescu, A. M., Popa, M., Chifiriu, M. C. (2016). Preparation and characterization of undoped and cobalt doped ZnO for antimicrobial use. *International Journal of Pharmaceutics*, 510, 430-438.
- [25] Husain, S., Alkhtaby, L. A., Bhat, I., Giorgetti, E., Zoppi, A., Miranda, M. M. (2014). Study of cobalt doping on structural and luminescence properties of nanocrystalline ZnO. *Journal of Luminescence*, 154, 430-436.
- [26] Tarwa, N. L., Gurav, K.V., Prem Kumar, T., Jeong, Y. K., Shim, H. S., Kim, I. Y., Kimd, J. H., Jang, J. H., Patil, P. S. (2014). Structure, X-ray photoelectron spectroscopy and photoluminescence investigations of the spray deposited cobalt doped ZnO thin films. *Journal of Analytical and Applied Pyrolysis*, 106, 26-32.
- [27] Senol, S. D., Ozugurlu, E., Arda, L. (2020). The effect of cobalt and boron on the structural, microstructural, and optoelectronic properties of ZnO nanoparticles. *Ceramics International*, 46 (6), 7033-7042.
- [28] Gençyılmaz, O., Atay, F., Akyüz, İ. (2015). Ellipsometric Investigation of Optical Parameters and Characterization of Spray Pyrolysis-Derived ZnO Films, *Metallurgical and Materials Transactions*, 46A, 4247-4254.
- [30] Fujiwara, H. (2007). *Spectroscopic Ellipsometry: Principles and Applications*. Jhon Wiley and Sons, Chichester.
- [31] Tompkins, H. G., Hilfiker, J. N., (2016). *Spectroscopic Ellipsometry: Practical Application to Thin Film Characterization*. Momentum Express, New York.
- [32] Woollam, J. A., Johs, B., Herzinger, C. M., Hilfiker J., Synowicki, R., Bunday, C. L. (1999). Overview of Variable Angle Spectroscopic Ellipsometry (VASE). Part II: Advanced Applications Proceedings CR72 3, 29-58.
- [33] Khoshman, J. M., Ingram, D. C., Kordesch, M. E. (2008). Growth and optical properties of amorphous $\text{Be}_{0.13}\text{Zn}_{0.38}\text{O}_{0.49}$ thin films prepared by radio frequency magnetron sputtering. *Journal of Non-Crystalline Solids*, 354, 2783-2786.
- [34] Jenkins, F. A., White, H. E. (1981). *Fundamentals of Optics*, 4th ed., McGraw-Hill, Inc.
- [35] Lehmann, E. L., George, C. (1998). *Theory of Point Estimation* (2nd ed.). New York: Springer.
- [36] Ramachandran, S., Tiwari, A., Narayan, J. (2004). *Applied Physics Letters*, 84, 5255.
- [37] Kim, K. J., Park, Y. R. (2002). Spectroscopic ellipsometry study of optical transitions in $\text{Zn}_{1-x}\text{Co}_x\text{O}$ alloys. *Applied Physics Letters*, 81 (8), 1420-1422.

- [38] Liu, X. C., Shi, E. W., Chen, Z., Zhang, H. W., Song, L. X., Wang, H., Yao, S. D., (2006). *Journal of Crystal Growth*, 296, 135–140.
- [39] Pankove, J. I. (1975). *Optical Processes in Semiconductors*. Dover Publication: Mineola, NY, USA.
- [40] Urbach, F (1953). The Long-Wavelength Edge of Photographic Sensitivity and of the Electronic Absorption of Solids. *Physical Review*, 92, 1324.
- [41] Boubaker, K. (2011). Atomic structures beyond the spherical approximation along with PNC as conjectured explanations to Urbach tailing in neutral isolated ytterbium. *European Physical Journal B*, 84, 235-239.,
- [42] Mohamed, S. H., El-Hagary, M., Emam-Ismail, M. (2010). Thickness and annealing effects on the optoelectronic properties of ZnS films. *Journal of Physics D: Applied Physics*, 43, 075401.

Chapter 5

DRUGS USED IN THE TREATMENT OF VIRAL INFECTIONS AND INNOVATIONS IN ANTIVIRAL THERAPY¹

Fatma ÇETİNKAYA
Hülya ÇELİK

¹ Ağrı Ibrahim Cecen University, Faculty of Pharmacy Department of Pharmaceutical Technology Departmenten 03200 Ağrı/TÜRKİYE

INTRODUCTION

Viruses

Virus: It exists in the cell as molecular particles. Most of the time, there is a core of nucleic acid in the center, which can crystallize, and the protein around it consists of a sheath. They are known as the smallest parasites that absolutely need bacteria, plant or animal cells in order to reproduce, that is, a host cell. Viruses are obligate intracellular organisms. They cannot be seen even with a light microscope. The parts of viruses that cause infection are the nucleic acids in the centre. In many cases, this part enters the appropriate cells and can cause disease on its own. The organism can disrupt virus division with the help of cytotoxic T-lymphoids that recognize virus-producing cells, or it can bind to extracellular virus fragments with antibodies that inactivate them. Antibiotics are useless in curing viral diseases. But it can be useful in cases where superinfections occur. The most important reason limiting the use of antiviral drugs is their low selectivity, and the fact that effective and toxic doses are very close to each other (Anonymous 2019a).

Since viruses are obligate intracellular parasites, they need the host cell to reproduce themselves. In host selection, the receptor relationship between the virus and the host cell determines the host spectrum. After establishing association with their specific receptors, viruses transmit their genetic material to the host cell by different mechanisms depending on whether they are enveloped or non-enveloped. In general, enveloped viruses enter the cell by endocytosis or membrane fusion, while non-enveloped viruses inject their genetic material into the host cell by penetration. They cause cancer, especially because enveloped viruses cause them to abolish contact inhibition on the host cell membrane. In general, RNA viruses cause cancer, while DNA viruses do not. For the replication of viruses entering the host cell, the envelope or capsid must be peeled off and the viral genome released. It is thought that the low pH of the endosome and some factors in the host cell are effective in this happening. Viral replication takes place by different mechanisms according to the genetic material of the virus. In general, the replication of DNA viruses occurs in the nucleus of the host cell, while the replication of RNA viruses occurs in its cytoplasm. New viruses leave the cell by budding, apoptosis, or exocytosis. While the vitality of the cell is preserved when viruses leave the host cell by budding and exocytosis, the development of apoptosis results in the death of the cell (Süzergöz 2016).

Antiviral Treatment

The concept of specific antiviral therapy first appeared in 1946 (for mumps and smallpox viruses). Initial trials were made with sulfonamides.

As a result, it was concluded that viruses are not sensitive to antibiotics and it is not possible to obtain selective toxicity for intracellular parasites. The first drug with antiviral properties was 'idoxuridine'. In 1959, Dr Bill Prusoff, during his antineoplastic drug studies, determined that idoxuridine had a specific inhibitory effect against DNA viruses, especially HSV (Büke 2012).

Antiviral Drugs Used in the Treatment of Viral Infections

There are 37 antiviral drugs licensed for the chemotherapy of viral infections. For the treatment of human immunodeficiency virus (HIV) infections, 19 compounds have been officially approved: (1) the nucleoside reverse transcriptase inhibitors (NRTIs) are zidovudine, didanosine, zalcitabine, stavudine, lamivudine, abacavir, and emtricitabine; (2) the nucleotide reverse transcriptase inhibitor (NtRTI) is known as tenofovir disoproxil fumarate; (3) non-nucleoside reverse transcriptase inhibitors (NNRTIs) are nevirapine, delavirdine, and efavirenz; (4) the protease inhibitors are known as saquinavir, ritonavir, indinavir, nelfinavir, amprenavir, lopinavir (4/1 combined with ritonavir) and atazanavir; and the viral entry inhibitor enfuvirtide. Adefovir dipivoxil together with lamivudine is also approved for the treatment of chronic hepatitis B virus (HBV) infections. Anti-herpesvirus agents include acyclovir, valacyclovir, penciclovir (when applied topically), famciclovir, idoxuridine and trifluridine (both applied topically), and brivudine, used to treat herpes simplex virus (HSV) and/or varicella-zoster virus (VZV) infections; and ganciclovir, valganciclovir, foscarnet, cidofovir, and fomivirsen (the latter on intravitreal injection) have proven useful in the treatment of cytomegalovirus (CMV) infections in immunocompromised patients (ie, AIDS patients with CMV retinitis). Following amantadine and rimantadine, the neuraminidase inhibitors zanamivir and oseltamivir have recently become available for the treatment (and prophylaxis) of influenza virus infections (De Clercq 2004).

Adverse Effects Due to Antiviral Drugs

Drugs targeting viral processes must first be able to enter host cells. Viruses generally affect cell division. Therefore, the drug acting on it also affects the host cell. Therefore, the treatment intervals are narrow. The most common adverse event is nephrotoxicity. The drug often causes the virus to hide (latent virus). In vivo and in vitro susceptibility tests of drugs may differ, since the drug is effective after activation. For most people, antiviral drugs and viral diseases for which they are used are limited. Their clinical use in veterinary medicine is not common. The emergence of the human immunodeficiency virus (HIV) and its development in the cat as a model of HIV has slightly increased the animal database (Filazi 2020).

Antiviral drug-induced nephrotoxicity

Drug-induced kidney injury is known as an important side effect in clinical practice, which often causes acute renal failure (ARF). Cases of Acute Renal Failure in patients admitted to the hospital or intensive care unit account for 2% and more than 15%, respectively. It is difficult to determine the exact frequency of nephrotoxicity caused by antiviral drugs. Antiviral drugs cause renal failure through various mechanisms. Direct renal tubular toxicity has a unique effect on renal epithelial cells. These include the antiviral drugs cidofovir, adefovir dipivoxil, tenofovir, and acyclovir. In addition, crystal deposits in the kidneys can increase the development of kidney failure. Several different drugs have been found to cause crystal nephropathy. These include acyclovir and the protease inhibitor indinavir. Kidney damage associated with antiviral drugs involves various processes that affect renal transporters other than renal tubular cells. (Izzedine et al 2005)

Antiviral drugs and acute kidney injury

The introduction of more effective antiviral drugs is a common cause of drug-induced acute kidney injury (AKI). Antiviral drugs cause nephrotoxicity, and its true prevalence has hardly been determined. Antiviral drugs cause AKI by many mechanisms such as acute tubular necrosis (ATN), allergic interstitial nephritis (AIN), and crystal nephropathy. ATN has been identified with antiviral drugs such as cidofovir, adefovir, and tenofovir that have effects on transporter defects, apoptosis, and mitochondrial damage. Atazanavir-induced AIN is known to have a rapid onset of AKI and is usually not oliguric but requires dialytic therapy due to severity. In addition, crystal nephropathy from acyclovir, indinavir, and foscarnet may cause AKI due to intratubular obstruction (Leowattana 2019).

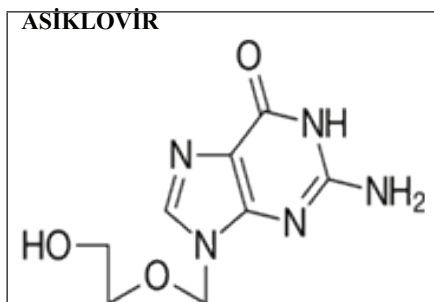
Antiviral Drugs Used in Herpes Treatment

Herpes simplex virus (HSV) infection can be treated with antiviral medications such as acyclovir (ACV). However, drug resistance is known to occur, especially in immunocompromised patients (prevalence approximately 5%) and allogeneic bone marrow transplant patients (prevalence up to 30%). Resistance to ACV is related to mutations in one of the two viral enzymes involved in ACV's mechanism of action: the enzyme thymidine kinase (TK) and DNA polymerase. In 95% of cases, ACV resistance is associated with mutations in the TK gene because this enzyme is not required for virus replication, unlike viral DNA polymerase which is rarely involved in resistance. ACV-resistant strains almost always show cross-resistance to other TC-dependent drugs (such as penciclovir and famciclovir). Resistant infections can be managed with foscarnet or cidofovir antiviral drugs, but both drugs are more toxic than ACV. These

drugs also have the ability to inhibit viral DNA polymerase, but because they are not TC dependent, they are active on most ACV-resistant HSV; however, due to a mutation in DNA polymerase, ACV-resistant virus may develop cross-resistance to these molecules. Resistance-related TK mutations are insertion or deletion or substitution. DNA polymerase mutations are especially found in conserved regions of the enzyme. It has been reported that there is a high level of gene polymorphism for these genes, especially for TK (Morfin and Thouvenot 2003).

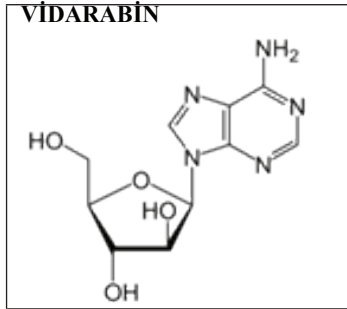
Herpes simplex virus (HSV) types 1 and 2 can cause infections with clinical manifestations ranging from benign and usually self-limiting blisters or sores in herpes and genital herpes to severe and, in rare cases, life-threatening infections. Currently, almost all approved treatments for the herpes simplex virus are nucleoside analogues. New antiviral methods include therapeutic vaccines that have successfully completed phase 2 clinical development. Some small molecule methods are also being developed to treat genital or lip HSV infections. Two novel compounds (amenamivir and pritelivir) of novel helical primerase inhibitors are of particular interest. (Birkmann and Zimmermann 2016).

Antiviral drugs used for this purpose are *Acyclovir*, *Pencyclovir*, *Famcyclovir*, *Ganciclovir*, *Vidarabine*, *Valacyclovir*, *Valgancyclovir*, *Brivudin*, *Sidofovir*, *Fomivirsen*, *Foskarnet*, *Idoxuridine*, *Trifluridine* (Büke 2012)

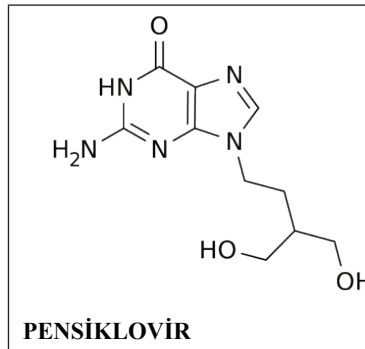


It is a drug that acts on various herpes virus and cytomegalovirus. Being highly selective and well tolerated among antiviral drugs are its superior features. It is a drug that inhibits cell proliferation of the herpes virus in vitro. The drug undergoes bioinactivation in infected cells where it inhibits DNA synthesis. In order for acyclovir to suppress the reproduction of the virus, it must first be converted to acyclovir monophosphate via the virus-specific thymidine kinase enzyme and then to acyclovir triphosphate by enzymes in the host cell. The resulting acyclovir triphosphate is known to act as a pseudo-substrate for Herpes virus DNA polymerase. Antiviral

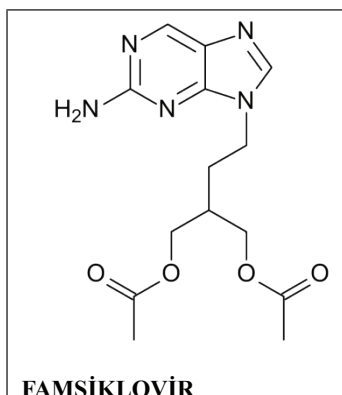
agents such as acyclovir are used in severe viral infections of the skin (Anonymous 2019b). Acyclovir and its 1-valyl ester prodrug valacyclovir are new generation antiviral drugs. Acyclovir is a safer drug than other antiviral drugs. (It will be safer if used with probenecid (Filazi 2020).



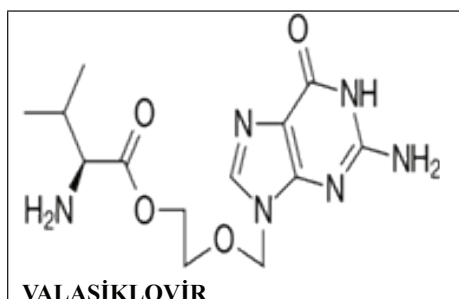
It is an adenosine derivative drug. It is the antiviral drug with the highest efficiency and lowest toxicity among the purine analogs. It is applied topically for ocular herpesvirus and systemically for hepatic encephalitis and neonatal herpes viral infections. When it reaches a high value in the blood, there are bone marrow suppression and CNS side effects (Filazi 2020).



It is an acyclic guanine analogue. It is chemically similar to acyclovir. Penciclovir is poorly absorbed from the gastrointestinal tract. Penciclovir is used topically. In viral infections called mucocutaneous herpes-recurrent herpes labialis, 1% cream containing Penciclovir is applied every 2 hours. Recovery is rapid with penciclovir and pain from the virus subsides rapidly. It is similar to acyclovir in its mechanism of action and spectrum. But although it is much less potent than Acyclovir, penciclovir accumulates in higher concentrations inside the cell. It is better tolerated than famciclovir. There is a contraindication for hypersensitivity (Büke 2012, Filazi 2020).



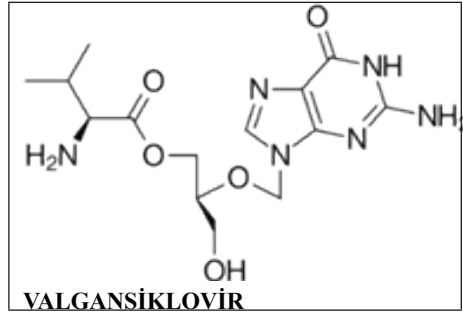
Famciclovir is the diacyl 6-deoxy analog of Penciclovir. Oral absorption is rapid. Its bioavailability reaches 77%. Famciclovir is metabolized to Penciclovir. The plasma concentration of penciclovir in the blood can reach a peak in 1 hour. Famciclovir is excreted by the kidneys as Penciclovir and Deoxy precursor in the body. It shows its effect with Penciclovir. Penciclovir triphosphate acts as a substrate for viral DNA polymerase and acts to suppress Herpes DNA synthesis. It is successfully used in the treatment of recurrent genital herpes virus infection and Recurrent herpes labialis virus infection. Interacts with probenecid. The most serious side effects of famciclovir are: headache, vomiting, rarely kidney failure (Bücke 2012).



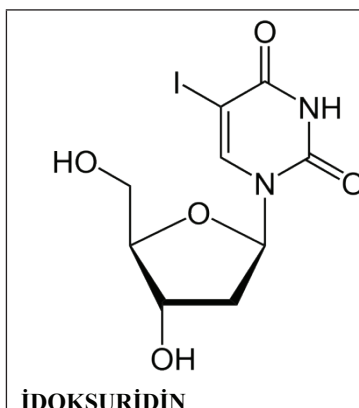
It is known as the L-valyl ester of acyclovir. But its bioavailability is 55% higher than acyclovir. After absorption, all are metabolized to acyclovir during the first intestinal transit and by hepatic metabolism. Serum reaches its highest concentration in 1-3 hours.

In addition, it was concluded that the serum acyclovir level was much higher in those using valacyclovir. It is used in the treatment of primary and recurrent herpes genitalis, and in the treatment of recurrent herpes labialis. It is used in the treatment of acute retinal neurosis. In the treatment of VZV, 500 mg tablets are used for 7 days with an interval of 12 hours.

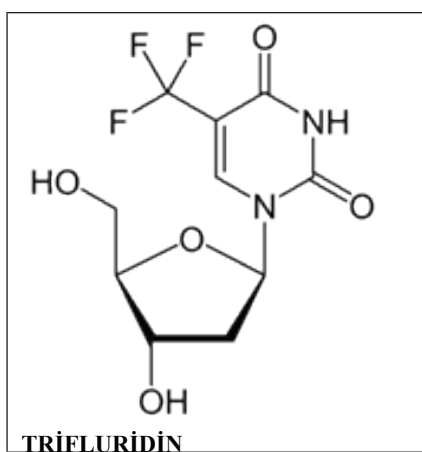
In the treatment of zoster, 1000 mg tablets are used every 8 hours for 7 days (the first dose should be given within the first 48 hours following the rash). It is also among the known information that it is used to prevent CMV in kidney Tx cases. It was not found to be effective in heart Tx, liver Tx, lung Tx, pancreatic Tx, small intestine Tx receptors. Side effects of valacyclovir are gastrointestinal system complaints (nausea, abdominal pain), myelosuppression and skin rash (Büke 2012).



It is the precursor of ganciclovir. Oral absorption of valganciclovir is very good. Valganciclovir is converted to Ganciclovir during the first intestinal transit and by hepatic metabolism. In addition, the bioavailability of Ganciclovir was 60% after taking it with food. Fatty foods increase bioavailability and peak level in serum. It reaches its highest value in plasma in 1-3 hours. It is excreted by the kidney. Valganciclovir is eliminated in the urine as ganciclovir with a half-life of approximately 4 hours in subjects with normal renal function. It shows its effect in the form of ganciclovir triphosphate. Valganciclovir acts as a substrate for CMV DNA polymerase and inhibits virus replication. Valganciclovir is used in the treatment of CMV retinitis in AIDS patients (450mg tbl. 900mg every 12 hours for 21 days), to prevent CMV disease in CMV D+/R-kidney, heart or kidney-pancreas Tx recipients, in many countries whole solid organ Tx It is used to prevent CMV in patients with . Approved to prevent CMV in pediatric heart and kidney Tx recipients. It is used in the preemptive treatment of asymptomatic CMV infections in Tx recipients. It has proven to be as effective as IV ganciclovir in the treatment of mild to moderate CMV disease in Tx recipients. The side effects of valganciclovir are as follows: most commonly, bone marrow suppression, gastrointestinal system complaints (nausea, vomiting, diarrhea) (Büke 2012).



It is converted to triphosphate metabolite in the host cell and thus becomes active. It inhibits viral DNA polymerase and, in particular, replaces thymidine in the viral DNA chain being synthesized and stops its replication and transcription. It is not very selective and can be harmful to the host cell. It is used only locally for the treatment of superficial layers of the cornea - herpesvirus keratitis and skin herpesvirus infection (Filazi 2020).

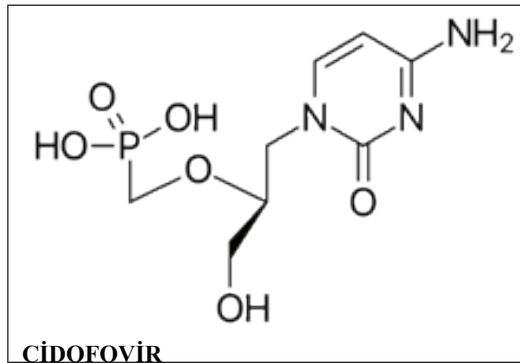


Trifluridine is an antiviral drug used in the treatment of primitive keratoconjunctivitis and recurrent epithelial keratitis due to herpes simplex virus types 1 and 2 in ophthalmic solutions. Trifluridine is used in combination with tipiracil as oral tablets. It has previously been used in the treatment of adult patients with metastatic colorectal cancer (Pubchem 2021a).

Trifluridine is a fluorinated pyrimidine nucleoside. It is structurally related to idoxuridine and thymidine (Pubchem 2021b). Trifluridine may cause mild local irritation of the conjunctiva and cornea when instilled, but these effects fade over time. May irritate skin, eyes and mucous membranes. The most common side effects of trifluridine 1% ophthalmic solution are mild, transient burning or stinging on installation (4.6%) and palpebral edema (2.8%). Local irritation of the conjunctiva and cornea is usually not permanent (pubchem 2021c).

Clinical analyzes report that elevations in serum enzyme concentration occur in up to 24% of patients receiving trifluridine/tipiracil therapy, but also in 27% of controls. . In this and subsequent studies, no clinically significant hepatic adverse reactions with trifluridine/tipiracil were reported (Pubchem 2021d).

There is no known antidote for trifluridine overdose: in the case of overdose, management should include conventional therapeutic and supportive medical intervention aimed at improving existing clinical signs and preventing potential complications. According to findings from animal studies, trifluridine can cause fetal toxicity when administered to pregnant patients (pubchem 2021e).



It has antiviral activity and is known as a synthetic, acyclic, monophosphate nucleotide analogue of deoxycytidine, which is mostly used against cytomegalovirus. After incorporation into the host cell, cidofovir is phosphorylated to its active metabolite cidofovir diphosphate by pyruvate kinases. Having structural similarity to the nucleotides, cidofovir diphosphate competes with deoxycytosine-5-triphosphate for viral DNA polymerase and is incorporated into the growing viral DNA chain. As a result, it prevents further DNA polymerization and disrupts DNA replication of viruses (Chem 2021a).

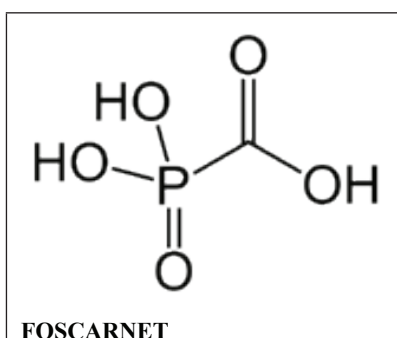
In addition, it settles in the developing DNA chain as an alternative

substrate and causes the destruction of the chain. Cidofovir is 5 times more effective against cytomegalovirus (CMV) *in vitro* than ganciclovir, but also acts against acyclovir-resistant Herpes simplex and varicella-zoster viruses, as well as Epstein-Barr virus and human herpes virus type 6. Azidothymidine and cidofovir show synergistic effects against CMV. Ganciclovir, on the other hand, shows a synergistic addition to CMV with cidofovir at low concentrations and an antagonist at high concentrations.

Wutzler and Thust stated that many nucleoside analogues, including cidofovir, induced chromosome aberration in mice and rats, but were inactive in gene mutation experiments. Carcinogenicity findings were observed to be variable in mice and rats (İlhan 2009).

Cidofovir is intracellularly phosphorylated and competes with cytosine, causing DNA strand termination and inhibition of DNA viral synthesis. Cidofovir acts against various herpes viruses, papilloma, polyoma, pox and adenoviruses in cell culture. Cidofovir is poorly absorbed orally. Therefore, it must be given intravenously. It is usually given with probenecid to inhibit rapid renal excretion. Cidofovir is used for the treatment of cytomegalovirus retinitis and is used off-label to treat severe adenovirus and acyclovir-resistant herpes simplex infections in immunocompromised individuals. Cidofovir was approved for use in the United States in 1996 and its use is largely limited due to its potential for nephrotoxicity (ncbi 2021a).

With the long intracellular half-life of its metabolites, cidofovir can be administered weekly during induction and biweekly during maintenance therapy. No viral resistance has been documented in patients treated with cidofovir to date, but improvement has been seen *in vitro* (Pubmed 2021a).



It has antiviral activity and is known as a synthetic, acyclic, monophosphate nucleotide analogue of deoxycytidine, which is mostly used against cytomegalovirus. After incorporation into the host cell, cidofovir is phosphorylated to its active metabolite cidofovir diphosphate

by pyruvate kinases. Having structural similarity to the nucleotides, cidofovir diphosphate competes with deoxycytosine-5-triphosphate for viral DNA polymerase and is incorporated into the growing viral DNA chain. As a result, it prevents further DNA polymerization and disrupts DNA replication of viruses (Chem 2021a).

In addition, it settles in the developing DNA chain as an alternative substrate and causes the destruction of the chain. Cidofovir is 5 times more effective against cytomegalovirus (CMV) *in vitro* than ganciclovir, but also acts against acyclovir-resistant Herpes simplex and varicella-zoster viruses, as well as Epstein-Barr virus and human herpes virus type 6. Azidothymidine and cidofovir show synergistic effects against CMV. Ganciclovir, on the other hand, shows a synergistic addition to CMV with cidofovir at low concentrations and an antagonist at high concentrations.

Wutzler and Thust stated that many nucleoside analogues, including cidofovir, induced chromosome aberration in mice and rats, but were inactive in gene mutation experiments. Carcinogenicity findings were observed to be variable in mice and rats (İlhan 2009).

Cidofovir is intracellularly phosphorylated and competes with cytosine, causing DNA strand termination and inhibition of DNA viral synthesis. Cidofovir acts against various herpes viruses, papilloma, polyoma, pox and adenoviruses in cell culture. Cidofovir is poorly absorbed orally. Therefore, it must be given intravenously. It is usually given with probenecid to inhibit rapid renal excretion. Cidofovir is used for the treatment of cytomegalovirus retinitis and is used off-label to treat severe adenovirus and acyclovir-resistant herpes simplex infections in immunocompromised individuals. Cidofovir was approved for use in the United States in 1996 and its use is largely limited due to its potential for nephrotoxicity (ncbi 2021a)

With the long intracellular half-life of its metabolites, cidofovir can be administered weekly during induction and biweekly during maintenance therapy. No viral resistance has been documented in patients treated with cidofovir to date, but improvement has been seen *in vitro* (Pubmed 2021a),

Antiviral Drugs Used in the Treatment of Influenza

What is influenza?

Caused by influenza A and B viruses, spreading rapidly, causing disease in all age groups; It is known as a highly contagious, febrile, acute respiratory system disease. The frequency of infection is higher in children. Frequency of death from influenza; It is higher in people over 65 years of age, in children under 2 years of age, and in high-risk people with other underlying diseases. It is confused with other infectious diseases of the

upper respiratory tract. But it can be distinguished by its unique complaints and findings. For the diagnosis of influenza, there are ways such as rapid antigen tests, fluorescent staining techniques, nucleic acid recognition methods, virus culture and serological methods that can detect the virus quickly. There are ways to protect against influenza and its complications: To comply with prevention measures (such as hand hygiene, avoiding close contact with patients) and to vaccinate people in the risk group (Tosun 2017a).

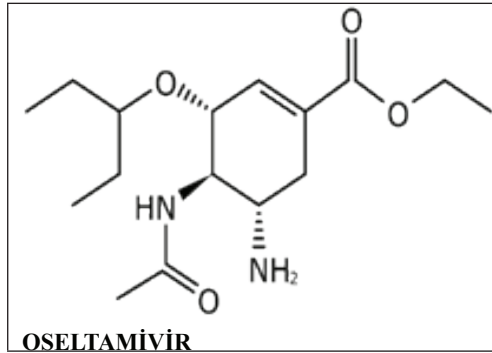
How is influenza transmitted?

Influenza viruses are transmitted to healthy people by droplets from the respiratory secretions of people carrying these viruses. It is transmitted very easily by direct or indirect contact with an infected person, through micron-level droplets dispersed by the patient's sneezing, coughing or even speaking. The survival of the virus takes place in humidity and low temperature, so the disease is more common in autumn and winter. Indoor living, public transport, fast and modern international travel are important factors in the spread of the virus. The spread and severity of the disease are related to many factors. Among these, the transmission of the virus and the sensitivity of the society are known to be the leading factors (Tosun 2017b).

Influenza treatment

influenza infection, if the person is previously healthy and does not have an immunosuppressive condition, he/she recovers completely in approximately 1-2 weeks. However, various severe complications such as pneumonia may occur in the elderly, children and other susceptible groups. It has been revealed that influenza B can cause Reye's Syndrome in children who use aspirin continuously due to acute rheumatic fever. Influenza cases have often created a self-limiting picture in healthy individuals without immune system problems. However, morbidity and mortality rates are high in high-risk groups. Antibiotics do not affect viral infections, so their use in the treatment of influenza is of no use unless complications develop. Therefore, the treatment of influenza cases is symptomatic and supportive treatment. Analgesics, antipyretics, and sometimes antihistamines are effective in reducing complaints. In terms of supportive treatment, the person is in a warm and comfortable environment, avoiding heavy physical activities, taking bed rest for at least 48 hours in cases where fever and other symptoms are severe, consuming at least 8 glasses of fluid a day to soften the mucus, provide drainage and regain the lost fluid. Gargling with warm, salty water to reduce sore throat, using humidifiers and water vapor are very effective methods to increase the ambient humidity. Smoking increases throat irritation and coughing. For this reason, the person should

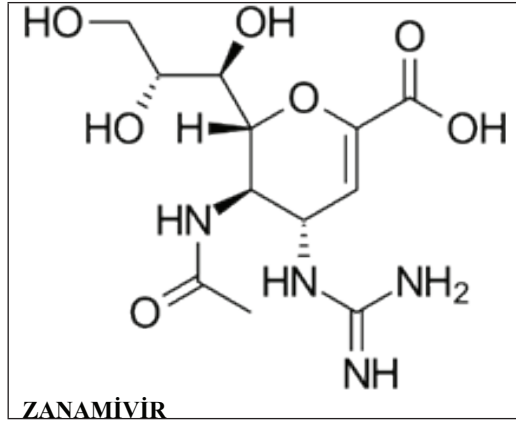
definitely not smoke, and also should not smoke in the environment. Antivirals are used for influenza prophylaxis and treatment. These specific antivirals include neuraminidase inhibitors zanamivir and oseltamivir. Adamantan group drugs (amantadine and rimantadine) are drugs that are effective only against influenza A. These drugs are no longer used in practice due to the developing high resistance. The main expected benefit of treatment is the shortening of the duration of influenza symptoms. When zanamivir and oseltamivir are started in the early period of the disease at the onset of symptoms, they affect susceptible viruses and reduce the severity and duration of the disease (Tosun 2017c). Drugs Used:



Oseltamivir, unlike zanamivir, is a pro-drug form with good bioavailability when used orally. 75-80% of the oral dose is easily absorbed from the gastrointestinal tract. In addition, more than 90% of liver cells are metabolized to its active metabolite, oseltamivir carboxylate, via hepatic carboxylesterases is being converted. Ingestion of oseltamivir with food has little effect on plasma density, but may delay the time to reach peak concentration. Oseltamivir carboxylate is well distributed to areas of viral infection in the upper and lower respiratory tract. The excretion of both the prodrug, oseltamivir phosphate, and its active metabolite, oseltamivir carboxylate, occurs unchanged in the urine via tubular secretion. In patients with renal insufficiency with a creatinine clearance of less than 30 mg/mL, the dose should be adjusted. There is insufficient information about whether dose adjustment is necessary in patients with hepatic insufficiency. The plasma half-life of oseltamivir carboxylate is between 6 and 10 hours. This makes it possible to give it twice a day. The pharmacokinetic properties of oseltamivir, such as low plasma protein binding and an independent metabolism of cytochrome P450 and glucuronidase systems, indicate that it will not cause any problems in terms of drug interactions through these mechanisms. No serious interactions of oseltamivir with other drugs are

known. Oseltamivir is a drug that generally has few side effects. The most common side effect is related to the gastrointestinal system. While vomiting is observed in about 15% of children using the drug, diarrhea, abdominal pain, nausea, insomnia, dizziness, headache and ear disorders are other side effects that occur. Resistance development is; oseltamivir resistance Oseltamivir resistance was detected as 0.9% in influenza A (H1N1) pdm 09 viruses tested by the Center for Disease Control and Prevention as of October 1, 2015. No resistance was detected in influenza A (H3N2) and influenza B viruses. On the other hand, the prevalence of influenza A (H1N1) pdm 09 virus, which showed resistance to oseltamivir during the 2013-2014 influenza season, was approximately 1% in the USA and was found at a low value (Çiftçi et al. 2016).

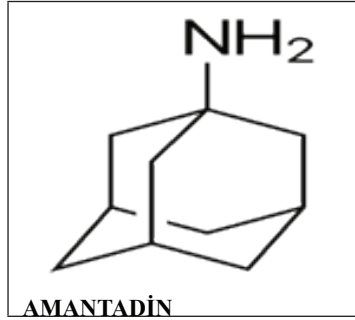
Neuropsychiatric disorders such as convulsions and delirium have been observed in patients treated with oseltamivir for influenza, especially in children and adolescents. On the other hand, the safety and efficacy of oseltamivir treatment or prophylaxis in immunocompromised patients has not been conclusively proven. In the post-marketing experience of oseltamivir-containing preparations, serious skin reactions such as anaphylaxis and toxic epidermal necrolysis, Stevens-Johnson Syndrome and erythema multiforme have also been reported (Anonymous 2020a).



Zanamivir oseltamivir gibi bir nöraminidaz inhibitörüdür. Bu iki ilacın etki mekanizması birbirine benzemektedir. Oral biyoyararlanımı zayıf olduğu için solunum yolu ile uygulanmaktadır. Alışılmış doz günde iki kez verilen 10 mg şeklinde verilir. Zanamivir öncelikle böbreklerden atılmakla birlikte, sistemik biyoyararlanımı düşük bir ilaç olduğu için böbrek yetmezliğinde doz ayarlamasına gerek yoktur. Zanamivirin solunum yollarından uygulanması, bronkospazma neden olabilmektedir. Bu

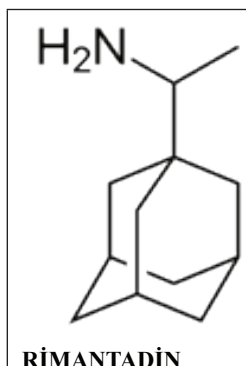
nedenle, kronik obstrüktif akciğer hastalarında sorun meydana getirebilir (Kurt vd. 2013).

Zanamivir antiviral ilacının oral biyoyararlanımı yoktur ve bir inhaler aracılığı ile oral inhalasyon yoluyla kullanılmaktadır. Aktif ilacın % 10-20'si akciğerlere erişmektedir kalanı ise orofarenkste kalır. Bu sistemik ilaç etkisi istenmediğinde bir avantaj olarak kabul edilebilmektedir. İnhibitör etkisi 10 saniye içerisinde başlar ve nöraminidaz enziminin IC50 değerinin 1000 kat konsantrasyonlara ulaşabilmektedir. Zanamivirin sağlıklı erişkinlerde yapılan erken çalışmalarında hastalık başlangıcından itibaren ilk 36-48 saatte ilacın alınması durumunda semptomatik hastalıkta 1-2 gün azalma görülmüştür. Başlangıçtaki çalışmalarda oral inhalasyon yanına eklenen intranazal uygulamanın ekstra bir yarar getirmediği görülmüştür. İlaç 2002'den önce yapılan çift kör kontrollü çalışmalarında median semptom süresini çocuklarda 1.0, sağlıklı erişkinlerde 0.8, yaşlı veya komorbiditesi olanlarda 0.9 gün olarak kısaltmıştır. Zanamivir 7 yaş üstü çocuklarda kullanılabilir. Zanamivir doz ve tedavi süresi günde iki kez 10 mg (iki 5 mg'lık inhalasyon) olmak üzere toplam 5 gündür. Zanamivir öksürük, bronkospazm ve astım ya da diğer kronik akciğer hastalığı olanlarda solunum fonksiyonlarında geçici olarak bir azalma da meydana getirir. Kronik akciğer hastalığı olanların yanında kısa etkili bir bronkodilatör taşımaları da tavsiye edilir (Korten 2006).



Amantadine is also known as an M2 inhibitor. Amantadine targets the M2 protein of influenza A, which creates a protein channel necessary for viral replication. Amantadine is not effective against influenza B viruses or influenza A virus. Not recommended for the treatment or prophylaxis of influenza in 2019-2020. Because resistance to amantadine has developed. Not recommended for use. Despite this, amantadine is an approved drug for the treatment of influenza A viral infections in children older than 1 year (Anonymous 2020b). Amantidine and ramantidine produce a marked reduction in symptoms, especially when used within the first 48 hours of infection. However, its usage area has narrowed due to the resistance

developed against the agent. In the trials, it is known that amantadine and rimantadine have similar effects. However, neurological side effects are lower in rimantadine compared to amantadine (Küçük and Yıldırım 2019).



Rimantadine is a drug known as a cyclic amine and alpha-methyl derivative of amantadine with antiviral activity. Although the mechanism of action of rimantadine is not fully understood, this drug exerts its antiviral effect against influenza A virus by interfering with the function of the transmembrane domain of the viral M2 protein. Thus, it prevents the coating and subsequent release of the virus (Pubchem 2020a).

Rimantadine is used for the prophylaxis of respiratory tract infections caused by influenza A virus in adults and children and for the treatment of respiratory tract infections caused by influenza A virus in adults (Pubchem 2020b). Rimantadine Hydrochloride tablets are commercially available. These tablets should be stored in tight and light resistant containers at 15-30 degrees (Pubchem 2020c). Despite widespread use, there is little evidence that rimantadine causes serum enzyme elevations or liver damage when administered orally (Pubchem 2020d). The oral LD in rats is 50, 640 mg/kg. Overdoses of a related carpet, amantadine, produce agitation, hallucinations, cardiac arrhythmia, and death (Pubchem 2020e).

In elderly patients, especially in chronic care centres, rimantadine produces adverse effects, particularly central nervous system and gastrointestinal, compared to younger adults or children (Pubchem 2020f). Tablet and syrup formulations are absorbed evenly after oral administration. It shows good absorption. 40% of typical plasma concentrations are protein bound. Rimantadine is extensively metabolized in the liver and less than 25% of the dose is excreted in the urine as unchanged drug. Glucuronidation and hydroxylation are known as major metabolic pathways (Drugbank 2020).

2.4 Antiviral Drugs Used in the Treatment of Chronic HBV

Hepatitis B virus infection has become a major public health problem worldwide. Approximately 30% of the world's population still shows serological evidence of current or past infection. The hepatitis B virus is a partially double-stranded DNA virus: HBsAg and anti-HBs, HBeAg and anti-HBe, and anti-HBc IgM and IgG. It is transmitted through contact with infected blood and semen. A safe and effective vaccine has been available since 1981 and, although variable, the implementation of universal vaccination in infants has led to a sharp decline in prevalence. Hepatitis B virus is not cytopathic. That is, both liver injury and viral control - and thus clinical outcome - depend on complex interactions between virus replication and the host immune response. Overall, 40% of men and 15% of women with perinatally acquired hepatitis B virus infection die from liver cirrhosis or hepatocellular carcinoma. Along with reducing liver inflammation, long-term antiviral therapy may reverse cirrhosis and reduce hepatocellular carcinoma. It is aimed to develop new treatments that can improve HBsAg clearance and virological recovery (Trepo et al. 2014).

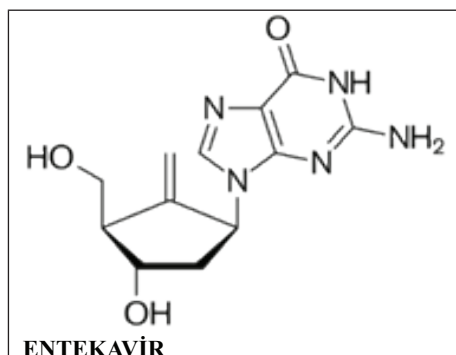
Long-term (> 10 years) studies in patients over 30 years of age show that HBeAg seropositivity is associated with an increased risk due to disease progression, and the risk of cirrhosis and HCC begins to increase at 10 HBV DNA levels. Therefore, elimination of HBV, or at least suppression of HBV, requires reducing hepatitis and thus stopping or preventing disease progression. It has been reported that treatment with interferon-alpha or a direct antiviral agent reduces the risk of cirrhosis and prevents the disease from getting worse (Liaw 2006).

It is known that the most important goal of antiviral therapy for chronic hepatitis B is to prevent the development of cirrhosis and hepatocellular carcinoma. Methods such as viral suppression, alanine aminotransferase normalization, hepatitis B antigen loss, hepatitis B surface antigen loss, and improvement in liver histology are used to determine treatment success. The treatment is determined by various factors according to the patient's age, hepatitis B e antigen (HBeAg) status, and hepatitis B virus (HBV) replication status, which is modulated by patient preference, and the stage of liver disease. A total of seven treatments were approved, including two interferon formulations and five orally administered nucleoside analogues. These therapies act to suppress HBV replication and also prevent disease progression (Jafri and Lok 2010).

Hepatitis B virus (HBV) is known as the etiologic agent of humanity's most serious liver disease. Although the availability of a vaccine has somewhat reduced the number of new HBV infections, the vaccine still does not benefit the approximately 350 million people chronically infected

with the virus. Most drugs approved by the FDA for the treatment of hepatitis B target reverse transcriptase (RT or the P gene product) and are known as nucleoside RT inhibitors (NRTIs), which suppress viral replication. However, long-term monotherapy with a single target leads to the emergence of virus resistance. (Michailidis et al. 2012).

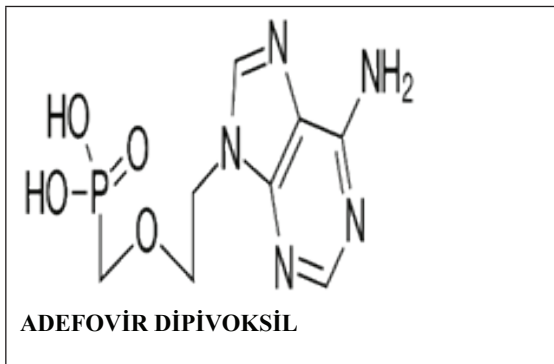
Today, chronic hepatitis B (CHB) treatment is done with interferon/pegylated interferon and various nucleoside/nucleotide analogues. The nucleoside analogues in the treatment are as follows; lamivudine, entecavir, and telbivudine. Tenofovir and adefovir are nucleotide analogues. However, with the use of these drugs, mutations occur in various regions of the viral polymerase gene. This may reduce the effectiveness of the drug by causing antiviral resistance. Lamivudine is used as an oral antiviral. Mutant strains emerge as a result of long-term use of this drug. Resistant mutants can reach up to 60% in a period of 4-5 years, and this results in a decrease in the virological response rate (Timur et al.2017). Antiviral drugs used:



Entecavir is a guanosine nucleoside analog with potent and selective activity against HBV polymerase. It is an antiviral drug approved by the FDA in 2005 for use in the treatment of CHB. In our country, its license was obtained in 2007 and its use started. It is phosphorylated to the active triphosphate (TP) form. Intracellular TP levels are directly related to extracellular entecavir concentrations and do not accumulate significantly beyond baseline plateau levels. Entecavir-TP, which competes with the natural substrate deoxyguanosine-TP, acts in three distinct phases of HBV replication. It inhibits the initiation of HBV reverse transcriptase activity, blocks reverse transcriptase activity, and inhibits DNA-dependent cccDNA synthesis and functional activity. The absorption of entecavir is reduced by 18-20% when taken with food. Therefore, it should be taken on an empty stomach 2 hours before or 2 hours after meals. Entecavir is eliminated mainly by the kidneys. Entecavir is excreted in the urine at a rate of 60-70%. It should be used in high doses in patients resistant to lamivudine, but

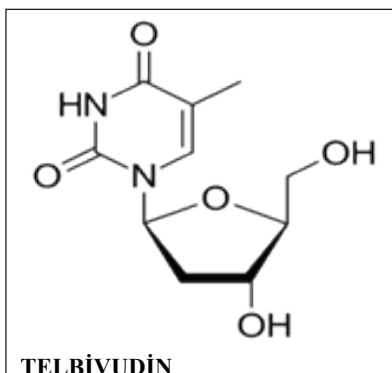
in patients resistant to adefovir, normal dose use is prescribed. May cause severe HBV flare-up when discontinued in an uncontrolled manner. For this reason, it should be followed up more closely for a few months after the end of the treatment (Çelik 2013).

Unlike other nucleoside or nucleotide analogues, ETV-TP inhibits HBV replication in 3 separate steps. Three-step inhibition of HBV resulted in high suppression rates of HBV-DNA, and in-vitro studies showed that entecavir is a more potent antiviral than lamivudine and adefovir. It has been shown that entecavir suppresses viral replication 30-2200 times more than lamivudine in cell cultures consisting of hepatoma cells (Tarhan 2013).



Adefovir dipivoxil is an oral prodrug form of the adefovir nucleotide analogue. It is used for the treatment of chronic hepatitis B in adults. Adefovir dipivoxil 10 mg/day significantly improved histological, biochemical, and virological outcomes in hepatitis B e antigen (HBeAg)-positive and -negative patients, and serologic outcomes in HBeAg-positive patients. Two studies had recipients with histological improvement in the liver. The proportion of adefovir dipivoxil recipients was approximately twice that of placebo recipients. In two studies in patients chronically infected with lamivudine-resistant hepatitis B virus (HBV), switching to adefovir dipivoxil or adding adefovir dipivoxil was significantly more effective in lowering serum HBV DNA levels than continued lamivudine monotherapy. In treatment-naïve patients, 1-year treatment with adefovir dipivoxil plus lamivudine demonstrated similar efficacy to lamivudine plus placebo; however, lamivudine-resistant HBV occurred in significantly more patients receiving lamivudine plus placebo. Adefovir dipivoxil has also been reported to show efficacy in noncomparative studies in patients with decompensated liver disease, HIV co-infected patients, and patients before or after liver transplantation. During the 96-week treatment period with adefovir dipivoxil, a resistance conferring mutation emerges in

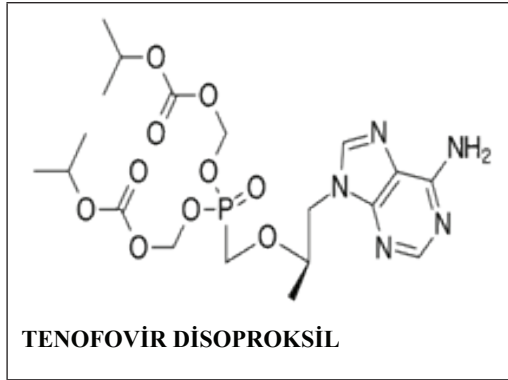
viral isolates from 1.6% of patients. In vitro, these viral isolates were susceptible to lamivudine, while lamivudine-resistant HBV isolates remained susceptible to adefovir dipivoxil. Adefovir dipivoxil 10 mg/day is generally well tolerated. Analysis of 48-week data from the two studies revealed no significant differences in adverse events or laboratory abnormalities between adefovir dipivoxil and placebo recipients (Dando and Plosker 2003).



Telbivudine is known as a synthetic nucleoside analog that inhibits the replication of hepatitis B virus (HBV). It is used to treat adults with chronic hepatitis B (CHB) with evidence of viral replication and persistently elevated serum ALT and/or AST levels and/or histological evidence of active disease.

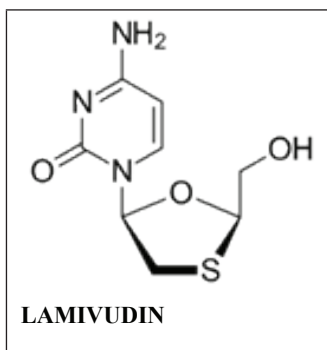
Telbivudine is a potent antiviral drug that provides effective and sustained viral suppression in patients with compensated CHB. In clinical studies, treatment outcomes have been shown to improve significantly with telbivudine 600 mg once daily compared to lamivudine 100 mg once daily or adefovir 10 mg once daily, and patients treated with telbivudine also had significantly less viral resistance than patients treated with lamivudine. HBeAg-positive patients achieved increased rates of hepatitis B e antigen (HBeAg) seroconversion during continuous telbivudine therapy for up to 4 years, and seroconversion became permanent in most patients during the 2-year, non-treatment follow-up. Telbivudine is associated with a moderate genetic barrier to resistance, and as patients with undetectable HBV DNA levels have significantly improved outcomes, their HBV DNA levels at week 24 (and every 6 months thereafter) if viremia is present to reduce the risk of resistance(Roadmap Concept). Telbivudine was generally well tolerated in clinical studies for periods up to 4 years and had a tolerance profile similar to lamivudine. A small proportion of patients treated with telbivudine experience creatinine kinase elevation, usually transient, and myopathy is rare. Modeled cost-effectiveness studies

are available in several Asian countries. In these studies, treatment with telbivudine Roadmap was cost-effective in HBeAg-positive patients. Thus, telbivudine offers a valuable treatment option in CHB (McKeage and Keam 2010).



Tenofovir disoproxil fumarate (tenofovir DF) is an oral prodrug form of the drug tenofovir, a nucleotide (nucleoside monophosphate) analog that is effective against retroviruses including HIV-1, HIV-2, and hepadnaviruses. Tenofovir is an antiviral drug that is intracellularly metabolized to the active anabolite tenofovir diphosphate, which is a competitive inhibitor of HIV-1 reverse transcriptase and terminates the growing DNA chain. Following absorption, tenofovir DF is rapidly converted to Tenofovir. Tenofovir produces antiviral effects on a variety of cell types, including resting cells. Tenofovir shows a longer serum (17 hours) and intracellular (60 hours) half-life than its nucleoside analogues. The pharmacokinetics of tenofovir are dose-proportional and similar in healthy volunteers and HIV-infected subjects.

The oral bioavailability of tenofovir is increased by a high-fat meal, but is similar at steady state when administered alone or with a typical meal. Tenofovir is not a substrate, inducer or inhibitor of human cytochrome P450 enzymes in vitro or in vivo. No clinically significant drug interactions have been observed with tenofovir DF, with the exception of didanosine and atazanavir drugs that require dose modifications. The recommended oral dose of tenofovir DF for adults is 300 mg/day. Tenofovir is eliminated by renal elimination, including tubular secretion, and dose range adjustments are required for tenofovir DF in patients with significant renal impairment. No dose adjustment is required for tenofovir DF in patients with liver disease (Kearney et al 2004).



Lamivudine is the first L-nucleoside analogue drug licensed and put into use in the treatment of chronic hepatitis B in 1998. The usage area of lamivudine is wide. Lamivudine is an effective antiviral drug in the treatment of HBeAg positive and negative chronic HBV infections, patients with compensated or decompensated cirrhosis, and chronic HBC infections in children. It is not clear exactly how long it will be used in the treatment of HBeAg-negative patients. Studies have reported that lamivudine suppresses HBV DNA in most patients after one year of use. However, very high levels of relapse appear to occur after treatment is discontinued. For this reason, it is recommended to give lamivudine for another six months after HBV DNA becomes negative. In addition, Lamivudine can be used safely in patients who do not respond to interferon alfa treatment (Tarhan 2013).

The only disadvantage of lamivudine compared to other antiviral agents used in the treatment of chronic hepatitis B is the drug resistance seen during the lamivudine treatment process.

The “viral, chemical and histological breakthrough” that occurs after the development of lamivudine resistance causes undesirable events during the treatment, causing the disease to return to the pre-clinical stage of treatment and even worsen. Therefore, early detection of resistance development is necessary and patients should be closely monitored while under treatment. Factors that may be associated with the development of lamivudine resistance have been reported in the literature as HBV genotype, HBeAg positivity, pre-treatment serum ALT and HBV-DNA level, pathological condition of the liver before treatment, age, gender and body-mass index of the patient to be treated. There are also studies that associate the combination of lamivudine with other antiviral drugs with a decrease in resistance development (Doğan et al. 2010).

Lamivudine is well absorbed after oral administration (mean bioavailability 86-88%). The drug is not extensively bound to plasma

proteins (36%), but distributes into the total body fluid (volume of distribution 1.3 L/kg) and crosses the placenta (the drug is found in the amniotic fluid). Here the concentrations seem to come into equilibrium between maternal proteins. (Jarvis and Faulds 1999).

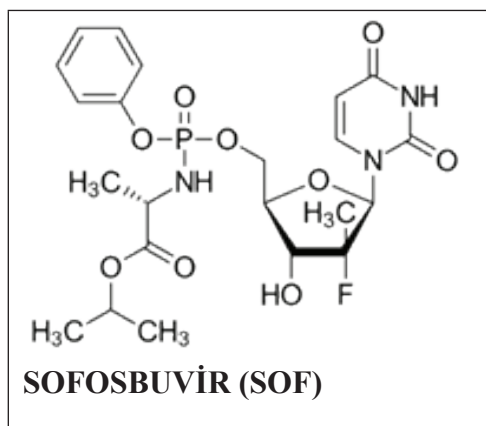
2.5 Antiviral Drugs Used in the Treatment of Chronic Hepatitis C

Hepatitis C virus (HCV) is known as a ribonucleic acid (RNA) virus from the flaviviridea family, which can cause both acute and chronic hepatitis, with a diameter of 40-50 nm and an outer lipid envelope. According to the World Health Organization data, it is estimated that approximately 1-5% of the world's population is infected with HCV. In addition, it is known that around 350 thousand people die annually due to HCV infection all over the world. According to the burden of disease study published by the World Health Organization in 2013 and covering the years 1999-2005, our country is in the group of Middle East/North African countries. The prevalence of countries in this group was classified as moderate, with 3.6%. It is estimated that the number of infected people in our country is between 700 thousand and 1 million. AntiHCV positivity was found in 6-18% of people with chronic hematological disease who are frequently transfused, and 14-61% in chronic hemodialysis patients. The virus is most commonly transmitted sexually and parenterally. After acute infection, chronic infection has been observed in approximately 80% of patients. Acute hepatitis is usually self-limited, rarely producing acute liver failure. However, it often progresses to chronic hepatitis. CHC may progress over the years to cause cirrhosis, HCC, and this process may result in liver transplantation in the future. The goal of treatment in CHC is to destroy HCV RNA. 3 to 6 months after the end of the treatment, HCV RNA is checked with the polymerase chain reaction (PCR) method. If it is not seen in the blood, treatment success can be mentioned (Aydın and Dülger 2018).

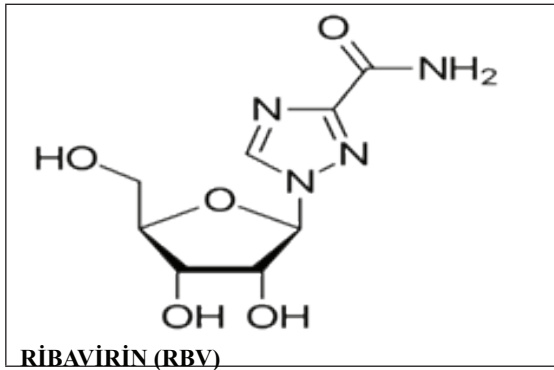
It has been calculated as a result of studies that 71 million people worldwide are infected with hepatitis C. In epidemiological studies conducted in our country, the prevalence of hepatitis C was found to be between 0.5 and 0.95%. During replication in the organism, hepatitis C virus uses viral replication proteins such as E2, NS3/4A and NS5A. In this way, the virus multiplies rapidly and escapes from the immune system of the organism it is in. A billion hepatitis C viruses reproduce and are destroyed every 24 hours in the body of a person infected with the hepatitis C virus. Hepatitis C virus replication is rapid and mutative. It can lead to the formation of variants resistant to antiviral agents in the virus population in the body. Unlike hepatitis B, hepatitis C infection becomes chronic at a rate of 80%. Chronic hepatitis C can be seen in a wide spectrum from asymptomatic to various diseases such as cirrhosis and hepatocellular cancer. Transmission occurs mainly

through blood. The rate of transmission through perinatal transmission from mother to baby and through sexual activity is extremely low. Precautions specified for hepatitis B should be taken to prevent transmission. However, an effective vaccine for hepatitis C has not been developed. Today, the main transmission route of hepatitis C is through needle sharing and/or use of non-sterile needles in people with intravenous drug use. In addition, prisons, military service, student dormitories, AMATEMs (Alcohol and Substance Treatment Center) and elderly care centers are also high-risk places for hepatitis C transmission. Necessary precautions should be taken for people living or sheltering here. Especially in 2013, with the introduction of orally administered direct-acting antiviral (DEA) agents to the market, a very important success has been achieved in the treatment of chronic hepatitis C. With DEAs, whose varieties are increasing day by day and more effective new molecules are found and released to the market, in all patient groups and all sub-genotypes (elderly, decompensated cirrhosis, end-stage chronic renal failure, kidney transplant, liver transplant, genotype 3 infected patients, HIV/HCV) co-infected patients, patients using IV drugs), a success rate of 100% is achieved with 8-12 weeks of treatment. In 1991, chronic hepatitis C treatment was first performed with standard interferon. Here, the success rate was 6%. Today, nearly one hundred percent success rate has been achieved. On top of these success rates achieved thanks to DEA agents, WHO set some targets in 2016. According to these targets, it is among the targets to diagnose 90% of patients with hepatitis C, to treat 80% of them and to reduce mortality by 65% by 2030. In our country, the Turkish Viral Hepatitis Prevention and Control Program (2018-2023) was accepted by the Ministry of Health in 2018 and started to be implemented. Within the framework of this Control Program, studies such as increasing awareness, training of family physicians, facilitating access to treatment, increasing cooperation with stakeholder associations are carried out (Anonymous 2021).

Drugs Used:



It is known as NS5B nucleoside polymerase inhibitor. It shows pangenotypic effect. It is an antiviral drug with a high genetic barrier. It is available for use as 400 mg tb 1x1/day, PO with or without food. The most common side effects are known as fatigue and headache (in use with RBV). 80% is excreted by the kidney and 15% is excreted through the feces. It is detoxified and excreted in the urine. Renal function should be monitored in regimens containing sofosbuvir. Concomitant use of Sofosbuvir with Amiodorone (an antiarrhythmic drug) is contraindicated. It is recommended to start SOF-based regimens 3 months after the discontinuation of amiodoron therapy. SOF is not metabolized by cytochrome P450. It is carried by intestinal P-gp. Rifampicin, carbamazepine, phenytoin, St. John's Wort are known as inducers of P-gp. It should not be used with them. No significant drug interactions have been identified between SOF and antiretroviral agents. Renal function should be closely monitored, as antiretroviral regimens containing pharmacokinetic enhancers such as ritonavir or cobicistat will increase tenofovir concentration (Örmen 2017)



Used as 200mg tb, PO. 75 kg 1200mg/G is taken in two doses. The most common side effects are rash, cough, and hemolytic anemia. It has a teratogenic effect. Women of childbearing age and their partners should use effective contraception during regimens containing Ribavirin and for 6 months after treatment. Dose restriction is required in severe renal failure (Örmen 2017).

According to 2017 consensus guidelines from the 2017 American Association for the Study of Liver Disease (AASLD) and the Canadian Association for the Study of the Liver (CASL), ribavirin is typically used as an adjunct therapy to various first- and second-line combinations. The purpose of adding ribavirin to the treatment course is to accelerate viral clearance in its early stages and reduce relapse rates. When used in the treatment of hepatitis C virus (HCV) infections, ribavirin as monotherapy is not always very effective in the treatment of chronic hepatitis C infection,

so it is always used as part of combination therapies. In addition, there is the possibility that including ribavirin in the regimen may increase the risk of anemia (Drugbank 2021).

Innovations IN Antiviral Therapy

Viral diseases have occurred in isolated populations in the past and have been easily controlled. Today, however, due to the cheap and easy access of airways, tourists are able to visit different regions frequently, thus increasing the possibility of new viral diseases spreading and reaching the world. For this reason, it is important for world health authorities to monitor possible potential risks and take appropriate measures when necessary. For example, if various measures related to the spread of severe Acute Respiratory Syndrome (SARS) in 2003 in the Far East were not taken in time, it could have led to a much larger epidemic worldwide. Still, the spread of SARS has shown how dangerous viral infections can actually be and is a warning of the time. Considering the potential effects of viruses on societies, it can be estimated how significant the risks that may arise due to viruses can reach. Therefore, this situation has revealed the importance of developing new antiviral drugs that can be effective. At the first Antiviral Agents Conference organized by the New York Academy of Sciences half a century ago, it was reported that viral replication is brought about by cellular enzymes, and that selective inhibition is also very difficult. Shortly thereafter, in 1967, Kates and McAuslan introduced the first viral enzyme, RNA polymerase, which binds to pox virus DNA, laying the first basis for selective antiviral drugs, and many more viral enzymes followed later on, and the discovery of many viral enzymes. (Dar et al. 2019). Let us now examine the developments in the treatment of chronic hepatitis B and C virus infections: In today's conditions, chronic hepatitis B virus (HBV) and hepatitis C virus (HCV) infections are accepted as an important public health problem worldwide. In recent years, very important developments have been achieved in the treatment of chronic HBV and HCV infections (Kasirga 2018).

The historical development of chronic hepatitis B treatment has been with the approval of tenofovir disoproxil fumarate (TDF) in 2008. There has been a stagnation in treatment development for nearly eight years after it was approved in 2008. No new drug development was observed. Our country and world guidelines have started to recommend entecavir, TDF and Peg-Interferon-a agents among the available treatments. In fact, there is suppression of HBV-DNA with these treatments. However, several studies have been published that show that there may be bone and kidney-related disorders due to TDF over time, and that the existing risks are much higher, especially in patients with osteoporosis, bone fractures, and elderly patients, as well as in patients with chronic kidney risk. For the treatment

process, tenofovir alafenamide (TAF) was developed in 2016 to eliminate these existing risks, and TAF was approved in 2016. In our country, for now, it is used in risky patients, provided that it is within the framework of certain criteria. Hepatitis B virus integrates into the DNA inside the cell, so it cannot be eradicated with existing drugs. However, recently, new drugs have been tried to be developed for the eradication of hepatitis B and the situation continues. Phase studies of these drugs are still ongoing (Anonymous 2021).

Chronic Hepatitis B Treatment

Agents approved for use in the treatment of chronic HBV infection in adults include interferon-alpha (IFN-alpha), pegylated interferon alpha (PEG-IFN), lamivudine, adefovir, entecavir, tenofovir, and telbivudine. Among these agents, IFN-alpha, lamivudine, adefovir, entecavir and tenofovir agents have been approved for use in children (Kasırga 2018).

Agents used in the treatment of chronic hepatitis B

Interferon alpha (IFN-alpha)

Interferons have antiviral, antiproliferative and immunomodulatory effects. IFN alfa2b (Intron-A®) is also the first approved treatment for chronic HBV infection. IFN alfa-2b is a protein produced by recombinant DNA technology. In patients with chronic HBV infection, 30-40% of the patients receive a response from the treatment with IFN therapy. It usually has a specific treatment period of 6 months and does not cause the development of resistant viral strains, which is one of the most important advantages of treatment with IFN. It is seen as a good treatment option for patients who are more likely to respond. But IFN therapy is expensive and has some side effects. For children with chronic HBV infection with positive HBeAg value, 6-month interferon alfa2b treatment is usually applied and the patients are observed for 6-12 months. In patients with chronic HBV infection with negative HBeAg value, a 1-year treatment is usually applied (Kasırga 2018).

Pegylated interferon (PEG-IFN)

It has an important place as a treatment option in adults with chronic HBV. It is taken by injection under the skin once a week. It has a 48-week treatment period. Its efficacy in children with chronic HBV infection has not yet been fully proven. But the necessary clinical studies on this subject are still continuing. Pegylated interferon may be a good treatment option for children in the immune active phase of HBV infection. However, it suppresses prepubertal growth. This situation should not be forgotten. Pegylated interferon is not licensed for use in Chronic HBV infection, although it can be used for people with active liver disease and post-pubertal

children under 18 years of age. Treatment with pegylated interferon should be avoided in patients with liver cirrhosis (Kasirga 2018).

The main side effects of IFNs are; These are influenza-like effects such as malaise, chills, fever, myalgia, and headache. These symptoms begin after the first injection and usually end within 12 hours. With subsequent injections, such acute side effects gradually decrease, but fatigue, headache, myalgia, irritability, depression and bone marrow suppression, etc. chronic side effects occur. Serious side effects such as autoimmune disease, bacterial infection, epilepsy, severe depression, acute cardiac and renal failure or pneumonia occur in approximately 2% of patients (Leblebicioğlu et al. 2001).

Chronic Hepatitis C Treatment

The treatment of chronic HCV infection is changing rapidly. In the first studies with IFN monotherapy, permanent virological responses were obtained at rates ranging from 33-45% in children with HCV. These sustained virological response rates are higher in children than in adults. In addition, the sustained virological response rates achieved with IFN monotherapy are lower than with the combination of IFN and ribavirin. Therefore, IFN alone has no use in the treatment of chronic HCV. PEG-IFN is used instead of IFN in combination therapy. Because nowadays it has a longer lasting effect and the number of doses is less frequent. Until recently, standard treatment in adults has been a combination of PEG-IFN and ribavirin for 48 weeks for HCV genotypes 1, 4, 5 and 6 and for 24 weeks for genotypes 2 and 3. A sustained virological response was achieved in 40-50% of genotype 1 patients and 80% of genotypes 2, 3, 5, and 6 patients treated with the combination of PEG-IFN and ribavirin. The development of combination drug regimens and direct-acting antiviral agents has played an important role in the treatment of hepatitis C in adults. It has been possible to use more effective, well tolerated, orally administered and IFN-free treatment modalities or regimens with direct-acting antiviral agents. It is expected that these new treatments applied in adults will also be implemented in children in the near future (Kasirga 2018).

Especially in 2013, with the introduction of direct-acting antiviral (DEA) agents that can be used orally, a revolutionary success has been achieved in the treatment of chronic hepatitis C. The variety of DEAs is increasing day by day, and more effective new molecules are found and introduced to the market. With these, success rates of up to 100% are achieved with a treatment period of 8-12 weeks in all patient groups and all sub-genotypes. In 1991, chronic hepatitis C treatment was performed for the first time with standard interferon and the success rate was 6%.

Today, this value is close to one hundred percent. With this, what the success rate means is much better understood. In 2016, WHO set some targets on these success rates with DEA agents. According to these targets, by 2030, 90% of patients diagnosed with hepatitis C should be diagnosed, 80% treated, and mortality reduced by 65%. In our country, the Turkish Viral Hepatitis Prevention and Control Program (2018-2023) was accepted by the Ministry of Health in 2018 and started to be implemented. Within the framework of this determined program, training of family physicians, increasing awareness, increasing cooperation with stakeholder associations, facilitating access to treatment, etc. studies are carried out (Anonymous 2021).

CONCLUSION AND RECOMMENDATIONS

In this study, we talked about the drugs used in the treatment of viral infections and the developments in antiviral therapy. The aim of antiviral therapy is to minimize viral disease symptoms and contagiousness and to shorten the treatment process. New scientific activities, new drugs and new treatment methods are emerging every day. This is promising for the treatment of viral diseases. Knowing the mechanism by which they act so that virus infections can be controlled makes drugs applicable and developable. For this reason, the mechanism of viruses in the host cell should be well known. Accordingly, necessary antiviral treatment should be recommended. Since the division of viruses occurs through cellular enzymes, it is very difficult to inhibit only the virus without damaging the host cell. It is very important that the developed drug affects the virus. Therefore, new antiviral drugs are being developed and new treatment methods are being researched. New antiviral strategies are needed for new antiviral drug discovery. Health institutions should increase vaccine and antiviral drug studies.

Acknowledgement

This study was prepared from Fatma Çetinkaya's Research Project Thesis.

REFERENCES

- Anonim 2021. Erişim 19 Şubat 2021. platformu, t. k., & içerikleri, S. Kronik hepatit B ve C: yeni ümitler.
- Anonim 2019a, 2019b. ‘Antiviral İlaçlar’. Erişim 21 Kasım2020https://acikders.ankara.edu.tr/pluginfile.php/103673/mod_resource/content/0/Antiviral%2C_antineoplastik-2019.pdf.
- Anonim 2020b. ‘Amantadin’. Erişim 12 Ocak 2021. <https://www.eczacidergisi.com.tr/influenza-a-ve-bde-ilac-tedavisi/>
- Anonim 2020a. Türkiye Cumhuriyeti Sağlık Bakanlığı.<https://covid19.saglik.gov.tr/Eklenti/37220/0/oseltamivir-75-mg-sert-kapsul--guncelleme-tarihi-14042020pdf.pdf>
- Aydın, M., & Dülger, A. C. (2018). Kronik Hepatit C Genotip 1 de Güncel Tedavi. *Van Tıp Dergisi*, 25(4), 547-551.
- Azap, A. ve Kurt, H. 2001.Varisella Zoster Virüs Enfeksiyonları. Ankara Üniversitesi Tıp Fakültesi Mecmuası. 54 (9): 364-365
- Birkmann, A. and Zimmermann, H. 2016. HSV Antivirals-Current And Future Treatment Options. *Current Opinion In Virology*, 9-13.
- Büke, Ç. 2012. Yeni Antiviraller. İzmir, s. 2-55
- Pubmed 2021a. ‘Cidofovir’. Erişim 12 Ocak 2021. <https://pubmed.ncbi.nlm.nih.gov/8841740/>
- Drugbank 2021. ‘Ribavirin’. Erişim 4 Mart 2021. <https://go.drugbank.com/drugs/DB00811Chem> 2021a. ‘Cidofovir’. Erişim 11 Ocak 2021. <https://chem.nlm.nih.gov/chemidplus/sid/0113852372>
- Çelik, Ç. (2013). *Guanozin analogu olan entekavir'in in vitro genotoksik etkisi*. Yüksek lisans Tezi. Adıyaman Üniversitesi Fen Bilimleri Enstitüsü, Adıyaman.
- Çiftçi, E., Karbuz, A. ve Kendirli, T. 2016. İnfluenza Ve Oseltamivir Kullanımı. *Türk Pediatri Arşivi*. Sayı:51; 63-71
- Dando, TM ve Plosker, GL (2003). Adefovir dipivoksil. *İlaçlar* , 63 (20), 2215-2234
- Dar, B. P. W., Öksüz, Z., & Algül, Ö. (2019). Antiviral ilaçlardaki gelişmeler ve değerlendirilmesi. *Mersin Üniversitesi Tıp Fakültesi Lokman Hekim Tıp Tarihi ve Folklorik Tıp Dergisi*, 9(2), 160-170.
- De Clercq E. (2004). Antiviral drugs in current clinical use. *Journal of clinical virology : the official publication of the Pan American Society for Clinical Virology*, 30(2), 115–133. <https://doi.org/10.1016/j.jcv.2004.02.009>
- Doğan,M. Müderrisoğlu,C. Fincancı,M. Ceylan,B. Eren Özdemir,G. Polat,H. (2010). Kronik Hepatit B’de Lamivudin Direnci Ve Lamivudin Diren-

- ci Gelişimi Üzerine Etkili Faktörler. Nobel Medicus, 6(1), 56-60. Filazi 2020. ‘ Antiviral İlaçlar’. Erişim 21 Kısım 2020.https://acikders.ankara.edu.tr/pluginfile.php/103101/mod_resource/content/0/ANT%C4%B0V%C4%B0RAL%20%C4%B0LA%C3%87LAR-14.hafta-Filazi.pdf
- Flora 1997a, 1997b. ‘Foskarnet’. Erişim 12 Ocak 2021. http://www.floradergisi.org/getFileContent.aspx?op=html&ref_id=58&file_name=1997-2-4-227-235.htm&_pk=7f398669-aa65-4df5-9bdf-47de32947f27
- Izzedine, H., Launay-Vacher, V., & Deray, G. (2005). Antiviral drug-induced nephrotoxicity. *American journal of kidney diseases : the official journal of the National Kidney Foundation*, 45(5), 804–817. <https://doi.org/10.1053/j.ajkd.2005.02.010>
- İlhan, A. 2009. Tamiflu’nun İnsan Periferal Lenfositlerinde İn Vitro Genotoksik Ve Sitotoksik Etkileri. Yüksek Lisans Tezi. Çukurova Üniversitesi Fen Bilimleri Enstitüsü, Adana.
- Jafri, S. M., & Lok, A. S. (2010). Antiviral therapy for chronic hepatitis B. *Clinics in liver disease*, 14(3), 425–438. <https://doi.org/10.1016/j.cld.2010.05.005>
- Jarvis, B., & Faulds, D. (1999). Lamivudine. *Drugs*, 58(1), 101-141.
- Kasırga, P. (2018). Kronik Hepatit Tedavisinde Yenilikler. Klinik Tıp Pediatri Dergisi, 10 (3), 31-37.
- Kearney, BP, Flaherty, JF ve Shah, J. (2004). Tenofovir disoproksil fumarat. *Klinik farmakokinetik*, 43 (9), 595-612.
- Korten, V. 2006. İnfluenza Tedavisi. Ankem Dergisi, 20(Ek 2):263-265.
- Kurt, H. Gündeş, S ve Geyik, M. F. 2013. Enfeksiyon Hastalıkları. Nobel Tıp Kitap Evleri, 121-124, İstanbul.
- Küçük, A. ve Yıldırım, Y. 2019. Antiviral İlaçlar. Etlik Veteriner Mikrobiyoloji Dergisi, 30 (1): 100-108.
- Leblebicioğlu, H., Sünbül, M., Aydın, K., Aygen, B., Akbulut, A., Hoşoğlu, S., ... & Ulusoy, S. (2001). Kronik Hepatit B ve Kronik Hepatit C Hastalarında İnterferon Tedavisine Yanıtın Değerlendirilmesi. *Flora*, 6(3), 159-163.
- Leowattana W. (2019). Antiviral Drugs and Acute Kidney Injury (AKI). *Infectious disorders drug targets*, 19(4), 375–382
- Liaw Y. F. (2006). Hepatitis B virus replication and liver disease progression: the impact of antiviral therapy. *Antiviral therapy*, 11(6), 669–679.
- McKeage, K. ve Keam, SJ (2010). Telbivudin. *İlaçlar*, 70 (14), 1857-1883.
- Michailidis, E., Kirby, K. A., Hachiya, A., Yoo, W., Hong, S. P., Kim, S. O., Folk, W. R., & Sarafianos, S. G. (2012). Antiviral therapies: focus on hepatitis B reverse transcriptase. *The international journal of biochemistry & cell biology*, 44(7), 1060–1071. <https://doi.org/10.1016/j.biocel.2012.04.006>

- Morfin, F. ve Thouvenot, D. (2003). Antiviral ilaçlara herpes simpleks virüsü direnci. *Klinik Viroloji Dergisi* , 26 (1), 29-37.
- Ncbi 2021a. ‘Cidofovir’. Erişim 11 Ocak 2021. <https://www.ncbi.nlm.nih.gov/books/NBK548417/>
- Örmen, B. (2017). Kronik Hepatit C Tedavisi. 19. Viral Hepatit Sempozyumu’nda Sunulmuştur. Malatya, Türkiye
- Pubchem 2020a. ‘Rimantadin Farmakolojisi’. Erişim 12 Ocak 2021. <https://pubchem.ncbi.nlm.nih.gov/compound/5071#section=Pharmacology->
- Pubchem 2020b. ‘Rimantadin Terapötik Kullanımı’. Erişim 12 Ocak 2021. <https://pubchem.ncbi.nlm.nih.gov/compound/5071#section=Therapeutic-Uses>
- Pubchem 2020c. ‘Rimantadin Saklama Koşulu’. Erişim 12 Ocak <https://pubchem.ncbi.nlm.nih.gov/compound/5071#section=Disposal-Methods> 2021.
- Pubchem 2020d. ‘Rimantadin Hepatotoksitesitesi’. Erişim 12 Ocak <https://pubchem.ncbi.nlm.nih.gov/compound/5071#section=Toxicity> 2021.
- Pubchem 2020e. ‘Rimantadin Toksikite Özeti’. Erişim 12 Ocak 2021. <https://pubchem.ncbi.nlm.nih.gov/compound/5071#section=Toxicity-Summary>
- Pubchem 2020f. ‘Rimantadin İlaç Uyarıları’. Erişim 12 Ocak <https://pubchem.ncbi.nlm.nih.gov/compound/5071#section=Toxicity-Summary> 2021.
- Drugbank 2020. ‘Rimantadin’. Erişim 12 Ocak 2021.
- Pubchem 2021a. ‘Trifluridin İlaç Endikasyonu’. Erişim 11 Ocak 2021. <https://pubchem.ncbi.nlm.nih.gov/compound/Trifluridine#section=Drug-and-Medication-Information>
- Süzerğöz, F. 2016. Virüslerin Hücreye Giriş Ve Hücre İçi İşleniş Mekanizmaları. *Türkiye Klinikleri*, 9 (3): 27-32
- Tarhan, A. 2013. Kronik Hepatit B Hastalarında Antiviral Tedavi Stratejilerinin Maliyet Etkililik Analizi. Yüksek Lisans Tezi. Türkiye Cumhuriyeti Ankara Üniversitesi Sağlık Bilimleri Enstitüsü, Ankara.
- Timur, D., Ökahmetoğlu, S., Özüberk, O., Sezgin, G. C., Parkan, Ö. M., & Kaan, Ö. 2017. Kronik Hepatit B İçin Antiviral Tedavi Alan Hastalarda Antiviral İlaç Direncinin Araştırılması. *Türk Mikrobiyol Cem Dergisi* 47(1):1-5
- Pubchem 2021c. ‘Trifluridin Deri, Göz Ve Solunum Yolu Tahrişleri’. Erişim 11 Ocak 2021. <https://pubchem.ncbi.nlm.nih.gov/compound/Trifluridine#section=Hazard-Classes-and-Categories>
- Pubchem 2021d. ‘Trifluridin Hepatotoksitesitesi’. Erişim 11 Ocak 2021. <https://pubchem.ncbi.nlm.nih.gov/compound/Trifluridine#section=Hepatotoxicity>
- Pubchem 2021e. ‘Trifluridin Toksikite Özeti’. Erişim 11 Ocak 2021. <https://pubchem.ncbi.nlm.nih.gov/compound/Trifluridine#section=Toxicity-Summary7>

- Pubchem 2021b. 'Trifluridin Genel Üretim Bilgisi'. Erişim 11 Ocak 2021.<https://pubchem.ncbi.nlm.nih.gov/compound/Trifluridine#section=General-Manufacturing-Information>
- Tosun, S. (2017). İNFLUENZA (GRİP) NEDİR, NE DEĞİLDİR?. İzmir Tabip Odası.
- Trépo, C., Chan, H. L., & Lok, A. (2014). Hepatitis B virus infection. *Lancet (London, England)*, 384(9959), 2053–2063. [https://doi.org/10.1016/S0140-6736\(14\)60220-8](https://doi.org/10.1016/S0140-6736(14)60220-8)
- Usta, D. Y., & Teksin, Z. Ş. (2020). COVID-19 Tedavisinde Kullanılan İlaçların Biyofarmasötik, Farmakokinetik ve Patent Değerlendirmeleri: Ülkemizde Eşdeğer İlaçların Geliştirilmesindeki Güncel Durum. *GMJ*, 31, 498-509.

Chapter 6

SYNTHESIS OF BORON NITRIDE BY SOLID STATE REACTIONS: DESIGNATION OF BARIUM SALTS EFFECT

Muhammed OZ¹

Asaf Tolga ULGEN²

1 Assoc.Prof., Abant Izzet Baysal University, Department of Chemical and Chemical Processing Technologies, Bolu-Turkey, 14030 Orcid ID 0000-0003-0049-0161

2 Assoc.Prof, Sirtak University, Department of Electric-Electronic Engineering, Sirtak-Turkey, 73000 Orcid ID 0000-0002-7112-5607

1. Introduction

Solid-state reaction (SSR) is one of the solvent-free methods carried out in a dry media reaction. Thus, the method is an economic, highly yielding, and friendly for the environment (Ropp, 2003). Most of solids react at the interface of another solid which means the reaction takes place between two different adjacent atoms (Rijnders, 1996). When two particles are involved in reaction very close to each other to form a new compound, the SSR performs inevitably due to the transportation or interchange of cations and/or anions. Therefore, the degree of dispersion and mixing of one reacting solid with another is known to drive force for the overall mechanism of solid-state reaction (Rijnders, 1996). In this method, the furnace techniques are generally used at high temperatures to encourage reactions without solvents. Furthermore, the gaseous materials are preferred for the SSR medium as a reagent material.

Some of boron chemicals are synthesized by the SSR method due to the ease of reaction conditions. Boron is a valuable chemical element since it has a low abundance in the Earth's crust and constitutes about 0.001 percent by weight of Earth's crust. Accordingly, its worthiness makes Turkey very lucky owing to the existence of seventy percent of world's boron reserves. It is obvious that the boron possesses a special importance for Turkey since the boron-rich country is also in a very advantageous position in the production of boron chemicals. The production of boron chemicals will be able to increase the Value-Added Tax (VAT) to the corresponding country. For this reason, many products made from boron have participated our life, and one can say that the boron is preferred in many industrial areas as a consequence of its distinct behaviour.

Boron nitride, which has great industrial importance, is one of the synthetic chemicals of boron and used in many application areas (Mishima & Era, 2000). Boron nitride is produced synthetically and has naturally been observed in Tibet very few as a form of cubic structure on the earth's surface (*Dobrzhinetskaya et al., 2014*). The fact that the boron nitride product is produced synthetically shows that there may be more studies in this field and it is obvious that this field will be the subject of many scientific studies. That is, the boron nitride derivative compounds and functionally developed boron nitride products can only be obtained synthetically. Therefore, the academic studies on boron nitride will always be up to date. Moreover, the use of boron nitride is constantly updated, and it is among the advanced technology products.

The boron nitride consisting of two atoms adjacent to carbon in the periodic table is the isoelectronic with carbon chemical structure. In other words, there is the same number of electrons obtained in the boron and

nitrogen coupling as the result of the carbon-carbon interaction. The boron nitride compounds have the same crystal structures as the polymorphs of carbon, and their properties vary according to the crystal structure that they have. Therefore, the boron nitride has a structure similar to the carbon in general and possesses the allotropes such as carbon (Haubner, Wilhelm, Weissenbacher, & Lux, 2002; Paine & Narula, 1990). As in the carbon, the boron and nitrogen atoms can have crystal structures such as hexagonal, cubic, and turbostratic morphologies depending on the hybridization types. Two most widely known forms are cubic and hexagonal boron nitride (cBN and hBN, respectively). The boron nitride exhibits sp^2 hybridization at the hexagonal form while showing the cubic when the boron and nitrogen atoms are sp^3 hybridized form (Haubner, Wilhelm, Weissenbacher, & Lux, 2002). Cubic boron nitride (cBN) is the hardest material after diamond in nature and is also called “artificial diamond” and replaces diamond, which is further used as a cutting and abrasive material today. Unlike the diamond, it is resistant to high temperatures and its structure does not deteriorate up to the temperature value of 1370 °C. hBN is called ‘white graphite’ because its crystal structure is layered and white in colour different from graphite. There are strong covalent bonds between the boron and nitrogen atoms in the lateral coordination, and weak Van der Waals bonds between plates (Öz et al., 2016). Moreover, the crystal structure of hBN has superior chemical and physical properties such as low density, high-temperature stability, high thermal conductivity, low dielectric constant, and chemical inertness (Haubner, Wilhelm, Weissenbacher, & Lux, 2002; Paine & Narula, 1990); hence the hBN presents a great extent of attraction in the researchers over the worldwide. It is used as a refractory material due to its out of ordinary properties such as the superior resistant characteristics at the high temperatures, large oxidation resistance and non-wetting [Lin & Connell, 2012; Zhi, Bando, Tang, & Golberg, 2010]. Another usage area is under the high temperature lubrication applications due to its high temperature stability as well as lubricating properties [Haubner, Wilhelm, Weissenbacher, & Lux, 2002]. One can encounter the material in the industrial application fields; namely, the gas sensors (Gautam et al., 2016), bone generation (Gautam et al., 2018), glass composite (Bansal, Hurst, & Choi, 2006), and hydrogen storage material (Okan et al., 2012), and etc.

The high-temperature processes are necessary for the inorganic compounds at solid-state synthesis due to their low diffusion coefficient. The crystal structure deeply affects the chemical and physical properties such as the thermal stability, oxidation behaviour, specific surface area, particle shape, and size by the nucleation and growth reactions of hBN, (Matović et al., 2016). By using the action of molten boric acid on potassium cyanide, the first synthesis of BN was achieved by W. H. Balmain in 1842;

however, the product was unstable, and BN did not become a commercial material until 1950s because of the difficulties in synthesis and high cost of methods (Balmain, 1842).

The solid state synthesis of hBN mainly includes the reaction both boron and nitrogen containing compounds that is carried out at high temperatures such as above 1600°C which is commonly preferred at the industrial processes (Thomas, Weston & O'Connor, 1962; O'Connor, 1962; Bernard, Salameh, & Miele, 2016). Nowadays, many studies carry out at the high temperature trials to obtain boron nitride by the easy way, and the additives generally called as the fluxes are widely used in these studies (Ruprecht et al., 1985; Vaynman & Fine, 1999; Wang et al., 2004). The main purpose of additives is to ensure that the boron nitride can be synthesized within the desired properties at relatively lower temperatures by means of the solid-state methods. However, not all additives show the same interest, thus only positive contributions are widely preferred. In addition, the prices of additives have negative effects on the formation of boron nitride, and by choosing cheap additives the process of boron nitride is investigated in many studies. In the current study, the barium salts (with their positive flux properties) which are comparatively cheap and abundant chemical are selected to synthesize hBN relatively lower temperature as compared to the temperature of industrial scale (Kresse et al., 2007). Unlike elemental form, the barium salts turn into a less harmful chemicals in case of higher annealing temperature.

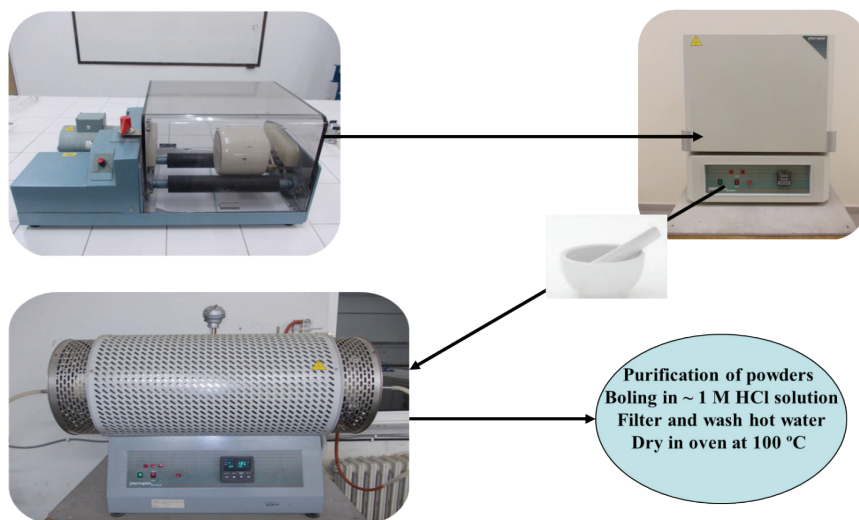
The barium salts preferred in this study are barium carbonate (BaCO_3), barium oxide (BaO) and barium chloride (BaCl_2). These are inorganic compounds that the materials of BaCO_3 and BaO poorly exhibit the solubility in contrast to the compound of BaCl_2 . In a commercial sense, the BaCO_3 is one of the most important barium compounds since it is widely used in the ceramics industry as an ingredient in glazes. In contrast to the material of BaCl_2 , the compounds of BaCO_3 and BaO act as a flux, a matting and crystallizing agent. Another important feature that makes the barium oxide stand out is to be used as a catalyst for the reaction of ethylene oxide and alcohols. These specific properties of barium salts make them a strong candidate for both as a catalyst and a surface propagating agent at the synthesis of hBN by solid state reaction.

2. Material and Methods

The chemicals of boron oxide (Fluka, 97%), urea (Fluka, 99%), ammonia gas (Linde Co. 99.9%) ethanol (Merck, 96%), hydrochloric acid (Merck, 37%), BaCO_3 (alfa Aesar, 99,9%) BaO (Sigma Aldrich, 97%) and BaCl_2 (Sigma Aldrich, 99,9%) purchased commercially were directly used for the synthesis of crystalline and hexagonal boron nitride. In this study, the

mixture of urea and boron oxide was prepared by four-hour ball mill process with the adjustment of composition within 1.0 and 2.0 g, respectively. Then 20 % (w/w) barium salts were doped into the constant mass of plain mixture similar to the previous studies of Öz. et.al, (Öz, 2020; Öz, 2021; Öz et al., 2016). After the dry homogenization, the initial heat treatment was applied to each sample and plain mixture obtained by pulverization of only urea and boron oxide at a lower temperature which yielded to the precursor samples. The second heat treatment of every sample was performed at a higher temperature that is commonly known as O'Connor method (Thomas, Weston & O'Connor, 1962; O'Connor, 1962). Besides, it was the one of the two-step solid state processes and was used for the synthesize hBN due to its practicality and simplicity.

2. MATERIALS AND METHODS



The heating process is bluntly explained that the mixture of starting pulverized compounds were initially heated for the annealing process of 2 hours at 200 °C in the atmospheric air and the main heating processes of samples were carried out at the temperature of 1450 °C with a range of 5 °C/min in reacting ammonia gas atmosphere at a tubular furnace. The thermally constant temperature was adjusted for 3 hours at 1450 °C during the experimental processes while the cool down period (laid naturally out) decreased to the room temperature. Besides, the cleaning process was applied by washing 10 % HCl solution, percolating with white band filter paper and drying in the oven at 100 °C. Following instrumental devices were simultaneously used for the fundamental characteristic features of samples produced: that were a Shimadzu 8400S spectrometer in the

range of 400-4000 cm^{-1} , Rigaku DMAX 2000/PC and Rigaku Multiflex diffractometer, and by JEOL JST-6400 scanning electron microscope (SEM) for FTIR, XRD, and surface analysis respectively. FTIR spectra of barium salts doped hBN samples were collected by a Shimadzu 8400S spectrometer in the range of 400-4000 cm^{-1} with the 2 % sample containing KBr discs. After the first findings of hBN, the further characterization of powder hBN samples was performed with Rigaku DMAX 2000/PC and Rigaku Multiflex diffractometer between the 2theta degrees of 10° and 90°. The surface visualization of powders was determined by JEOL JST-6400 scanning electron microscope (SEM) on which the samples were formerly located carbon grid and coated by gold.

3. Results and Discussion

Hexagonal boron nitride (hBN) is commonly synthesized by the solid-state method, and the following results successively explore the effect of barium salts on the formation of hBN at the melting period. Powder samples formed after annealing and bleaching process were analysed by the different types of instrumental methods such as FTIR, XRD and SEM for the determination of the product quality of hBN. The heating process included two main steps that the first one is main heating process at the 2 hours at 200 °C temperature treatment in the atmospheric air by furnace to remove moisture and produce the starting monomers (Öz et al., 2016). Second one was the high temperature annealing at 1450 °C for 3 hours to perform the reaction of boron with the nitrogen in melt from the utilized starting chemicals such as boron oxide, urea, ammonia, and fluxes. In addition, the synthesized powder samples were bleached for removal of any impurities. Thus, the purely obtained hBN samples were instrumentally analysed to demonstrate whether the samples were formed only hBN or not.

FTIR spectroscopy is commonly preferred for searching of vibrational mutual effect at the infrared active compounds as it is found between boron and nitrogen. Accordingly, it is drawn to examine the types of chemical bonds in the hBN products obtained. One can see the FTIR spectra of hBN sample synthesized by dopant barium salts in Fig. 1. It is apparent from the figure that the assignments performed at the vibrations of 1380 cm^{-1} and 780 cm^{-1} (in-plane and interplanetary) B-N tension are observed in the FTIR spectrum of hBN prepared by adding barium salts (Figure 1). FTIR peaks belonging to the O-H and N-H end groups of BN material are observed in the wavenumber range of 3400 cm^{-1} (Hubáček & Ueki, 1996; Yuan et al., 2008). As seen in Fig. 1, it has been reported in various studies that the peaks may occur when a mixture of boron oxide and urea is used as starting material due to the end groups stretching vibrations (Chen et al., 2005; Hu et al., 1999; Hubáček, Sato, & Ishii, 1994). The FTIR spectroscopy

obtained in this study appears to be in agreement with literature (Sachdev et al., 1997). To sum up, the experimental results interpreted from the FTIR spectra indicate that the usage of barium salts affects clearly the formation of hBN positively.

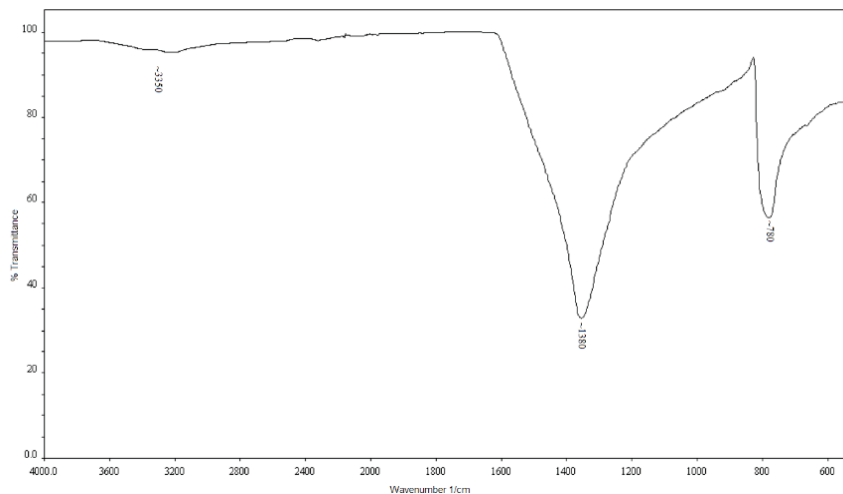


Figure 1 A sample of FTIR spectra of the hBN sample

After formation of hBN synthesized with barium salt additives were determined by FTIR spectroscopy, the complementary results were obtained with XRD crystallography which is another more accurate method indicating hBN formation in products apparently. The XRD analysis is executed with an X-ray source of $\text{CuK}\alpha$ radiation, and the identification of unknown crystalline compounds is accomplished by Bragg Brentano method. Meanwhile, fixed parameters depending on the material under the consideration are adjusted by the scan step size, collection time, range, X-ray tube voltage and current. Phase identification for a large variety of crystalline phases especially in the hexagonal lattice is revealed by comparison with the standard database (ICDD database) for the XRD pattern. By the XRD crystallography, the electron density has been utilized to determine the chemical bonds, disharmony in the crystal structure, lateral distances, lattice parameters and assessment of the average locations of atoms in the crystal structure rather than the amorphous structure. In this context, the XRD analysis was performed to find the crystal structure properties such as lattice parameters, interlayer distance and crystalline average size of hBN samples that are prepared by using different barium salts (Hamilton, et al., 1995; Thomas, Weston, & O'Connor, 1962).

The formation of hBN is confirmed as the observation of 002, 100, 101, 102, 004, 110 and 112 planes which are found in the original XRD pattern (Balint & Petrescu, 2009). International Centre for Diffraction Data (ICDD) 34-421 card includes the Miller indices of pure hBN. This card is aligned with XRD patterns of boron nitrides synthesized by barium salt dopants and undoped sample (Fig. 2.). It is found that all the samples which were prepared with the dopants had the similar patterns as the corresponding ICDD card in the present of hBN structure signals. Unlike doped samples, the plain mixture which was obtained by homogenization of the only boron oxide and urea had 002, 10X, 004, 110 and 112 planes indicating the turbostratic nature of BN that is out of trim. In the plain mixture, 100 and 101 planes form together and 102 plane disappears immediately while the barium salts doped samples have former planes separately, and latter plane significantly becomes clear as the designation of regular structure of hBN. In addition, 002 peak which was mainly used for determination of grain size of BN samples sharpened at the additive used samples while it was found a broad peak in the diffractogram of plain mixture (Choi et al., 1993).

Another property calculated from XRD patterns is lattice parameters for the barium salts doped and undoped hBN samples. The dimension of unit cells (a , b and c) for hexagonal systems has equal quantity as “ a ” and “ b ” cell size; however, the extent of the “ c ” cell size is greater than the two sizes. Besides the numerical values of these cell parameters and interplanar distance of the synthesized hBN samples are given in Table 1. The commercial hBN and ICDD have lattice parameters as $b = a = 2.504 \text{ \AA}$, $c = 6.656 \text{ \AA}$, $d = 3.328 \text{ \AA}$); however, the doped samples were found to exhibit approximate results to the constant values (Table 1). Moreover, this experimental finding shows that the values found were in good agreement with the literature values (Hubáček & Ueki, 1996). If the distance between the layers is “ d ”, it changes in direct proportion to the “ c ” cell parameter, and when BaO was added, it indicates the nearest value to the literature value among those additives. Although the lattice parameters have decent values when the barium salts were used, it is clearly understood that the best one is obtained in terms of lattice parameters when BaO was preferred as a dopant according to the XRD results.

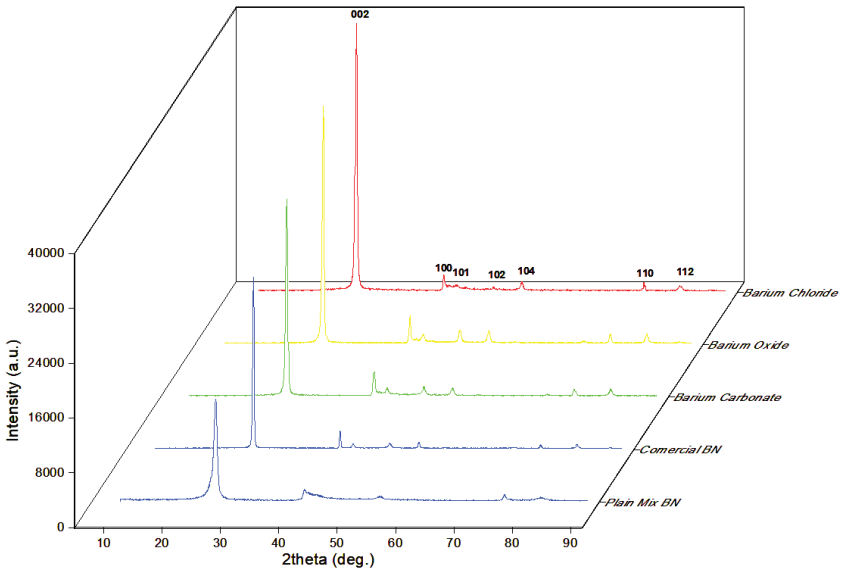


Figure 2 XRD diffractograms of the undoped, Barium salts doped and commercial hBN

Table 1 Lattice Parameters and Crystallinity Properties of hBN Synthesized by the Presence of Barium Salts

Dopant compound	Lattice Parameters (nm)				Average Grain Size (nm)	Number of plates
	a	b	c	d		
Plain mix	0.2504	0.2504	0.6693	0.3346	3.61	11
BaCO ₃	0.2504	0.2504	0.6682	0.3341	31.18	93
BaO	0.2498	0.2498	0.6612	0.3306	39.31	119
BaCl ₂	0.2504	0.2504	0.6672	0.3336	48.88	147

XRD measurements are also used to calculate the crystallite or average grain size parameters by Debye-Scherrer equation (Eq. 1) which is an approximation and works best for nearly spherical particles. However, it has been used many studies to get the average grain size (Scherrer, 1918)

$$D = \frac{K \lambda}{\beta \cos \theta} \tag{Eq. (1)}$$

where K is the shape factor (which is 0.941), D is the average grain size, λ is the wavelength, B is the FWHM of Bragg peak and θ is the Bragg angle [20]. The average grain size of hBN samples was obtained to be comparably higher than the plain mixture (3,61 nm) that was synthesized by only urea and boric oxide; nevertheless, the variety of dopants also alters the grain size. For instance, the barium carbonate usage as an additive increased tenfold the grain size but the best contribution to grain size (calculated to be 48.88 nm) among the barium salts is derived from the barium chloride dopant. One could measure an approximate number of plates from the division of average grain size by interlayer distance that might be the agglomeration of the crystallite size. The number of plates is found for the hBN samples as 11, 93, 119 and 147 for plain mix, BaCO₃, BaO and BaCl₂, respectively.

The scanning electron microscopy (SEM) is a handy instrumental method that is available for the examination and analysis of microstructural characteristics of solid conduction materials. A major reason for the SEM's usefulness is the high resolution which can be obtained when the bulk objects are examined. In the current study, the SEM experiments were applied to clarify the surface morphology of barium salts added BN samples after the purification process (Shimomura, Funahashi & Koitabashi, 1995). SEM images include the homogenous bulk hBN as provided in Fig. 3a-c, and the measured areas on the sample are taken from 65, 45, and 25 μm^2 at figures given in a to c respectively (Goldstein et al., 2018). Microstructural images consist of 0.1-3 μm particles in one length which was result of agglomeration of low length average grain sizes and all samples have the planar nature as it is expected in the form of hexagonal morphology. The average grain sizes of sub-particles calculated from the XRD diffractograms were found as approximately 100 nm where the agglomeration of 10 to 30 small particles causes greater particles in the SEM images.

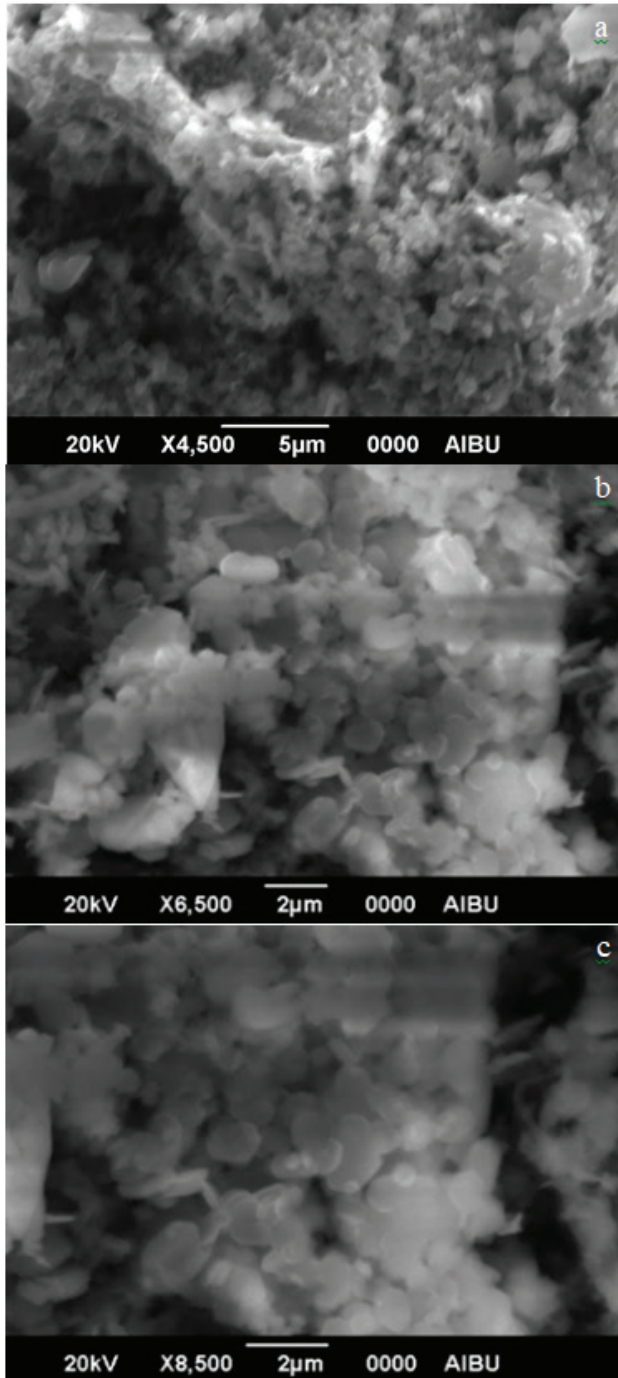


Figure 3 SEM images of Barium salts doped hBN samples a) $BaCO_3$, b) BaO and c) $BaCl_2$

4. Conclusion

A variety of methodologies was discussed to prepare boron nitride powders in literature with different sizes and purities by the ease of many additives. In this study, the formation of hexagonal polymorph of BN materials was investigated in the view of different kinds of barium salts such as barium carbonate, barium oxide and barium chloride. Besides, the effect of barium salts as a crystallization promoter was demonstrated by heating of mixtures at 1450°C and influence of synthesis species on the phase composition and morphology of the final products in the mixture was also investigated by the standard characterization methods including the Shimadzu 8400S spectrometer in the range of 400-4000 cm^{-1} , Rigaku DMAX 2000/PC and Rigaku Multiflex diffractometer, and by JEOL JST-6400 scanning electron microscope (SEM) for FTIR, XRD, and surface analysis respectively. Therefore, highly crystalline hexagonal boron nitride was successfully synthesized by B_2O_3 and urea powders when the compounds of BaCO_3 , BaO and BaCl_2 salts were used as a dopant in the starting materials at 1450°C in ammonia atmosphere by the O'Connor model. The samples were instrumentally characterized by infrared spectroscopy, powder X-ray diffraction analysis and scanning electron microscopy.

According to the results of instrumental analysis, the BaCO_3 , BaO and BaCl_2 dopants had a positive effect on the formation hBN in mixture while the BaCl_2 exhibited the most positive contribution to the crystallinity and grain size of hBN material due to not only the barium electronic interactions and expanded coordination number but also the strengths of anion reducing property of chlorine ion in the melted contexture. The BaO increased electronic interaction between the particles in the melt resulting in the better lattice parameters while the compound of BaCO_3 enhanced the reaction surface by the evolution of CO_2 gas at the decomposition stage at high temperature. Therefore, the BaCO_3 yields both electronic interaction and solid-liquid interface effect. Besides, the BaCl_2 reduced the potential of chloride anion. In this context, this study declares that the barium salts can be used as the dopant at the annealing of plain mixtures for the formation of hBN structure at relatively lower temperatures than that of O'Connor method.

References

- Balint M.G., & Petrescu M.I. An attempt to identify the presence of polytype stacking faults in hBN powders by means of X-ray diffraction. *Diamond and Related Materials*. 2009; 18(9): 1157–1162.
- Balmain, W. H. 1842. Bemerkungen über die Bildung von Verbindungen des Bors und Siliciums mit Stickstoff und gewissen Metallen. *Journal für Praktische Chemie* 27: 422–430.
- Bansal Narottam P., Hurst Janet B., & Choi Sung R. Boron Nitride Nanotubes-Reinforced Glass Composites. *Journal of the American Ceramic Society*. 2006; 89 (1): 388– 390.
- Bernard S., Salameh C., & Miele P. Boron nitride ceramics from molecular precursors: synthesis, properties and applications. *Dalton Transactions*. 2016; 45(3): 861– 873.
- Choi, J. Y., Kang, S. J. L., Fukunaga, O., Park, J. K., & Eun, K. Y. (1993). Effect of B₂O₃ and hBN crystallinity on cBN synthesis. *Journal of the American Ceramic Society*, 76(10), 2525– 2528.
- Dobrzhinetskaya, L.F.; et al. (2014). “Qingsongite, natural cubic boron nitride: The first boron mineral from the Earth’s mantle”(PDF). *American Mineralogist*. 99 (4): 764–772.
- Goldstein J.I., Newbury D.E., Michael J.R., Ritchie N.W.M., Scott J.H.J., Joy D.C. (2018) SEM Image Interpretation. In: *Scanning Electron Microscopy and X-Ray Microanalysis*. Springer, New York, NY.
- Hamilton, E. J., Dolan, S. E., Mann, C. M., Colijn, H. O., & Shore, S. G. (1995). Preparation of amorphous boron nitride from the reaction of haloborazines with alkali metals and formation of a novel tubular morphology by thermal annealing. *Chemistry of Materials*, 7(1), 111– 117.
- Haubner R., Wilhelm M., Weissenbacher R. and Lux B. 2002. Boron Nitrides - Properties, Synthesis and Applications. *High Performance Non-Oxide Ceramics II Structure & Bonding*, 102: 1–45
- Hu, J. Q., Lu, Q. Y., Tang, K. B., Yu, S. H., Qian, Y. T., Zhou, G. E., ... Wu, J. X. (1999). Synthesis and characterization of nanocrystalline boron nitride. *Journal of Solid State Chemistry*, 148(2), 325– 328.
- Hubáček, M., & Ueki, M. (1996). Chemical reactions in hexagonal boron nitride system. *Journal of Solid State Chemistry*, 123(2), 215– 222.
- Kresse, Robert; Baudis, Ulrich; Jäger, Paul; Riechers, H. Hermann; Wagner, Heinz; Winkler, Jochen; Wolf, Hans Uwe (2007). “Barium and Barium Compounds”. *Ullmann’s Encyclopedia of Industrial Chemistry*. Weinheim: Wiley-VCH.

- Lin, Y., & Connell, J. W. (2012). Advances in 2D boron nitride nanostructures: Nanosheets, nanoribbons, nanomeshes, and hybrids with graphene. *Nanoscale*, 4(22), 6908– 6939.
- Matović, B., Luković, J., Nikolić, M., Babić, B., Stanković, N., Jokić, B., & Jelenković, B. (2016). Synthesis and characterization of nanocrystalline hexagonal boron nitride powders: XRD and luminescence properties. *Ceramics International*, 42(15), 16655– 16658.
- Mishima, O. and Era, K. 2000. Science and Technology of Boron Nitride. In: Kumashiro, Y. (ed.): *Electric Refractory Materials*. 498. Merceel Dekker, Inc. New York.
- O'Connor, T. E. (1962). Synthesis of boron nitride. *Journal of the American Chemical Society*, 84(9), 1753– 1754.
- Okan, B., Kocabaş, Z. O., Nalbant Ergün, A., Baysal, M., Letofsky-Papst, I., & Yürüm, Y. (2012). Effect of reaction temperature and catalyst type on the formation of boron nitride nanotubes by chemical vapor deposition and measurement of their hydrogen storage capacity. *Industrial & Engineering Chemistry Research*, 51(35), 11341– 11347.
- Öz, M. (2020). Temperature dependency on crystallinity and durability of mineral dolomite doped nanocrystalline hexagonal boron nitride. *Journal of Inorganic and Organometallic Polymers and Materials*, 30(3), 758– 766.
- Öz, M. (2021). Characterization of caesium carbonate-doped porous non-activated graphitic (hexagonal) boron nitride and adsorption properties. *Arabian Journal for Science and Engineering*, 1– 10.
- Öz, M., Saritekin, N. K., Bozkurt, Ç., & Yildirim, G. (2016). Synthesis of highly ordered hBN in presence of group I/IIA carbonates by solid state reaction. *Crystal Research and Technology*, 51(6), 380– 392.
- Paine, R. T., & Narula, C. K. (1990). Synthetic routes to boron nitride. *Chemical Reviews*, 90(1), 73– 91.
- Rijnders, M. R., 1996. Periodic Layer Formation During Solid State Reactions. Ph.D. Thesis, Faculty of Chemical Engineering and Chemistry, Eindhoven University of Thecnology, Nedherlands.
- Ropp, R.C., *Solid State Chemistry*. 2003. Mechanisms and Reactions in the Solid State. 129–150 Elsevier Science B.V. First Edition New Jersey, USA.
- Ruprecht, P., Konkol, W., Cornils, B., Langhoff, J., Brunke W. and Schäfer, W. 1985. Slagging gasification of coal under addition of flux agents. *Fuel Processing Technology* 11 (1): 1–12.
- Sachdev, H., Haubner, R., Nöth, H., & Lux, B. (1997). Investigation of the c-BN/h-BN phase transformation at normal pressure. *Diamond and related Materials*, 6(2-4), 286-292.
- Scherrer, P. (1918). Nachrichten von der Gesellschaft der Wissenschaften zu Göttingen. *Mathematisch-Physikalische Klasse*, 2, 98– 100.

- Shimomura, J., Funahashi, T., & Koitabashi, T. (1995). Electron microscopy of hexagonal boron nitride powder. *Journal of Materials Science*, 30(12), 3193–3199.
- Thomas, J. R., Weston, N. E., & O'Connor, T. E. (1962). Turbostratic boron nitride, thermal transformation to ordered-layer-lattice boron nitride. *Journal of the American Chemical Society*, 84(24), 4619–4622.
- Vaynman S. and Fine, M.E., 1999. Development of Fluxes for Lead-Free Solders Containing Zinc. *Scripta Materialia* 41 (12): 1269–1271.
- Wang, D.Y., Liu, C.J., Shi, P.Y., Jiang, M.F. 2004. Effect of Rare Earth Oxide on Crystallization Temperature of Mold Flux for Continuous Casting. *Journal of Iron and Steel Research* 16 (5): 28–32.
- Yuan, S., Zhu, L., Fan, M., Wang, X., Wan, D., Peng, S., & Tang, H. (2008). Fluffy-like boron nitride spheres synthesized by epitaxial growth. *Materials Chemistry and Physics*, 112(3), 912–915.
- Zhi, C., Bando, Y., Tang, C., & Golberg, D. (2010). Boron nitride nanotubes. *Materials Science and Engineering: R: Reports*, 70(3–6), 92–111.

Chapter 7

DYNAMICS OF CHIRONOMIDAE (DIPTERA) LARVAL IN OĞULPAŞA STREAM (EDİRNE/ TURKEY)

Nurcan ÖZKAN¹

¹ Nurcan ÖZKAN, Assoc. Prof. Dr., University of Trakya, Faculty of Education, Department of Mathematics and Science Education, nurcanozkan@hotmail.com, ORCID: 0000-0001-5045-6186

1. INTRODUCTION

Aquatic macroinvertebrates are critical to the ecosystem in most basic events such as energy, displacement and nutrient flow through top-down and bottom-up ecosystem regulation (Hellmann et al., 2015). Chironomidae larvae are important components of water beetles. They are valuable for their taxon richness, role in the food web and their use as aquatic bioindicators (Zamora-Muñoz and Alba-Tercedor, 1996; Türkmen and Kazancı, 2008; Kalyoncu and Gülboy, 2009).

Due to Turkey's strategic geographical location, this study was conducted to fill the gaps as a Eurasian country. Aquatic insects are generally well studied in a wide variety of inland waters and biotopes in Turkey (Taşdemir et al., 2008; Ustaoglu et al., 2008; Kazancı and Türkmen, 2012; Zeybek et al., 2012). However, there are still unfinished areas and need to be revised.

2. MATERIAL AND METHOD

Oğulpaşa Stream, located within the provincial borders of Edirne, originates near Sarıdanışment village and flows in a north-south direction for approximately 65-70 km. It joins the Ergene River south of Sazlımalkoç Village within the provincial borders of Kırklareli (Figure 1).

The study was carried out in monthly periods for 12 months between September 2015 and August 2016 in the Oğulpaşa Stream, a tributary of the Ergene River, which forms a part of the streams of the Meriç-Ergene Basin. In the study, 3 stations were determined in Oğulpaşa Stream. The 1st station is 1 km from Abalar Village from above, the 2nd station was chosen from the Şerbettar Village entrance and the 3rd station was selected from the Sazlımalkoç Village exit (Figure 1). Ekman-Birge grab (15x15 cm²) were used to collect mud samples from the stream in the study area. Two samplings were made from each station. Mud samples were washed in sieves with different mesh sizes (0.1-0.5 mm). Organisms collected with fine-tipped forceps were fixed in plastic bottles containing 70% ethyl alcohol. It was cleaned and diagnosed under the microscope. Identification of Chironomidae species Moller Pillot (1977-1978, 1984), Fittkau and Roback (1983), Şahin (1984, 1991), Kırgız (1988) and Özkan (2003) were used.



Figure 1. Oğulpaşa Stream sampling stations: 1. Abalar Village (478818.70 E, 4601035.05 N); 2. Şerbettar Village (480249.32 E, 4591347.00 N); 3. Sazlımalkoç Village (490444.56 E, 4577381.90 N)

However, a sample could not be taken from the stream in February due to heavy rains and floods. In addition, sampling could not be made because the stream bed was dry in June, July and September and the water level was very high in March and April.

Quantitative analyzes were based on the number of Chironomid larvae per m², which is considered to be the unit area of the riverbed surface. Distribution of Chironomidae larvae in the study area according to months, stations and seasons at total and species level is given.

In addition, some physicochemical properties of water were determined. For chemical analysis in the stream, water samples were taken with Ruttner bottles at each station, placed in 1-liter colored glass bottles and brought to the laboratory. In addition, water and air temperature were measured with a thermometer.

3. RESULTS

Considering the results of the study carried out in Oğulpaşa Stream between September 2015 and August 2016, 1317 larvae were found, consisting of 52 species belonging to 4 subfamilies of the Chironomidae family. These;

I) Subfamily Tanypodinae: *Tanypus punctipennis*, *T. kraatzi*, *Procladius (Holotanypus) sp.*, *Psectrotanypus varius*, *Macropelopia nebulosa*, *Macropelopia goetghebueri*, *Ablabesmyia aequidensi*, *A. monilis*, *Natarsia punctata*, *Monopelopia tenuicalcar*.

II) Subfamily Prodiamesinae: *Prodiamesa olivacea*.

III) Subfamily Orthocladiinae: *Smittia aquatilis*, *Bryophaenocladus virgo*, *Cricotopus bicinctus*, *C. fuscus*, *C. flavocinctus*, *C. albiforceps*, *C. annulator*, *C. sylvestris*, *Halocladus fucicola*, *Hydrobaenus pilipes*, *Psectrocladius sordidellus*, *Limnophyes pusillus*, *Orthocladus thienemanni*, *Zalutschia megastyla*.

IV. Subfamily Chironominae: Tribus I – Chironomini: *Chironomus halophilus*, *C. reductus*, *C. riparius*, *C. anthracinus*, *C. viridicollis*, *C. plumosus*, *C. tentans*, *Polypedilum nubifer*, *Polypedilum sp.*, *P. nubeculosum*, *P. convictum*, *P. exsectum*, *Stictochironomus longipugionis*, *S. yalvacii*, *Cryptochironomus defectus*, *Cladopelma laccophila*, *Endochironomus tendens*, *Einfeldia pagana*, *Dicrotendipes nervosus*, *D. tritonus*, *Harnischia fuscimana*, *Cryptotendipes holsatus*, Tribus II – Tanytarsini: *Cladotanytarsus mancus*, *Paratanytarsus lauterborni*, *Tanytarsus gregarius*, *Virgatanytarsus arduennensis*, *Rheotanytarsus exiguus*.

In the total distribution of Chironomidae larvae in m² according to the stations, respectively; Station 3 comes with 2263 individuals and 48.73% multiplicity rate, 2nd station with 1953 individuals and 42.05% multiplicity rate, 1st station with 428 individuals and 9.22% multiplicity rate (Table 1).

In the same table, when the monthly distributions of the stations are examined, according to the multiplicity rate, 20.76% (3007) October, 16.27% (2356) May, 16.26% (2355) September, 14.42% (2089) August, 11.51% (1667) December, 5.99% (867) November, 5.73% (830) January, 4.92% (712) June, 1.99% (289) July, 1.92% with (278) April and 0.23% (33) March.

Considering the relationship between the station and the months in the distribution of the larvae, the highest number was found in the 1st station in June (1067), the 2nd station in May (5689) and the 3rd station in October (5511). The lowest values were shown in March and August (22, 22) at the

1st station, in March (44) at the 2nd station, and in May (444) at the 3rd station.

In the distribution of the seasonal totals of Chironomidae larvae according to the stations, the 3rd station comes with 47.16% (2080), the 2nd station with 43.79 (1931) and the 1st station with 9.05% (399) respectively (Table 2).

Table 1. Numerical and Proportional Distribution of Chironomidae (Diptera) Larvae of Oğulpaşa Stream by Stations and Months (Individual/m²)

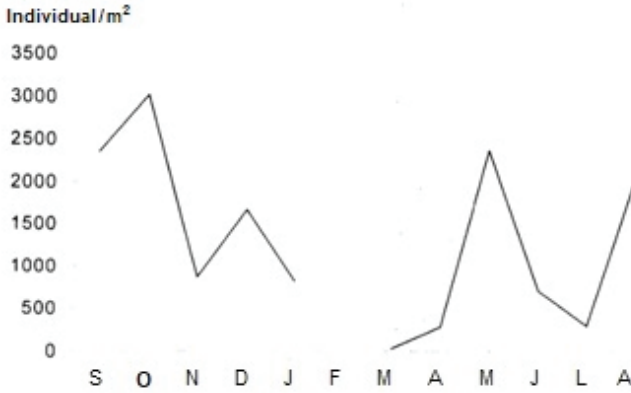
Months Stations	September	October	November	December	January	February	March	April	May	June	July	August	Total	Average
1	578	644	400	133	-	-	22	400	934	1067	511	22	4711	428
%	12,27	7,14	15,38	2,66	-	-	33,33	71,94	13,22	74,98	88,41	0,35	11,84	9,22
2	4133	2867	1178	2267	1111	-	44	156	5689	356	67	3622	21490	1953
%	87,73	31,78	45,31	45,34	44,64	-	66,67	28,06	80,5	25,02	11,59	57,8	54,03	42,05
3	-	55,11	1022	2600	1378	-	-	-	444	-	-	2622	13577	2263
%	-	61,08	39,31	52	55,36	-	-	-	6,28	-	-	41,85	34,13	48,73
Total	4711	9022	2600	5000	2489	-	66	556	7067	1423	578	6266	39778	4644
%	100	100	100	100	100	-	100	100	100	100	100	100	100	100
Average	2355	3007	867	1667	830	-	33	278	2356	712	289	2089	14483	1317
%	16,20	20,76	5,99	11,51	5,73	-	0,23	1,92	16,27	4,92	1,99	14,42	100	

Table 2. Numerical and Proportional Distribution of Chironomidae (Diptera) Larvae of Oğulpaşa Stream by Seasons (Individual/m²)

Seasons Stations	Spring	Summer	Autumn	Winter	Total	Average
1	452	534	541	67	1594	399
%	15,81	11,86	8,28	1,79	9,04	0,05
2	1963	1348	2726	1689	7726	19,31
%	68,66	29,93	41,23	45,1	43,79	43,79
3	444	26,22	3266	1989	8321	2080
%	15,53	58,21	49,99	53,11	47,17	47,16
Total	2859	4504	6533	3745	17641	4410
%	100	100	100	100	100	100
Average	953	1501	2178	1248	5880	1470
%	16,21	25,53	37,04	21,22	100	

In their seasonal distribution according to the station averages; 37.04% (2178) autumn, 25.53% (1501) summer, 21.22% (1248) winter and 16.21% (953) spring (Figure 2).

Figure 2. Seasonal Distribution of Chironomidae (Diptera) Larvae by Station and Average in Oğulpaşa Stream



According to the relationship between stations and seasons in the distribution of larvae, all stations showed the highest numerical lowest values in winter (67), station 2 in summer (1348) and station values in autumn (541, 2726, 3266, respectively). Station 1 had the 3 in spring (444).

3.1. Distribution of Chironomidae Species by Station in Oğulpaşa Stream

Among the Chironomid species identified in Oğulpaşa Stream, *Tanytus punctipennis*, *Procladius (Holotanytus) sp.*, *Cricotopus bicinctus*, *C. fuscus*, *C. sylvestris*, *Chironomus anthracinus*, *C. viridicollis*, *C. plumosus*, *C. tentans*, *Polypedilum nubeculosum*, *Cryptochironomus defectus*, *Dicrotendipes nervosus* and *Paratanytarsus lauterborni* were found at all stations. *Tanytus kraatzi*, *Macropelopia nebulosa*, *M. goetghebueri*, *Ablabesmyia aequidensi*, *Natarsia punctata*, *Monopelopia tenuicalcar*, *Prodiamesa olivacea*, *Smittia aquatilis*, *Bryophaenocladus virgo*, *Cricotopus annulator*, *Halocladus fucicola*, *Psectrocladius sordidellus*, *Limnophyes pusillus*, *Orthocladus thienemanni*, *Zalutschia megastyla*, *Chironomus riparius*, *Polypedilum sp.*, *P. exsectum*, *Stictochironomus yalvacii*, *Cladopelma laccophila*, *Einfeldia pagana*, *Harnischia fuscimana*, *Cryptotendipes holsatus*, *Tanytarsus gregarius*, *Rheotanytarsus exiguus* and *Virgatanytarsus arduennensis* were recorded from only one station (Table 3).

If we look at the numerical values of the species determined on the basis of the averages of the stations in the stream, *Polypedilum nubifer* (384) was determined as the most abundant species. This is followed by *Tanytus punctipennis* (114) and *Chironomus plumosus* (74), respectively. *Tanytus kraatzi*, *Macropelopia goetghebueri*, *Ablabesmyia aequidensi*,

Natarsia punctata, *Monopelopia tenuicalcar*, *Prodiamesa olivacea*, *Smittia aquatilis*, *Cricotopus annulator*, *Chironomus riparius*, *Polypedium* sp., *P. exsectum*, *Cladopelma laccophila*, *Endochironomus tendens*, *Einfeldia pagana*, *Harnischia fuscimana* and *Cryptotendipes holsatus*, they were found to be the least with only 1 individual.

Considering the total number of species at each station, the 2nd station with 32 species (1953), the 3rd station with 29 species (1234), and the 1st station (428) with 30 species are listed according to their abundance.

Table 3. Numerical and Proportional Distribution of Larval Chironomidae (Diptera) Species in Oğulpaşa Stream by Stations (Individual/m²).

Species	Stations	1	2	3	Total	Average
<i>Tanyus punctipennis</i>		42	194	107	343	114
	%	9.81	9.93	8.67	9.48	9.47
<i>Tanyus kraatzi</i>		-	4	-	4	1
	%	-	0.2	-	0.11	0.08
<i>Procladius (Holotanyus) sp.</i>		26	27	54	107	35
	%	6.07	1.38	4.38	2.95	2.91
<i>Psectrotanyus varius</i>		109	-	2	111	37
	%	25.47	-	0.16	3.07	3.08
<i>Macropelopia nebulosa</i>		-	-	14	14	5
	%	-	-	1.14	0.39	0.42
<i>Macropelopia goetghebueri</i>		2	-	-	2	1
	%	0.47	-	-	0.06	0.08
<i>Ablabesmyia aequidensi</i>		2	-	-	2	1
	%	0.47	-	-	0.06	0.08
<i>Ablabesmyia monilis</i>		2	6	-	8	3
	%	0.47	0.31	-	0.22	0.25
<i>Natarsia punctata</i>		-	-	2	2	1
	%	-	-	0.16	0.06	0.08
<i>Monopelopia tenuicalcar</i>		2	-	-	2	1
	%	0.47	-	-	0.06	0.08
<i>Prodiamesa olivacea</i>		-	-	2	2	1
	%	-	-	0.16	0.06	0.08
<i>Smittia aquatilis</i>		4	-	-	4	1
	%	0.93	-	-	0.11	0.08
<i>Bryophaenocladus virgo</i>		8	-	-	8	3
	%	1.87	-	-	0.22	0.25
<i>Cricotopus bicinctus</i>		8	93	14	115	38
	%	1.87	4.76	1.14	3.18	3.16

<i>Cricotopus fuscus</i>	8	10	2	20	7
%	1.87	0.51	0.16	0.55	0.58
<i>Cricotopus flavocinctus</i>	12	4	-	16	5
%	2.8	0.2	-	0.44	0.42
<i>Cricotopus albiforceps</i>	4	38	-	42	14
%	0.93	1.95	-	1.16	1.16
<i>Cricotopus annulator</i>	-	-	2	2	1
%	-	-	0.16	0.06	0.08
<i>Cricotopus sylvestris</i>	14	102	12	128	42
%	3.27	5.22	0.97	3.54	3.49
<i>Halocladius fucicola</i>	-	44	-	44	15
%	-	2.25	-	1.22	1.25
<i>Hydrobaenus pilipes</i>	2	-	20	22	7
%	0.47	-	1.62	0.61	0.58
<i>Psectrocladius sordidellus</i>	-	-	59	59	19
%	-	-	4.78	1.63	1.58
<i>Limnohyes pusillus</i>	-	-	40	40	13
%	-	-	3.24	1.11	1.08
<i>Orthocladius thienemanni</i>	-	-	6	6	2
%	-	-	0.49	0.17	0.17
<i>Zalutschia megastyla</i>	6	-	-	6	2
%	1.4	-	-	0.17	0.17
<i>Chironomus halophilus</i>	-	26	53	79	26
%	-	1.33	4.29	2.19	2.16
<i>Chironomus reductus</i>	-	26	6	32	11
%	-	1.33	0.49	0.89	0.92
<i>Chironomus riparius</i>	2	-	-	2	1
%	0.47	-	-	0.06	0.08
<i>Chironomus anthracinus</i>	54	79	75	208	69
%	12.62	4.05	6.08	5.75	5.73
<i>Chironomus viridicollis</i>	40	54	75	169	56
%	9.35	2.76	6.08	4.67	4.65
<i>Chironomus plumosus</i>	25	89	109	223	74
%	5.84	4.56	8.84	6.16	6.15
<i>Chironomus tentans</i>	14	102	85	201	67
%	3.27	5.22	6.89	5.56	5.56
<i>Polypedilum nubifer</i>	-	736	416	1152	384
%	-	37.69	33.71	31.86	31.89
<i>Polypedilum sp.</i>	-	-	2	2	1
%	-	-	0.16	0.06	0.08
<i>Polypedilum nubeculosum</i>	2	8	2	12	4
%	0.47	0.41	0.16	0.33	0.33

<i>Polypedilum convictum</i>	4	12	-	16	5
%	0.93	0.62		0.44	0.42
<i>Polypedilum exsectum</i>	-	4	-	4	1
%		0.2		0.11	0.08
<i>Stictochironomus longipugionis</i>	-	88	63	151	50
%		4.51	5.11	4.18	4.15
<i>Stictochironomus yalvacii</i>	-	51	-	51	17
%		2.62		1.41	1.41
<i>Cryptochironomus defectus</i>	8	34	2	44	15
%	1.87	1.74	0.16	1.22	1.25
<i>Cladopelma laccophila</i>	-	4	-	4	1
%		0.2		0.11	0.08
<i>Endochironomus tendens</i>	-	2	2	4	1
%		0.1	0.16	0.11	0.08
<i>Einfeldia pagana</i>	2	-	-	2	1
%	0.47			0.06	0.08
<i>Dicrotendipes nervosus</i>	2	14	2	18	6
%	0.47	0.72	0.16	0.49	0.5
<i>Dicrotendipes tritomus</i>	4	8	-	12	4
%	0.93	0.41		0.33	0.33
<i>Harnischia fuscimana</i>	2	-	-	2	1
%	0.47			0.06	0.08
<i>Cryptotendipes holsatus</i>	-	-	2	2	1
%			0.16	0.06	0.08
<i>Cladotanytarsus mancus</i>	6	48	-	54	18
%	1.4	2.46		1.49	1.5
<i>Paratanytarsus lauterborni</i>	12	4	4	20	7
%	2.8	0.2	0.33	0.5	0.58
<i>Tanytarsus gregarius</i>	-	16	-	16	5
%		0.82		0.44	0.42
<i>Virgatanytarsus arduennensis</i>	-	14	-	14	5
%		0.72		0.39	0.42
<i>Rheotanytarsus exiquus</i>	-	12	-	12	4
%		0.62		0.33	0.33
Total	428	1953	1234	3615	1204
	100	100	100	100	100

Polypedilum nubifer (736) was the most common species in the 2nd station according to the number of the determined species in m² according to the stations, again *Polypedilum nubifer* (416) at the 3rd station, *Psectrotanytus varius* (109) at the 1st station, *Chironomus plumosus* (109) at the 3rd station is following. There are at least 2 individuals with *Macropelopia goetghebueri*, *Ablabesmyia aequidensis*, *A. monilis*,

Monopelopia tenuicalcar, *Hydrobaenus pilipes*, *Chironomus riparius*, *Polypedilum nubeculosum*, *Einfeldia pagana*, *Dicrotendipes nervosus* and *Harnischia fuscimana* at station 1. Again with 2 individuals, the least number of *Endochironomus tendens* at station 2, *Psectrotanypus varius*, *Natarsia punctata*, *Prodiamesa olivacea*, *Cricotopus fuscus*, *C. annulator*, *Polypedilum* sp., *P. nubeculosum*, *Cryptochironomus defectus*, *Endochironomus tendens*, *Dicrotendipes nervosus* and *Cryptotendipes holsatus* 3. located at the station.

3.2. Seasonal Distributions of Chironomidae Species in Oğulpaşa Stream

Procladius (Holotanypus) sp., *Cricotopus sylvestris*, *Chironomus halophilus*, *C. reductus*, *C. anthracinus*, *C. viridicollis*, *C. plumosus*, *Polypedilum nubifer*, *Stictochironomus longipugionis*, *Cryptochironomus defectus* and *Cladotanytarsus mancus* were found in the stream in all seasons. *Tanypus kraatzi*, *Macropelopia goetghebueri*, *Ablabesmyia aequidensi*, *A. monilis*, *Natarsia punctata*, *Cricotopus flavocinctus*, *Halocladius fucicola*, *Zalutschia megastyla*, *Polypedilum exsectum*, *Stictochironomus yalvacii*, *Cladopelma laccophila*, *Dicrotendipes tritonus*, *Harnischia fuscimana* and *Rheotanytarsus exiquus* in spring, *Chironomus riparius*, *Cryptotendipes holsatus* and *Virgatanytarsus arduennensis* in summer, *Monopelopia tenuicalcar*, *Cricotopus annulator*, *Polypedilum* sp. and *Einfeldia pagana* in autumn, *Macropelopia nebulosa*, *Prodiamesa olivacea*, *Limnophyes pusillus* and *Orthocladius thienemanni* were found only in winter (Table 4).

Considering the averages of the number of species detected in all seasons per m², they are ranked with *Polypedilum nubifer* (400), *Chironomus plumosus* (183) and *Tanypus punctipennis* (136) individuals in order of abundance. *Tanypus kraatzi*, *Macropelopia goetghebueri*, *Ablabesmyia aequidensi*, *Natarsia punctata*, *Monopelopia tenuicalcar*, *Prodiamesa olivacea*, *Cricotopus annulator*, *Chironomus riparius*, *Polypedilum* sp., *P. exsectum*, *Cladopelma laccophila*, *Endochironomus tendens*, *Einfeldia pagana*, *Harnischia fuscimana* and *Cryptotendipes holsatus* were the least found species with 1 individual each.

The distribution of Chironomidae species according to the seasons is autumn with 28 species consisting of 2082 individuals, winter with 24 species consisting of 1254 individuals, summer with 20 species consisting of 1032 individuals, and spring with 37 species consisting of 898 individuals (Table 4).

Considering the number of detected species in m² according to the seasons, *Polypedilum nubifer* was found the most in autumn and summer (730, 563) and *Tanypus punctipennis* (436) in autumn. At least 2 individuals

Macropelopia goetghebueri, *Ablabesmyia aequidensi*, *Chironomus halophilus* and *Polypedilum nubeculosum* were recovered in spring, and *Cricotopus bicinctus*, *C. sylvestris*, *Hydrobaenus pilipes*, *Polypedilum* sp., *Endochironomus tendens* and *Paratanytarsus lauterborni* in autumn.

Table 4. Numerical and Proportional Distribution of Larval Chironomidae (Diptera) Species in Oğulpaşa Stream According to Seasons (Individual/m²).

Species	Stations	Spring	Summer	Autumn	Winter	Total	Average
<i>Tanytus punctipennis</i>		23	86	436	-	545	136
	%	2.56	8.33	20.94	-	10.34	10.32
<i>Tanytus kraatzi</i>		4	-	-	-	4	1
	%	0.45	-	-	-	0.08	0.08
<i>Procladius (Holotanytus) sp.</i>		35	36	31	63	165	41
	%	3.9	3.48	1.48	5.02	3.13	3.11
<i>Psectrotanytus varius</i>		5	11	144	-	160	39
	%	0.56	1.07	6.92	-	3.04	2.96
<i>Macropelopia nebulosa</i>		-	-	-	26	26	6
	%	-	-	-	2.07	0.49	0.46
<i>Macropelopia goetghebueri</i>		2	-	-	-	2	1
	%	0.22	-	-	-	0.04	0.08
<i>Ablabesmyia aequidensi</i>		2	-	-	-	2	1
	%	0.22	-	-	-	0.04	0.08
<i>Ablabesmyia monilis</i>		10	-	-	-	10	3
	%	1.11	-	-	-	0.19	0.23
<i>Natarsia punctata</i>		4	-	-	-	4	1
	%	0.45	-	-	-	0.08	0.08
<i>Monopelopia tenuicalcar</i>		-	-	4	-	4	1
	%	-	-	0.19	-	0.08	0.08
<i>Prodiamesa olivacea</i>		-	-	-	4	4	1
	%	-	-	-	0.32	0.08	0.08
<i>Smittia aquatilis</i>		4	-	-	4	8	2
	%	1.45	-	-	0.32	0.15	0.15
<i>Bryophaenocladus virgo</i>		-	-	7	4	11	3
	%	-	-	0.34	0.32	0.21	0.23
<i>Cricotopus bicinctus</i>		135	4	2	-	141	35
	%	15.03	0.39	0.1	-	2.68	2.66
<i>Cricotopus fuscus</i>		33	-	-	4	37	9
	%	3.67	-	-	0.32	0.7	0.68
<i>Cricotopus flavocinctus</i>		28	-	-	-	28	7
	%	3.12	-	-	-	0.53	0.53
<i>Cricotopus albiforceps</i>		15	-	-	63	78	19
	%	1.67	-	-	5.02	1.48	1.44
<i>Cricotopus annulator</i>		-	-	4	-	4	1
	%	-	-	0.19	-	0.08	0.08

<i>Cricotopus sylvestris</i>	138	4	2	26	170	42
%	15.37	0.39	0.1	2.07	3.23	3.18
<i>Halocladus fucicola</i>	54	-	-	-	54	14
%	6.01	-	-	-	1.03	1.06
<i>Hydrobaenus pilipes</i>	-	-	2	37	39	10
%	-	-	0.1	2.95	0.74	0.76
<i>Psectrocladius sordidellus</i>	-	-	35	56	91	23
%	-	-	1.68	4.47	1.73	1.75
<i>Limnohyes pusillus</i>	-	-	-	74	74	18
%	-	-	-	5.9	1.41	1.36
<i>Orthocladus thienemanni</i>	-	-	-	12	12	3
%	-	-	-	0.96	0.23	0.23
<i>Zalutschia megastyla</i>	11	-	-	-	11	3
%	1.22	-	-	-	0.21	0.23
<i>Chironomus halophilus</i>	2	12	37	67	118	29
%	0.22	1.16	1.78	5.34	2.24	2.2
<i>Chironomus reductus</i>	7	12	11	15	45	11
%	0.58	1.16	0.53	1.2	0.85	0.84
<i>Chironomus riparius</i>	-	4	-	-	4	1
%	-	0.39	-	-	0.08	0.08
<i>Chironomus anthracinus</i>	30	71	114	93	308	77
%	3.34	6.88	5.47	7.42	5.84	5.85
<i>Chironomus viridicollis</i>	40	41	58	126	265	66
%	4.45	3.97	2.78	10.04	5.03	5.01
<i>Chironomus plumosus</i>	5	40	202	86	333	83
%	0.56	3.88	9.7	6.86	6.32	6.3
<i>Chironomus tentans</i>	-	62	183	45	290	72
%	-	6.01	8.78	3.59	5.5	5.47
<i>Polypedilum nubifer</i>	4	563	730	304	1601	400
%	0.45	54.55	35.06	24.24	30.4	30.37
<i>Polypedilum sp.</i>	-	-	2	-	2	1
%	-	-	0.1	-	0.04	0.08
<i>Polypedilum nubeculosum</i>	2	-	5	11	18	5
%	0.22	-	0.24	0.88	0.34	0.37
<i>Polypedilum convictum</i>	10	4	7	-	21	5
%	1.11	0.39	0.34	-	0.4	0.37
<i>Polypedilum exsectum</i>	5	-	-	-	5	1
%	0.56	-	-	-	0.09	0.08
<i>Stictochironomus longipugionis</i>	89	25	10	103	227	57
%	9.91	2.42	0.48	8.21	4.31	4.33
<i>Stictochironomus yalvacii</i>	62	-	-	-	62	20
%	6.9	-	-	-	1.18	1.52
<i>Cryptochironomus defectus</i>	18	13	16	19	66	16
%	2	1.26	0.77	1.52	1.25	1.21
<i>Cladopelma laccophila</i>	4	-	-	-	4	1
%	0.45	-	-	-	0.08	0.08

<i>Endochironomus tendens</i>	4	-	2	-	6	1
%	0.45	-	0.1	-	0.11	0.08
<i>Einfeldia pagana</i>	-	-	4	-	4	1
%	-	-	0.19	-	0.08	0.08
<i>Dicrotendipes nervosus</i>	20	-	4	-	24	6
%	2.23	-	0.19	-	0.46	0.46
<i>Dicrotendipes tritonus</i>	15	-	-	-	15	4
%	1.67	-	-	-	0.28	0.3
<i>Harnischia fuscimana</i>	4	-	-	-	4	1
%	0.45	-	-	-	0.08	0.08
<i>Cryptotendipes holsatus</i>	-	4	-	-	4	1
%	-	0.39	-	-	0.08	0.08
<i>Cladotanytarsus mancus</i>	32	13	21	8	74	18
%	3.56	1.26	1.01	0.64	1.41	1.36
<i>Paratanytarsus lauterborni</i>	20	-	2	4	26	6
%	2.23	-	0.1	0.32	0.49	0.46
<i>Tanytarsus gregarius</i>	7	7	7	-	21	5
%	0.78	0.68	0.34	-	0.4	0.37
<i>Virgatanytarsus arduennensis</i>	-	20	-	-	20	5
%	-	1.94	-	-	0.38	0.37
<i>Rheotanytarsus exiguus</i>	15	-	-	-	15	4
%	1.67	-	-	-	0.28	0.3
Total	898	1032	2082	1254	5266	1317
	100	100	100	100	100	100

3.3. Some Physicochemical Properties of Water in Oğulpaşa Stream

Some physicochemical analyzes of water are given below (Table 5).

3.3.1. Electrical Conductivity (E.C.): Electrical conductivity measurements were found at the 3rd station with the lowest value of 230.46 M.Mhos, while the highest value was determined at the 2nd station with 250.27 M.Mhos. The average value of the stations is 242.97 M.Mhos, and it has been observed that the measurements made in the summer months (May, June, July, and August) are above the normal values.

3.3.2. pH: The pH of the water was measured as the lowest value at the 1st station with 6.86 and the highest value with 7.23 at the 2nd station. The mean pH value was 7.1 and all values were within normal limits during the study period.

3.3.3. Dissolved Oxygen (D.O.): The lowest amount of dissolved oxygen in the water was determined at station 1 with 5.56 mg/lit and the highest value was determined at station 3 with 8.9 mg/lit. The average value is 7.71 mg/lit, and it was observed that the dissolved oxygen amount was below normal only in August.

3.3.4. Biological Oxygen Demand (B.O.D.5): Biological oxygen demand was the lowest at station 1 with 2.32 mg/l, and the highest at station 2 with 4.78 mg/l. The average value is 55.55 mg/l. During the study period, it was determined that it showed normal values except July.

3.3.5. Chemical Oxygen Demand (C.O.D.): Chemical oxygen demand was measured at the 3rd station with the lowest value of 39.73 mg/l and the highest value at the 2nd station with 81.33 mg/l. During the study period, it was determined that it showed normal values except July.

3.3.6. Calcium (Ca^{+2}): The lowest amount of calcium in the water was measured at station 3 with 66.62 mg/l, and the highest value was measured at station 1 with 90.25 mg/l. The average value is 77.84 mg/l and it was found to be above the normal value in October, January, March, April, May, June, as well as at the 1st and especially the 2nd station. During the year, decreases were observed in the amount of calcium from the 1st station to the 3rd station.

3.3.7. Magnesium (Mg^{+2}): The lowest amount of magnesium in the water was measured at the 3rd station with 25.52 mg/l and the highest value was measured at the 1st station with 31.97 mg/l. The average value is 28.59 mg/l and it has normal values during the study and a decrease was observed from the 1st station to the 3rd station, as in the amount of Ca^{+2} .

3.3.8. Chloride (Cl^{-1}): The lowest amount of chloride in the water was measured at the 3rd station with 110.08 mg/l, and the lowest value was measured at the 2nd station with 147.96 mg/l. The mean value was 134.85 mg/l and it was observed to be above the normal limits throughout the study.

3.3.9. Nitrate (NO_3^{-1}): The lowest amount of nitrate in the water was found at the 3rd station with 6.89 mg/l, and the highest value was found at the 2nd station with 13.42 mg/l. The average value was 9.19 mg/l and it was found to be above the normal value in March, April, June, and July and at the 2nd station.

3.3.10. Nitrite (NO_2^{-1}): The lowest amount of nitrite in the water was measured at station 1 with 0.077 mg/l and the highest at station 2 with 0.214 mg/l. The average value is 0.148 mg/l. During the study, it was observed that the water measurements made in November, March, April, May, June, July and at the 2nd and 3rd stations were above the normal values.

3.3.11. Phosphate (PO_4^{-3}): The lowest amount of phosphate in the water was measured at station 2 with 0.064 mg/l and the highest at station 1 with 0.162 mg/l. The average value was 0.103 mg/l, and it was observed that the water measurements made during the study were within normal

values.

3.3.12. Chromium (Cr⁶): Chromium in the water was measured at the 3rd station with the lowest 0.101 mg/lit and at the second station with the highest 0.138 mg/lit. The average value is 0.119 mg/lit and it was found to be above the normal values in September, November, March, June, and July and at the 1st and 2nd stations.

3.3.13. Ammonia (NH₃): The lowest amount of ammonia in the water was determined at station 1 with 0.113 mg/lit and the highest at station 2 with 0.218 mg/lit. The average value was 0.15 mg/lit, and it was observed that the water measurements made during the study were within normal values.

3.3.14. Water temperature (°C): The water temperature was measured at the 3rd station as the lowest value with 13.44 °C and as the highest value at the 2nd station with 16.37 °C. The average temperature value is 14.89 °C and the air temperature changes depending on seasonal factors.

Table 5. *Some Physicochemical Values of the Stations According to the Monthly Averages of Oğulpaşa Stream*

Stations	1	2	3	Average
Parameter				
Conductivity (M.Mhos)	248.18	250.27	230.46	242.97
pH	6.86	7.23	7.21	7.1
D.O. (mg/lit)	5.56	8.66	8.9	7.71
B.O.D.5 (mg/lit)	2.32	4.78	4.15	3.75
C.O.D. (mg/lit)	45.59	81.33	39.73	55.55
Ca ⁺² (mg/lit)	90.25	76.65	66.62	77.84
Mg ⁺² (mg/lit)	31.97	28.28	25.52	28.59
Cl ⁻¹ (mg/lit)	146.51	147.96	110.08	134.85
NO ₃ ⁻¹ (mg/lit)	7.26	13.42	6.89	9.19
NO ₂ ⁻¹ (mg/lit)	0.077	0.214	0.154	0.148
PO ₄ ⁻³ (mg/lit)	0.162	0.064	0.083	0.103
Cr ⁺⁶ (mg/lit)	0.118	0.138	0.101	0.119
NH ₃ (mg/lit)	0.113	0.218	0.119	0.15
Water temperature (°C)	14.86	16.37	13.44	14.89
Air temperature (°C)	16	16.5	16.13	16.21

3.3.15. Air temperature (°C): While the air temperature was found at the 1st station with the lowest value at 16 °C, the highest value was measured at the 2nd station with 16.5 °C. The average temperature value is 16.21 °C and varies depending on seasonal factors.

4. DISCUSSION AND CONCLUSION

In this study, Chironomid species of Oğulpaşa Stream were analyzed quantitatively and qualitatively and water analyzes were made.

The existence of 52 species, belonging to 4 subfamilies, was determined. 10 species belonging to Tanypodinae subfamily, 1 belonging to Prodiamesinae subfamily, 16 species belonging to Orthocladiinae subfamily and 29 species belonging to Chironominae subfamily were found. Potamal fauna of Chironomidae (Diptera-Insecta) in Oğulpaşa Stream the Chironominae subfamily was dominant among the populations. Species of this subfamily have adapted to living in mild conditions because sediments, temperatures and sometimes lower oxygen concentrations they were able to tolerate higher (Armitage, 1995). Although the number of species is similar at the stations studied in the stream, the number of larvae of each species differs. Station 1 is poorer than the other stations in terms of the number of individuals and species. When the species were examined in the Oğulpaşa Stream, *Procladius (Holotanypus) sp.*, *Chironomus anthracinus*, *C. viridicollis* and *Polypedilum aberrans* were the most abundant. The genera *Tanypus*, *Cricotopus*, *Polypedilum* and *Chironomus* are cosmopolitan (Polatdemir ve Şahin, 1997) and are frequently encountered in all kinds of aquatic environments. The rate of these species in the family is high.

Although electrical conductivity, calcium, magnesium, chlorine, nitrate, nitrite and chromium from the physicochemical properties of the stream are above the normal limits, they are not excessively high.

REFERENCES

- Armitage P.D. (1995). *Chironomidae as Food*. p. 423-435. in: P.D. Armitage, P.S. Cranston and L.C.V. Pinder (eds.), *the chironomidae: the biology and ecology of non-biting midges*. Chapman & Hall, London.
- Fittkau, E.J. & Roback, S.S. (1983). *The Larvae of Tanypodinae (Diptera: Chironomidae) of the Holarctic Region (keys and diagnoses)*. Entomology Scandinavian Supplementum. 19, 33 – 110. Lund, Sweden.
- Hellmann, J.K., Erikson J.S., & Queenborough, S.A. (2015). Evaluating Macroinvertebrate Community Shifts in the Confluence of Freestone and Limestone Streams. *J Limnol*, 74: 64-74.
- Kalyoncu, H., & Gülboy, H. (2009). Benthic Macroinvertebrates from Daniören and Isparta Streams (Isparta/Turkey) – Biotic Indices and Multivariate Analysis. *J Appl Biol Sci*, 3: 85-92.
- Kazancı, N., & Türkmen, G. (2012). The Checklist of Ephemeroptera (Insecta) Species of Turkey. *Review of Hydrobiology*, 5: 143-156.
- Kırgız, T. (1988). Seyhan Baraj Gölü Chironomidae (Diptera) Larvaları Üzerinde Morfolojik ve Ekolojik Bir Çalışma. *Doğa TU Zooloji Dergisi*. 12(3): 245–255.
- Moller Pillot, H.K.M. (1978-1979). *De Larven der Nederlandse Chironomidae (Diptera)*. Leiden, I – I – IX. 2. 7.
- Moller Pillot, H.K.M. (1984). *De Larven der Nederlandse Chironomidae (Diptera) (Orthocladinae sensu lato)*. Leiden. S: 1 – 164.
- Özkan, N. (2003). *Trakya Bölgesi (Kırklareli, İstanbul ve Çanakkale) Chironomid (Chironomidae; Diptera) Türlerinin Tespiti*. Trakya Üniversitesi Bilimsel Araştırmalar Projeleri - TÜBAP – 320: 17-65.
- Polatdemir, N. & Şahin, Y. (1997). Eskişehir ve Çevresi Durgunsu Sistemleri Chironomidae (Diptera) Larvaları. *Tr: J. of Zoology*, 212: 315-319.
- Şahin, Y. (1984). *Doğu ve Güneydoğu Anadolu Bölgeleri Akarsu ve Göllerindeki Chironomidae (Diptera) Larvalarının Teşhisi ve Dağılımları*. Anadolu Üniversitesi Yayınları, No: 57, Fen Edebiyat Fakültesi Yayını, No: 2, Eskişehir.
- Şahin, Y. (1991). *Türkiye Chironomidae Potamofaunası*. Tübitak – Proje No: TBAG –869 (and VHAG – 347, TABG – 669, TBAG – 792), 1.
- Taşdemir, A., Ustaoglu, M.R., Balık, S., & Hasan, M.S. (2008). Diptera and Ephemeroptera Fauna of Some Lakes in Western Black Sea Region (Turkey). *J. FisheriesSciences.com* 2: 252-260
- Türkmen, G., & Kazancı, N. (2008). Water Quality Evaluation of Reference Sites by Using Saprobic Index in Some Running Waters in the Province of Bolu. *Review of Hydrobiology*, 2: 93-118.

- Ustaoglu, M.R., Balık, S., Sarı, H.M., Özdemir-Mis, D., Aygen, C., Özbek, M., İlhan, A., Taşdemir, A., Yıldız, S., & Topkara, E.T. (2008). A Faunal Study of the Glacier Lakes and Rivers on Uludağ (Bursa) Mountain. *E.Ü. Su Ürünleri Dergisi*, 25: 295-299.
- Zamora- Muñoz, C., & Alba-Tercedor, J. (1996). Bioassessment of Organically Polluted Spanish Rivers, Using a Biotic Index and Multivariate Methods. *Journal of the North American Benthological Society*, 15(3): 332-352.
- Zeybek, M., Kalyoncu, H., Ertan, Ö.O., & Çiçek, N.L. (2012). Köprüçay Irmağı (Antalya) Bentik Omurgasız Faunası. *S.D.Ü. Fen Bilimleri Enstitüsü Dergisi*, 16: 146-153.

Chapter 8

INFLUENCE OF CADMIUM ADDITION ON ELECTRICAL AND SUPERCONDUCTING FEATURES OF BULK $BI_{2.1}SR_{2.0}CA_{1.1}CU_{2.0}O_Y$ SUPERCONDUCTING MATERIALS

Asaf Tolga ULGEN¹

Mustafa Burak TURKOZ²

Muhammed OZ³

¹ Assoc.Prof, Sirnak University, Department of Electric-Electronic Engineering, Sirnak–Turkey, 73000 Orcid ID 0000-0002-7112-5607

² Assoc.Prof., Karabuk University, Department of Electric and Electronic Engineering, Karabuk-Turkey, 78000 Orcid ID 0000-0002-4127-7650

³ Assoc.Prof., Abant Izzet Baysal University, Department of Chemical and Chemical Processing Technologies, Bolu-Turkey, 14030 Orcid ID 0000-0003-0049-0161

1. Introduction

In the year of 1911, the superconductivity phenomenon for the solid mercury metal appeared immediately when the material was cooled down to the temperature of 4.2 K [1]. After that period, the superconducting materials have attracted widespread interest of researchers studied on the heavy-industrial technology, cooling technology, medical diagnosis and hydrogen society applications [2–5]. In the materials science history it is possible to see different kinds of materials such as pure elements (metals or semi-metals), organic-compounds, alloys, carbon-based compounds, carbonaceous sulfur hydride, heavy fermion-containing materials, chalcogens, rare-earth borocarbide, chevre phase-samples, nickelates, inorganic-based compounds, pyrochlore oxides, lanthanum decahydride, silicon-containing samples, magnesium diboride, iron-based materials, A-15 compounds, rutheno-cuprates and oxygen deficit multi-layered perovskite based ceramic cuprates including Tl-, Bi- and Hg-based compounds driving the superconducting nature [6,7]. Thus, the researchers have widely tried to discover new superconducting parents and improve their problematic features. Especially the Bi-containing parents with 3 valuable members has attracted a great deal of interest in several application fields due to their appealing characteristics: namely, extremely greater critical transition temperature, thermodynamic stability, magnetic field and current carrying capability, enormously lower energy consumption and losses [8–10]. As for the preparation conditions, the family of Bi-based materials exhibits the promising features as regards the cheap and harmless chemical powders, easy production process, relatively cheap cooling system, resistant towards to humid environment and stability to compositional content and oxygen [11–13]. On the other hand it is, of course, that the Bi-containing compound parents possess the problematic features (low mobile hole carrier densities, randomly oriented microcrystals, brittleness behavior, sensitivity to applied magnetic fields and current, multiple phase compositions, large penetration depth, short coherence length, grain alignment distributions/orientations, intra and inter-grain boundary couplings) due to the intrinsic weakly coupled Cu-O₂ layers in the Bi-based material crystal structure [14,15].

The problematic features play an important role of critical transition temperature parameters of Bi-based superconductors. In

the present work, the influence of manganese addition in the polycrystalline $\text{Bi}_{2.1}\text{Sr}_{2.0}\text{Ca}_{1.1}\text{Cu}_{2.0}\text{O}_y$ superconducting crystal system on the basic superconducting parameters of onset (T_c^{onset}) and offset (T_c^{offset}) critical transition temperatures and related broadening degree ($\Delta T_c = T_c^{\text{onset}} - T_c^{\text{offset}}$) values is examined by means of temperature-dependent resistivity measurements performed temperature intervals 30 K-105 K. According to the experimental results obtained, it is found that the manganese addition is ploughed to improve the fundamental superconducting parameters of $\text{Bi}_{2.1}\text{Sr}_{2.0}\text{Ca}_{1.1}\text{Cu}_{2.0}\text{O}_y$ materials.

2. Experimental Procedures for Cadmium Added $\text{Bi}_{2.1}\text{Sr}_{2.0}\text{Ca}_{1.1}\text{Cu}_{2.0}\text{O}_y$ Superconducting Compounds

In the current work, the cadmium added Bi-2212 superconducting series within the stoichiometric of $\text{Bi}_{2.1}\text{Sr}_{2.0}\text{Ca}_{1.1}\text{Cu}_{2.0}\text{Cd}_x\text{O}_y$ (here x is varying from 0 to 0.30) are meticulously produced by the conventional solid-state reaction technique. The oxide and carbonate chemicals (CdO , SrCO_3 , CuO , Bi_2O_3 , and CaCO_3) with high purity about %99.99 are purchased from exclusive distributor in Ankara. Firstly, all the powder of chemicals is separately weighed by the electronic balance in a molar ratio of 2.1:2:1.1:2.0 for the $\text{Bi}_{2.1}\text{Sr}_{2.0}\text{Ca}_{1.1}\text{Cu}_{2.0}\text{Cd}_x\text{O}_y$ superconducting system to obtain a total of approximately 3 mg of chemicals. Right after, the mixture of powder is thoroughly pulverized by a hand-pounder in the agate mortar for an hour in medium of air atmosphere.

The calcination processes of homogenous mixed powders are performed at 800 °C constant temperature for 36-hour duration in the standard box type muffle furnace and cooled down to the room temperature. Meanwhile, both the heating and cooling rates are adjusted to be 5 °C/min. The mixture of powders is removed from the furnace and realized that the color of resultant powder turns into the blackish. Then, the blackish powder is separately re-milled for an hour in the agate mortar. The re-ground powder is pressed into pellets with sizes of $1.5 \times 0.5 \times 0.2 \text{ cm}^3$ by 300 MPa in the atmospheric air to improve the interaction between the superconducting grains and especially reduce remarkably the opening between layers, defects and voids in the crystal system. After that, the solidified powders are subjected to the main heating process at 850 °C for the time of 24 h.

The stoichiometric of bulk $\text{Bi}_{2.1}\text{Sr}_{2.0}\text{Ca}_{1.1}\text{Cu}_{2.0}\text{Cd}_x\text{O}_y$ ceramic compounds fabricated by different molar ratios including $x=0, 0.01, 0.03, 0.05, 0.07, 0.10$ and 0.30 will thenceforward be presented as Cd-free/pure and Cd-1, Cd-2, Cd-3, Cd-4, Cd-5 and Cd-6, respectively.

The effect of cadmium impurity addition on the fundamental electrical and superconducting features belonging to the solid $\text{Bi}_{2.1}\text{Sr}_{2.0}\text{Ca}_{1.1}\text{Cu}_{2.0}\text{Cd}_x\text{O}_y$ ceramic superconducting compounds is experimentally scrutinized in the temperature range of 30 K-105 K in the He closed-cycle cryostat system with the assistant of the conventional four-probe method. The experimental measurements of the dc electrical resistivity versus temperature are taken from the sample surfaces using the dc current of 5 mA. The measurement signals within the accuracy of $\pm 0.01 \text{ m}\Omega\cdot\text{cm}$ are gathered by the programmable nano-voltmeter and current source. The experimental findings enable us to determine the residual resistivity (ρ_{res}), electrical resistivity at the temperature of 90 K (ρ_{90K}), room temperature resistivity (ρ_{300K}) and residual resistivity ratios (RRR). Similarly, using the dc electrical signals we determine the variation of the offset and onset critical transition temperatures (T_c^{offset} and T_c^{onset} , respectively) and related broadening degree ($\Delta T_c = T_c^{onset} - T_c^{offset}$) values with the cadmium impurity addition level.

4. Results and discussion

4.1. Variation of superconducting features of Bi-2212 ceramics prepared by Cadmium addition

In this part of chapter, the influence of different cadmium impurity level ($0.0 \leq x \leq 0.30$) on the fundamental superconducting features including the offset (T_c^{offset}) and onset (T_c^{onset}) critical transition temperatures, degree of broadening ($\Delta T_c = T_c^{onset} - T_c^{offset}$) and mobile hole carrier concentration (P_{hole}) parameters is examined with the aid of the temperature-dependent dc electrical resistivity measurement tests. The experimental measurements are executed at the temperature rang of 30 K-105 K. Here, the T_c^{onset}

parameter inferred from the dc resistivity electrical curve is related to the beginning temperature of superconductivity for the materials.

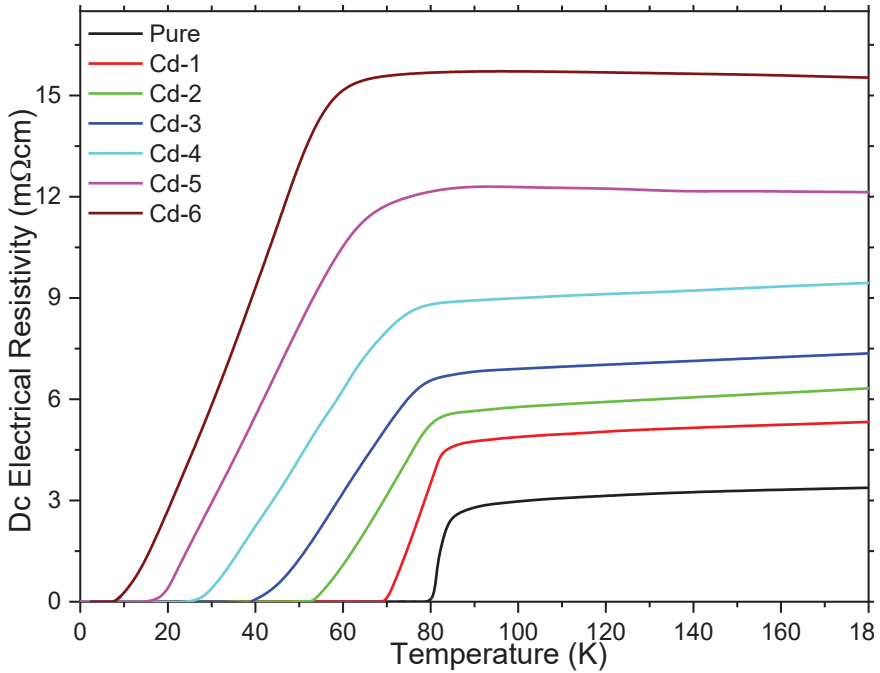


Fig. 1 Variation of superconducting findings over temperature of $\text{Bi}_{2.1}\text{Sr}_{2.0}\text{Ca}_{1.1}\text{Cu}_{2.0}\text{O}_y\text{Cd}_x$ superconducting materials

Therefore, the compound exhibits the superconducting nature in case of lower temperature value than the onset critical transition temperatures. The T_c^{onset} parameter enables us to define some critical parameters related to the quantum mechanical and material thermodynamical properties such as hybridization mechanism, energy gap coefficient, pair binding energy, thermodynamic stability, hole trap energy, overlapping mechanism between Cu-3d and O-2p wave functions, phase coherence, amplitude of pair wave function, dirty/clean limit, polarons/bipolarons in polarizable lattices, mobile charge carrier concentrations, fields of electron-phonon couplings, weak grain boundary couplings, distribution and orientation of

superconducting grains and barrier regions, localization of density of states at Fermi energy state [16–18].

Table 2 Critical Temperatures of cadmium added Bi-2212 superconducting ceramics

<i>Samples</i>	T_c^{offset} (K)	T_c^{onset} (K)	ΔT_c (K)	P_{hole}
<i>Pure</i>	80.021	83.530	3.509	0.13337
<i>Cd-1</i>	69.709	81.734	12.025	0.113332
<i>Cd-2</i>	53.031	79.068	26.037	0.092522
<i>Cd-3</i>	39.606	77.065	37.459	0.079592
<i>Cd-4</i>	26.375	73.063	46.688	0.068622
<i>Cd-5</i>	16.411	65.059	48.648	0.061161
<i>Cd-6</i>	8.283	57.516	49.233	0.055469

As for the second critical transition temperature parameter of offset value (T_c^{offset}), the phases of intergranular and intragrain components in the crystal system transit into the superconducting phase [18,19]. In other words, the T_c^{offset} value is in a relation with the phase volume fractions [19]. Hence, at the T_c^{offset} value, the formation of much more electron-phonon coupling probabilities begins in the superconducting crystal system [20-22] due to the fact that the whole specimen exhibits the superconducting nature. At the same time, the broadening degree of ΔT_c is directly associated with the quality of material. According to Fig. 1, we determine the T_c^{onset} , T_c^{offset} and ΔT_c parameters and numerically embedded in Table 2.

Table 2 Offset, onset critical transition temperatures and broadening degrees for pristine and cadmium added Bi-2212 superconducting ceramics

<i>Materials</i>	ρ_{300K} ($m\Omega cm$)	ρ_{res} ($m\Omega cm$)	ρ_{90K} ($m\Omega cm$)	$\Delta \rho$ (ρ_{300K} - ρ_{90K}) ($m\Omega cm$)	$\frac{RR}{R}$ ($\frac{\rho_{300K}}{\rho_{90K}}$)
<i>Pure</i>	3.709	2.578	2.835	0.874	1.308
<i>Cd-1</i>	5.924	4.632	4.752	1.172	1.247
<i>Cd-2</i>	7.099	5.161	5.775	1.324	1.229
<i>Cd-3</i>	8.267	6.265	6.874	1.393	1.203
<i>Cd-4</i>	10.311	8.532	8.762	1.549	1.177
<i>Cd-5</i>	12.221	12.405	12.298	-0.077	0.994
<i>Cd-6</i>	15.29	15.936	15.741	-0.451	0.971

According to the data in Table 2, it is obvious that both onset and offset critical transition temperatures are found to decrease dramatically with the increase in the cadmium impurity addition level in the solid $\text{Bi}_{2.1}\text{Sr}_{2.0}\text{Ca}_{1.1}\text{Cu}_{2.0}\text{O}_y\text{Cd}_x$ superconducting crystal system. This is in attribution to the fact that the presence of cadmium impurity in the bulk Bi-2212 superconducting system harms significantly the formation of super-electrons and electron-phonon couplings in the Bi-2212 crystal system. Besides, the differentiation of T_c^{onset} and T_c^{offset} parameters with the cadmium ions confirms the successful introduction of foreign ions in the superconducting system. Numerically, the pristine compound possesses the highest T_c^{offset} value of 80.021 K and T_c^{onset} value of 83.530 K. On the other hand, the T_c^{onset} parameters are observed to be in a range of 81.734 K-57.516 K whereas the T_c^{offset} values are detected to be temperature intervals 69.709 K-8.283 K, respectively. On this basis, the Cd-6 sample with the highest Cd-dopant level exhibits the smallest T_c^{offset} value of 80.021 K and T_c^{onset} value of 83.530 K. Based on the experimental measurement results, it is clear that the T_c^{offset} parameters are much more affected depending on the cadmium addition level as compared to the T_c^{onset} ones. All in all, as we discussed above the cadmium impurity addition damages much more the phase volume fractions belonging to the main superconducting phase of Bi-2212 due to the rapid reduction of T_c^{offset} parameters. Similarly, the cadmium impurity leads to delay the phase transition of intergranular and intragrain components into the superconducting phase. Thus, it is not wrong to claim that the formation of electron-phonon coupling probabilities decreases based on the Cd addition level in the superconducting crystal system. As for the decrement in the T_c^{onset} parameters, the experimental results show that the quantum mechanical and material thermodynamical properties are noted to diminish relatively [21, 22]. Moreover, it is to be mentioned here that the introduction of cadmium impurity into the bulk $\text{Bi}_{2.1}\text{Sr}_{2.0}\text{Ca}_{1.1}\text{Cu}_{2.0}\text{O}_y$ causes to begin new permanent structural problems [herhangi biri olur]. To point out seriously the effect of cadmium addition level on the T_c^{offset} and T_c^{onset} values, we depict

the change of critical superconducting transition temperature parameters with respect to the cadmium addition level in Fig. 2.

According to the figure, it is apparent that the difference between onset and offset critical transition temperatures systematically increases. Namely, the introduction of cadmium ions in the bulk $\text{Bi}_{2.1}\text{Sr}_{2.0}\text{Ca}_{1.1}\text{Cu}_{2.0}\text{O}_y$ superconducting system damages seriously the fundamental superconducting mechanisms in the solid Bi-2212 type-II superconducting ceramic materials.

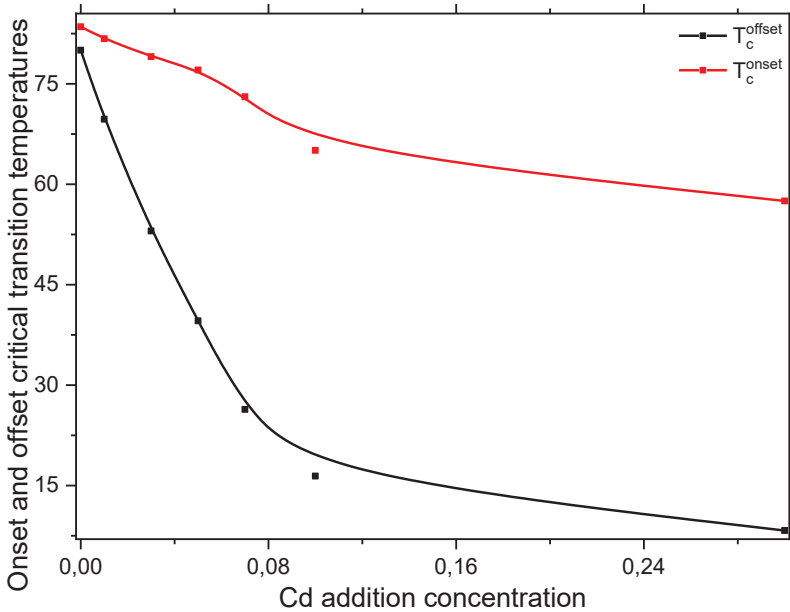


Fig. 2. T_c^{offset} and T_c^{onset} parameters for pure and cadmium added $\text{Bi}_{2.1}\text{Sr}_{2.0}\text{Ca}_{1.1}\text{Cu}_{2.0}\text{O}_y$ superconducting materials.

One can also encounter the variation of broadening degree (ΔT_c) parameters with the cadmium foreign impurity level in Table 2 and also Fig. 3. It is apparent from the table and figure that the ΔT_c parameter is found to increase gradually with the increment in the cadmium addition level. This is attributed to the fact that the increment trend of cadmium ions in the bulk Bi-2212 ceramic structure damages seriously the specimen quality. In this respect, the pure sample has the minimum ΔT_c value of 3.509 K while the Cd-6 sample with the maximum cadmium addition level inserted in the superconducting lattice presents the highest ΔT_c value of 49.233 K. The other samples exhibit the moderate ΔT_c parameters

(See Fig. 3). Moreover, it is visible from the table that the value of ΔT_c is found to decrease dramatically up to the value of $x=0.10$ after which the value decreases slowly. This is because, the crystal structure has already broken and in fact the impurity phases and other characteristic phases exist together in the crystal system, leading to the existence of pseudo-transitions.

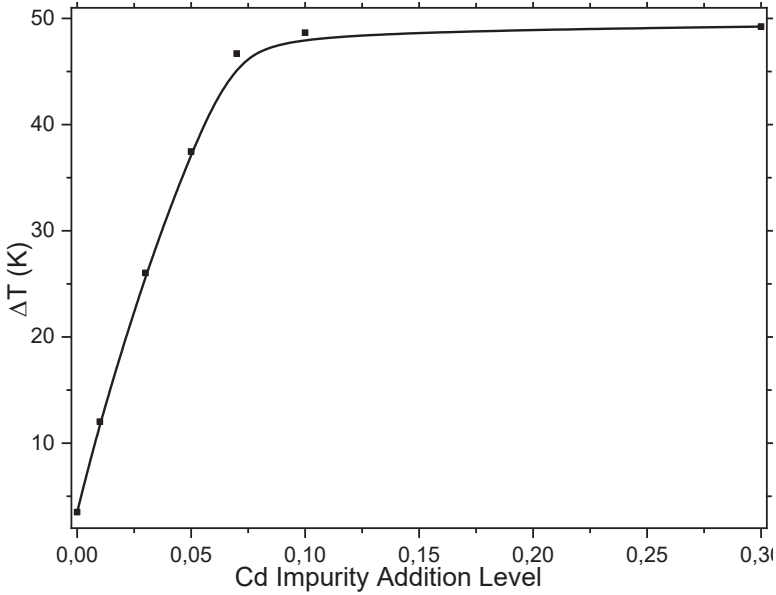


Fig. 3. Change of ΔT_c parameters belonging to $\text{Bi}_{2.1}\text{Sr}_{2.0}\text{Ca}_{1.1}\text{Cu}_{2.0}\text{O}_y\text{Cd}_x$ superconducting materials with regard to cadmium addition level.

Moreover, we also determine the effect of different molar cadmium addition in the bulk $\text{Bi}_{2.1}\text{Sr}_{2.0}\text{Ca}_{1.1}\text{Cu}_{2.0}\text{O}_y$ superconducting ceramic compound on the mobile hole carrier concentrations (abbreviated as P) per Cu ions in the valance bands with the aid of temperature-dependent dc resistivity tests using the following relation [23]:

$$P = 0.16 - \left[\left(1 - \frac{T_c^{offset}}{T_c^{max}} \right) / 82.6 \right]^{1/2} \tag{1}$$

where the abbreviation of T_c^{max} value is the temperature value of 85 K belonging to the Bi-2212 superconducting phase. In the formula,

the T_c^{offset} parameters are obtained from Table 2 so that we can easily calculate the variation of P_{hole} value with respect to the cadmium impurity concentration level. One can see all the computations in Table 2. Besides, to further emphasize the role of cadmium impurities on the mobile hole carrier concentrations, we depict Fig. 4 related to the differentiation of P_{hole} value with the cadmium ions in the crystal system.

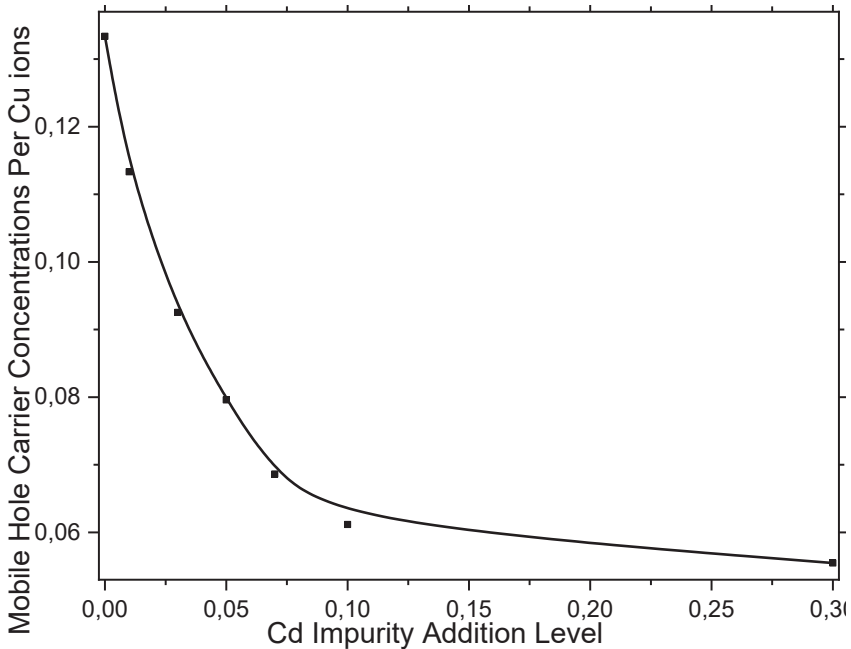


Fig. 4. Change of P parameters with different cadmium addition level of $\text{Bi}_{2.1}\text{Sr}_{2.0}\text{Ca}_{1.1}\text{Cu}_{2.0}\text{O}_y\text{Cd}_x$ superconducting materials.

According to the calculations in Fig. 4, it is obvious that the mobile hole carrier concentration level is observed to decrease systematically with the increment in the cadmium impurity concentration level. In fact, there is a rapid decrement trend up to the critical value of $x=0.1$. On this basis, the pristine compound possesses the largest hole carrier concentration level of about 0.13337. The P_{hole} values of 0.113332, 0.092522, 0.079592, 0.068622 and 0.061161 are calculated for the Cd-1, Cd-2, Cd-3, Cd-4 and Cd-5, respectively. As for the Cd-6 superconducting sample prepared with the maximum cadmium ions, the P_{hole} value

is computed to be about 0.055469 (global minimum value for this work). Namely, the existence of cadmium impurity addition in the bulk $\text{Bi}_{2.1}\text{Sr}_{2.0}\text{Ca}_{1.1}\text{Cu}_{2.0}\text{O}_y$ superconducting system automatically harms on the mobile hole carrier concentrations.

To sum up, this study shows that the main characteristic superconducting properties (the offset and onset critical transition temperatures, degree of broadening and mobile hole carrier concentration parameters) are found to degrade dramatically with the increment in the cadmium impurity addition level.

4. Conclusion

In the current work, we determine the role of manganese addition within the varied mole-to-mole ratios ($0.0 \leq x \leq 0.10$) on the basic superconducting parameters for the oxygen deficit multi-layered perovskite based polycrystalline $\text{Bi}_{2.1}\text{Sr}_{2.0}\text{Ca}_{1.1}\text{Cu}_{2.0}\text{O}_y\text{Mn}_x$ superconducting crystal structure with the aid of temperature-dependent electrical resistivity measurements performed in range of 30 K-105 K. The experimental curves show that the presence of manganese ions in the Bi-2212 crystal system damages seriously the characteristic T_c^{onset} , T_c^{offset} and ΔT_c quantities due to the degradation in the formation of bipolarons in the homogeneous clusters in the superconducting paths, mobile hole carrier concentrations, material quality founded on the permanent systematic structural problems, homogeneities in the oxidation state of superconducting grains and transition from the normal state of inter-granular component to superconducting phase. In this respect, the maximum T_c^{onset} and T_c^{offset} values are recoded to be about 84.15 K and 80.84 K for the pure sample, respectively. The related minimum ΔT_c parameter is calculated to be about 3.31 K. Similarly, the pure sample possesses the maximum mobile hole carrier concentration value of about 0.1357. Accordingly, it is obvious that the manganese addition is not a good idea for the polycrystalline Bi-2212 superconductors to be used in the heavy-industrial technology, cooling technology, medical diagnosis and hydrogen society application fields.

Acknowledgement: This work was supported by the Sırnak University Scientific Research Project Coordination Unit (Project Number: 2019.FNAP.06.02.01)

References

- [1] H.K. Onnes, Further experiments with Liquid Helium. D. On the change of Electrical Resistance of Pure Metals at very low Temperatures, etc. V. The Disappearance of the resistance of mercury, Koninklijke Nederlandsche Akademie van Wetenschappen Proceedings, 14 (1911) 113–115.
- [2] G. Yildirim, Determination of optimum diffusion annealing temperature for Au surface-layered Bi-2212 ceramics and dependence of transition temperatures on disorders, J. Alloy. Compd. 699 (2017) 247–255.
- [3] W. Buckel, R. Kleiner, Superconductivity: Fundamentals and Applications, 2nd ed., Wiley-VCH Verlag, Weinheim, (2004).
- [4] F.N. Werfel, U. Floegel-Delor, R. Rothfeld, T. Riedel, B. Goebel, D. Wippich, P. Schirrmeister, Superconductor bearings, flywheels and transportation, Supercond. Sci. Technol. 25 (2012) 014007.
- [5] M. Runde, Application of high- T_c superconductors in aluminum electrolysis plants, IEEE T. Appl. Supercond. 5 (1995) 813–816.
- [6] A.T. Ulgen, Y. Zalaoglu, G. Yildirim and T. Turgay, Development of a Relation Between Vickers Hardness and Microindentation Test Loads for Bi-2212 Crystal Structure Doped With Manganese Ions, 2nd International Baku Conference on Scientific Research, 28.04.2021 -30.04.2021, Baku.
- [7] A.T. Ulgen, Y. Zalaoglu, G. Yildirim and T. Turgay, Effect Of Manganese Addition on Dc Electrical Resistivity Quantities of Polycrystalline $\text{Bi}_{2.1}\text{Sr}_{2.0}\text{Ca}_{1.1}\text{Cu}_{2.0}\text{O}_y$ Superconducting Compounds, 2nd International Baku Conference on Scientific Research, 28.04.2021 -30.04.2021, Baku.
- [8] Zalaoglu, Y., Erdem, U., Bolat, F. C., Akkurt, B., Turgay, T., & Yildirim, G. (2021). Improvement in fundamental electronic properties of Bi-2212 electroceramics with trivalent Bi/Tm substitution: a combined experimental and empirical model approach. *Journal of Materials Science: Materials in Electronics*, 32(14), 19846-19858.
- [9] S.Y. Oh, H.R. Kim, Y.H. Jeong, O.B. Hyun, C.J. Kim, Joining of Bi-2212 high- T_c superconductors and metals using indium solders, Physica C 463–465 (2007) 464–467.
- [10] U. Erdem, Y. Zalaoglu, A.T. Ulgen, T. Turgay, G. Yildirim, Role of trivalent Bi /Tm partial substitution on active operable slip systems in Bi 2212 crystal structure, Cryogenics, 113 (2021) 103212.

[11] H. Yamauchi, M. Karppinen, Application of High-Pressure Techniques: Stabilization and Oxidation-State Control of Novel Superconductive and Related Multi-Layered Copper Oxides, *Supercond. Sci. Technol.* 13 (2000) R33–R52.

[12] M.E. Takayama, High-pressure synthesis of homologous series of high critical temperature (T_c) superconductors, *Chem. Mater.* 10 (1998) 2686–2698.

[13] A.T. Ulgen, G. Yildirim, Gece Kitapligi, Change in Key Mechanical Design Quantities of Bi-2212 Superconducting System with Various Annealing Ambient, pp. 331-349, Ankara, Turkey

[14] Erdem, U. (2021). Homovalent Ho/Bi substitution effect on characteristic properties of Bi-2212 superconducting ceramics. *Journal of Materials Science: Materials in Electronics*, 32(24), 28587-28604.

[15] C. Autret-Lambert, B. Pignon, M. Gervais, I. Monot-Laffez, A. Ruyter, L. Ammor, F. Gervais, J.M. Bassat, R. Decourt, Microstructural and transport properties in substituted $\text{Bi}_2\text{Sr}_2\text{CaCu}_2\text{O}_{8+\delta}$ modulated compounds, *J. Solid State Chem.* 179 (2006) 1698–1706.

[16] N.K. Sartekin, M. Pakdil, G. Yildirim, M. Oz, T. Turgay, Decrement in metastability with Zr nanoparticles inserted in Bi-2223 superconducting system and working principle of hybridization mechanism, *J. Mater. Sci: Mater. El.* 27 (2016) 956–965.

[17] S. Safran, H. Ozturk, F. Bulut, O. Ozturk, Experimental and theoretical approaches for electrical, magnetic, micromechanical, and structural characterization of BSCCO ceramic superconductors, *Ceramics International*, 44 (2018) 11674–11681.

[18] G. Burns, *High-temperature Superconductivity: an Introduction*, Academic Press, New York, (1991).

[19] R. Awad, A.I. Abou-Aly, M.M.H. Abdel Gawad, I. G-Eldeen, The influence of SnO_2 nano-particles addition on the vickers microhardness of (Bi, Pb)-2223 superconducting phase, *J. Supercond. Nov. Magn.* 25 (2012) 739–745.

[20] S.B. Guner, Y. Zalaoglu, T. Turgay, O. Ozyurt, A.T. Ulgen, M. Dogruer, G. Yildirim, A detailed research for determination of Bi/Ga partial substitution effect in Bi-2212 superconducting matrix on crucial characteristic features, *J. Alloy. Compd.* 772, (2019) 388–398.

[21] D. M. Rao, T. Somaiah, V. Haribabu, Y.C. Venudhar, Growth-kinetics of high- T_c and low- T_c phases in $\text{Bi}_{2-x}\text{Pb}_x\text{Ca}_2\text{Sr}_2\text{Cu}_3\text{O}_y$ superconducting compounds, *Cryst. Res. Technol.* 28 (1993) 285–298.

[22] X.L. Lin, S.S. Ma, H.Y. Wang, H. Xu, Characteristics of hopping conductivity in one-dimensional binary disordered system with off-diagonal correlations, *Acta Phys. Sin.* 56 (2007) 2852–2857.

[23] M. Dogruer, G. Yildirim, E. Yucel, C. Terzioglu, Role of diffusion-annealing temperature on the microstructural and superconducting properties of Cu-doped MgB_2 superconductors, *J. Mater. Sci: Mater. El.* 23 (2012) 1965–1970.

Chapter 9

ENERGY LOSS AND CSDA RANGE CALCULATIONS OF A-150 TISSUE EQUIVALENT PLASTIC AND MYLAR FOR ALPHA PARTICLE AND PROTONS

Metin USTA¹

¹ Metin USTA, Assoc. Prof. Dr., Hatay Mustafa Kemal University, Faculty of Arts and Sciences, Physics Department, musta280@gmail.com, ORCID: 0000-0002-7896-397X

1. INTRODUCTION

It has usage areas in many fields such as stopping power and range of matter for charged particles, health physics involving the interaction of radiation with matter, chemistry, space exploration, accelerators and nuclear power plants (Osman & Gümüş, 2022). Especially in radiation treatments, the energy losses of the charged particle per unit length are very important in terms of the ratio of the dose transferred to the environment. Therefore, according to the incoming charged particle, the energy accumulation in the environment, more precisely the stopping power value, should be calculated correctly (Garcia-Molina, Abril, de Vera, Kyriakou, & Emfietzoglou, 2014).

A-150 tissue equivalent plastic and polyethylene tetrapalate (mylar) materials are frequently used to increase the surface dose or to eliminate tissue deficiencies in order to determine the side effects that will occur on living tissues in cases where the dose limits are exceeded in radiotherapy. So, it is noteworthy to determine the energy loss rates and distances traveled by ionizing radiation in the above target materials in radiotherapy (Nichiporov, Moskvina, Fanelli, & Das, 2011).

In this study, collision stopping power and range values of A-150 tissue equivalent plastic and mylar were calculated for proton and alpha particles. For the stopping power calculations, the effective charge approach model based on the Bethe-Bloch (Bethe, 1930) relation and the Romberg method (Romberg, 1955) under the framework of the continuous slowing-down approach (CSDA) for the range were used. Roothaan-Hartree-Fock wavefunctions were chosen for the electronic charge densities of the targets. The stopping power and range values of each element constituting the targets were calculated separately, and the data of the materials were calculated according to the Bragg additivity rule. The results were compared with the ICRU 49 (ICRU, 1992) and SRIM (Ziegler, Biersack, & Ziegler, 2013) values available in the literature.

2. MATERIAL AND METHOD

2.1 Energy loss procedure

As charged particles pass through matter, they lose their energy by interacting with electrons in the ambient. In this case, the atoms in the environment are excited or ionized by the incoming charged particle. Therefore, the rate of energy loss per unit length of charged particles is defined as stopping power.

In this study, the effective charge approximation method, which includes the previously developed Bethe-Bloch theory, was used for the energy loss calculations of protons and alpha particles (Usta, 2021). Accordingly, the differential cross section between the Z_1e nuclear charged particle of mass M_1 and the target atom of mass M_2e with nuclear charge Z_2e can be written in the 1st Born approximation as follows:

$$\frac{d\sigma_{n,m}}{d\Omega} = \frac{M_1^2}{(2\pi)^2 \hbar^4} \frac{k}{k_0} \left| \langle nmk | V | n_0 m_0 k_0 \rangle \right|^2 \quad (1)$$

Where V is the interaction potential and n , m and k are the base vectors for the atomic transitions. Considering the target's weakly bound electrons for the interaction potential between the incoming charged particle and the target, the expression for the collision stopping power can be given as:

$$S_{coll.}(E) = \frac{4\pi e^4}{m_e c^2 \beta^2} Z_1^2 Z_2^* \ln \left(\frac{q_{\max}}{q_{\min}} \right) \quad (2)$$

Here, q_{\max} and q_{\min} are respectively the maximum and minimum momentum transfer from the incident charged particle to the target atom, $\beta = v/c$ the ratio of the speed of the particle to the speed of light, e the fundamental charge and m_e the mass of the electron. For the interaction potential between the charged particle and the target, the potential energy function, which takes into account the distance from which the weakly bound electrons in the target are stripped from the atom, is used (Usta, 2019):

$$V(r_s) = \left[-\pi\rho(r)r^4 \right] / 5 + C \quad (3)$$

Where, $\rho(r)$ is the electron density of the target material, r is the distance from the nucleus, and C is constant.

Clementi-Raimondi (Clementi & Raimondi, 1963) effective nuclear charge coefficients were employed for stopping power calculations and Roothaan-Hartree-Fock (Bunge, Barrientos, & Bunge, 1993) wavefunctions were used for electronic charge density. The mean excitation energies of each element were retrieved from the NIST database (M. J. Berger, 1999). By finding collision stopping power values for each element in Table 1, data for target materials were obtained according to the Bragg additivity rule (Bragg & Kleeman, 1905).

Table 1: The mean excitation energies, density and compositions of target materials.

Materials	Composition						ρ (g / cm ³)	I (eV)
	H	C	N	O	F	Ca		
A-150 ^a	0.10 1327	0.77550 1	0.035 057	0.05231 6	0.0174 22	0.0183 78	1.127	65.0 1
Mylar ^a	0.04 1959	0.62501 7		0.33302 5				

^aICRU 49

2.2 CSDA Range procedure

Assuming that a charged particle that enters any material constantly loses its own energy, the CSDA range of this particle is known as the path between the initial energy and final energy of the particle in the target material:

$$R = \rho_t \int_{E_f}^{E_p} \frac{dE}{S_{coll.}} \quad (4)$$

Here, E_b and E_l are the beginning and last energies of the charged particle, respectively, and ρ_t is the density of the target material.

It is quite difficult or even impossible to make CSDA range calculations analytically using the relation given above. Thus, methods that provide approximate solutions should be used for range calculations. In this study, Romberg method, which is one of the numerical integration methods, was preferred for CSDA range calculations. According to this method, the upper range relation can be expressed as follows:

$$R \approx R(0, 0) = h_1 \left(\frac{1}{S_{coll.}}(E_l) + \frac{1}{S_{coll.}}(E_b) \right) \quad (5)$$

$$R(n, 0) = \frac{1}{2} R(n-1, 0) + h_n \sum_{k=1}^{2^{n-1}} \frac{1}{S_{coll.}}(E_l + (2k-1)h_n) \quad (6)$$

$$R(n, m) = R(n, m-1) + \frac{1}{4^m - 1} (R(n, m-1) - R(n-1, m-1)) \quad (7)$$

Where $h_n = \frac{1}{2^n} (b - a)$, $n \geq m$ ve $m \geq 1$.

3. RESULT AND DISCUSSION

3.1 Energy loss calculations

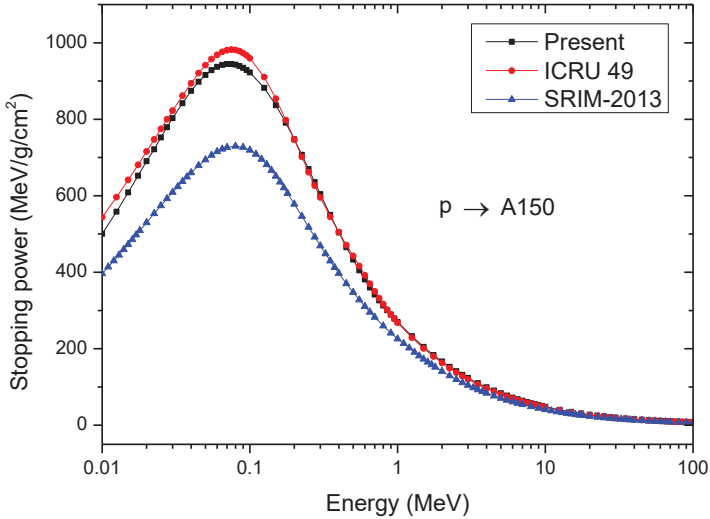


Figure 1: Collision stopping power values of A-150 tissue equivalent plastic for protons.

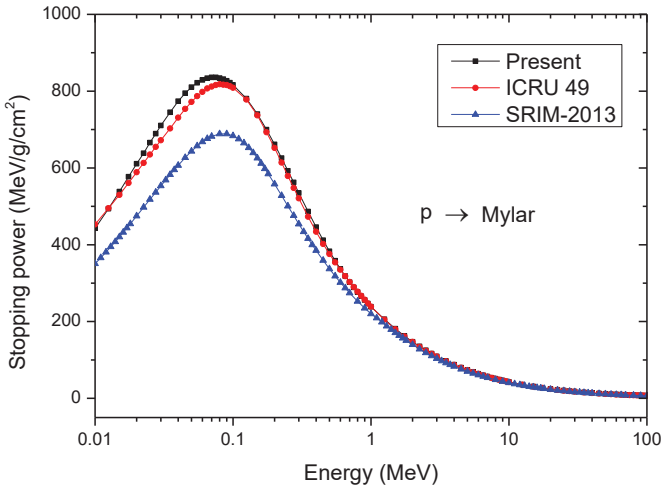


Figure 2: Collision stopping power values of mylar for protons.

Figures 1 and 2 display the collision stopping power data of A-150 and mylar for protons with 10 keV-100 MeV energies, respectively. When both figures are examined in detail, it is understood that the calculated stopping power values are generally compatible with the ICRU and SRIM data. The maximum energy loss per unit length is localized on average in the energy range of 80-90 keV. Differences are noticeable in the data, as expected at energies below the maximum value. The values obtained are closer to ICRU values than SRIM data. Accordingly, there is a tolerance of 5.82% and 4.34% between the values calculated for A150 and mylar and the ICRU data, respectively.

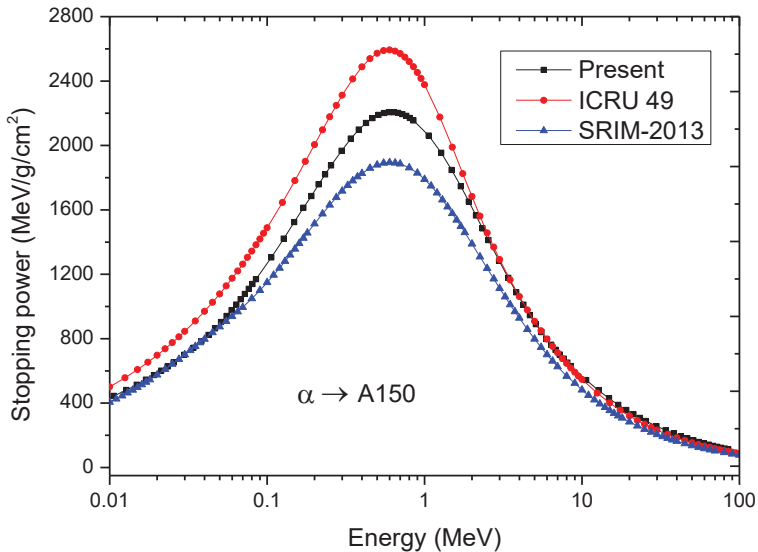


Figure 3: Collision stopping power values of A-150 tissue equivalent plastic for alpha particles.

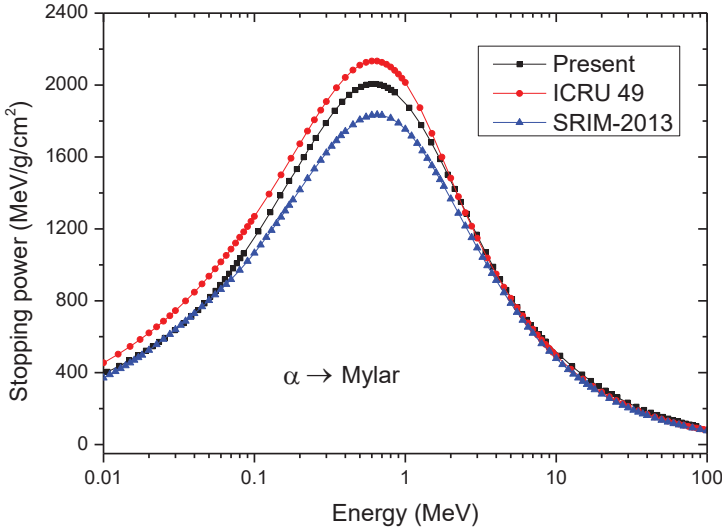


Figure 4: Collision stopping power values of Mylar for alpha particles.

Figures 3 and 4 indicate the collision stopping power values of tissue equivalent plastic and mylar, respectively, for alpha particles with 10 keV-100 MeV energies. Considering the envelope of the curves forming the obtained stopping power data, it is observed that the values are generally compatible with both ICRU and SRIM data. Accordingly, the calculated data is between ICRU and SRIM values, and there are differences in values at approximately 5 MeV and low energies. In both figures, the region with the highest energy loss corresponds to approximately 600-700 keV. Error rates between the presented values and the ICRU data varied between 9.61% and 8.35% for A-150 and mylar, respectively.

3.2 Range calculations

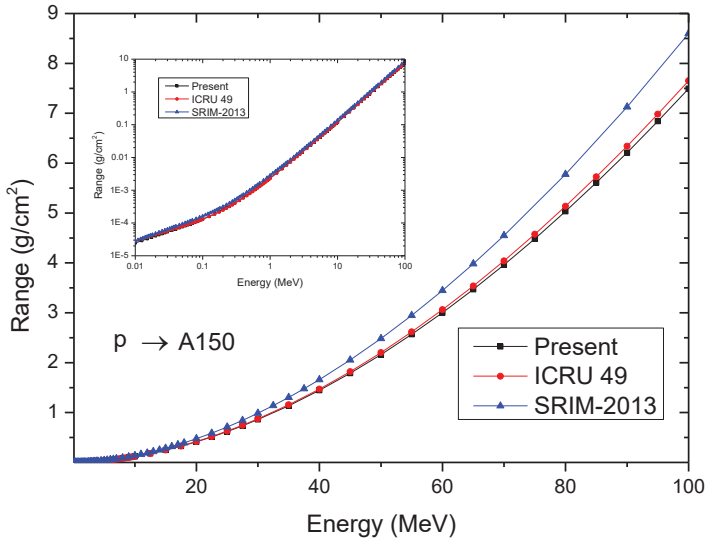


Figure 5: CSDA range values of A-150 tissue equivalent plastic for protons.

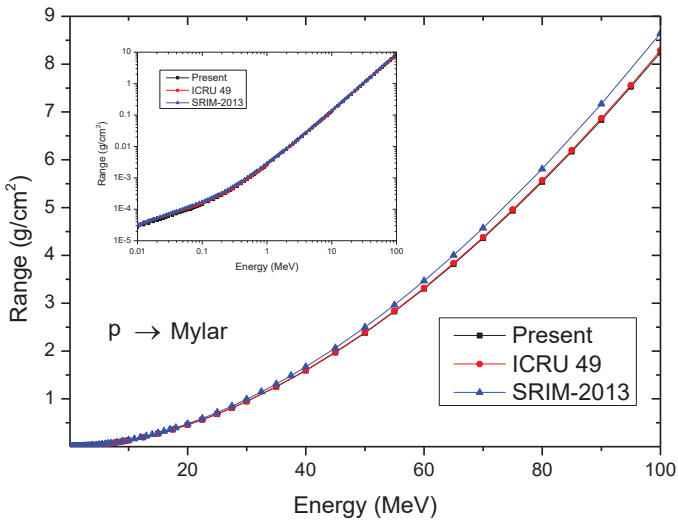


Figure 6: CSDA range values of Mylar for protons.

Figures 5 and 6 demonstrate the CSDA range values of A-150 tissue equivalent plastic and mylar for protons in the 10 keV-100 MeV energy range, respectively. It is clear that as the energy values of the particle coming from the figures increase, the range values also increase, and the calculated data are compatible with the ICRU and SRIM values. There are differences in the data starting from about 40 MeV, and from the figures embedded in the graphs, it is noteworthy that the data overlap even at low energies. The range values obtained for the A-150 and mylar and the ICRU data have error rates of 6.8% and 5.41%, respectively.

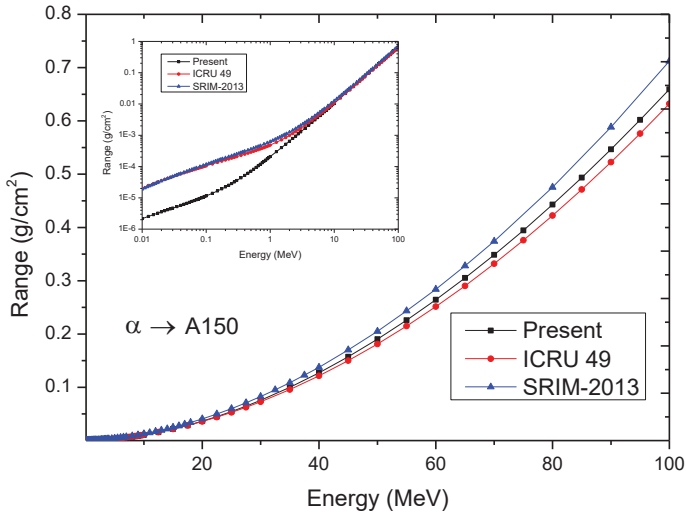


Figure 7: CSDA range values of A-150 tissue equivalent plastic for alpha particles.

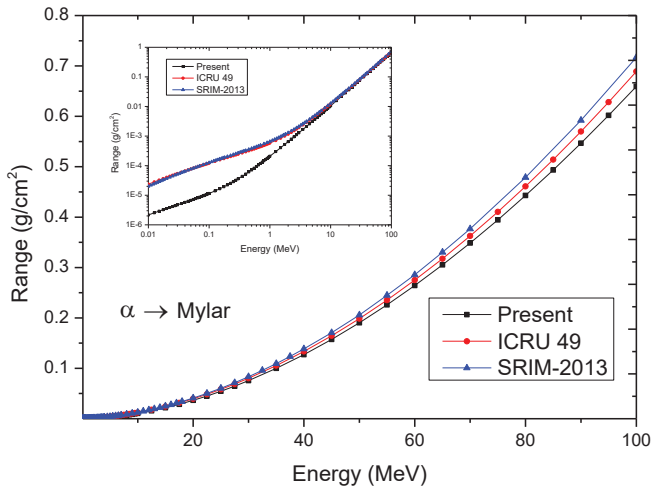


Figure 8: CSDA range values of Mylar for alpha particles.

In Figures 7 and 8, the CSDA ranges of tissue equivalent plastic and mylar are shown, respectively, for alphas with 10 keV-100 MeV energies. There are significant differences between the values both in these figures and in the graphics doped into the figures. The difference in the calculated range values, especially at 5 MeV and low energies, is remarkable. However, as the higher energies are increased, the data gets closer to each other. Therefore, in order to determine this difference, it is appropriate to divide the values into two according to the energy of the alpha particles and evaluate them. So, the error rates between the values obtained at 5 MeV and above energies and the ICRU data are 9.62% and 8.56% for A-150 and mylar, respectively. At energies below 5 MeV, these rates change as 17.09% and 16.47%, respectively.

Roothaan-Hartree-Fock wavefunctions based on Slater type orbitals were made use of calculate the electronic charge densities of the target materials. These functions use self-consistent field to calculate the wavefunctions and energy eigenvalues of electrons in complex systems. Therefore, in this study, these wavefunctions play an important role in determining the oscillator strengths required in collision stopping power calculations with the effective load calculation based on the Bethe-Bloch formula. Because the

integral of the electronic charge density of the target gives the atomic numbers of each material. However, as the number of atoms increases, the computation time becomes considerably longer. Although the Hartree-Fock wavefunctions are mostly used for atomic structure calculations based on fundamental quantum numbers, it is worth noting to do the same calculations using Gaussian type orbitals based on molecular orbital theory, which includes polycentric integration of wavefunctions. Stopping power calculations for protons and alpha particles can also be done using other methods, such as dielectric theory. Error rates can be minimized with this method, especially as we move towards lower energies.

In situations where it is impossible or very difficult to calculate a function analytically, it is convenient to use approximate answers to find a solution to the problem. Increasing the number of intervals in order to reduce the calculated error rates provides a certain level of improvement due to rounding errors. In order to eliminate this situation, Romberg method based on Richardson extrapolation (Richardson & Glazebrook, 1911) was used in this study to increase the accuracy of numerical integration for CSDA range calculations. In this method, the rounding errors that occur with the increase of the number of intervals are reduced by obtaining a more accurate third value by using the results of approximately two numerical integrals. Here, for the function containing the collision stopping power expression, firstly, a random value of h is integrated. Then a separate integral was taken for half of this h value. Finally, using these two integral results in Equation 5, range calculations were made as higher order analytical. However, the error rates in the range values of low-energy alpha particles are over 10%. Better integral estimates can be performed by placing these calculations in a table to reduce this error rate. Each extrapolation will reduce the error to h^4 , h^6 , h^8 ,... respectively. Therefore, by looking at the convergence, an appropriate value for the integral result can be found. In addition, Simpson 3/8 or Gaussian quadrature method from numerical integration methods can be used for the same calculations for comparison purposes.

4. CONCLUSION

It is very important to accurately determine the energy loss and range of the incoming charged particle in the target medium for flux-based dose calculations in radiotherapy. In this study, A-150 tissue equivalent plastic and mylar, which are generally used to investigate the effects of dose limit values in radiation oncology, were chosen as the target material. Proton and alpha particles were preferred for the projectiles, and the stopping power and range values of these particles on the relevant targets were calculated using the effective charge approach and Romberg method. Roothaan-Hartree-Fock wave functions were utilized for the charge density of the target. The stopping power and range values were found to be generally compatible with the literature data. The error rates between the calculated stopping power values and the ICRU data were determined below 10%. Significant differences, close to 20%, were observed in the range values of low-energy alpha particles. It is thought that this study will inspire studies to be carried out especially in the field of radiotherapy in the interaction of radiation with matter.

REFERENCES

- Bethe, H. (1930). Zur Theorie des Durchgangs schneller Korpuskularstrahlen durch Materie. *Annalen der Physik*, 397(3), 325-400. doi:10.1002/andp.19303970303
- Bragg, W. H., & Kleeman, R. (1905). XXXIX. On the α particles of radium, and their loss of range in passing through various atoms and molecules. *Philosophical Magazine Series* 6, 10(57), 318-340. doi:10.1080/14786440509463378
- Bunge, C. F., Barrientos, J. A., & Bunge, A. V. (1993). Roothaan-Hartree-Fock Ground-State Atomic Wave Functions: Slater-Type Orbital Expansions and Expectation Values for $Z = 2-54$. *Atomic Data and Nuclear Data Tables*, 53(1), 113-162. doi:<http://dx.doi.org/10.1006/adnd.1993.1003>
- Clementi, E., & Raimondi, D. L. (1963). Atomic Screening Constants from SCF Functions. *The Journal of Chemical Physics*, 38(11), 2686-2689. doi:10.1063/1.1733573
- Garcia-Molina, R., Abril, I., de Vera, P., Kyriakou, I., & Emfietzoglou, D. (2014). A study of the energy deposition profile of proton beams in materials of hadron therapeutic interest. *Appl Radiat Isot*, 83 Pt B, 109-114. doi:10.1016/j.apradiso.2013.01.006
- ICRU. (1992). *Photon, Electron, Proton, and Neutron Interaction Data for Body Tissues*. Retrieved from Bethesda:
- M. J. Berger, J. S. J., M. A. Zucker. (1999). Estar stopping-power and range tables for electrons Retrieved from <http://physics.nist.gov/Star>. from National Institute of Standards and Technology <http://physics.nist.gov/Star>
- Nichiporov, D., Moskvina, V., Fanelli, L., & Das, I. J. (2011). Range shift and dose perturbation with high-density materials in proton beam therapy. *Nuclear Instruments and Methods in Physics Research Section B: Beam Interactions with Materials and Atoms*, 269(22), 2685-2692. doi:<http://dx.doi.org/10.1016/j.nimb.2011.07.109>
- Osman, H., & Gümüş, H. (2022). Stopping power and CSDA range calculations of electrons and positrons over the 20 eV–1 GeV energy range in some water equivalent polymer gel dosimeters. *Applied Radiation and Isotopes*, 179, 110024. doi:<https://doi.org/10.1016/j.apradiso.2021.110024>
- Richardson, L. F., & Glazebrook, R. T. (1911). IX. The approximate arithmetical solution by finite differences of physical problems involving differential

equations, with an application to the stresses in a masonry dam. *Philosophical Transactions of the Royal Society of London. Series A, Containing Papers of a Mathematical or Physical Character*, 210(459-470), 307-357. doi:doi:10.1098/rsta.1911.0009

Romberg, W. (1955). *Vereinfachte numerische Integration*. Trondheim: F. Bruns Bokhandel.

Usta, M. (2019). The calculation of stopping power and range for radium, thorium and uranium using new electronic potential energy function. *Applied Radiation and Isotopes*, 152, 193-199. doi:https://doi.org/10.1016/j.apradiso.2019.06.005

Usta, M. (2021). Continuous slowing-down approximation ranges of biological materials for 0.05–10 MeV alpha particles by using different approach methods. *Applied Radiation and Isotopes*, 178, 109951. doi:https://doi.org/10.1016/j.apradiso.2021.109951

Ziegler, J. F., Biersack, J. P., & Ziegler, M. D. (2013). *SRIM, the Stopping and Range of Ions in Matter*: SRIM Company.

Chapter 10

ON THE ZAGREB AND RANDIC INDICES OF A GRAPH

*Gül Özkan KIZILIRMAK*¹

*Emre SEVGİ*²

1 Dr. Öğr. Üyesi Gül Özkan Kızıllırmak¹ ORCID: <https://orcid.org/0000-0003-3263-8685>.

2 Araş. Gör. Dr. Emre Sevgi^{1,*} ORCID: <https://orcid.org/0000-0003-2711-9880>. Gazi University, Faculty of Science, Department of Mathematics, Ankara, Turkey.

1. INTRODUCTION

Graphs are used in many fields. Especially studies in the field of chemistry are on topological indexes. A topological index is a numerical parameter of a graph and describes its topology. It describes the molecular shape numerically.

Some authors defined several special graphs and obtain the properties for these graphs (Fox et al., 2014; Arman et al., 2017; Yurttas, 2020; Taşcı, 2022).

Ivan Gutman who is a famous chemist-mathematician have carried the graph structure to the molecule structure. In a molecule structure, he used the atoms as the vertices and the chemical bonds as the edges (Figure 1.1).

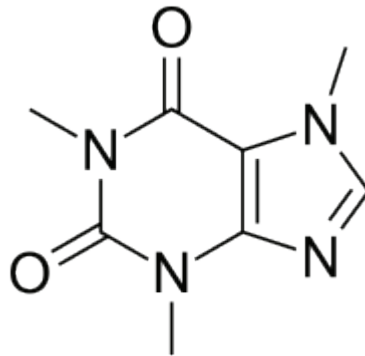


Figure 1.1

There are three types of topological indices: Degree-based, Distance-based, Spectral-based.

The Zagreb indices $M_1(G)$ and $M_2(G)$ were defined by Gutman et al. and examined some properties in (Clark and Gutman, 2002, 2006; Delorme et al., 2002). Some recent results on the Zagreb indices are investigated in (Bey, 2003; Chung, 1997; Hu et al., 2005). Using these indices, some properties of the molecular carbonatom skeleton have been studied and can therefore be seen as descriptors of molecular structure (Aouchiche, 2001).

First Zagreb index of a graph G is defined in (Clark and Gutman, 2002) as

$$M_1(G) = \sum_{u \in V} (d(u))^2.$$

Second Zagreb index of a graph G is defined in (Clark and Gutman, 2002) as

$$M_2(G) = \sum_{u \sim v} d(u)d(v).$$

General Zagreb index of a graph G is defined in (Das et al., 2015) as

$$M_\alpha(G) = \sum_{u \in V} (d(u))^\alpha.$$

Hyper Zagreb index of a graph G is defined in (Shirdel et al., 2013) as

$$HM(G) = \sum_{u \sim v} (d(u) + d(v))^2.$$

The chemist Milan Randić (Randić, 1975) proposed a topological index R , called the "branching index" in 1975. Using this index, he was able to measure the degree of branching of the carbon-atom skeleton of saturated hydrocarbons. After that, in 1998 Bollobás and Erdős (Bollobás and Erdős, 1998) generalized this index and defined the general Randić index.

Randić index of a graph G is defined in (Randić, 1975) as

$$R(G) = \sum_{u \sim v} \frac{1}{\sqrt{d(u)d(v)}}.$$

Reciprocal Randić index of a graph G is defined in (Randić, 1975) as

$$RR(G) = \sum_{u \sim v} \sqrt{d(u)d(v)}.$$

Randić Connectivity index of a graph G is defined in (Bollobás and Erdős, 1998) as

$$R_\alpha(G) = \sum_{u \sim v} (d(u)d(v))^\alpha.$$

Many authors worked on the indices of graphs and the bounds for these indices (Estrada et al., 1998; Furtula, 2009, 2010; Sedlar et al., 2015; Li and Zhao 2004; Gupta et al., 2016; Narumi and Katayama, 1984; Kızıllırmak et al., 2021).

In this study, we firstly mention about the basic graph concepts. Then, we give some bounds for Zagreb and Randic indices for a simple connected graph.

2. PRELIMINARIES AND DEFINITIONS

2.1. Basic Graph Concepts

The graph is called the binary structure $= (V, E)$, which consists of a finite set of non-empty $V = \{1, 2, \dots, n\}$ points whose elements are called points, and a finite set of E edges whose elements are called edges, and it is denoted by G for short. Here it is defined as $E = \{\{i, j\} : i, j \in V\}$. Also, for each $i, j \in V$, the elements of E corresponding to the i and j points are denoted as e_{ij} or ij for short. If there is at least one edge between any i and j points of G , it is said to be adjacent to i and j points and is denoted by $i \sim j$. In addition, if any of the e_i and e_j sides of a graph have a common point, these two sides are called adjacent sides and are denoted as $e_i \sim e_j$.

The number of sides connected to any point i of the graph $G = (V, E)$ is called the degree of i and is denoted by $d_G(i)$ or d_i for short. Also, the number $d(G) = \frac{1}{|V|} \sum_{i \in V} d_i$ is called the mean degree of G . Here $|V|$ is the cardinality of V , the number of elements of the set of points. The edge with the same starting and ending point is called a loop. If there is more than one edge between any two points of the graph, these edges are called folded edges or multiple edges. A point with a degree of 0 is called an isolated point, a point with a degree of 1 is called a pendant point or end point (Figure 2.1.1).

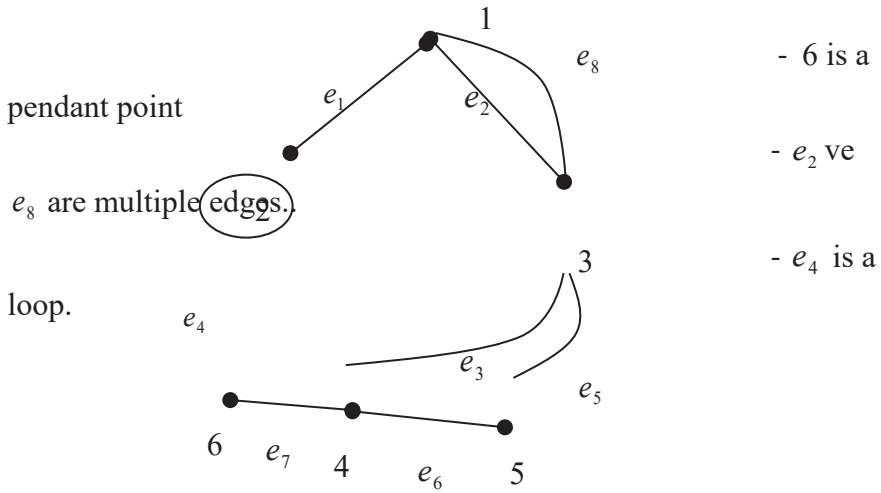


Figure 2.1.1. A Graph including loop, multiple edges and pendant point

There are seven bridges over the river Pregel, which passes through the city of Königsberg and divides the city into four parts, and connects these regions (Figure 2.1.2). The problem posed is as follows: Is it possible to take a walk on the condition of passing all bridges once and only once?

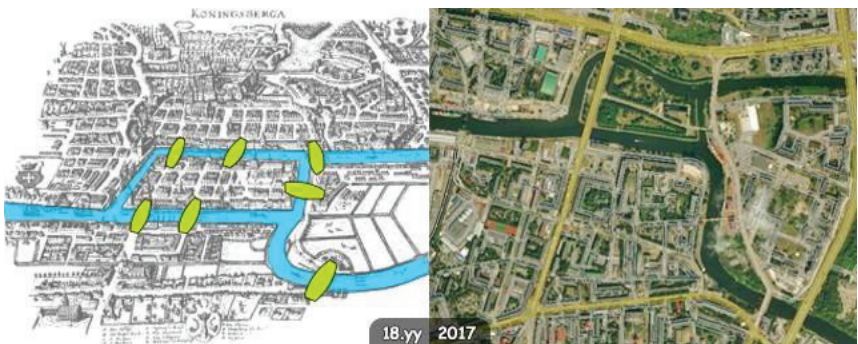


Figure 2.1.2. Königsberg

In 1736, (Euler, 1736) Euler proved that such a tour was not possible with his studies and published the article "Solutio problematis ad geometriam situs pertinentis". (Figure 2.1.3) This problem, which was initially posed as a pastime, heralded the discovery of topology and the first theorem of graph theory, a completely new branch of mathematics, with these researches of Leonhard Euler.

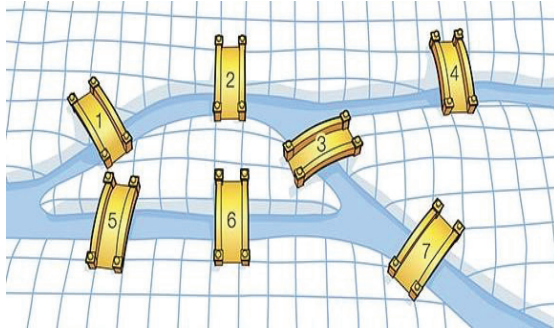


Figure 2.1.3 Seven Bridge Problem

A graph that has at most one edge between any two points and does not contain a loop is called a simple graph. A graph that contains more than one edge, that is, folded edge, or that contains at least one loop between any two points is called a multigraph. If there is an edge between any two points of a simple graph, this graph is called a complete graph and a complete graph with n points is denoted by K_n . The path graph is a tree with two vertices have degree 1, and the other vertices have degree 2 and denoted by P_n . A path graph is therefore a graph that can be drawn so that all of its vertices and edges lie on a single straight line.

A finite series of connected points and edges of a graph is called walking and is denoted by W . Walking where each edge and point is used at most once is called a path and is denoted by P . A graph with a path between any two points is called a connected graph.

3. BOUNDS FOR THE INDICES OF GRAPHS

In this section, we assume that G is a simple connected graph.

3.1. Bounds for the Zagreb Indices of Graphs

Lemma For the graph G with n vertices, we have

$$n\delta^\alpha \leq M_\alpha(G) \leq n\Delta^\alpha,$$

where δ is the minimum degree and Δ is the maximum degree of vertices in G .

Proof. Since δ is the minimum degree and Δ is the maximum degree of vertices in G , by assuming all vertices of G with maximum degree and minimum degree we get the lower and upper bound for the general Zagreb index of G , respectively. Thus, we obtain

$$n\delta^\alpha \leq M_\alpha(G) \leq n\Delta^\alpha.$$

Theorem For the graph G with n vertices, we have

$$r\delta^\alpha + (n - r)(\delta + 1)^\alpha \leq M_\alpha(G) \leq k\Delta^\alpha + (n - k)(\Delta - 1)^\alpha$$

where r is the number of the vertices with minimum degree and k is the number of the vertices with maximum degree in G .

Proof. If we take the r vertices with minimum degree δ and $n - r$ vertices with degree $\delta + 1$, we get the lower bound as

$$r\delta^\alpha + (n - r)(\delta + 1)^\alpha \leq M_\alpha(G).$$

If we take the k vertices with maximum degree Δ and $n - k$ vertices with degree $\Delta - 1$, we get the upper bound as

$$k\Delta^\alpha + (n - k)(\Delta - 1)^\alpha.$$

Corollary For the graph G with n vertices, we have

$$r + (n - r)(2)^\alpha \leq M_\alpha(G) \leq n(n - 1)^\alpha,$$

where r is the number of the vertices with minimum degree in G .

Proof. If we take the r vertices with degree 1 and $n - r$ vertices with degree 2, we get the lower bound as

$$r + (n - r)(2)^\alpha \leq M_\alpha(G).$$

If we take all vertices with maximum degree $n - 1$, we have the upper bound as

$$M_\alpha(G) \leq n(n - 1)^\alpha.$$

Lemma For the graph G with n vertices, we have

$$n\delta^2 \leq M_1(G) \leq n\Delta^2,$$

where δ is the minimum degree and Δ is the maximum degree of vertices in G .

Proof. Since δ is the minimum degree and Δ is the maximum degree of vertices in G , by assuming all vertices of G with maximum degree and minimum degree we get the upper and lower bound for the first Zagreb index of G , respectively. Thus, we obtain

$$n\delta^2 \leq M_1(G) \leq n\Delta^2.$$

Theorem For the graph G with n vertices, we have

$$r\delta^2 + (n - r)(\delta + 1)^2 \leq M_1(G) \leq k\Delta^2 + (n - k)(\Delta - 1)^2,$$

where r is the number of the vertices with minimum degree and k is the number of the vertices with maximum degree in G .

Proof. If we take the r vertices with minimum degree δ and $n - r$ vertices with degree $\delta + 1$, we get the lower bound as

$$r\delta^2 + (n - r)(\delta + 1)^2 \leq M_1(G).$$

If we take the k vertices with maximum degree Δ and $n - k$ vertices with degree $\Delta - 1$, we get the upper bound as

$$M_1(G) \leq k\Delta^2 + (n - k)(\Delta - 1)^2.$$

Corollary For the graph G with n vertices, we have

$$4n - 6 \leq M_1(G) \leq n(n - 1)^2,$$

where r is the number of the vertices with minimum degree in G .

Proof. The best graph to use when bounding the index from the lower is the path graph. Since there are $n - 1$ edges in P_n and two of these edges includes endpoints, the graph has 2 edges such that one of the vertices of these edges has 1 degree and the other has 2 degree. Also, the vertices of the remaining $n - 3$ edges are

with degree 2. Hence, we obtain the lower bound as $2 \cdot 1^2 + (n - 2)2^2 = 4n - 6 \leq M_1(G)$.

If we take all vertices with maximum degree $n - 1$, we have the upper bound as

$$M_1(G) \leq n(n - 1)^2.$$

Lemma For the graph G with m edges, we have

$$m\delta^2 \leq M_2(G) \leq m\Delta^2,$$

where δ is the minimum degree and Δ is the maximum degree of vertices in G .

Proof. Since δ is the minimum degree and Δ is the maximum degree of vertices in G , by assuming all vertices of G with maximum degree and minimum degree we get the lower and upper bound for the second Zagreb index of G , respectively. Thus, we obtain

$$m\delta^2 \leq M_2(G) \leq m\Delta^2.$$

Theorem For the graph G with m edges, we have

$$r\delta^2 + (m - r)\delta(\delta + 1) \leq M_2(G) \leq k\Delta^2 + (m - k)\Delta(\Delta - 1)$$

where r is the number of the edges which have the vertices with minimum degree and k is the number of the edges which have the vertices with maximum degree in G .

Proof. If we take the r edges which have the vertices with minimum degree δ and $m - r$ edges which have the vertices with degree δ and $\delta + 1$, we get the lower bound as

$$r\delta^2 + (m - r)\delta(\delta + 1) \leq M_2(G).$$

Also, if we take the k edges which have the vertices with maximum degree Δ and $m - k$ edges which have the vertices with degree Δ and $\Delta - 1$, we get the upper bound as

$$M_2(G) \leq k\Delta^2 + (m - k)\Delta(\Delta - 1).$$

Corollary For the graph G with n vertices and m edges, we have

$$4n - 8 \leq M_2(G) \leq k(n - 1)^2 + (m - k)(n - 1)(n - 2),$$

where k is the number of the vertices with maximum degree in G .

Proof. The best graph to use when bounding the index from the lower is the path graph. Since there are $n - 1$ edges in P_n and two of these edges includes endpoints, the graph has 2 edges such that one of the vertices of these edges has 1 degree and the other has 2 degree. Also, the vertices of the remaining $n - 3$ edges are with degree 2. Hence, we obtain the lower bound as

$$\begin{aligned} 2(1.2) + (n - 3)(2.2) &\leq M_2(G) \\ \Rightarrow 4n - 8 &\leq M_2(G). \end{aligned}$$

If we take k edges which have the vertices with maximum degree $n - 1$ and $m - k$ edges which have the vertices with maximum degree $n - 1$ and $n - 2$ we have the upper bound as

$$M_2(G) \leq k(n - 1)^2 + (m - k)(n - 1)(n - 2).$$

Lemma For the graph G with n vertices, we have

$$4m\delta^2 \leq HM(G) \leq 4m\Delta^2,$$

where δ is the minimum degree and Δ is the maximum degree of vertices in G .

Proof. Since δ is the minimum degree and Δ is the maximum degree of vertices in G , by assuming all vertices of G with maximum degree and minimum degree we get,

$$HM(G) \leq m(2\Delta)^2$$

and

$$m(2\delta)^2 \leq HM(G),$$

respectively. Thus, we obtain the bounds for the hyper Zagreb index of G as

$$4m\delta^2 \leq HM(G) \leq 4m\Delta^2.$$

Theorem For the graph G with n vertices, we have

$$\begin{aligned} 4r\delta^2 + (m - r)(2\delta + 1)^2 &\leq HM(G) \\ &\leq 4k\Delta^2 + (m - k)(2\Delta - 1)^2, \end{aligned}$$

where r is the number of the edges which have the vertices with minimum degree and k is the number of the edges which have the vertices with maximum degree in G .

Proof. If we take the r edges which have the vertices with minimum degree δ and $m - r$ edges which have the vertices with degree δ and $\delta + 1$, we get the lower bound as

$$\begin{aligned} r(\delta + \delta)^2 + (m - r)(\delta + \delta + 1)^2 &\leq HM(G) \\ \Rightarrow 4r\delta^2 + (m - r)(2\delta + 1)^2 &\leq HM(G) \end{aligned}$$

Also, if we take the k edges which have the vertices with maximum degree Δ and $m - k$ edges which have the vertices with degree Δ and $\Delta - 1$, we get the upper bound as

$$\begin{aligned} HM(G) &\leq k(\Delta + \Delta)^2 + (m - k)(\Delta + \Delta - 1)^2 \\ \Rightarrow HM(G) &\leq 4k\Delta^2 + (m - k)(2\Delta - 1)^2. \end{aligned}$$

Corollary For the graph G with n vertices and m edges, we have

$$16n - 30 \leq HM(G) \leq 4k(n - 1)^2 + (m - k)(2n - 3)^2,$$

where k is the number of the edges which have the vertices with maximum degree in G .

Proof. The best graph to use when bounding the index from the lower is the path graph. Since there are $n - 1$ edges in P_n and two of these edges includes endpoints, the graph has 2 edges such that one of the vertices of these edges has 1 degree and the other has 2 degree. Also, the vertices of the remaining $n - 3$ edges are with degree 2. Hence, we obtain the lower bound as

$$\begin{aligned} 2(1 + 2)^2 + (n - 3)(2 + 2)^2 &\leq HM(G). \\ \Rightarrow 16n - 30 &\leq HM(G). \end{aligned}$$

If we take k edges which have the vertices with maximum degree $n - 1$ and $m - k$ edges which have the vertices with maximum degree $n - 1$ and $n - 2$ we have the upper bound as

$$\begin{aligned} HM(G) &\leq k(2(n - 1))^2 + (m - k)(2n - 3)^2 \\ \Rightarrow HM(G) &\leq 4k(n - 1)^2 + (m - k)(2n - 3)^2. \end{aligned}$$

3.1. Bounds for the Randic Indices of Graphs

Lemma For the graph G with m edges, we have

$$\frac{m}{\Delta} \leq R(G) \leq \frac{m}{\delta}$$

where δ is the minimum degree and Δ is the maximum degree of vertices in G .

Proof. Since δ is the minimum degree and Δ is the maximum degree of vertices in G , by assuming all vertices of G with maximum degree and minimum degree we get the upper and lower bounds for the Randic index of G , respectively. Thus, we obtain

$$\frac{m}{\Delta} \leq R(G) \leq \frac{m}{\delta}.$$

Theorem For the graph G with n vertices, we have

$$\frac{k}{\Delta} + \frac{m-k}{\sqrt{\Delta(\Delta-1)}} \leq R(G) \leq \frac{r}{\delta} + \frac{m-r}{\sqrt{\delta(\delta+1)}}$$

where r is the number of the edges which have the vertices with minimum degree and k is the number of the edges which have the vertices with maximum degree in G .

Proof. If we take the r edges which have the vertices with minimum degree δ and $m-r$ edges which have the vertices with degree δ and $\delta+1$, we get the upper bound as

$$R(G) \leq \frac{r}{\delta} + \frac{m-r}{\sqrt{\delta(\delta+1)}}$$

Also, if we take the k edges which have the vertices with maximum degree Δ and $m-k$ edges which have the vertices with degree Δ and $\Delta-1$, we get the lower bound as

$$\frac{k}{\Delta} + \frac{m-k}{\sqrt{\Delta(\Delta-1)}} \leq R(G).$$

Corollary For the graph G with n vertices and m edges, we have

$$\frac{k}{n-1} + \frac{m-k}{\sqrt{(n-1)(n-2)}} \leq R(G) \leq \frac{2}{\sqrt{2}} + \frac{n-3}{2},$$

where k is the number of the edges which have the vertices with maximum degree in G .

Proof. The best graph to use when bounding the index from the lower is the path graph. Since there are $n - 1$ edges in P_n and two of these edges includes endpoints, the graph has 2 edges such that one of the vertices of these edges has 1 degree and the other has 2 degree. Also, the vertices of the remaining $n - 3$ edges are with degree 2. Hence, we obtain the upper bound as

$$R(G) \leq \frac{2}{\sqrt{2}} + \frac{n - 3}{2}.$$

If we take k edges which have the vertices with maximum degree $n - 1$ and $m - k$ edges which have the vertices with maximum degree $n - 1$ and $n - 2$ we have the lower bound as

$$\frac{k}{n - 1} + \frac{m - k}{\sqrt{(n - 1)(n - 2)}} \leq R(G).$$

Lemma For the graph G with m edges, we have

$$m\delta \leq RR(G) \leq m\Delta,$$

where δ is the minimum degree and Δ is the maximum degree of vertices in G .

Proof. Since δ is the minimum degree and Δ is the maximum degree of vertices in G , by assuming all vertices of G with maximum degree and minimum degree we get the lower and upper bounds for the reciprocal Randic index of G , respectively. Thus, we obtain

$$m\delta \leq RR(G) \leq m\Delta.$$

Theorem For the graph G with n vertices and m edges, we have

$$r\delta + (m - r)\sqrt{\delta(\delta + 1)} \leq RR(G) \leq k\Delta + (m - k)\sqrt{\Delta(\Delta - 1)},$$

where r is the number of the edges which have the vertices with minimum degree and k is the number of the edges which have the vertices with maximum degree in G .

Proof. If we take the r edges which have the vertices with minimum degree δ and $m - r$ edges which have the vertices with degree δ and $\delta + 1$, we get the lower bound as

$$r\delta + (m - r)\sqrt{\delta(\delta + 1)} \leq RR(G).$$

Also, if we take the k edges which have the vertices with maximum degree Δ and $m - k$ edges which have the vertices with degree Δ and $\Delta - 1$, we get the upper bound as

$$RR(G) \leq k\Delta + (m - k)\sqrt{\Delta(\Delta - 1)}.$$

Corollary For the graph G with n vertices and m edges, we have

$$\begin{aligned} 2\sqrt{2} + 2(n - 3) &\leq RR(G) \\ &\leq k(n - 1) + (m - k)\sqrt{(n - 1)(n - 2)}, \end{aligned}$$

where k is the number of the edges which have the vertices with maximum degree in G .

Proof. The best graph to use when bounding the index from the lower is the path graph. Since there are $n - 1$ edges in P_n and two of these edges includes endpoints, the graph has 2 edges such that one of the vertices of these edges has 1 degree and the other has 2 degree. Also, the vertices of the remaining $n - 3$ edges are with degree 2. Hence, we obtain the lower bound as

$$2\sqrt{2} + 2(n - 3) \leq RR(G).$$

If we take k edges which have the vertices with maximum degree $n - 1$ and $m - k$ edges which have the vertices with maximum degree $n - 1$ and $n - 2$ we have the upper bound as

$$RR(G) \leq k(n - 1) + (m - k)\sqrt{(n - 1)(n - 2)}.$$

Lemma For the graph G with m edges, we have

$$m\delta^{2\alpha} \leq R_\alpha(G) \leq m\Delta^{2\alpha},$$

where δ is the minimum degree and Δ is the maximum degree of vertices in G .

Proof. Since δ is the minimum degree and Δ is the maximum degree of vertices in G , by assuming all vertices of G with maximum degree and minimum degree we get the lower and upper bounds for the Randic connectivity index of G , respectively. Thus, we obtain

$$m\delta^{2\alpha} \leq R_\alpha(G) \leq m\Delta^{2\alpha}.$$

Theorem For the graph G with n vertices and m edges, we have

$$\begin{aligned} r\delta^{2\alpha} + (m - r)[\delta(\delta + 1)]^\alpha &\leq R_\alpha(G) \\ &\leq k\Delta^{2\alpha} + (m - k)[\Delta(\Delta - 1)]^\alpha, \end{aligned}$$

where r is the number of the edges which have the vertices with minimum degree and k is the number of the edges which have the vertices with maximum degree in G .

Proof. If we take the r edges which have the vertices with minimum degree δ and $m - r$ edges which have the vertices with degree δ and $\delta + 1$, we get the lower bound as

$$r\delta^{2\alpha} + (m - r)[\delta(\delta + 1)]^\alpha \leq R_\alpha(G).$$

Also, if we take the k edges which have the vertices with maximum degree Δ and $m - k$ edges which have the vertices with degree Δ and $\Delta - 1$, we get the upper bound as

$$R_\alpha(G) \leq k\Delta^{2\alpha} + (m - k)[\Delta(\Delta - 1)]^\alpha.$$

Corollary For the graph G with n vertices and m edges, we have

$$\begin{aligned} 2^{\alpha+1} + (n - 3)4^\alpha &\leq R_\alpha(G) \\ &\leq k(n - 1)^{2\alpha} + (m - k)[(n - 1)(n - 2)]^\alpha, \end{aligned}$$

where k is the number of the edges which have the vertices with maximum degree in G .

Proof. The best graph to use when bounding the index from the lower is the path graph. Since there are $n - 1$ edges in P_n and two of these edges includes endpoints, the graph has 2 edges such that one of the vertices of these edges has 1 degree and the other has 2 degree. Also, the vertices of the remaining $n - 3$ edges are with degree 2. Hence, we obtain the lower bound as

$$\begin{aligned} 2(1.2)^\alpha + (n - 3)(2.2)^\alpha &\leq R_\alpha(G) \\ \Rightarrow 2^{\alpha+1} + (n - 3)4^\alpha &\leq R_\alpha(G) \end{aligned}$$

If we take k edges which have the vertices with maximum degree $n - 1$ and $m - k$ edges which have the vertices with maximum degree $n - 1$ and $n - 2$ we have the upper bound as

$$R_\alpha(G) \leq k(n - 1)^{2\alpha} + (m - k)[(n - 1)(n - 2)]^\alpha.$$

REFERENCES

- Euler, L. (1736). Solutio problematis ad geometriam situs pertinentis. *Comment. Acad. Sci. U. Petrop*, 8, 128–40.
- Clark, L. and Gutman, I. (2006). The exponent in the general Randić index. *Journal of Mathematical Chemistry*, 43, 32–44.
- Clark, L.H., Gutman, I., Lepovic, M. and Vidovic, D. (2002). Exponent-dependent properties of the connectivity index. *Indian J. Chem.*, 41, 457–461.
- Delorme, C., Favaron, O. and Rautenbach, D. (2002). On the Randić index. *Discrete Math.*, 257 29–38.
- Bey, C. (2003). An upper bound on the sum of squares of degrees in a hypergraph. *Disc. Math.*, 269, 259–263.
- Chung, F.R.K. (1997). Spectral Graph Theory. American Math. Soc., Providence.
- Hu, Y., Li, X., Shi, Y., Xu, T. and Gutman, I. (2005). On molecular graphs with smallest and greatest zeroth order general Randić index. *MATCH Commun. Math. Comput. Chem.*, 54, 425–434.
- Aouchiche, M., Caporossi, G. and Hansen, P. (2001). Variable neighborhood search for extremal graphs. *Variations on Gradditi 105, Congr. Numer.*, 148, 129–144.
- Randić, M. (1975). On characterization of molecular branching, *Journal of American Chemistry Society*, 97, 6609–6615.
- Bollobas, B. and Erdos, P. (1998). Graphs of extremal weights. *Ars Combinatoria*. 50, 225–233.
- Das, K., Xu, K. and Nam, J. (2015). Zagreb indices of graphs. *Frontiers of Mathematics in China*, 10(3), 567–582.
- Shirdel, G.H., Rezapour, H. and Sayadi, A.M. (2013). The Hyper Zagreb Index of Graph Operations, *Iranian J. Math. Chem.*, 4, 213–220.
- Fox, K., Kinnersley, W. B., McDonald, D., Orlow, N. and Puleo, G. J. (2014). Spanning paths in Fibonacci-Sum graphs, *Fibonacci Quart.*, 52, 46–49.
- Arman, A., Gunderson, D.S. and Li, P.C. Properties of the Fibonacci-sum graph, arXiv:1710.10303v1[math.CO] 27 Oct 2017 <https://arxiv.org/abs/1710.10303>.
- Yurttas Gunes, A., Delen, S., Demirci, M., Cevik, A.S. and Cangul, I.N. (2020). Fibonacci Graphs, Symmetry, 12(1383).

- Taşcı, D., Özkan Kızılırmak, G., Sevgi, E. and Büyükköse, Ş., The Bounds for the Largest Eigenvalues of Fibonacci-sum and Lucas-sum Graphs, *TWMS J. App. Eng. Math*, to be published in 2022.
- Estrada, E., Torres, L., Rodriguez, L., and Gutman, I. (1998). An atom-bond connectivity index: Modelling the enthalphy of formation of alkanes, *Indian J. Chem.* 37A, pp. 849-855.
- Furtula, B., Graovac, A. and Vukicevic, D. (2010). Augmented Zagreb index, *J. Math. Chem.*, 48, 370--380,.
- Vukicevic, D. and Furtula, B. (2009). Topological index based on the ratios of geometrical and arithmetical means of end-vertex degrees of edges, *Journal of Mathematical Chemistry*, 46, 1369-1376.
- Sedlar, J., Stevanovic, D. and Vasilyev, A. (2015). On the inverse sum indeg index, *Discrete Applied Mathematics*, 184, 202-212 .
- Li, X. and Zhao, H. (2004). Trees with the First Three Smallest and Largest Generalized Topological Indices. *MATCH Commun. Math. Comput. Chem.*, 50, 57-62.
- Gupta, C. K., Loksha, V., Shwetha, S. B. and Ranjini, P.S. (2016). On the Symmetric Division deg Index of Graph, *Southeast Asian Bulletin of Mathematics*, 40, 1, 59-80.
- Narumi, H. and Katayama, M. (1984). Simple topological index. a newly devised index characterizing the topological nature of structural isomers of saturated hydrocarbons, *Mem. Fac. Engin. Hokkaido Univ.*, 16, 209--214.
- Özkan Kızılırmak, G., Sevgi, E. and Büyükköse, Ş. (2021), Bir Grafın GCD Spektral Yarıçapı ve GCD Enerjisi İçin Alt ve Üst Sınırlar. *GÜFFD*, 2(2), 14-18.
- Taşcı, D., Özkan Kızılırmak, G., Büyükköse, Ş. and Sevgi, E. (2020). Properties of Lucas-sum graph. *Journal of Science and Arts*, 20 (2), 313-316.

Chapter 11

VERTICES OF SUBORBITAL GRAPH $F_{u,N}$ AND SEQUENCE d_n DEFINED IN HECKE GROUP

*İbrahim GÖKCAN*¹

*Ali Hikmet DEĞER*²

¹ Dr., Artvin Çoruh University, ORCID:0000-0002-6933-8494, gokcan@artvin.edu.tr

² Doç. Dr., Karadeniz Technical University, ORCID:0000-0003-0764-715x, ahikmetd@ktu.edu.tr

INTRODUCTION

In this section, the main issues related to the essence of the study were included. By examining the Modular group in detail, the issue of obtaining the vertices found under the act of the Modular group with in continued fractions and matrices is discussed. The connection of Hecke group and Hecke group $H(\sqrt{q})$ with Modular group was examined. Vertices of suborbital graph $F_{u,N}$ on minimal length path in the Hyperbolic plane $\mathbb{H} = \{z \in \mathbb{C}: \text{Im}(z) > 0\}$ were demonstrated with Fibonacci numbers under given conditions by Değer (2017). In addition to this, Gökcan (2021) showed that vertices of suborbital graph $F_{u,N}$ in minimal length path were demonstrated with Lucas numbers under same conditions.

Yılmaz Özgür (2002) examined the matrix $M^n = \begin{pmatrix} 0 & -1 \\ 1 & \sqrt{q} \end{pmatrix}^n$. Also, the identities $d_{2n} = L_{2n+1}$ and $d_{2n+1} = \sqrt{5}F_{2n+2}$ are obtained specifically for $q = 5$ by Yılmaz Özgür (2002), where initial conditions are $d_0 = 1, d_1 = \sqrt{q}$ and recurrence relation is $d_n = \sqrt{q}d_{n-1} - d_{n-2}, n \geq 2$.

This paper attempts to show that values of vertices of suborbital graph $F_{u,N}$ demonstrated with sequences d_n , unlike Fibonacci and Lucas numbers. In the pages that follow, obtaining of matrix M^n with the help of Fibonacci and Lucas numbers be argued. At the same time, this study reports on a study which exploring some identities related with d_n , Fibonacci and Lucas number sequences.

Fibonacci and Lucas Number Sequences

In the Middle Ages, the number sequence 1,1,2,3,5,8,13,... carried to Europe by Leonardo Fibonacci with his work Liber Abaci. The perfect working of nature, rations of mathematical number and related concepts were found to be related to the Fibonacci number sequence and ratios. Graph theory is one of the areas where Fibonacci and Lucas number sequences take place. For Graph

theory and with related studies, Ruohonen (2008) can be examined. In addition to, Fibonacci and Lucas number sequences and related operations are studied extensively in mathematics and are associated with many disciplines of mathematics. For related studies, Koshy (2001), Alfred (1965) and Bicknell vd., (1973) can be reviewed. Similar concepts were introduced in the 1800s for the Lucas number sequences 1,3,4,7,11,... and their ratios. The recurrence relation $F_n = F_{n-1} + F_{n-2}$ is defined, where F_n is the n^{th} term of Fibonacci number sequence. In other words, the sum of two consecutive terms gives the next term. For the Lucas number sequence, the recurrence relation $L_n = L_{n-1} + L_{n-2}$ is defined as in the Fibonacci number sequence, where L_n is the n^{th} term of Lucas number sequence. Fibonacci and Lucas number sequences are studied extensively in the literature. Obtaining identities related to generalized Fibonacci and Lucas number sequences with the help of the n^{th} powers of some matrices formed in the elements of Fibonacci and Lucas number sequences can be given as an example. For more detailed information, (Koshy, 2001) can be examined.

Graph Theory

In this section, we will give some basic definitions and concepts related to Graph theory. Recently, researchers have shown an increased interest in Graph Theory. So, a considerable literature has grown up around the theme of Graph theory. With the discovery of non-Euclidean geometries, Graph theory began to be studied in this field. In this study, we will examine graph theory defined on Hyperbolic geometry, non-Euclidean and its elements.

Definition 1. A simple graph is a graph that consists of vertices and the edges connecting these vertices and does not give any geometrical information.

Definiton 2. The element located at both ends of an edge is called a vertex.

Definition 3. The element between two vertices in a graph is called an edge.

Definition 4. Graphs whose edges contain direction information are called directional graphs. All or none of the edges in a graph have direction information.

Definition 5. Since the elements of the Modular group Γ send Hyperbolic lines to Hyperbolic lines, the edges of the graph $F_{u,N}$ for proper visualization are half-lines perpendicular to the real axis in the upper half plane of $\mathbb{H} = \{z \in \mathbb{C} : \text{Im}(z) > 0\}$ and half-lines with the center on \mathbb{R} are shown as hyperbolic geodesics (Anderson, 2005).

Definition 6. The path $v_0 \rightarrow v_1 \rightarrow \dots \rightarrow v_m$ in the graph $F_{u,N}$ to have minimal length, $v_i \leftrightarrow v_j$ where $i < j - 1$, $i \in \{0, 1, \dots, m - 2\}$, $j \in \{2, 3, \dots, m\}$ and vertex v_{i+1} should be the farthest vertex that connects to vertex v_i (Değer, 2017).

For more information about definitions related with Graph theory, Rouhonen (2008) can be examined.

Modular Group

Definition 7. Let $* X \times X \rightarrow X$ transform be defined, with X being different from the empty set. If this transformation is a binary operation in X , then $(X, *)$ is an algebraic structure (Taşcı, 2007).

Definition 8. Let $* X \times X \rightarrow X$ binary operation be defined, with X being different from the empty set. The algebraic structure $(X, *)$ is a group if this algebraic structure satisfies the closure, union, unit, and inverse element properties (Taşcı, 2007).

Definition 9. If X has finite elements, $(X, *)$ is a finite group and the number of elements of the group is the order of the group (Çallıalp, 2001).

Definition 10. For the $(X, *)$ group, if $X = \{a^n : n \in \mathbb{N}\}$ is provided, it is called a cyclic group and $a \in \mathbb{N}$ is a generator of this group (Taşcı, 2007).

For $n \geq 1$, $n \times n$ type invertible matrices form a group according to the multiplication operation defined in the matrices. This group is specifically called the n -order linear group on \mathbb{R} and is denoted by $GL(n, \mathbb{R})$ (Asar, 2009).

If $n = 2$, the set of matrices with a determinant of 1 is denoted by $SL(2, \mathbb{R})$.

For $a, b, c, d \in \mathbb{Z}$, Möbius transform

$$\begin{pmatrix} a & b \\ c & d \end{pmatrix} : z \rightarrow \frac{az+b}{cz+d} \tag{1}$$

is defined in \mathbb{H} . However, Möbius transforms can be represented by matrices of the 2×2 type. The matrix fg corresponds to the

$$(f \circ g)(z) \tag{2}$$

composite operation, where $f(z) = -\frac{1}{z}$ and $g(z) = z + 1$ for $\lambda = 1$ are Möbius transforms. From here, it becomes

$$m(z) = \frac{-1}{z+1} \tag{3}$$

$$\text{for } m = fg = \begin{pmatrix} 0 & -1 \\ 1 & 0 \end{pmatrix} \begin{pmatrix} 1 & 1 \\ 0 & 1 \end{pmatrix} = \begin{pmatrix} 0 & -1 \\ 1 & 1 \end{pmatrix}.$$

For $a, b, c, d \in \mathbb{Z}$ and $ad - bc = 1$, set of Möbius transforms is a group according to the composite operation of functions, this group is named as Modular group and especially showed with Γ . Γ Modular group is a division group of $SL(2, \mathbb{Z})$ with $\{\mp I\}$.

$$\Gamma = PSL(2, \mathbb{Z}) \cong SL(2, \mathbb{Z}) / \{\mp I\} = \left\{ \mp \begin{pmatrix} a & b \\ c & d \end{pmatrix} \in \Gamma \mid a, b, c, d \in \mathbb{Z} \text{ and } ad - bc = 1 \right\} \tag{4}$$

Since each matrix will be equal to its negative, the difference \pm is not taken into account. Γ is defined by the relation $A^2 * B^3 = I$, where $A = \begin{pmatrix} 0 & 1 \\ -1 & 0 \end{pmatrix}$ and $B = \begin{pmatrix} 0 & -1 \\ 1 & 1 \end{pmatrix}$ are members of the Modular group.

The act of Γ on $\widehat{\mathbb{Q}}$ is transitive, so for $v \in \widehat{\mathbb{Q}}$ each suborbit contains the (∞, v) pair. If $v = \frac{u}{N}$ for $N \geq 0$ and $(u, N) = 1$, this suborbital is denoted by $O_{u,N}$ and the suborbital graph $G(\infty, v)$ corresponding to the suborbital is also denoted by $G_{u,N}$. $F_{u,N}$ is the subgraph of $G_{u,N}$ consisting of the $[\infty] = \left\{x, y \in \widehat{\mathbb{Q}} \mid y \equiv 0 \pmod{N}\right\}$ block whose vertices contain ∞ . So, $G_{u,N}$ is consist of $F_{u,N}$ discrete copies. $F_{u,N}$ must satisfy

$$x \equiv ur \pmod{N} \text{ and } ry - sx = N$$

conditions in the right directed suborbital graph and

$$x \equiv -ur \pmod{N} \text{ ve } ry - sx = -N$$

conditions in the left directed suborbital graph, where $\frac{r}{s}$ and $\frac{x}{y}$ are vertices in $F_{u,N}$. For more detailed information about act of $F_{u,N}$ on $\widehat{\mathbb{Q}}$, Sims (1967), Jones, G., A. and Singerman, D. (1987), Jones etc. (1991) and Akbaş (2001) can be examined.

Hecke Groups

Hecke groups was produced with continued linear fractions $f(z) = -\frac{1}{z}$ and $g(z) = z + \lambda$ and was defined in (Hecke ,1936). From here, Möbius transform is

$$m(z) = \frac{-1}{z+\lambda} \tag{5}$$

for $m = fg = \begin{pmatrix} 0 & -1 \\ 1 & 0 \end{pmatrix} \begin{pmatrix} 1 & \lambda \\ 0 & 1 \end{pmatrix} = \begin{pmatrix} 0 & -1 \\ 1 & \lambda \end{pmatrix}$. The element of the Modular group representing the Möbius transformation is $\begin{pmatrix} 0 & -1 \\ 1 & \lambda \end{pmatrix}$. Hecke demonstrated that Hecke groups are discrete for $\lambda \geq 2$ or $\lambda = \lambda_q = 2\cos\left(\frac{\pi}{q}\right), q \in \mathbb{N}, q \geq 3$. These groups is showed $H(\lambda)$ for $\lambda \geq 2$ and $H(\lambda_q)$ for $\lambda < 2$. Hecke group is equal to Modular group for $q = 3$ as follows.

$$H(\lambda_3) = H\left(2\cos\left(\frac{\pi}{3}\right)\right) = H\left(2\frac{1}{2}\right) = H(1) = \text{PSL}(2, \mathbb{Z}) \tag{6}$$

The Hecke group $H(\lambda_q)$ is isomorphic to the

$$X_2 * X_q \tag{7}$$

where X_2 and X_q are two finite cyclic groups of order 2 and q , respectively and $*$ free product (Cangül, 1996) . Similarly, Hecke group $H(\lambda)$ is isomorphic to

$$X_2 * X_\infty = X_2 * \mathbb{Z} \tag{8}$$

where X_2 and X_∞ are two finite cyclic groups of order 2 and ∞ , respectively (Yılmaz Özgür, 2002). Lehner common Hecke groups $H_{p,q} = \langle S, T : S^p, T^q \rangle$ are isomorphic to

$$\mathbb{Z}_p * \mathbb{Z}_q \tag{9}$$

for $S(z) = -\frac{1}{z-\lambda_p}$ and $T(z) = -\frac{1}{z+\lambda_q}$. From here,

$$\lambda_p = 2\cos\left(\frac{\pi}{p}\right) \tag{10}$$

and

$$\lambda_q = 2\cos\left(\frac{\pi}{q}\right) \tag{11}$$

is defined for $2 \leq p \leq q \leq \infty$ and $p + q > 4$. It becomes Modular group for $p = 2$ and $q = 3$ (Lehner 1975). $S(z) = -\frac{1}{z-\lambda_p}$ can be demonstrated as element of Modular group with $S = \begin{pmatrix} 0 & -1 \\ 1 & -\lambda_p \end{pmatrix}$. Since $\lambda_2 = 2\cos\left(\frac{\pi}{2}\right) = 0$ for $p = 2$, $S^2 = -\begin{pmatrix} 1 & 0 \\ 0 & 1 \end{pmatrix}$. Similarly, $T(z) = -\frac{1}{z+\lambda_q}$ can be demonstrated as element of Modular group with $T = \begin{pmatrix} 0 & -1 \\ 1 & \lambda_q \end{pmatrix}$. Since $\lambda_3 = 2\cos\left(\frac{\pi}{3}\right) = 1$ for $q = 3$, $T^3 = -\begin{pmatrix} 1 & 0 \\ 0 & 1 \end{pmatrix}$. Hence, $S^2 * T^3 = I$ is obtained from S^2 and T^3 matrices.

Hecke Group $H(\sqrt{q})$

The case of $\lambda = \sqrt{q}$ for prime numbers $q \geq 5$ in the Hecke group was studied by Yılmaz Özgür (2002) and this group was denoted by $H(\sqrt{q})$. If $K = MN$ for $K = \begin{pmatrix} 0 & -1 \\ 1 & 0 \end{pmatrix}$ and $M = \begin{pmatrix} 0 & -1 \\ 1 & \sqrt{q} \end{pmatrix}$, the group $H(\sqrt{q})$ can be given as

$$\langle K, M; M^2 = K^\infty = (KM)^\infty = 1 \rangle \tag{12}$$

The sets of elements of the Hecke group $H(\sqrt{q})$ have the form

$$\left\{ \begin{pmatrix} a\sqrt{q} & b \\ c & d\sqrt{q} \end{pmatrix} : a, b, c, d \in \mathbb{Z}, adq - bc = 1 \right\} \tag{13}$$

and

$$\left\{ \begin{pmatrix} a & b\sqrt{q} \\ c\sqrt{q} & d \end{pmatrix} : a, b, c, d \in \mathbb{Z}, ad - bcq = 1 \right\} \tag{14}$$

However, not every matrix of this type has to be in the Hecke group $H(\sqrt{q})$.

Theorem 1. By taking n^{th} power of $M \in H(\sqrt{q})$, where $q \geq 5$ is a prime number, the recurrence relation $d_n = \sqrt{q}d_{n-1} - d_{n-2}$ is obtained with the initial conditions $d_0 = 1, d_1 = \sqrt{q}$ (Yılmaz Özgür, 2002).

□

Moreover, for $M \in H(\sqrt{q})$ and $n \in \mathbb{Z}$, " $M^n \equiv \mp I \pmod{p}$, p is an odd number" is found as

$$M^n = \begin{pmatrix} -d_{n-2} & -d_{n-1} \\ d_{n-1} & d_n \end{pmatrix} = \begin{pmatrix} -d_{n-2} & -d_{n-1} \\ d_{n-1} & \sqrt{q}d_{n-1} - d_{n-2} \end{pmatrix} \tag{15}$$

From the initial conditions $d_0 = 1, d_1 = \sqrt{q}$ and recurrence relation $d_n = \sqrt{q}d_{n-1} - d_{n-2}, n \geq 2$, the identities $d_{2n} = L_{2n+1}$ and $d_{2n+1} = \sqrt{5}F_{2n+2}$ are obtained specifically for $q = 5$ (Yılmaz Özgür, 2002).

Relation Between Continued Fractions and Matrices

$b_0 + \frac{a_1}{b_1 + \frac{a_2}{b_2 + \frac{a_3}{b_3 + \dots}}}$ is a continued fraction, where $a_m \in \mathbb{Z} - \{0\}$ and $b_m \in \mathbb{Z}$ for $\forall m \in \mathbb{N} \cup \{0\}$. This continued fraction is demonstrated with

$$b_0 + K_{m=1}^{\infty} \left(\frac{a_m}{b_m} \right) \tag{16}$$

as symbolic. Accordingly, n^{th} approximation is

$$f_n = b_0 + K_{m=1}^n \left(\frac{a_m}{b_m} \right). \tag{17}$$

For $i \geq 1, (\{a_i\}_{i \in \mathbb{N}}, \{b_i\}_{i \in \mathbb{N} \cup \{0\}}), a_i \neq 0$ and $t_0(s) = s, t_n(s) = \frac{a_n}{b_n + s}, T_0(s) = t_0(s), T_n(s) = T_{n-1}(t_n(s))$ and $f_n = T_n(0) \in \widehat{\mathbb{R}} = \mathbb{R} \cup \{\infty\}$ for $n \geq 1$ form series of linear continued fraction $\{t_n(s)\}_{n \in \mathbb{N} \cup \{0\}}$ and $\{T_n(s)\}_{n \in \mathbb{N} \cup \{0\}}$ and from here series $\{f_n\}$ are obtained. Consequently, a continued fraction can be written as a sequence

$$\left((\{a_i\}_{i \in \mathbb{N}}, \{b_i\}_{i \in \mathbb{N} \cup \{0\}}), \{f_n\} \right) \tag{18}$$

$T_n(s) = (t_0 o t_1 o t_2 o \dots o t_n)(s)$ can be written for “o” composite operation. From here,

$$(t_0 o t_1)(s) = t_0(t_1(s)) \tag{19}$$

and

$$t^n(s) = \left(\underbrace{t o t o \dots o t}_{n \text{ times}} \right) (s) \tag{20}$$

are obtained. The number of n^{th} modified approaches becomes

$$T_n(S_n) \in \widehat{\mathbb{R}} \tag{21}$$

for the sequence $\{S_n\}_{n \in \mathbb{N} \cup \{0\}}$. For more detailed information about continued fractions can be examined (Jones, 1980) and (Cuyt, 2008).

If $a_n = -1, b_n = -k$ is taken every $n \geq 0$ integer in the recurrence relation

$$\begin{pmatrix} p_n \\ q_n \end{pmatrix} = \left\{ b_n \begin{pmatrix} p_{n-1} \\ q_{n-1} \end{pmatrix} + a_n \begin{pmatrix} p_{n-2} \\ q_{n-2} \end{pmatrix}, n = 1, 2, 3, \dots \right\} \tag{22}$$

where p_n is the n^{th} numerator and q_n is the n^{th} denominator of a continued fraction, value of n^{th} vertex is

$$\frac{u+T_n(0)}{N} = \frac{u+\frac{p_n}{q_n}}{N} = \frac{p_{n+1}u-p_n}{p_{n+1}N} \tag{23}$$

from relation between matrices and continued fractions for $q_n = -p_{n+1}$ on the minimal length path in the suborbital graph $F_{u,N} \cdot \begin{pmatrix} p_{n-1} & p_n \\ -p_n & -p_{n+1} \end{pmatrix} = \begin{pmatrix} 0 & -1 \\ 1 & -k \end{pmatrix}^n$ is obtained from matrices

$$x_n = \begin{pmatrix} 0 & a_n \\ 1 & b_n \end{pmatrix}, X_n = x_1 x_2 x_3 \cdots x_n = \begin{pmatrix} p_{n-1} & p_n \\ q_{n-1} & q_n \end{pmatrix}. \tag{24}$$

For more detailed information about continued fractions and suborbital graphs can be investigated (Değer 2011) and (Değer vd., 2011).

Recurrence relation becomes

$$\begin{pmatrix} p_n \\ q_n \end{pmatrix} = -k \begin{pmatrix} p_{n-1} \\ q_{n-1} \end{pmatrix} - \begin{pmatrix} p_{n-2} \\ q_{n-2} \end{pmatrix} \tag{25}$$

for $a_n = -1$ and $b_n = -k$. So, $p_n = -kp_{n-1} - p_{n-2}$ and $q_n = -kq_{n-1} - q_{n-2}$ are found. In the first equation,

$$p_{n+2} + kp_{n+1} + p_n = 0 \tag{26}$$

is obtained by substituting $n \rightarrow n + 2$ variables. If it is converted to quadratic form and examining the roots, we find

$$p_n = (-1)^n n \tag{27}$$

for $k = 2$ and

$$p_n = (-1)^n 2^{1-n} \sum_{t=1}^n (k + \sqrt{k^2 - 4})^{n-t} (k - \sqrt{k^2 - 4})^{t-1} \tag{28}$$

for $k > 2$ (Değer, 2017).

Lemma 1. $F_{2n}p_{n+1} + F_{2n+2}p_n = 0$ where p_n is the n^{th} numerator of the continued fraction $K_{m=1}^{\infty} \left(\frac{-1}{-3} \right)$ (Değer, 2017).

Lemma 2. $F_{2n} = (-1)^n p_n$ and $F_{2n+1} = (-1)^{n+1} (p_{n+1} + p_n)$ for $n = 0, 1, 2, 3, \dots$ (Değer, 2017).

Conclusion 1.
$$\begin{pmatrix} (-1)^{n-1} F_{2n-2} & (-1)^n F_{2n} \\ (-1)^{n+1} F_{2n} & (-1)^n F_{2n+2} \end{pmatrix} = \begin{pmatrix} 0 & -1 \\ 1 & -3 \end{pmatrix}^n$$
 (Değer, 2017).

Conclusion 2. $F_{4n+2} = -p_{2n+1}$ for $n = 0, 1, 2, 3, \dots$ (Değer, 2017).

Conclusion 3. $F_{2n} = \frac{1}{3} (F_{2n+2} + F_{2n-2})$ for $n = 0, 1, 2, 3, \dots$ (Değer, 2017).

Conclusion 4. $F_{2n-2} = \frac{1}{2} (F_{2n+2} - 3F_{2n-1})$ for $n = 0, 1, 2, 3, \dots$ (Değer, 2017).

Conclusion 5. $F_{2n-1} = \frac{1}{3} (F_{2n+1} + F_{2n-3})$ for $n = 0, 1, 2, 3, \dots$ (Değer, 2017).

OBTAINING THE MATRIX M^n FROM ELEMENTS OF THE FIBONACCI AND LUCAS NUMBER SEQUENCES AND RELATED IDENTITIES

In this part, the matrix M^n , which was obtained from the number sequences d_n in previous studies, was written as Fibonacci and Lucas numbers.

If $n \rightarrow 2n$ is taken specifically in the matrix

$$M^n = \begin{pmatrix} -d_{n-2} & -d_{n-1} \\ d_{n-1} & d_n \end{pmatrix}, \text{ the generalized matrix}$$

$$M^{2n} = \begin{pmatrix} -d_{2n-2} & -d_{2n-1} \\ d_{2n-1} & d_{2n} \end{pmatrix} \quad (29)$$

is obtained. In order to write the elements of the matrix M^{2n} as the elements of the Fibonacci number sequence, if $n \rightarrow n - \frac{1}{2}$ variable substitution is applied in identity $d_{2n+1} = \sqrt{5}F_{2n+2}$,

$$d_{2n} = \sqrt{5}F_{2n+1} \quad (30)$$

identity is obtained. Similarly, if $n \rightarrow n - 1$ variable substitution is applied to the identity $d_{2n+1} = \sqrt{5}F_{2n+2}$,

$$d_{2n-1} = \sqrt{5}F_{2n} \quad (31)$$

is found. Also, if $n \rightarrow n - 1$ variable substitution is applied to the identity $d_{2n} = \sqrt{5}F_{2n+1}$,

$$d_{2n-2} = \sqrt{5}F_{2n-1} \quad (32)$$

is found. From here, M^{2n} is obtained as

$$\begin{pmatrix} -d_{2n-2} & -d_{2n-1} \\ d_{2n-1} & d_{2n} \end{pmatrix} = \begin{pmatrix} -\sqrt{5}F_{2n-1} & -\sqrt{5}F_{2n} \\ \sqrt{5}F_{2n} & \sqrt{5}F_{2n+1} \end{pmatrix} \quad (33)$$

with elements of Fibonacci number sequence. For $n \in \mathbb{N}$ and $n \rightarrow \infty$, approximate value of $F_n = \frac{\alpha^n - \beta^n}{\alpha - \beta}$ is

$$F_n = \frac{\alpha^n - \beta^n}{\sqrt{5}} = \frac{\alpha^n}{\sqrt{5}} \left(1 - \left(\frac{\beta}{\alpha}\right)^n\right) \approx \frac{\alpha^n}{\sqrt{5}} \tag{34}$$

where $\alpha = \frac{1+\sqrt{5}}{2}$ and $\beta = \frac{1-\sqrt{5}}{2}$. If the last approximate value found is substituted in the identity $F_{2n} = F_n \cdot L_n$, it becomes

$$F_{2n} = F_n \cdot L_n \approx \frac{\alpha^n}{\sqrt{5}} \cdot L_n. \tag{35}$$

Since $d_{2n-1} = \sqrt{5}F_{2n}$ is $\frac{d_{2n-1}}{\sqrt{5}} = F_{2n}$, the identity

$$d_{2n-1} \approx \alpha^n L_n \tag{36}$$

is obtained from $\frac{d_{2n-1}}{\sqrt{5}} \approx \frac{\alpha^n}{\sqrt{5}} L_n$.

From (36), matrix M^{2n} can be obtained with help of Lucas number sequences as follows.

If $n \rightarrow n - 1$ variable substitution is applied in identity $d_{2n} = L_{2n+1}$,

$$d_{2n-2} = L_{2n-1} \tag{37}$$

identity is obtained. From here,

$$\begin{pmatrix} -d_{2n-2} & -d_{2n-1} \\ d_{2n-1} & d_{2n} \end{pmatrix} \approx \begin{pmatrix} -L_{2n-1} & -\alpha^n L_n \\ \alpha^n L_n & L_{2n+1} \end{pmatrix} \tag{38}$$

matrix is obtained.

Let's obtain the determinants of the matrices given in (33) and (38) for $n = 1$ and $\alpha = 1.618$.

$$\begin{aligned} & \left| \begin{pmatrix} -\sqrt{5}F_1 & -\sqrt{5}F_2 \\ \sqrt{5}F_2 & \sqrt{5}F_3 \end{pmatrix} \right| = -5 \\ & \left| \begin{pmatrix} -L_{19} & -\alpha^{10}L_{10} \\ \alpha^{10}L_{10} & L_{21} \end{pmatrix} \right| \approx -1,38 \end{aligned}$$

Lemma3. $L_{2n+1}d_{2n-1} - \alpha^n L_n d_{2n} \approx 0$ for $n = 0, 1, 2, \dots$

Proof. From (36) and $d_{2n} = L_{2n+1}$,

$$L_{2n+1}d_{2n-1} - \alpha^n L_n d_{2n} \approx 0 \tag{39}$$

is found for $\frac{d_{2n-1}}{d_{2n}} \approx \frac{\alpha^n L_n}{L_{2n+1}}$.

□

OBTAINING THE MATRIX $\begin{pmatrix} 0 & -1 \\ 1 & -3 \end{pmatrix}^n$ AND THE VERTICES OF THE SUBORBITAL GRAPH $F_{u,N}$ WITH HELP OF ELEMENTS OF THE SEQUENCE d_n AND RELATED IDENTITIES

In this section, the vertex value of the suborbital graph $F_{u,N}$, which was written with elements of Fibonacci and Lucas number sequences in previous studies, was obtained with help of the elements of the sequence d_n . Some identities were obtained. However, by giving special values to the suborbital graph $F_{u,N}$, the value of the 10^{th} vertex was obtained with the elements of the Fibonacci number sequence and sequences d_n .

If variable substitution $n \rightarrow n - 1$ is applied in identity $d_{2n-1} = \sqrt{5}F_{2n}$, then

$$d_{2n-3} = \sqrt{5}F_{2n-2} \tag{40}$$

is obtained. Also, if variable substitution $n \rightarrow n + 2$ is applied in identity $d_{2n-1} = \sqrt{5}F_{2n}$, then

$$d_{2n+1} = \sqrt{5}F_{2n+2} \tag{41}$$

is obtained. From here, $\begin{pmatrix} 0 & -1 \\ 1 & -3 \end{pmatrix}^n$ becomes

$$\begin{pmatrix} (-1)^{n-1} \frac{d_{2n-3}}{\sqrt{5}} & (-1)^n \frac{d_{2n-1}}{\sqrt{5}} \\ (-1)^{n+1} \frac{d_{2n-1}}{\sqrt{5}} & (-1)^n \frac{d_{2n+1}}{\sqrt{5}} \end{pmatrix} \tag{42}$$

with help of the elements of sequence d_n . Vertices of suborbital graph $F_{u,N}$ are obtained as

$$\frac{u+T_n(0)}{N} = \frac{u+\frac{F_{2n}}{F_{2n+2}}}{N} = \frac{u+\frac{(-1)^n \frac{d_{2n-1}}{\sqrt{5}}}{(-1)^n \frac{d_{2n+1}}{\sqrt{5}}}}{N} = \frac{u+\frac{d_{2n-1}}{d_{2n+1}}}{N} \tag{43}$$

with the elements of sequence d_n .

Conclusion 6. $F_{2n}d_{2n+1} - F_{2n+2}d_{2n-1} = 0$ for $n = 0,1,2,3, \dots$.

Proof. From (43),equality $F_{2n}d_{2n+1} - F_{2n+2}d_{2n-1} = 0$ is obtained.

□

Conclusion 7. $F_{2n+1} = \frac{1}{\sqrt{5}}(d_{2n+1} - d_{2n+1})$ for $n = 0,1,2,3, \dots$.

Proof. From Lemma 2 and (31), $d_{2n-1} = \sqrt{5}(-1)^n p_n$ is obtained.

Then, $p_n = \frac{d_{2n-1}}{\sqrt{5}(-1)^n}$. So, $p_{n+1} = \frac{d_{2n+1}}{\sqrt{5}(-1)^{n+1}}$. From here, $F_{2n+1} = (-1)^{n+1}(p_{n+1} + p_n) = (-1)^{n+1} \left(\frac{d_{2n+1}}{\sqrt{5}(-1)^{n+1}} + \frac{d_{2n-1}}{\sqrt{5}(-1)^n} \right) = \frac{1}{\sqrt{5}}(d_{2n+1} - d_{2n+1})$ is obtained.

□

Conclusion 8. $F_{2n} = \frac{1}{3\sqrt{5}}(d_{2n+1} + d_{2n-3})$ for $n = 0,1,2,3, \dots$.

Proof. From $d_{2n+1} = \sqrt{5}F_{2n+2}$, $F_{2n+2} = \frac{d_{2n+1}}{\sqrt{5}}$ is obtained. Also,

$d_{2n-3} = \sqrt{5}F_{2n-2}$ is obtained from $d_{2n+1} = \sqrt{5}F_{2n+2}$ for $n \rightarrow n - 2$. Then, $F_{2n-2} = \frac{d_{2n-3}}{\sqrt{5}}$. So, $F_{2n} = \frac{1}{3}(F_{2n+2} + F_{2n-2}) = \frac{1}{3} \left(\frac{d_{2n+1}}{\sqrt{5}} + \frac{d_{2n-3}}{\sqrt{5}} \right) = \frac{1}{3\sqrt{5}}(d_{2n+1} + d_{2n-3})$.

□

Example 1. Let $u = 1$ and $N = 2$ in the suborbital graph $F_{u,N}$ for $k = 3$ and $u^2 + 3u + 1 \equiv 0 \pmod{N}$. For the suborbital graph

$F_{1,2}$, the value of the farthest $(n + 1)^{th}$ vertex to which n^{th} vertex can be connected on an infinite path of minimal length is $\frac{u + \frac{F_{2n}}{F_{2n+2}}}{N}$. For example, the value of the farthest 10^{th} vertex to which 9^{th} vertex can be connected is obtained with help of

$$\begin{pmatrix} 0 & -1 \\ 1 & -3 \end{pmatrix}^9 = \begin{pmatrix} (-1)^{n-1}F_{2n-2} & (-1)^nF_{2n} \\ (-1)^{n+1}F_{2n} & (-1)^nF_{2n+2} \end{pmatrix} = \begin{pmatrix} F_{16} & -F_{18} \\ F_{18} & -F_{20} \end{pmatrix} = \begin{pmatrix} 987 & -2584 \\ 2584 & -6765 \end{pmatrix} \tag{44}$$

matrix. Then, value of 10^{th} vertex is

$$\frac{1 + \frac{F_{18}}{F_{20}}}{2} = \frac{1 + \frac{2584}{6765}}{2} = 0.8819660015. \tag{45}$$

Value of same vertex is obtained as

$$\frac{u + \frac{d_{2n-1}}{d_{2n+1}}}{N} = \frac{1 + \frac{d_{17}}{d_{19}}}{2} = \frac{1 + \frac{\sqrt{5}F_{18}}{\sqrt{5}F_{20}}}{2} = \frac{1 + \frac{F_{18}}{F_{20}}}{2} = 0.8819660015 \tag{46}$$

with help of elements of sequence d_n .

References

- Akbaş, M. (2001). On Suborbital Graphs for Modular Group, *Bull. London Math. Soc.*, 33, 647-652.
- Alfred, B.U. (1965). *An Introduction to Fibonacci Discovery*.
- Anderson, J. W. (2005). *Hyperbolic Geometry*, Second Edition, Southampton: Springer.
- Asar, A.O., Arıkan, A. (2009). *Cebir*, Ankara: Eflatun Yayınevi.
- Bicknell, M., Hoggatt V.E. (1973). *A Primer for the Fibonacci Numbers*.
- Cangül, İ.N. (1996). The Group Structure of Hecke Groups $H(\lambda q)$. *Turkish Journal of Mathematics*, 20, 203-207.
- Cuyt, A., Petersen, V.B., Verdonk, B., Waadeland, H. and Jones, W.B. (2008). *Handbook of Continued Fractions for Special Functions*, New York:Springer.
- Çallıalp, F.(2001). *Örneklerle Soyut Cebir*. İstanbul :Birsen Yayınevi.
- Değer, A.H. (2011). Curves of Minimal Length with $\widehat{\mathbb{Q}}$ Vertex on Suborbital Graphs of the Group $\Gamma_0(n)$, Phd. Thesis. Trabzon: Karadeniz Technical University.
- Deger, A.H., Besenk, M. and Guler, B.O. (2011). On Suborbital Graphs and Related Continued Fractions. *Applied Mathematics and Computation*, 218(3), 746-750.
- Deger, A.H. (2017). Relationships with the Fibonacci Numbers and the Special Vertices of the Suborbital Graphs. Gümüşhane University, *The Graduate School of Natural and Applied Sciences*, 7,168-200.
- Deger, A.H. (2017). Vertices of Paths of Minimal Lengths on Suborbital Graphs, *Filomat*, 31(4), 913-923.
- Gökcan,İ.(2021). Some Relations Between Special Vertex Values of Suborbital Graphs and Special Number Sequences. Phd. Thesis. Trabzon: Karadeniz Technical University.
- Hecke, E. (1936). Über die Bestimmung Dirichletscher Reihen durch ihre Funktionalgleichungen. *Math. Ann.*, 112, 664–699.
- Jones, W.B.,Thron, W.J. (1980). *Continued Fractions Analytic Theory and Applications*, *Encyclopedia of Mathematics and It's Applications*. London:Addison-Wesley Publishing Company.
- Jones, G.A., Singerman, D. (1987). *Complex Functions: An Algebraic and Geometric Viewpoint* ,UK :Cambridge University Press.
- Jones, G.A., Singerman, D. and Wicks, K. (1991). The Modular Group and Generalized Farey Graphs, *London Math. Soc. Lecture Note Ser.*, 160, 316-338.

Koshy, T. (2001). *Fibonacci and Lucas Numbers with Applications*, New York :Wiley-Interscience Publication.

Lehner, J. (1975). Uniqueness of a class of Fuchsian groups, *Illinois Journal of Mathematics*, 19, 308-315.

Rankin, R.A. (1977). *Modular Forms and Functions*. Cambridge University Press.

Ruohonen, K. (2008). *Graph Theory*, Tampere University of Technology.

Sims, C.C. (1967). Graphs and Finite Permutation Groups. *Mathematische Zeitschrift*, 95, 76-86.

Taşçı, D. (2007). *Soyut Cebir*. Ankara :Alp Yayınevi.

Yılmaz Özgür, N. (2002). Generalizations of Fibonacci and Lucas sequences. *Note Di Matematica*, 21(1), 113-125.

Chapter 12

ON THE CHARACTERIZATION OF DUAL LINES IN D^3

Muhsin Incesu¹

¹ Asst.Prof. Dr. Muhsin Incesu, Mus Alparslan University, Math. Edu. Dept. ORCID: <https://orcid.org/0000-0003-2515-9627>

1. Introduction

After the introducing of dual numbers by Clifford (1873), there were good developments in the theory of mechanisms and especially in robot technology. After Study (1891), many scientists have worked in this field by reducing the study of ruled surfaces to the study of dual spherical curves. Especially Müller (1962), Hacısalihoğlu (1972; 1983), Mc Carthy and Roth (1981), Ting and Soni (1983), Tiler and Hanson (1984), Hoschek (1985), Gürsoy [1990a; 1990b, 1992], Potmann (1995), Zha (1997), Gursoy and Kucuk (1999; 2004), Tas and Ilarslan (2019), Nesovic et al. (2016), Hathout, Bekar and Yayli (2017), Guler and Kasap (2018), Taş (2016), Taş and Gürsoy (2018), Küçük (2004), Kazaz, Özdemir and Guroğlu (2008), Mevroidis and Roth (1997), Incesu and Gürsoy (2004; 2018), Incesu (2021) were studied the ruled surfaces and kinematics.

In this paper the dual lines in dual space \mathbb{D}^3 have been investigated. When this study is examined, it will be seen that a line congruence in real space R^3 corresponds to a line L given in space \mathbb{D}^3 . In addition, in this study, the situations of dual lines against each other are discussed. Situations such as parallelism or intersection of these lines are examined.

2. Methods and Materials

2.1. Dual Numbers and D-module

Let two operations called addition and multiplication be defined on two dimensional Euclidean spaces E^2 as follows:

$$\begin{aligned} &+: E^2 \times E^2 \rightarrow E^2 \\ (A, B) &\rightsquigarrow A + B = (a_1 + b_1, a_2 + b_2) \\ &.: E^2 \times E^2 \rightarrow E^2 \end{aligned}$$

$$(A, B) \rightsquigarrow A \cdot B = (a_1 b_1, a_1 b_2 + a_2 b_1)$$

where $A = (a_1, a_2)$ and $B = (b_1, b_2)$. Under these operations the set E^2 is a ring and called the set of dual numbers. This set is denoted by \mathbb{D} . Any element $A = (a, a^*)$ of \mathbb{D} , can be written as

$$A = a(1,0) + a^*(0,1) \quad (1)$$

where the element $(1,0)$ is called real unit, and the element $(0,1)$ is called dual unit and denoted by ε . It is clearly visible that $\varepsilon^2 = 0$. Any element $(r, 0)$ is isomorphic to $r \in R$. Hence any dual number $A = (a, a^*)$ can be written as $A = a + \varepsilon a^*$, where $a, a^* \in R$. If a dual number $A = a + \varepsilon a^*$ be given then a and a^* are called the real and dual part of A respectively. The conjugate number of a dual number $A = a + \varepsilon a^*$ is $\bar{A} = a - \varepsilon a^*$ (Hacısalihoglu,1983).

The inner product of two dual vectors $\hat{U} = U + \varepsilon U^*$ and $\hat{V} = V + \varepsilon V^*$ be defined as. $\langle \hat{U}, \hat{V} \rangle = \langle U, V \rangle + \varepsilon(\langle U^*, V \rangle + \langle U, V^* \rangle)$ and the norm of a dual vector $\hat{U} = U + \varepsilon U^*$ is defined as

$$\|\hat{U}\| = \sqrt{\langle \hat{U}, \hat{U} \rangle} = \sqrt{\langle U, U \rangle + 2\varepsilon\langle U, U^* \rangle} = \|U\| + \varepsilon \frac{\langle U, U^* \rangle}{\|U\|} = u + \varepsilon u^* \in D$$

if the real part of the dual vector is different from zero. i.e. $U \neq 0$.

Theorem 2.1. (E.Study) (Hacısalihoglu,1983): Every unit vector on the dual unit sphere $\hat{U} = U + \varepsilon U^*$ ($U \neq 0$) corresponds to oriented line in real space R^3 by one to one.

3. Main Results

Let \mathbb{D} be denoted to set of dual numbers. Let the line L in dual 3-space \mathbb{D}^3 be given. The director vector of the line L be given as $\vec{D} = \vec{d} + \varepsilon \vec{d}^*$. Any point on the line L be denoted as $\hat{A} = A + \varepsilon A^*$ (see Fig.1). Any point $\hat{X} = X + \varepsilon X^*$ can be written in the vectoral form as

$$\vec{\hat{X}} = \vec{\hat{A}} + \Lambda \vec{D}$$

Where $\Lambda = \lambda + \varepsilon \lambda^* \in \mathbb{D}$. This equation can be written as

$$X + \varepsilon X^* = (A + \lambda \vec{d}) + \varepsilon(A^* + \lambda \vec{d}^* + \lambda^* \vec{d})$$

or

$$X = A + \lambda \vec{d} \quad \text{and} \quad X^* = A^* + \lambda \vec{d}^* + \lambda^* \vec{d}$$

If $X = (x, y, z)$; $X^* = (x^*, y^*, z^*)$; $\vec{d} = (d_1, d_2, d_3)$; $\vec{d}^* = (d_1^*, d_2^*, d_3^*)$; $A = (a, b, c)$ and $A^* = (a^*, b^*, c^*)$ be choosen then the line L can be stated in parametric equation as

$$x = a + \lambda d_1 \qquad x^* = a^* + \lambda d_1^* + \lambda^* d_1$$

$$\lambda, \lambda^* \in R \quad y = b + \lambda d_2 \quad \text{and} \quad y^* = b^* + \lambda d_2^* + \lambda^* d_2$$

$$z = c + \lambda d_3 \quad z^* = c^* + \lambda d_3^* + \lambda^* d_3$$

This equation (1) is the parametric equation of a dual line L in the direction $\vec{D} = \vec{d} + \varepsilon \vec{d}^*$ passing through $\hat{A} = A + \varepsilon A^*$. The linear equation of this line can be written as follows:

$$\begin{aligned} \lambda + \varepsilon \lambda^* &= \frac{x-a}{d_1} + \varepsilon \left(\frac{x^*-a^*}{d_1} - \frac{(x-a)d_1^*}{d_1^2} \right) = \frac{y-b}{d_2} + \varepsilon \left(\frac{y^*-b^*}{d_2} - \frac{(y-b)d_2^*}{d_2^2} \right) \\ &= \frac{z-c}{d_3} + \varepsilon \left(\frac{z^*-c^*}{d_3} - \frac{(z-c)d_3^*}{d_3^2} \right) \end{aligned}$$

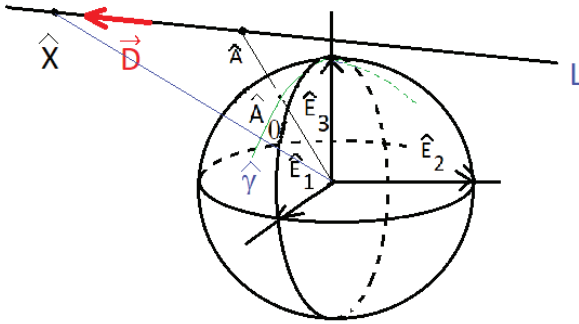


Fig. 1: The line L in D^3

If $\Lambda = \lambda + \varepsilon \lambda^* = 0$ be chosen ($\lambda = \lambda^* = 0$) then the points $\hat{X} = X + \varepsilon X^*$ and $\hat{A} = A + \varepsilon A^*$ on the line L coincide.

If $\lambda = 0$ and $\lambda^* \neq 0$ then only real parts of the points $\hat{X} = X + \varepsilon X^*$ and $\hat{A} = A + \varepsilon A^*$ on the line L coincides (i.e. $X = A$) and the dual part of \hat{X} lies on the line passing through A^* and in direction \vec{d} i.e.

$$\lambda^* = \frac{x^*-a^*}{d_1} = \frac{y^*-b^*}{d_2} = \frac{z^*-c^*}{d_3}$$

Satisfies. If $\lambda^* = 0$ and $\lambda \neq 0$ be chosen then

$$\lambda = \frac{x-a}{d_1} = \frac{y-b}{d_2} = \frac{z-c}{d_3} = \frac{x^*-a^*}{d_1^*} = \frac{y^*-b^*}{d_2^*} = \frac{z^*-c^*}{d_3^*}$$

satisfies. This means that two real lines, the line l_1 passing through A with direction \vec{d} and the line l_2 passing through A^* with direction \vec{d}^* , have the same velocity. That means that the points X and X^* moves on the lines l_1 and l_2 with same direction and same velocity.

Now, let these dual points $\hat{\mathcal{S}}_0 = \mathcal{S}_0 + \varepsilon\mathcal{S}_0^*$, $\hat{\mathcal{S}}_1 = \mathcal{S}_1 + \varepsilon\mathcal{S}_1^*$, $\hat{\mathcal{S}}_2 = \mathcal{S}_2 + \varepsilon\mathcal{S}_2^*$ in 3-dual space D^3 be collinear. Then these vectors $\vec{\hat{\mathcal{S}}}_i$, ($i=0,1,2$) are linearly dependent. So the determinant value $G = \det(\hat{\mathcal{S}}_0, \hat{\mathcal{S}}_1, \hat{\mathcal{S}}_2)$ must be zero. From the determinant properties this determinant can be written as sum of six determinant values as follows:

$$G = \det(\hat{\mathcal{S}}_0, \hat{\mathcal{S}}_1, \hat{\mathcal{S}}_2) \\ = \det(\mathcal{S}_0, \mathcal{S}_1, \mathcal{S}_2) + \varepsilon[\det(\mathcal{S}_0^*, \mathcal{S}_1, \mathcal{S}_2) + \det(\mathcal{S}_0, \mathcal{S}_1^*, \mathcal{S}_2) + \det(\mathcal{S}_0, \mathcal{S}_1, \mathcal{S}_2^*)]$$

$$+ \varepsilon^2[\det(\mathcal{S}_0^*, \mathcal{S}_1^*, \mathcal{S}_2) + \det(\mathcal{S}_0, \mathcal{S}_1^*, \mathcal{S}_2^*) + \det(\mathcal{S}_0^*, \mathcal{S}_1, \mathcal{S}_2^*)] + \varepsilon^3\det(\mathcal{S}_0^*, \mathcal{S}_1^*, \mathcal{S}_2^*)$$

Since $\varepsilon^2 = 0$ then

$$G = \det(\mathcal{S}_0, \mathcal{S}_1, \mathcal{S}_2) + \varepsilon[\det(\mathcal{S}_0^*, \mathcal{S}_1, \mathcal{S}_2) + \det(\mathcal{S}_0, \mathcal{S}_1^*, \mathcal{S}_2) + \det(\mathcal{S}_0, \mathcal{S}_1, \mathcal{S}_2^*)] = 0$$

or

$$\det(\mathcal{S}_0, \mathcal{S}_1, \mathcal{S}_2) = 0 \\ \det(\mathcal{S}_0^*, \mathcal{S}_1, \mathcal{S}_2) + \det(\mathcal{S}_0, \mathcal{S}_1^*, \mathcal{S}_2) + \det(\mathcal{S}_0, \mathcal{S}_1, \mathcal{S}_2^*) = 0$$

must be satisfied. So this following theorem can be stated.

Theorem 3.1: *If the dual points $\hat{\mathcal{S}}_0 = \mathcal{S}_0 + \varepsilon\mathcal{S}_0^*$, $\hat{\mathcal{S}}_1 = \mathcal{S}_1 + \varepsilon\mathcal{S}_1^*$, $\hat{\mathcal{S}}_2 = \mathcal{S}_2 + \varepsilon\mathcal{S}_2^*$ in 3-dual space D^3 be collinear then*

$$i) \det(\mathcal{S}_0, \mathcal{S}_1, \mathcal{S}_2) = 0$$

ii)

$$\det(\mathcal{S}_0^*, \mathcal{S}_1, \mathcal{S}_2) + \det(\mathcal{S}_0, \mathcal{S}_1^*, \mathcal{S}_2) + \det(\mathcal{S}_0, \mathcal{S}_1, \mathcal{S}_2^*) = 0$$

satisfied.

Let the dual line L be given. Then the projection curve of the line L to dual unit sphere is a dual curve $\hat{\gamma}$. In this projection, the point $\hat{X} = X + \varepsilon X^*$ on the line L projects to a spherical point $\hat{X}_0 = X_0 +$

εX_0^* of this spherical curve $\hat{\gamma}$. (See Fig.1) So this following theorem can be given.

Theorem 3.2: Let a dual line L in the direction $\vec{D} = \vec{d} + \varepsilon\vec{d}^*$ passing through $\hat{A} = A + \varepsilon A^*$ be given. Then the point $\hat{X} = X + \varepsilon X^*$ on the line L projects to a spherical point $\hat{X}_0 = X_0 + \varepsilon X_0^*$ of this spherical curve $\hat{\gamma}$ such that

$$X_0 = \frac{X}{\|X\|}$$

$$X_0^* = \frac{X^*}{\|X\|} - \frac{\langle X, X^* \rangle X}{\|X\|^3}$$

satisfied.

Proof: it can be proved easily by unit dual vector's definition.

Using equations (1) this theorem can be clearly stated as follows:

Theorem 3.3: Let a dual line L in the direction $\vec{D} = \vec{d} + \varepsilon\vec{d}^*$ passing through $\hat{A} = A + \varepsilon A^*$ be given. If $X = (x, y, z)$; $X^* = (x^*, y^*, z^*)$; $\vec{d} = (d_1, d_2, d_3)$; $\vec{d}^* = (d_1^*, d_2^*, d_3^*)$; $A = (a, b, c)$ and $A^* = (a^*, b^*, c^*)$ be choosen then the point $\hat{X} = X + \varepsilon X^*$ on the line L projects to a spherical point $\hat{X}_0 = X_0 + \varepsilon X_0^*$ on the curve $\hat{\gamma}$ such that

$$X_0 = \frac{(a + \lambda d_1, b + \lambda d_2, c + \lambda d_3)}{\sqrt{(a + \lambda d_1)^2 + (b + \lambda d_2)^2 + (c + \lambda d_3)^2}}$$

$$X_0^* = \frac{(a^* + \lambda d_1^* + \lambda^* d_1, b^* + \lambda d_2^* + \lambda^* d_2, c^* + \lambda d_3^* + \lambda^* d_3)}{\sqrt{(a + \lambda d_1)^2 + (b + \lambda d_2)^2 + (c + \lambda d_3)^2}}$$

$$- \frac{[(a + \lambda d_1)(a^* + \lambda d_1^* + \lambda^* d_1) + (b + \lambda d_2)(b^* + \lambda d_2^* + \lambda^* d_2) + (c + \lambda d_3)(c^* + \lambda d_3^* + \lambda^* d_3)]}{[(a + \lambda d_1)^2 + (b + \lambda d_2)^2 + (c + \lambda d_3)^2]^{3/2}} (a + \lambda d_1, b + \lambda d_2, c + \lambda d_3)$$

satisfied.

By the E. Study's theorem any dual spherical point corresponds to a directed line in real 3- space R^3 . In this case, let's examine the surface to which the line L corresponds in real 3- space.

From Taş and Ilarslan (2019) for every $\lambda, \lambda^* \in R$ the position vector α and the director curve is written as

$$\alpha(\lambda, \lambda^*) = \frac{X \times X^*}{\|X\|^2} \quad \text{and} \quad \beta(t) = X_0$$

respectively. Then the ruled surface corresponding to the projection curve $\hat{\gamma}$ of dual line L for every $\lambda, \lambda^*, \nu \in R$ is

$$M(\lambda, \lambda^*, \nu) = \alpha + \nu\beta(t) = \frac{X \times X^*}{\|X\|^2} + \nu \frac{X}{\|X\|}$$

is obtained. This surface is a line congruence in R^3 . So the dual line L corresponds to the line congruence $M(\lambda, \lambda^*, \nu)$ by projecting to dual unit sphere. So this theorem can be given as follows:

Theorem 3.4: *Let a dual line L in the direction $\vec{D} = \vec{d} + \varepsilon\vec{d}^*$ passing through $\hat{A} = A + \varepsilon A^*$ be given. If $X = (x, y, z)$; $X^* = (x^*, y^*, z^*)$; $\vec{d} = (d_1, d_2, d_3)$; $\vec{d}^* = (d_1^*, d_2^*, d_3^*)$; $A = (a, b, c)$ and $A^* = (a^*, b^*, c^*)$ be choosen. Then by projecting to a spherical point $\hat{X}_0 = X_0 + \varepsilon X_0^*$ on the curve $\hat{\gamma}$, the point $\hat{X} = X + \varepsilon X^*$ on the line L corresponds to a line congruence M in R^3 such that*

$$M(\lambda, \lambda^*, \nu) = \frac{(a+\lambda d_1, b+\lambda d_2, c+\lambda d_3) \times (a^*+\lambda d_1^*+\lambda^* d_1, b^*+\lambda d_2^*+\lambda^* d_2, c^*+\lambda d_3^*+\lambda^* d_3)}{(a+\lambda d_1)^2+(b+\lambda d_2)^2+(c+\lambda d_3)^2} + \nu \frac{(a+\lambda d_1, b+\lambda d_2, c+\lambda d_3)}{\sqrt{(a+\lambda d_1)^2+(b+\lambda d_2)^2+(c+\lambda d_3)^2}}$$

Satisfies.

If this line congruence can be written as

$$M(\lambda, \lambda^*, \nu) = (M_1(\lambda, \lambda^*, \nu), M_2(\lambda, \lambda^*, \nu), M_3(\lambda, \lambda^*, \nu))$$

then these coordinat functions ca be stated as follows

$$M_1(\lambda, \lambda^*, \nu) = \frac{(bc^* - cb^*) + \lambda(bd_3^* - d_3 b^* + cd_2^* - d_2 c^*) + \lambda^*(bd_3 - cd_2) + \lambda^2(d_2 d_3^* - d_3 d_2^*)}{(a + \lambda d_1)^2 + (b + \lambda d_2)^2 + (c + \lambda d_3)^2} + \frac{\nu(a + \lambda d_1)}{\sqrt{(a + \lambda d_1)^2 + (b + \lambda d_2)^2 + (c + \lambda d_3)^2}}$$

$$M_2(\lambda, \lambda^*, \nu) = \frac{(ca^* - ac^*) + \lambda(cd_1^* - d_1 c^* + d_3 a^* - ad_3^*) + \lambda^*(cd_1 - ad_3) + \lambda^2(d_3 d_1^* - d_3^* d_1)}{(a + \lambda d_1)^2 + (b + \lambda d_2)^2 + (c + \lambda d_3)^2} + \frac{\nu(b + \lambda d_2)}{\sqrt{(a + \lambda d_1)^2 + (b + \lambda d_2)^2 + (c + \lambda d_3)^2}}$$

$$M_3(\lambda, \lambda^*, \nu) = \frac{(ab^* - ba^*) + \lambda(ad_2^* - d_2 a^* + d_1 b^* - bd_1^*) + \lambda^*(ad_2 - bd_1) + \lambda^2(d_1 d_2^* - d_1^* d_2)}{(a + \lambda d_1)^2 + (b + \lambda d_2)^2 + (c + \lambda d_3)^2} + \frac{\nu(c + \lambda d_3)}{\sqrt{(a + \lambda d_1)^2 + (b + \lambda d_2)^2 + (c + \lambda d_3)^2}}$$

When this line congruence is examined the directrix surface is quadratic by means of the parameter λ and is linear by means of the parameter λ^* . This congruence can be roughly envisioned as following figure (fig.2).

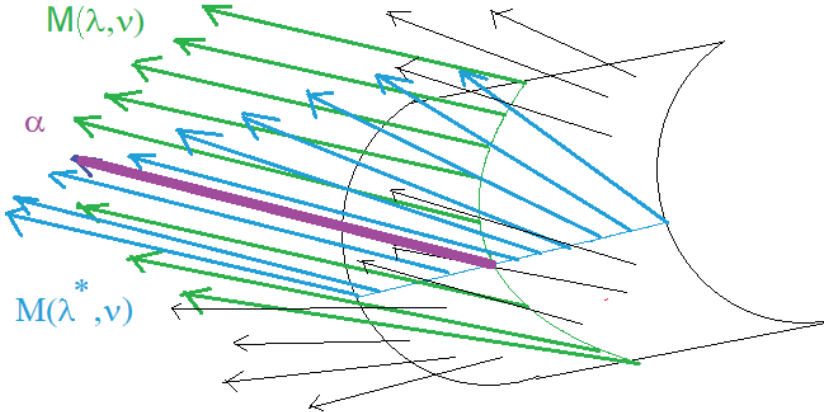


Fig.2: Line congruence $M(\lambda, \lambda^*, \nu)$ corresponding to a dual line L

In Figure 2, the set formed by the green colored lines is a ruled surface $M(\lambda, \nu)$, which is the real space correspondent of the points $\lambda^* = 0$ selected from the points on the line L in dual space.

Similarly the set formed by the blue colored lines is a ruled surface $M(\lambda^*, \nu)$, which is the real space correspondent of the points $\lambda = 0$ selected from the points on the line L in dual space.

And the line α colored by purple in fig.2, is a line corresponding to the point \hat{A} on the line L according to $\lambda = 0$ and $\lambda^* = 0$.

As point \hat{A} moves on the line L , the green and blue colored ruled surfaces will also move on the directrix surface. As a result of this $M(\lambda, 0, \nu) = M(\lambda, \nu)$, $M(0, \lambda^*, \nu) = M(\lambda^*, \nu)$, $M(0, 0, \nu) = \alpha$ can be obtained.

Remark 3.1: Examining the statement of the theorem, the following result is obtained: Starting from the curve α on the congruence, no matter which direction we move on the directrix surface of the congruence (whatever value is chosen in the λ), the direction of the neighboring principal lines will deviate from the direction of the α towards the direction \vec{d} .

Example:

Let a dual line L in the direction $\vec{D} = \vec{d} + \epsilon\vec{d}^*$ passing through $\hat{A} = A + \epsilon A^*$ be given. If $\vec{d} = (1, -1, 2)$; $\vec{d}^* = (-1, 1, -1)$; $A = (0, 2, 1)$ and $A^* = (-1, 0, 4)$ be choosen. Then the ruled surface M corresponding dual line L can e parametrized as follows:

$$M_1(\lambda, \lambda^*, v) = \frac{8 + 3\lambda + 5\lambda^* - \lambda^2}{(\lambda)^2 + (2 - \lambda)^2 + (1 + 2\lambda)^2} + \frac{\lambda v}{\sqrt{(\lambda)^2 + (2 - \lambda)^2 + (1 + 2\lambda)^2}}$$

$$M_2(\lambda, \lambda^*, v) = \frac{-1 - 7\lambda - \lambda^* - \lambda^2}{(\lambda)^2 + (2 - \lambda)^2 + (1 + 2\lambda)^2} + \frac{v(2 - 2\lambda)}{\sqrt{(\lambda)^2 + (2 - \lambda)^2 + (1 + 2\lambda)^2}}$$

$$M_3(\lambda, \lambda^*, v) = \frac{2 + \lambda - 2\lambda^*}{(\lambda)^2 + (2 - \lambda)^2 + (1 + 2\lambda)^2} + \frac{v(1 + 2\lambda)}{\sqrt{(\lambda)^2 + (2 - \lambda)^2 + (1 + 2\lambda)^2}}$$

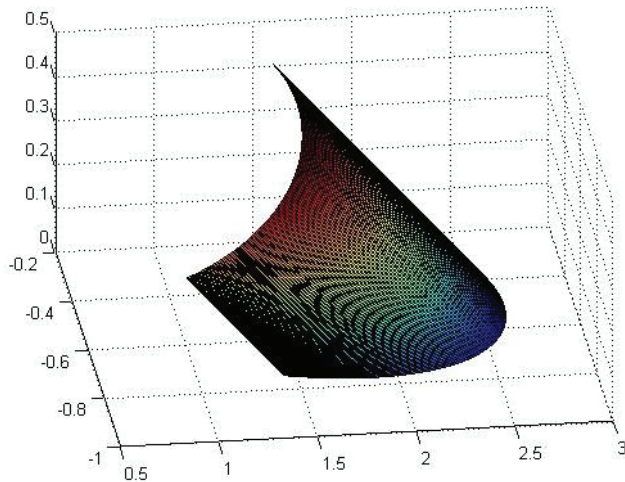


Fig.3: The directrix surface of line congruence corresponding to dual line L

Cases on Two Lines:

Let two lines L_1 and L_2 be given. Let's examine the states of these two lines relative to each other.

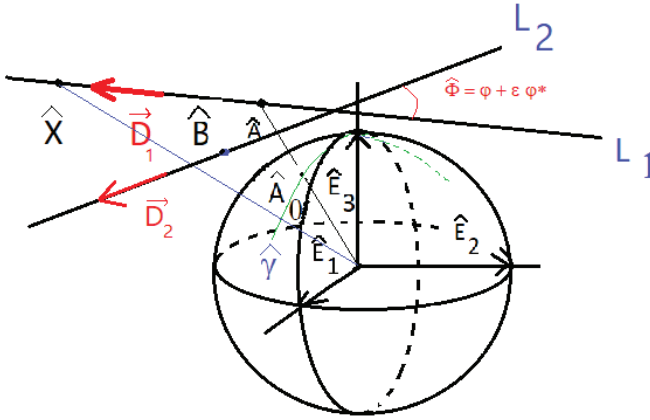


Fig. 4: Two lines in $D^{\wedge}3$

Let two lines L_1 passing through the point $\hat{A} = A + \varepsilon A^*$ and in the direction $\vec{D}_1 = \vec{d}_1 + \varepsilon \vec{d}_1^*$, and L_2 passing through the point $\hat{B} = B + \varepsilon B^*$ and in the direction $\vec{D}_2 = \vec{d}_2 + \varepsilon \vec{d}_2^*$ be given. (see Fig.4) Let $\vec{d}_1 = (d_{11}, d_{12}, d_{13})$, $\vec{d}_2 = (d_{21}, d_{22}, d_{23})$, $\vec{d}_1^* = (d_{11}^*, d_{12}^*, d_{13}^*)$, $A = (a_1, a_2, a_3)$, $\vec{d}_2^* = (d_{21}^*, d_{22}^*, d_{23}^*)$, $A^* = (a_1^*, a_2^*, a_3^*)$, $B = (b_1, b_2, b_3)$, $B^* = (b_1^*, b_2^*, b_3^*)$ be denoted. In 3- space for two lines there are 3 cases: to be parallel, to coincide, or to be separate.

First of all we define the dual angle between two lines L_1 and L_2 . It is clear that the dual angle between L_1 and L_2 is an angle between director vectors \vec{D}_1 and \vec{D}_2 of these lines.

$$\begin{aligned} \hat{\Phi} = \sphericalangle(L_1, L_2) &= \sphericalangle(\vec{D}_1, \vec{D}_2) = \arccos \left(\frac{\langle \vec{D}_1, \vec{D}_2 \rangle}{\|\vec{D}_1\| \|\vec{D}_2\|} \right) \\ &= \arccos \left(\frac{\langle \vec{d}_1 + \varepsilon \vec{d}_1^*, \vec{d}_2 + \varepsilon \vec{d}_2^* \rangle}{\|\vec{d}_1 + \varepsilon \vec{d}_1^*\| \|\vec{d}_2 + \varepsilon \vec{d}_2^*\|} \right) \\ &= \arccos \left(\frac{\langle \vec{d}_1, \vec{d}_2 \rangle + \varepsilon [\langle \vec{d}_1, \vec{d}_2^* \rangle + \langle \vec{d}_1^*, \vec{d}_2 \rangle]}{\left(\|\vec{d}_1\| + \varepsilon \frac{\langle \vec{d}_1, \vec{d}_1^* \rangle}{\|\vec{d}_1\|} \right) \left(\|\vec{d}_2\| + \varepsilon \frac{\langle \vec{d}_2, \vec{d}_2^* \rangle}{\|\vec{d}_2\|} \right)} \right) \\ &= \arccos \left(\frac{\langle \vec{d}_1, \vec{d}_2 \rangle}{\|\vec{d}_1\| \|\vec{d}_2\|} + \varepsilon \left[\frac{\langle \vec{d}_1, \vec{d}_2^* \rangle + \langle \vec{d}_1^*, \vec{d}_2 \rangle}{\|\vec{d}_1\| \|\vec{d}_2\|} - \frac{\langle \vec{d}_1, \vec{d}_2 \rangle}{\|\vec{d}_1\| \|\vec{d}_2\|} \left(\frac{\langle \vec{d}_2, \vec{d}_2^* \rangle}{\|\vec{d}_2\|^3} + \frac{\langle \vec{d}_1, \vec{d}_1^* \rangle}{\|\vec{d}_1\|^3} \right) \right] \right) \\ &= \varphi + \varepsilon \varphi^* \end{aligned}$$

is obtained. So taking the cosine of both sides of the equation and considering the property

$$\cos \widehat{\Phi} = \cos(\varphi + \varepsilon\varphi^*) = \cos\varphi - \varepsilon\varphi^* \sin\varphi$$

the real part of these dual angle φ is the real angle between the vectors \vec{d}_1, \vec{d}_2 . If the vectors \vec{d}_1, \vec{d}_2 are nonzero and linearly independent then the real and dual part of the dual angle is

$$\varphi = \text{arc cos} \left(\frac{\langle \vec{d}_1, \vec{d}_2 \rangle}{\|\vec{d}_1\| \|\vec{d}_2\|} \right)$$

and

φ^*

$$= \frac{\langle \vec{d}_1, \vec{d}_2 \rangle \left(\frac{\langle \vec{d}_2, \vec{d}_2^* \rangle}{\|\vec{d}_2\|^3} + \frac{\langle \vec{d}_1, \vec{d}_1^* \rangle}{\|\vec{d}_1\|^3} \right) - \langle \vec{d}_1, \vec{d}_2^* \rangle - \langle \vec{d}_1^*, \vec{d}_2 \rangle}{\|\vec{d}_1 \times \vec{d}_2\|}$$

or

$$\varphi^* = \text{cot} \varphi \left(\frac{\langle \vec{d}_2, \vec{d}_2^* \rangle}{\|\vec{d}_2\|^3} + \frac{\langle \vec{d}_1, \vec{d}_1^* \rangle}{\|\vec{d}_1\|^3} \right) - \left[\frac{\langle \vec{d}_1, \vec{d}_2^* \rangle + \langle \vec{d}_1^*, \vec{d}_2 \rangle}{\|\vec{d}_1 \times \vec{d}_2\|} \right]$$

are obtained. So this following theorem can be given.

Theorem 3.5: Let two lines L_1 passing through the point $\hat{A} = A + \varepsilon A^*$ and in the direction $\vec{D}_1 = \vec{d}_1 + \varepsilon \vec{d}_1^*$, and L_2 passing through the point $\hat{B} = B + \varepsilon B^*$ and in the direction $\vec{D}_2 = \vec{d}_2 + \varepsilon \vec{d}_2^*$ be given. (see Fig.4) Let $\vec{d}_1 = (d_{11}, d_{12}, d_{13}), \vec{d}_2 = (d_{21}, d_{22}, d_{23}), \vec{d}_1^* = (d_{11}^*, d_{12}^*, d_{13}^*), A = (a_1, a_2, a_3), \vec{d}_2^* = (d_{21}^*, d_{22}^*, d_{23}^*), A^* = (a_1^*, a_2^*, a_3^*), B = (b_1, b_2, b_3), B^* = (b_1^*, b_2^*, b_3^*)$ be denoted. Then the dual angle between L_1 and L_2 is an angle $\widehat{\Phi} = \varphi + \varepsilon\varphi^*$ such that

$$\varphi = \text{arc cos} \left(\frac{\langle \vec{d}_1, \vec{d}_2 \rangle}{\|\vec{d}_1\| \|\vec{d}_2\|} \right)$$

and

$$\varphi^* = \frac{\langle \vec{d}_1, \vec{d}_2 \rangle \left(\frac{\langle \vec{d}_2, \vec{d}_2^* \rangle}{\|\vec{d}_2\|^3} + \frac{\langle \vec{d}_1, \vec{d}_1^* \rangle}{\|\vec{d}_1\|^3} \right) - \langle \vec{d}_1, \vec{d}_2^* \rangle - \langle \vec{d}_1^*, \vec{d}_2 \rangle}{\|\vec{d}_1 \times \vec{d}_2\|}$$

or

$$\varphi^* = \cot \varphi \left(\frac{\langle \vec{d}_2, \vec{d}_2^* \rangle}{\|\vec{d}_2\|^3} + \frac{\langle \vec{d}_1, \vec{d}_1^* \rangle}{\|\vec{d}_1\|^3} \right) - \left[\frac{\langle \vec{d}_1, \vec{d}_2^* \rangle + \langle \vec{d}_1^*, \vec{d}_2 \rangle}{\|\vec{d}_1 \times \vec{d}_2\|} \right]$$

satisfies if the vectors \vec{d}_1, \vec{d}_2 are nonzero and linearly independent.

Case 1: to be parallel of two lines L_1 and L_2 .

If two lines L_1 passing through the point $\hat{A} = A + \varepsilon A^*$ and in the direction $\vec{D}_1 = \vec{d}_1 + \varepsilon \vec{d}_1^*$, and L_2 passing through the point $\hat{B} = B + \varepsilon B^*$ and in the direction $\vec{D}_2 = \vec{d}_2 + \varepsilon \vec{d}_2^*$ are parallel then these following results can be given.

Theorem 3.6: 1- $L_1 \parallel L_2$ if and only if \vec{D}_1 and \vec{D}_2 linearly dependent.

2- $L_1 \parallel L_2$ if and only if $\vec{D}_1 \times \vec{D}_2 = 0$

3- $L_1 \parallel L_2$ if and only if $\vec{d}_1 \times \vec{d}_2 = 0$ and $\vec{d}_1 \times \vec{d}_2^* + \vec{d}_1^* \times \vec{d}_2 = 0$

4- $L_1 \parallel L_2$ if and only if there exist $\lambda, \mu \in R$ such that $\vec{d}_2 = \lambda \vec{d}_1$ and

$$\vec{d}_2^* = \mu \vec{d}_1 + \lambda \vec{d}_1^* \text{ satisfies.}$$

5- $L_1 \parallel L_2$ if and only if the real angle φ between the vectors \vec{d}_1, \vec{d}_2 is zero or π and

$$\langle \vec{d}_1, \vec{d}_2^* \rangle + \langle \vec{d}_1^*, \vec{d}_2 \rangle = \left(\frac{\|\vec{d}_1\| \|\langle \vec{d}_2, \vec{d}_2^* \rangle\|}{\|\vec{d}_2\|^2} + \frac{\|\vec{d}_2\| \|\langle \vec{d}_1, \vec{d}_1^* \rangle\|}{\|\vec{d}_1\|^2} \right)$$

Satisfies

Now If the lines L_1 and L_2 are parallel, let's examine the states of the congruences corresponding to these lines. Let the directed line corresponding to the point \hat{A} on the line L_1 be denoted as α and the directed line corresponding to the point \hat{B} on the line L_2 be denoted as β . Then this following remark can be stated.

Remark 3.2: From Theorem 3.1, if the lines L_1 and L_2 are parallel then Starting from the curve α and β on the congruences M1 and M2 corresponding these lines, no matter which direction we move on their directrix surfaces of these congruences, the direction of the neighboring principal lines will deviate from the direction of the α and β towards the same direction \vec{d} .

Second case: to coincide or to be separate (not parallel) of two lines L_1 and L_2 .

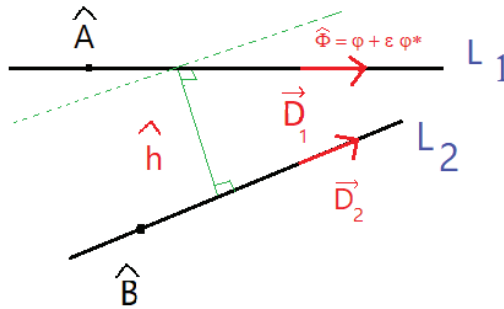


Fig.5: Separate lines in D^3

In this case the angle between given two lines L_1 and L_2 is $\hat{\Phi} = \varphi + \varepsilon\varphi^*$ and the dual distance between given two lines L_1 and L_2 is $\hat{h} = h + \varepsilon h^*$. If two lines L_1 and L_2 are coincide then $\hat{h} = 0$.

$$\begin{aligned}
 \hat{h} &= \frac{\langle \overrightarrow{A\hat{B}}, \overrightarrow{D_1} \times \overrightarrow{D_2} \rangle}{\|\overrightarrow{D_1} \times \overrightarrow{D_2}\|} \\
 &= \frac{\langle (B - A) + \varepsilon(B^* - A^*), \overrightarrow{d_1} \times \overrightarrow{d_2} + \varepsilon(\overrightarrow{d_1} \times \overrightarrow{d_2^*} + \overrightarrow{d_1^*} \times \overrightarrow{d_2}) \rangle}{\|\overrightarrow{d_1} \times \overrightarrow{d_2}\| + \varepsilon \left(\frac{\langle \overrightarrow{d_1} \times \overrightarrow{d_2}, (\overrightarrow{d_1} \times \overrightarrow{d_2^*} + \overrightarrow{d_1^*} \times \overrightarrow{d_2}) \rangle}{\|\overrightarrow{d_1} \times \overrightarrow{d_2}\|} \right)} \\
 &= \frac{\langle B - A, \overrightarrow{d_1} \times \overrightarrow{d_2} \rangle + \varepsilon [\langle B - A, \overrightarrow{d_1} \times \overrightarrow{d_2^*} \rangle + \langle B - A, \overrightarrow{d_1^*} \times \overrightarrow{d_2} \rangle + \langle B^* - A^*, \overrightarrow{d_1} \times \overrightarrow{d_2} \rangle]}{\|\overrightarrow{d_1} \times \overrightarrow{d_2}\| + \varepsilon \left(\frac{\|\overrightarrow{d_1}\|^2 \langle \overrightarrow{d_2}, \overrightarrow{d_2^*} \rangle + \|\overrightarrow{d_2}\|^2 \langle \overrightarrow{d_1}, \overrightarrow{d_1^*} \rangle - \langle \overrightarrow{d_1}, \overrightarrow{d_2} \rangle \langle \overrightarrow{d_1}, \overrightarrow{d_2} + \overrightarrow{d_2^*} \rangle}{\|\overrightarrow{d_1} \times \overrightarrow{d_2}\|} \right)} \\
 &= \\
 &\frac{\langle B - A, \overrightarrow{d_1} \times \overrightarrow{d_2} \rangle}{\|\overrightarrow{d_1} \times \overrightarrow{d_2}\|} + \\
 &\varepsilon \left[\frac{\langle B - A, \overrightarrow{d_1} \times \overrightarrow{d_2^*} \rangle + \langle B - A, \overrightarrow{d_1^*} \times \overrightarrow{d_2} \rangle + \langle B^* - A^*, \overrightarrow{d_1} \times \overrightarrow{d_2} \rangle}{\|\overrightarrow{d_1} \times \overrightarrow{d_2}\|} - \right. \\
 &\left. \frac{\langle B - A, \overrightarrow{d_1} \times \overrightarrow{d_2} \rangle \left[\|\overrightarrow{d_1}\|^2 \langle \overrightarrow{d_2}, \overrightarrow{d_2^*} \rangle + \|\overrightarrow{d_2}\|^2 \langle \overrightarrow{d_1}, \overrightarrow{d_1^*} \rangle - \langle \overrightarrow{d_1}, \overrightarrow{d_2} \rangle \langle \overrightarrow{d_1}, \overrightarrow{d_2} + \overrightarrow{d_2^*} \rangle \right]}{\|\overrightarrow{d_1} \times \overrightarrow{d_2}\|^3} \right] \\
 &= h + \varepsilon h^*
 \end{aligned}$$

is obtained. Here h is the distance between the real lines ℓ_1 passing through the point A and in the direction $\overrightarrow{d_1}$, and ℓ_2 passing through the point B and in the direction $\overrightarrow{d_2}$. So the following theorem can be given.

Theorem 3.7: If two lines L_1 passing through the point $\hat{A} = A + \varepsilon A^*$ and in the direction $\overrightarrow{D_1} = \overrightarrow{d_1} + \varepsilon \overrightarrow{d_1^*}$, and L_2 passing through the point $\hat{B} = B + \varepsilon B^*$ and in the direction $\overrightarrow{D_2} = \overrightarrow{d_2} + \varepsilon \overrightarrow{d_2^*}$ be given. Then the dual distance between given two lines L_1 and L_2 is $\hat{h} = h + \varepsilon h^*$ where

$$h = \frac{\langle B - A, \overrightarrow{d_1} \times \overrightarrow{d_2} \rangle}{\|\overrightarrow{d_1} \times \overrightarrow{d_2}\|}$$

and

$$\begin{aligned}
 h^* &= \\
 &= \frac{[\langle B - A, \overrightarrow{d_1} \times \overrightarrow{d_2^*} \rangle + \langle B - A, \overrightarrow{d_1^*} \times \overrightarrow{d_2} \rangle + \langle B^* - A^*, \overrightarrow{d_1} \times \overrightarrow{d_2} \rangle]}{\|\overrightarrow{d_1} \times \overrightarrow{d_2}\|} \\
 &- \frac{\langle B - A, \overrightarrow{d_1} \times \overrightarrow{d_2} \rangle \left[\|\overrightarrow{d_1}\|^2 \langle \overrightarrow{d_2}, \overrightarrow{d_2^*} \rangle + \|\overrightarrow{d_2}\|^2 \langle \overrightarrow{d_1}, \overrightarrow{d_1^*} \rangle - \langle \overrightarrow{d_1}, \overrightarrow{d_2} \rangle \langle \overrightarrow{d_1}, \overrightarrow{d_2} + \overrightarrow{d_2^*} \rangle \right]}{\|\overrightarrow{d_1} \times \overrightarrow{d_2}\|^3}
 \end{aligned}$$

Here h is the distance between the real lines ℓ_1 passing through the point A and in the direction \vec{d}_1 , and ℓ_2 passing through the point B and in the direction \vec{d}_2 .

Theorem 3.8: Let the two lines L_1 passing through the point $\hat{A} = A + \varepsilon A^*$ and in the direction $\vec{D}_1 = \vec{d}_1 + \varepsilon \vec{d}_1^*$, and L_2 passing through the point $\hat{B} = B + \varepsilon B^*$ and in the direction $\vec{D}_2 = \vec{d}_2 + \varepsilon \vec{d}_2^*$ be intersect at point $\hat{C} = C + \varepsilon C^*$. Then the congruences M1 and M2 corresponding to these lines contain the same directed line corresponding to the dual point \hat{C} .

Example:

Let the two lines L_1 passing through the point $\hat{A} = (1,0,2) + \varepsilon(0,1,-1)$ and in the direction $\vec{D}_1 = (1,-1,2) + \varepsilon(2,-1,1)$, and L_2 passing through the point $\hat{B} = (0,-3,0) + \varepsilon(6,-4,-1)$ and in the direction $\vec{D}_2 = (1,1,-1) + \varepsilon(-1,2,1)$ be considered. These lines can be parametrized as

$$\begin{aligned} \lambda + \varepsilon\lambda^* &= \frac{x-1}{1} + \varepsilon\left(\frac{x^*}{1} - \frac{(x-1)2}{1}\right) \\ &= \frac{y}{-1} + \varepsilon\left(\frac{y^*-1}{-1} - \frac{(-1)y}{1}\right) \\ &= \frac{z-2}{2} + \varepsilon\left(\frac{z^*+1}{2} - \frac{(z-2)}{4}\right) \end{aligned}$$

and

$$\begin{aligned} \mu + \varepsilon\mu^* &= \frac{x}{1} + \varepsilon\left(\frac{x^*-6}{1} - \frac{(-1)x}{1}\right) \\ &= \frac{y+3}{1} + \varepsilon\left(\frac{y^*+4}{1} - \frac{(y+3)2}{1}\right) \\ &= \frac{z}{2} + \varepsilon\left(\frac{z^*+1}{-1} - \frac{(z)}{1}\right) \end{aligned}$$

Thus $\lambda + \varepsilon\lambda^* = 1 + \varepsilon$ and $\mu + \varepsilon\mu^* = 2 - \varepsilon$ are obtained when these equations solve with together. So two lines coincide at the dual point $\hat{C} = (2, -1, 4) + \varepsilon(3, -1, 2)$.

According to Theorem 3.4 these lines corresponds to the following line congruences:

L_1 :

$$M_1(\lambda, \lambda^*, \nu) = \frac{-2 - 5\lambda + 2\lambda^* + \lambda^2}{(\lambda)^2 + 5(1 + \lambda)^2} + \frac{\nu(1 + \lambda)}{\sqrt{(\lambda)^2 + 5(1 + \lambda)^2}}$$

$$M_2(\lambda, \lambda^*, \nu) = \frac{+1 + 4\lambda + 3\lambda^2}{(\lambda)^2 + 5(1 + \lambda)^2} - \frac{\nu\lambda}{\sqrt{(\lambda)^2 + 5(1 + \lambda)^2}}$$

$$M_3(\lambda, \lambda^*, \nu) = \frac{\lambda^2 - \lambda^* + 1}{(\lambda)^2 + 5(1 + \lambda)^2} + \frac{\nu(2 + 2\lambda)}{\sqrt{(\lambda)^2 + 5(1 + \lambda)^2}}$$

L_2 :

$$M_1(\lambda, \lambda^*, \nu) = \frac{+3 - 6\lambda + 3\lambda^* + 3\lambda^2}{2\lambda^2 + (-3 + \lambda)^2} + \frac{\nu\lambda}{\sqrt{2\lambda^2 + (-3 + \lambda)^2}}$$

$$M_2(\lambda, \lambda^*, \nu) = \frac{-5\lambda}{2\lambda^2 + (-3 + \lambda)^2} + \frac{\nu(-3 + \lambda)}{\sqrt{2\lambda^2 + (-3 + \lambda)^2}}$$

$$M_3(\lambda, \lambda^*, \nu) = \frac{3\lambda^2 + 3\lambda^* - 13\lambda + 18}{2\lambda^2 + (-3 + \lambda)^2} - \frac{\nu\lambda}{\sqrt{2\lambda^2 + (-3 + \lambda)^2}}$$

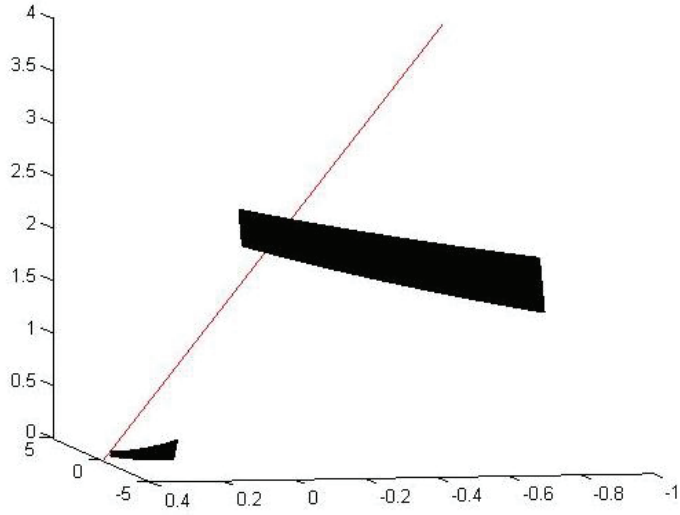


Fig.6: directrix surfaces and common line of of two line congruences corresponding to lines L_1 and L_2

References

1. W. K. Clifford, (1873) Preliminary sketch of bi-quaternions. Proceedings of the London Mathematical Society, s1-4(1):381-395.
2. E. Study (1891), Von den bewegungen und umlegungen. Mathematische Annalen, 39, 441-566.
3. H.R.Müller, Sphärische Kinematik, VEB Deutscher Verlag der Wissenschaften, Berlin 1962.
4. H. H. Hacısaliholu, On the pitch of a ruled surface, *Mech. Mach. Theory*, Great Britain **7** (1972) 291-305, doi: 10.1016/0094-114X(72)90039-0.
5. J. M. McCarthy and B. Roth, The curvature theory of line trajectories in spatial kinematics, *J. Mech. Design* **103**(4) (1981) 718-724, doi: 10.1115/1.3254978.
6. Hacısalihoğlu, H. H. (1983). *Hareket geometrisi ve kuaterniyonlar teorisi*. Gazi Üniversitesi.
7. K.-L. Ting and A. H. Soni, Instantaneous kinematics of a plane in spherical motion, *J. Mech. Transmissions, and Automation in Design* **105**(3) (1983) 560-567, doi:10.1115/1.3267395.
8. Tiller W. and Hanson E., (1984) Offsets of two- dimensional profiles, *IEEE Computer Graphics and Applications*, 4, 36-46.
9. Hoschek J., (1985) Offset curves in the plane, *Computer Aided Design*, 17, 2, 77-82.
10. GURSOY, O. (1990a), The Dual Angle of A Closed Ruled Surface, *Mech. Mach. Theory*, 25 (2), 131-140.
11. GURSOY, O. (1990b), On Integral Invariant of A Closed Ruled Surface, *Journal of Geometry*, vol.39, 80-91.
12. GURSOY, O. (1992), Some Results on Closed Ruled Surfaces and Closed space Curves *Mech. Mach. Theory*, 27, 323-330
13. Potmann H., (1995) Rational curves and surfaces with rational offsets, *Computer Aided Geometric Design*, 12, 175-192.
14. X. F. Zha, (1997) A new approach to generation of ruled surfaces and its applications in engineering, *Int. J. Adv. Manuf. Technol.* **13** 155-163, doi: 10.1007/BF01305867.
15. GURSOY, O., Küçük A. (1999), On the Invariants of Trajectory Surfaces, *Mech. Mach. Theory*, 34, 587-597.
16. GURSOY, O., Küçük A., (2004) On the Invariants of Bertrand Trajectory Surfaces Offsets, *Applied Mathematics and Computation*, 151(3), 763-773.
17. F. Taş, K. İlarıslan (2019) A new approach to design the ruled surface, *International Journal of Geometric Methods in Modern Physics* Vol. 16, No. 6, 1950093 (16 pages)
18. F. Taş, On the Design and Invariants of a Ruled Surface, <https://arxiv.org/ftp/arxiv/papers/1706/1706.00267.pdf>
19. Emilija Nešović, Ufuk Öztürk, Esra B. Koç Öztürk, Kazım İlarıslan, (2016) On ruled surfaces with pseudo null base curve in Minkowski 3-space, *Int. Electron. J. Geom.* **9**(2) 9-20.
20. F. Hathout, M. Bekar and Y. Yaylı, (2017) Ruled surfaces and tangent bundle of unit 2-sphere, *Int. J. Geom. Meth. Mod. Phys.* **14** 1750145.

21. F. Güler and E. Kasap, (2018) A path planning method for robot end effector motion using the curvature theory of the ruled surfaces, *Int. J. Geom. Meth. Mod. Phys.* **15** 1850048.
22. F. Taş, (2016) A method of determining dual unit spherical B'ezier curves and line surfaces, *J. Logic Math. Linguistics Appl. Sci.* **1** 1–6.
23. F. Taş and O. Gürsoy, (2018) On the line congruences, *Int. Electron. J. Geom.* **11**(2) 47–53.
24. Küçük A. (2004) On the developable timelike trajectory ruled surfaces in Lorentz 3-space $3_1 \mathbb{R}$. *App Math and Comp*; 157: 483-489
25. Kazaz M, Özdemir A, Güröğlü T. (2008) On the determination of a developable timelike ruled surface. *SDÜ Fen-Edebiyat Fakültesi Fen Dergisi (E-Dergi)*; 3(1): 72-79
26. Mavroidis C. and Roth B., (1997) On the Geometry of Spatial Polygons and Screw Polygons, *Journal of Mechanical Design Transactions of the ASME*, 119, 246-252.
27. Incesu, M., & Gursoy, O. (2004). B'ezier Yüzeylerinde Esas Formlar ve Eğrilikler. *XVII Ulusal Matematik Sempozyumu*, 146-157.
28. Choi B.K.,(1991) *Surface Modeling for CAD/CAM*, Elsevier Science Publishers B.V., Amsterdam.
29. Liming R., (1944) *Practical Analytic Geometry with Applications to Aircraft*, Macmillan.
30. Muhsin incesu, (2021) The new characterization of Ruled surfaces corresponding Dual B'ezier curves, *Mathematical Methods in the Applied Sciences*, MMA7398, 17038625, doi: <https://doi.org/10.1002/mma.7398>
31. Muhsin incesu, Osman Gürsoy, (2018) On the Bertrand Dual Curve Pairs, INTERNATIONAL CONFERENCE ON MATHEMATICS “An Istanbul Meeting for World Mathematicians” Minisymposium on Approximation Theory & Minisymposium on Math Education 3-6 July 2018, İstanbul, Turkey pp: 149-154
32. Gray A., (1998) *Modern Differential Geometry of curves and surfaces with Mathematica*, 2nd edition, CRC Press LCC, Boca Raton, Florida.
33. Divjak, Blaženka, and Zcaron Milin-Šipuš. (2002) "Special curves on ruled surfaces in Galilean and pseudo-Galilean spaces." *Acta Mathematica Hungarica* 98.3: 203-215.